Reversible Immobilisation of DNA and Metal Nanoparticles on Engineered Surfaces using the Fluorous Effect.

Hammed Ayantola Onilude

April 2024

A Thesis Submitted to the

Division of Biomedical Engineering

School of Engineering, University of Glasgow

In Fulfilment of the Requirements for

The Degree of Doctor of Philosophy (Ph.D.)

Abstract

This thesis investigates the reversible attachment of nanomaterials to modified surfaces via the fluorous effect, a hydrophobic and non-covalent interaction involving perfluorinated molecules or molecules with a high fluorine content. The study introduces a novel approach to utilising the fluorous effect for the reversible attachment of fluorous-tagged nanomaterials, such as DNA and nanoparticles, on fluorous-modified patterned glass surfaces.

In the first method, the stability of perfluorinated DNA when immobilised on solid support was evaluated based on factors including size, the number of fluorine atoms attached, branching systems, and the incorporation of a spacer/linker. The results revealed that the attachment strength of the DNA to the solid support increases with the length of the DNA chain, the number of branches, and a higher number of incorporated fluorine atoms. Consequently, the methanol concentration necessary to detach these strands from the solid support correlates with the number of attached fluorines. Additionally, the study compared the selective removal of different fluorous-tagged DNA structures (single and branched) based on their attachment strength to the fluorous-modified solid support. The results revealed that as the number of branch systems increases from one to four, the strength of attachment increases with the highest strength from the tetra-branch (four branches) without a linker, and the perfluorinated chains can be selectively removed from the solid support. This method is suitable for multiplex systems to identify and selectively remove target probes.

The second method extends this approach to the reversible attachment of thiol-modified metal nanoparticles (gold and silver) in aqueous environments. Here, citrate-coated gold nanoparticles of varying sizes (15 nm, 20 nm, and 45 nm) and chloride-coated silver nanoparticles (52 nm) were functionalised and reversibly attached to an 800 μm-sized fluorous-modified micropatterned surface. This method enables the repeatable and switchable attachment of gold and silver nanoparticles on the same reusable surface multiple times without damaging the fluorous-modified layer.

Finally, the fluorous effect facilitated the self-assembly of 55 nm gold nanoparticles on a fluorous-modified nanopatterned surface (sub-500 nm). This method demonstrated repeatability at 500 nm without unwanted aggregation and

promising outcomes in the sub-100 nm region, enabling single-particle attachment.

Overall, this research highlights the potential of the fluorous effect in the self-assembly of nanomaterials, offering a practical method for microarray development and the reversible attachment of nanomaterials on solid supports.

Table of Contents

List of Tables

List of Figures

Acknowledgement

I appreciate TETFUND and the Nigerian Government for providing this platform. Without this initiative, achieving this feat may be difficult for scholars.

I want to express my sincere gratitude to my supervisor, Professor Alasdair W Clark, for his exceptional mentorship and guidance. Thank you for your expertise, unwavering support, and insightful feedback. I also want to thank my second supervisor, Professor Steven L Neale, for his support during this period. Your contributions to my academic and professional growth will always be appreciated.

I would also like to recognise the contribution of Dr. Jamie M. Withers, Dr. Andrea Sender, and Professor Burley from the Burley group at the University of Strathclyde for their collaboration and support during this research. It was a pleasant experience collaborating with your group on this fluorous ‘journey’.

Additionally, I wish to extend my profound appreciation to my esteemed colleague, Marina Santana Vega, whose guidance, expertise, and support were invaluable during the final stages of this research. Your input was always invaluable in sticking those metal nanoparticles on those surfaces, and I am genuinely grateful for her contributions to my academic endeavours. To Justin Sperling, I remembered the first day this started. Thank you for the journey. I appreciate you guys setting the pace for me at each research stage.

To my colleagues, Ashley Stammers, Jiajia Zhou, Sara Angelucci, Iain Christie, Greig Govenlock, Badri Aekbote, Sara Shadman, Sathkumara Mudalige, and Rebecca Setford, I want to express my heartfelt gratitude. You guys are amazing. Despite the challenges we faced in the lab, it's always a pleasure to work with such a supportive team. I will always cherish those moments when our ideas were tested and how we overcame the odds.

I would also like to thank all JWNC staff, professors, committees, and all those who have supported this journey from the University of Glasgow and beyond.

Furthermore, I extend my heartfelt appreciation to my friends Wandiayhel Yaduma, Prince Ubiaru, Mark Sanda, and Lydia Jylantikiri for their unwavering support and encouragement. I am happy that we were able to create this support base for one another during this Doctoral journey.

To Agboola Odesanya, this section would not have been complete without you. It was nice giving each other those necessary distractions to maintain our sanity.

Last but certainly not least, I would like to express my deep gratitude to my family for their unending support, understanding, and relentless encouragement throughout this academic pursuit. Your love, encouragement, and belief in my abilities have been the cornerstone of my achievements, and I am genuinely thankful for this.

My dear wife, you are truly outstanding. I cannot thank you enough for always being there for me throughout this journey. Without your support, nothing would have been achieved. To my kids, it is time to resume our pillow ‘fight’ and spend more time together.

Thank you for walking this journey with me!

Author's Declaration

'I declare that, except where explicit reference is made to the contribution of others, this thesis is the result of my work and has not been submitted for any other degree at the University of Glasgow or any other institution.'

Signature……

Date…..……

Hammed Ayantola Onilude

University of Glasgow

Chapter 1 Introduction

1.1 Research Motivation

Using the fluorous effect, this thesis investigates a novel strategy to reversibly attach nanomaterials (DNA and metal nanoparticles) onto micro and nanopatterned surfaces. Microarrays are tools for examining gene activity, identifying genes, and studying protein interactions on a larger scale. They play a crucial role in medical research by enabling the identification, measurement, and analysis of various analytes for various applications. Over the years, these methods have been improved to enhance our understanding of diseases, their diagnosis, prognosis, and the monitoring of essential biomarkers or molecules using sophisticated equipment.[1–3]

Despite significant progress in the microarray industry, the challenge of achieving selective, specific, and reusable functional surfaces persists. Current methods often require the complete removal of surfaces for immobilisation, which can damage them and reduce overall efficiency. Additionally, time, cost, and the need to prevent nanoparticles from drying on the surface during attachment are significant limiting factors that could prevent the creation of efficient re-usable protocols. [4, 5] Therefore, there is an urgent need for new and less laborious platforms capable of overcoming these common challenges.

This research proposes using the fluorous effect to immobilise fluorous-modified oligonucleotides of varying lengths, fluorine content, linkers, and branch systems on lithographically patterned fluorous surfaces. By utilising the fluorous effect, we expect to address some of the major concerns associated with other methods currently available for immobilising various oligonucleotides used in detecting, measuring, and diagnosing infections. [6–8]

Specifically, we anticipate that the fluorous effect can selectively remove modified oligonucleotides of different strengths from the same fluorous-patterned surface. This approach would be highly desirable for developing reconfigurable metasurfaces suitable for the repeatable immobilisation of nanomaterials without noticeable damage.

Also investigated is the use of the fluorous effect to deposit and remove optically active nanoparticles. Metal nanoparticles, such as gold and silver, exhibit colour change based on their size, shape, composition, and surroundings of the metal nanoparticle rather than a pigment or dye. Metal nanoparticles can be used as

alternative fluorescent dyes for tagging and observing molecules. Unlike fluorescent tags, gold and silver nanoparticles have high extinction coefficients, enabling visual observation during colour change at very low concentrations (nano and picomolar). They exhibit strong absorption in the UV-vis and near-infrared regions, high surface energy that can be tailored for molecule adsorption, and are not susceptible to photobleaching (i.e., they do not fade over time).

This research uses the fluorous effect to precisely control and immobilise gold and silver nanoparticles on fluorous-modified surfaces. The objective is to achieve single-particle immobilisation, making it suitable for reconfigurable metasurfaces. This method holds promising potential for addressing significant challenges in the microarray industry, where the attachment of nanomaterials, including high signal-to-noise ratio, sensitivity, selectivity, and unintended aggregation. [9–12]

Research Aim

This research aims to develop a micro and nano-patterned surface capable of specific, selective, and reversible immobilisation using the fluorous effect. Such a reconfigurable surface has the potential to revolutionise micro and nano-technological advancements by creating a robust and flexible platform for various applications.

1.2 Fluorous Chemistry

The term "fluorous" was initially used for molecules with superhydrophobic properties during fluorous-phase separation techniques using the fluorous biphasic system (FBS). This system consists of the fluorous phase containing a dissolved reagent or catalyst and another phase, which could be any common organic or non-organic solvent with limited or no solubility in the fluorous phase.[13] Historically, M. Vogt was the first to describe the use of perfluorinated polyether to immobilise homogeneous catalysts. [14] However, it was in 1994 that Horva´th and Ra´bai received much attention for their applications as an alternative in the liquid-liquid extraction phase in FBS and, recently, other applications. [15] Since then, a pioneer definition of the term ‘fluorous’ has been explicitly stated in the work of Gladysz and Curann. [16] Unlike the sp^3 hybridised C-F bond, aromatic (sp^2) hybridised carbon does not exhibit enough dipole-dipole interactions. Hence,

it is much more soluble in organic solvents, e.g., aryl and perfluoroalkyl-containing ligands. [17]

Using earlier works on the FBS, different terminologies were proposed to classify fluorous from non-fluorous counterparts. [18]

a. **Presence of Fluorine:** According to the definition from Horvath and co, the presence of a high number of fluorine atoms in the structure of a molecule gives a strong indication of being a fluorous molecule with a tendency for strong affinity for other molecules or compounds with a high or similar amount of fluorine atoms. It is therefore essential to note that *'not all that glitters is gold and not all that contain fluorine atom (s) are automatically 'fluorous' in nature'.*

b. **Fluorous Tag:** This could be used to induce the presence of fluorous nature in a molecule or compound. A fluorous tag is a distinct and characteristic functional group or moiety attached to a molecule. As a rule, using a perfluoroalkyl tag with at least three fluorine atoms in the R_F group (where R_F is a perfluorinated alkyl group represented by $-C_nF_{2n+1}$ and $n \geq 3$) would, at least, qualify the molecule as fluorous.

c. **Hydrophobicity:** Due to the high number of fluorine atoms in a molecule, the fluorous molecules exhibit high hydrophobicity and can easily interact, with strong affinity, between the fluorine atoms and hydrophobic surfaces. Apart from this, due to this high hydrophobicity, they are immiscible with water and other organic solvents compared to their non-fluorous counterparts.

d. **Solubility in Fluorous Solvents:** Fluorous molecules are 'fluorophilic' in nature and, by extension, have high solubility in perfluorinated solvents, including perfluorocarbons and perfluorinated ethers.

e. **Fluorous - Phase Separation (FPS)**: Another way a molecule or solvent can be termed fluorous is if it can be efficiently separated from non-fluorous compounds using the widely known fluorous-phase separation techniques.

f. **Compatibility with Fluorous Materials:** A molecule will likely have a fluorous character or nature if it has a high chance of interacting with fluorous materials or surfaces, including fluorous silica gel or other fluorous stationary phases.

Although the properties are not exclusive, they could serve as a guide to indicating the presence of a fluorous molecule. Therefore, it is expected that some molecules would not fit in to be termed "fluorous" if the conditions are not met. Using 5-fluorouracil with extra fluorine, for example, is not fluorous, even though it has a fluorine atom and exhibits some properties due to the presence of a fluorine atom in its structure, while perfluoro hexane is fluorous. In between these, there are many developing structures where these yardsticks can be used as a guide to determine if they are fluorous or not.

1.2.1 Incorporating Fluorine and its Applications

Fluorine ($1s^2$, $2s^2$, $2p^5$) is the most electronegative element [19] and belongs to group 7 of the periodic table. It is highly reactive and electronegative, with high ionisation energy but low polarizability. Due to this small size compared to its high electronegativity, it is difficult for other elements to form favourable interactions with the electron-withdrawing fluorine atoms. This property ensures specific interactions with other fluorine atoms and can be tailored for different applications.[20] Therefore, an adequate number of fluorine atoms in the molecule can induce the fluorous effect. Due to the non-covalent nature of the interactions, it is therefore reversible due to the presence of several van der Waal's forces. During the interaction leading to fluorous effect, several types of other bonds have been identified, including F…F, C-F…H, C-F…π, and C-F…C=O). However, the non-covalent fluorous-fluorous interaction was recognised as the dominant and strongest attractive force, while other research is ongoing to determine the contending nature of these interactions. [21, 22] Also, one of the significant reasons fluorine-containing molecules would continue to gain more attention is the distinct properties attributed to fluorine atoms. Being the most electronegative atom with a very small atomic radius (except for neon gas), fluorine has a small atomic radius of 50 pm compared to hydrogen atoms (25 pm) and other halogens such as chlorine (100 pm), bromine (115 pm), and iodine (140 pm).[23, 24] Also, the carbon-fluorine bond is extremely strong, approximately 14

kcal/mol stronger than a C–H bond. Hence, this makes the resulting perfluorinated carbons inert to substitution reactions. The van der Waals radius of fluorine (1.47 Å) is significantly longer than that of hydrogen (1.20 Å) in the C–F bond. This size difference creates steric hindrance or conformational changes when a hydrogen atom in a C-H bond is replaced by a fluorine atom, especially when there is more than one substitution, as in the transition from a methylene (CH_2) to a difluoromethylene group (CF_2).

Apart from this, the overlap between the 2s orbital of the fluorine atom and the 2p orbitals of the corresponding carbon atom allows the formation of a dipolar structure that favours multiple fluorine-substituted carbons. Hence, the C-F bond is highly polarised to form sp^3 carbon (δ+) to the fluorine (δ-) due to the high electronegativity exhibited by the fluorine atom. Because of this, the electrons are drawn towards fluorine atoms in the opposite direction of the C-H bond. With these properties (high electronegativity and low polarizability), they exhibit non-covalent characteristics along the C-F bond and the stronger energy bond conferred upon them compared to other halogens when bonded to carbon atoms. [25–30] These attributes of halogens significantly affect the physicochemical properties of molecules or compounds when they switch from C_mH_n to C_mF_n. (where m equals the number of carbon and hydrogen or fluorine, respectively) including electronegativity, reactivity, hydrophobicity, lipophilicity, and bond stability. Hence, their electron-withdrawing ability creates a repulsive and attractive electrostatic environment that alters their reaction rates, preferences, and molecular stability due to the strength conferred on the carbon–halogen (C-F) bond. For instance, the stability of the C-F bond is increased as the number of fluorine atoms bound to the same carbon atom increases. [31–34]

Due to this, they find applications in different fields of science.[35–38] For example, research by the Clark group revealed that incorporating fluorous tags in molecules can direct the hierarchical assembly of DNA origami nanostructures, improving the efficiency of self-assembling nanostructures.[39] In this research, fluorous-tagged oligonucleotides were synthesised using solid-phase methods and then purified using reverse-phase HPLC and MALDI-MS. Single-stranded M13mp18 DNA was combined with staple strands in a buffer solution containing TAE and magnesium acetate to assemble the DNA origami structures. A core set of staple strands was retained for origami with modified edges, and unique staple strands were added for each specific configuration. Heterodimer assemblies were created

by mixing the filtered monomer solutions. Excess staple strands were removed through filtration, and the concentration of the filtered origami was measured using a UV/vis spectrophotometer. Agarose gel electrophoresis was conducted to analyse the assembled origami structures, while atomic force microscopy (AFM) was used to image over 275 origami dimers that formed the origami assemblies.

Hence, this research introduces an innovative method for the hierarchical assembly of DNA origami nanostructures using a molecular recognition strategy. By combining Watson-Crick base pairing with the fluorous effect, the study demonstrates the creation of a complementary range of non-covalent interactions that efficiently form discrete dimeric species within the model origami system. Notably, this combined molecular recognition approach proves to be more effective than using either strategy alone. Compared to traditional DNA-based techniques, the orthogonal nature of this attachment method suggests that the observed benefits could extend to other DNA-based origami tiling systems, enabling the assembly of complex three-dimensional structures. This method offers several advantages: it is easy to synthesise, produces small-sized structures, and utilises the strength and mobility of the fluorous effect. These features make a DNA structure known as R_F-DNA a promising tool in structural DNA nanotechnology.

Moreover, the research indicates that fluorous-directed assembly of DNA nanostructures could be applied to create functional assemblies on a micron scale. The authors also propose the potential for integrating fluorous-directed assembly with other components to facilitate the targeted delivery of biological materials to specific cell types. This development has significant implications for biosensing, molecular computing, drug delivery, and Plasmonics applications.[40] In addition, Flynn et al. (2017) from the Clark group also used the fluorous effect to immobilise DNA onto specific patterns, allowing for reversible and rewritable patterning with no degradation in binding efficiency even after multiple removal and attachment cycles of different DNA sequences. In this method, short fluorous tags enabled the immobilisation of water-soluble oligodeoxyribonucleotides (ODNs) from aqueous solutions onto lithographically defined, micro-patterned fluorous surfaces. This method eliminates the need for direct sample spotting while the immobilised ODNs remain available for hybridisation with complementary strands. Notably, the genetic information can be removed entirely using a straightforward wash with organic solvents, allowing for the replacement with new genetic material during

a brief incubation period. This process was successfully performed five times without any noticeable surface degradation. This has been presented for applications in reconfigurable nanophononics and the microarray industry.[41]
This thesis aims to expand the applications of the described protocol by facilitating the reversible immobilisation of various nanomaterials, specifically DNA and metal nanoparticles, on fluorous patterned surfaces. By achieving reversible immobilisation at the level of individual nanoparticles, this approach seeks to enhance the functionality of these nanomaterials in various applications. It will also contribute to developing more sophisticated nanostructured surfaces that can be engineered for specific uses in sensing, drug delivery, and nanomedicine.

The ability to reversibly immobilise single nanoparticles could significantly advance the precision and efficiency of deploying nanomaterials in various scientific and industrial processes. Also, passivating surfaces with high-density perfluoro alkane brushes can improve the accuracy of single-molecule measurements and minimise protein complexes' irreversible binding and trapping. This technique has applications in several industries, including medical diagnostics, the biofouling release of marine organisms, and other biomedical applications.[42] Using fluorous tags, nanomaterials can be easily immobilised onto various surfaces, which can be reversed by simple washing or extraction. This provides a convenient way to functionalise nanomaterials and offers a possible pathway to developing new nanomaterial-based therapies.

1.2.2 Plasmonics

Plasmonics is an interdisciplinary field of science that explores the manipulation and interaction of light with nanoscale structures, particularly using noble metals such as gold and silver.[43] This interaction occurs by combining the properties of light with the excited electrons present in metals, which have a fixed positive core. In metals, the electrons are delocalised, meaning they are free to move in relation to the fixed positive core. A plasmon refers to the collective oscillation of these free electrons in a metal material in relation to the fixed positive ions.
Surface plasmon resonance (SPR) or surface plasmon polariton (SPP) refers to the evanescent propagation of light waves between the interface of metals and dielectrics. For instance, when light interacts with a metal or an insulator, it

behaves differently because of the fields generated by free electrons in metals. SPP are transverse waves propagating between materials of differential permittivity (positive and negative). The behaviour is influenced by the permittivity or dielectric constant of the medium. This property allows intentional engineering of surfaces with exceptional characteristics, enabling the generation of surface plasmon polaritons (SPPs) that effectively concentrate electromagnetic fields. By manipulating surface properties, researchers and engineers can design structures that control electromagnetic wave behaviour, leading to potential applications in photonics, sensing, and nanoscale optical devices. This enables the creation of devices that manipulate light at the nanoscale, offering potential advancements in communication, imaging, and information processing technologies. This property of SPP, along with the increasing demand for miniaturised photonic components, is generating exponentially growing interest in SPP-mediated applications. [44, 45]

These surface plasmons fall into two classes: propagating surface plasmons (PSPs) and localised surface plasmons (LSPs).

Due to challenges associated with plasmon excitation on bulk metal surfaces, many techniques have been adopted to resolve this. The PSPs can be excited on thin layers of metallic films using various approaches, especially the Kretschmann [46] and Otto prism couplers, [47] and optical waveguide couplers. In contrast, the LSPR can be excited on noble metal nanoparticles, including silver and gold nanoparticles, where strong enhancement of the electromagnetic fields can be induced (resonance amplification).

Since the propagation constant of surface plasmon is greater than that of light waves of the same polarisation state in a dielectric medium due to differences in refractive index values for metal and dielectric, direct light cannot excite surface plasmon at a specific metal-dielectric interface, hence different configuration is needed to increase the momentum and the wave vector of the incoming light from the electromagnetic spectrum into the dielectric medium($\varepsilon_m<0$ for a given metal and $\varepsilon_s>0$ for a dielectric) (equation 1). [48] Therefore, the maximum propagation constant of the light wave at frequency ω, propagating through the dielectric medium, is given as

$$K_s = \omega/c * (\varepsilon_s)^{1/2} \qquad \text{equation} \quad (1)$$

By combining plane polarised light with the decay properties of propagating waves using Maxwell's equations, the propagating constant of the surface plasmon that is continuous through the dielectric interface can be obtained.

$$K_{sp} = \omega/c\ (\varepsilon_m\varepsilon_s/\varepsilon_m + \varepsilon_s)^{1/2} \qquad \text{equation (2)}$$

Two common methods are used to generate Surface Plasmon Polaritons (SPPs): Otto and Kretschmann.The Kretschmann method is more popular due to its simpler and more efficient design for coupling light to SPPs between the metal and dielectrics. This dielectric supports the SPPs accompanied by the evanescent longitudinal electric field with maximum field intensity at the interface.

For the Otto configurations, the evanescent wave is coupled with the surface plasmon wave that travels along the metal-dielectric interface. This surface plasmon wave is highly sensitive to changes in the medium's interference. The coupling occurs at the base of the coupling prisms when the angle of incidence is greater than the critical angle of the prism-air interface. When the angle of incidence and the wavelength of light match the momentum of the SPPs, the SPPs become excited at the metal-dielectric interface.

The wave vector represents the mathematical expression of the relationship between these:

$$K_{ev} = \omega/c\ (\varepsilon_p * \sin\theta)^{1/2} \qquad \text{equation (3)}$$

During the excitation of the plasmon, the k value must have a required value during the ATR, where K_{ev} = x-component of the wave vector of the evanescent or decaying SPPs in the metal-dielectric medium. By introducing a metal layer into a decaying evanescent field between a metal layer and a prism, an air gap can still be created. This can excite the surface plasmon and make them extremely useful in many sensing applications. However, this arrangement is quite challenging, as the metal needs to be introduced at the nanoscale region (around 200 nm).

The limitation in the Otto configuration was addressed and improved using the Kretschmann excitation method. Unlike the Otto configuration, the Kretschmann configuration involves using a high refractive index glass prism at ATR conditions. The light is shone through the glass at the glass-metal interface, coated with a thin layer of metal (less than 100 nm). This metal layer is in direct contact with the metal and the dielectric (the substrate) and is at an angle equal to or greater than the angle needed for ATR.

This creates an evanescent wave that extends across the interface into the metal layer. When the wave vector of the evanescent wave matches that of the SPPs at

the metal-dielectric interface, resonance occurs, maximally transferring energy from the incoming photons to the plasmons, effectively exciting SPPs. Due to this phenomenon, a coherent and collective oscillation of the valence electrons occurs in phase, producing a phenomenon called Surface plasmon.

Therefore, the surface plasmon excites when the wave vector of the propagating evanescent wave from the photon equals that of the plasmon. This happens if they have similar frequency, state of polarisation, specific angle of incidence, and other resonance conditions.

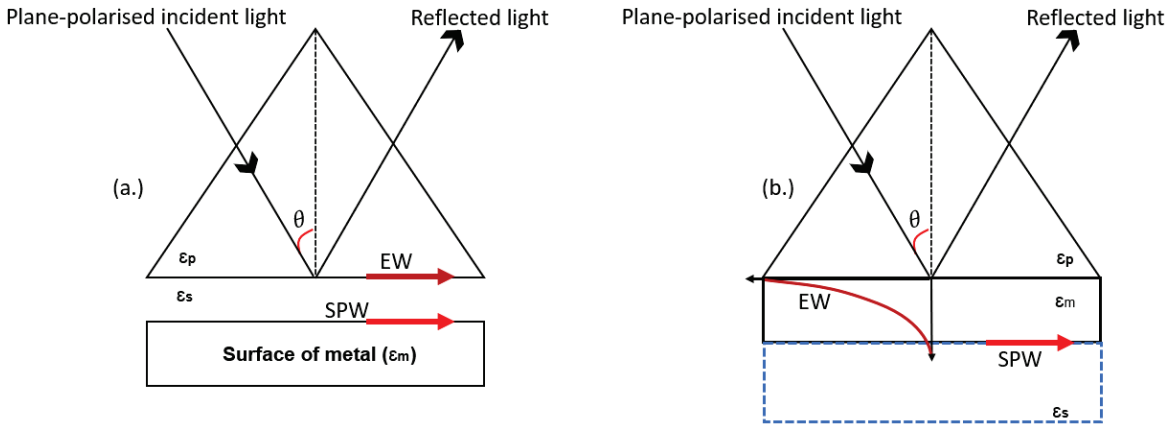

Figure 1: Schematics illustrating (a.) Otto and (b.) Kretschmann configuration methods are used during the excitation of SPPs. The Otto configuration uses a metal film on a separate substrate with an air gap, while the Kretschmann configuration has the metal film directly on the prism. Light in the Otto configuration hits the prism first, and the resonance wavelength can be tuned using the air-gap distance. Conversely, the light interacts directly with the metal film in the Kretschmann configuration and the resonance wavelength can be tuned by increasing the air-gap distance between the metal film and prism.

Where:

ε_m = The permittivity of metal

ε_s = The permittivity of space or dielectric

ε_p = The permittivity of glass

SPW = Surface plasmon wave

EW = Electromagnetic wave

Mathematically, this can be expressed as

$$\omega/c * (\varepsilon p)^{1/2} = \omega/c * (\varepsilon_m \varepsilon_s/\varepsilon_m + \varepsilon_s)^{1/2} \quad \text{equation (4)}$$

Using this method to excite the SPPs, the excitation efficiency can be affected by several factors, including the angle of incidence, the properties of the metals

(e.g., permittivity), the quality of the optical components, and the dielectric properties. Hence, the working principle that guides SPR-based applications is based on equation (4). Therefore, using different coupling principles, this metal-light interaction can be applied to create different plasmonic nanostructures with extraordinary potential for diverse applications. [49–52]

1.3 Localised Surface Plasmon Resonance (LSPR)

Unlike the challenges associated with SPR to couple light to the surface plasmon of bulk metal, using nanoparticles offers a simpler opportunity to enhance the electromagnetic field. LSPR is one of the main concepts in plasmonic study. When light of a specific wavelength and frequency interacts with nanoparticles, the free conduction band electrons of the nanoparticles collectively oscillate at 180° due to the impact of the instantaneous electric field. However, due to the influence of the positively charged nuclei, the electrons are attracted or restored to phase and returned to the equilibrium positions after back-and-forth movements like in a harmonic oscillator. Once the free frequency of the incoming light equals the frequency of the oscillating electron, the resonance condition is met, and the particle efficiently scatters and absorbs light depending on its size. Additionally, the spatial distribution of the valence shell electron is affected by the size or cross-sectional areas of the nanoparticles. As the size or cross-sectional areas of the nanoparticles increase, their total extinction coefficient and ability to scatter or absorb light increases with respect to their immediate environment. Hence, their interactions with light create a substantial field enhancement around the surface of the nanoparticles. [53, 54] The electric field generated from these nanoparticles is highly localised but decays rapidly away from the nanoparticles interface into the dielectric background. This process creates an oscillating dipole in the metal during the interaction with the electromagnetic radiation of light. Therefore, an enhanced electric field is formed when there is appropriate interparticle distance or proximity between the particles. Hence, the efficiency of this interaction and coupling depends on the incident angle, light polarisation, and shape of the nanoparticles. This type of interaction has been applied to different phenomena of practical biomedical applications and research. For example, in sensing applications, LSPR is used where a change in refractive index could indicate a change in the optical characteristics of a biosensor with characteristics sensitivities of various orders compared to conventional methods

to detect a single or few molecules. [55, 56] Also, due to the isotropic nature of signals obtained from spherical or quasi-spherical nanoparticles, the plasmonic signal falls within the UV-vis region of the electromagnetic spectrum and has been used extensively for several biomedical applications. Conversely, this has limitations in other applications where the range of its applications needed is far beyond the UV-visible regions, which limits their applications.[57] Therefore, unlike spherical or quasi-spherical colloidal nanoparticles, nanorods have an anisotropic shape with adjustable plasmonic properties in near-infrared regions. This property confers extra advantages in several biomedical applications. [58]

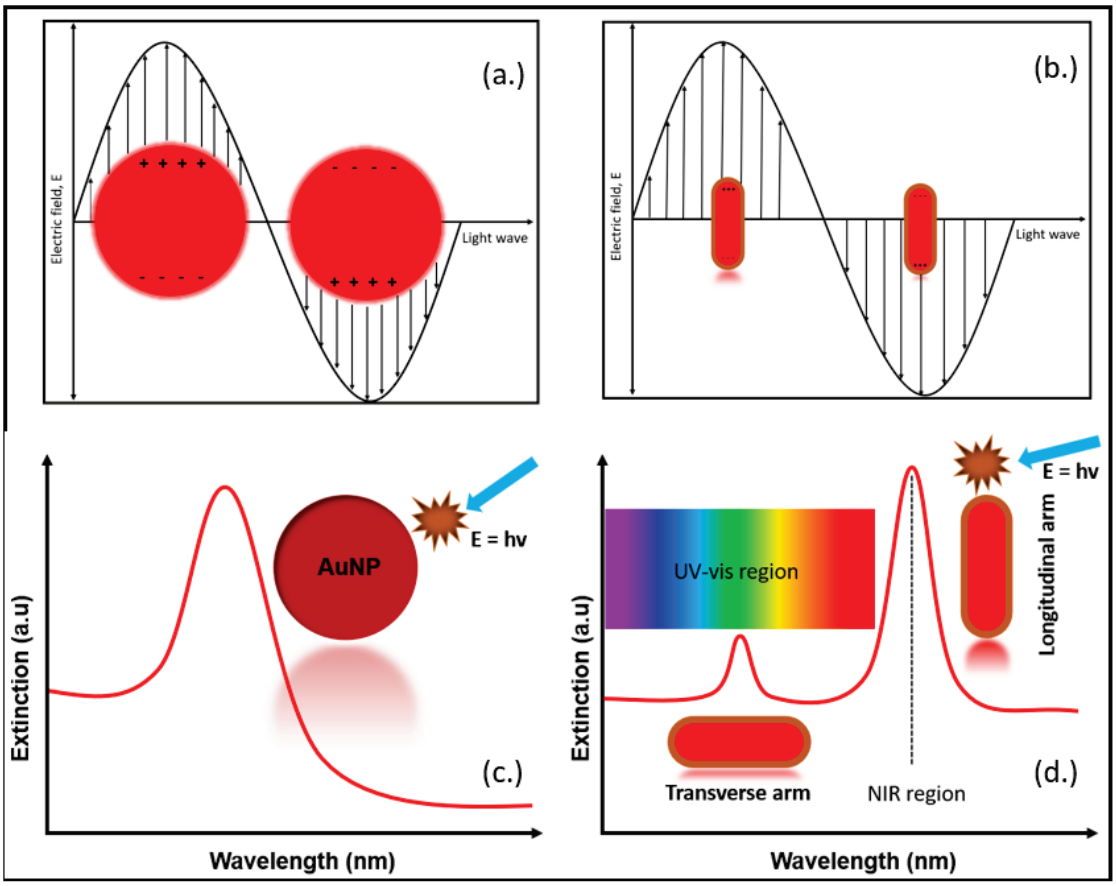

Figure 2 (a-d): Schematics illustrating the impact of shape on the delocalisation of valence shell electrons of nanoparticles upon interaction with electromagnetic radiation via surface plasmon resonance of (a.) isotropic and (b.) anisotropic nanoparticles. (c.) and (d.) illustrates the interaction of light with the valence shell electron in the presence of (c.) isotropic and (d.) anisotropic nanoparticles in the visible and NIR regions, respectively.

Unlike LSPR, which occurs on thin nanometer-sized metallic nanoparticles or surfaces when excited by light, SPR occurs by propagating surface plasmon along a continuous metallic film that is tens of nanometers thick and at the interface between the metal and the dielectric (air or water). Apart from this, the resonance condition of the LSPR depends on the size, shape, and type of

nanoparticles (Figure 2) and the dielectric medium. In contrast, the resonance condition of the SPR depends on the angle of incident light, the dielectric constant of the metal and the nature of the materials in contact with the dielectric materials. With these properties, the sensitivity of LSPR is localised and depends on the refractive index close to the surface of the nanoparticles. This refractive index sensitivity also applies to SPR but takes place over a wide length of the metallic surface due to a longer decay time. In addition, the plasmonic shift in the peak wavelength or intensity is usually used to monitor the LSPR absorption in the optical spectrum. In contrast, changes in the angle or intensity of the reflected light are usually used to monitor the sensitivity of SPR equipment. Based on the above, the LSPR method is suitable for single-molecule detection because of its high local sensitivity compared to the SPR method, which measures bulk changes across a larger area or region. [59–61]

Even though metal nanoparticles are increasingly used in several biomedical applications to increase their plasmonic coupling for enhanced sensing properties or applications, this does not usually occur without a proper ligand exchange via conjugation with other molecules. Several strategies are used for signal amplifications, including the ones reported in [62]

1.4 Metasurfaces and their applications in Microarray Technology

Metasurfaces are thin, two-dimensional layers that can be engineered to have adjustable properties when interacting with electromagnetic waves, such as light.[63, 64]

By engineering these surfaces, we can dynamically control various parameters of electromagnetic waves, including phase, amplitude, polarisation, and frequency. This adaptability allows for various applications, such as sensing, communication, imaging, and more. To achieve reconfigurability, metasurfaces often rely on external stimuli, such as electrical voltage, light, or temperature changes, which modify the resonant behaviour of these predefined constituent nanostructures. However, traditional methods of achieving reconfigurability pose challenges, including thermal issues, fabrication complexity, and integration defects. [65] Incorporating or attaching metal nanoparticles to these metasurfaces can create

a dynamic and reconfigurable surface tailored to developing strong localised surface plasmon resonance (LSPR) with improved sensitivity.

As described earlier, gold and silver nanoparticles are known for their unique optical properties, influenced by their size, shape, molecular interaction, and surrounding environment. Specifically, the surface area to volume ratio of these MNPs affects their stability and reactivities, greatly impacting their surface energy (increases with the number of surface atoms). To achieve stability by the MNPs, the nanoparticles adjust themselves in such a way as to minimise the surface energy in a process called the Wulff construction principle. This explains that during the crystal growth of nanoparticles, the shape that minimises the equilibrium between the internal energy and the surface areas will be favoured, leading to various types of shapes or morphology.[66, 67] Therefore, smaller nanoparticles are less stable due to their high surface energy stabilising them is necessary. Hence, this impact of size must be explored and functionalised with a surfactant or stabiliser of interest (e.g. thiol) [68, 69], and tailored for specific applications, including colourimetric,[70] biomedical [7–9], bioimaging, optics, [74] and sensing. [75][12, 13]

Additionally, efficient chemical and biological species identification is essential for real-time environmental monitoring, disease diagnosis and public health analysis. However, rapidly detecting these species using simple techniques with high sensitivity and specificity is challenging. Traditional methods, including chromatography, electrochemistry, fluorescent microscopy, and dyes conjugated with other molecules, require expensive and cumbersome instruments with skilled personnel to operate them. Hence, they are unsuitable for home use or point-of-care analysis. [78] Colourimetric assays offer an attractive alternative method to identify, monitor, and analyse samples due to their simplicity and convenience. They offer the opportunity for real-time data analysis at a low cost, with the option for on-site detection or point-of-care analysis.

Gold and silver NPs are attractive because they can respond to their local environment through a change in their plasmonic spectra. This is in contrast to using dyes, which comes with many challenges, including photobleaching, low extinction coefficient, stability, narrow range of measurement, and interference with other molecules. [79] NPs, therefore, make for attractive alternatives to dye-based systems for applications in reconfigurable metasurface. [80–82], catalysis [83], and optics. [84] To tailor the nanoparticles to different applications, such as

molecular tagging or label-free colourimetric assays, surface modification using ligand exchange is needed to replace the coated surfactant with a suitable functional group. This singular step (or in conjunction with other steps) is essential to overcome the common challenges (highlighted below) associated with the immobilisation of metal NPs on a platform or surface:

1. If the gold and silver nanoparticles are not correctly conjugated, there is a high chance that the eventual immobilisation will fail, even when other steps used during the protocol are well optimised. Therefore, the appropriate use of functional groups, stability, and the inherent ability of NPs to bind the preferred surface are essential factors to consider. [85]

2. Using glass as the immobilisation platform is cheap and common. However, impurities and lack of uniformity can prevent the immobilisation of the preferred nanoparticles or biomolecules from interacting with the activated surface. Hence, a suitable cleaning protocol with acetone, methanol and Isopropanol is essential to remove organic and inorganic impurities from the surface. An oxygen plasma asher can also be employed to remove other organic impurities with the advantage of activating the surface for subsequent reaction and a pristine surface with good surface chemistry. In addition to this, once nanoparticles are stuck to the glass surface via evaporation, they are hard to remove using common solvents, including acetone, methanol, IPA, and ethanol.

3. Control of nanoparticle size during immobilisation: The size distribution of nanoparticles needs to be controlled during the immobilisation process. This is required because of unwanted growth of the nanoparticles either via size increase or unintended aggregation. This challenge can easily misdirect or clog the surface of the materials (e.g., glass). [86]

4. Stability of the nanoparticles:

Several factors, including the size, shape, storage condition, ionic strength, pH, and functional group can affect the stability of the nanoparticles. Silver NPs, especially, are susceptible to oxidation, which can interfere with their reactivities and stability over time. [87–89]

5. Selective immobilisation: Direct and selective immobilisation of these MNPs is challenging, especially on a nanopatterned surface. Factors such as concentration, unwanted aggregations, non-specific interaction, and lack of reversible interactions or immobilisation are a few of the major challenges that must be overcome. [90, 91]

Therefore, by exploring the fluorous effect with the colourimetric properties of these nanoparticles, a reconfigurable metasurface capable of reversible attachment of metal NPs with a simple solvent wash can be created.

1.5 Colloids and Colloidal System

Colloids, colloidal particles, or colloidal systems consist of a heterogeneous mixture in which one microscopically dispersed insoluble particles (1-100 nm in diameter) phase are evenly dispersed in a continuous phase. They are very useful in DLS analysis.[92–94]

The dispersed phase contains particles (or micelles) with a linear dimension between 1 nm and 1 mm. Due to their size range, colloidal particles are subjected to Brownian motion. However, as their size increases, they are affected by gravity and drag, which can be modelled with Stoke's law, which states that the friction experienced by colloidal particles in solution is related to their radius and the viscosity of the solvent. [95] Colloidal particles can also be classified as Primary, coalescence, ripening, aggregated, and agglomerates. Primary particles are the smallest unit of the structure where other structures are built. When these particles come together, they can coalesce to form bigger-sized particles with entirely different surface areas than the sum of the two. Also, these particles, especially the smaller ones, have higher surface strain, creating higher surface energy that makes them energetically unstable. Over time, this process (Ostwald ripening) creates preferential solubility of the smaller particles compared to the larger ones. Consequentially, these small particles can contribute to the size of the other particles in the solution. Unlike the ripening process, when the inter-particle distance between two primary NPs reduces to a critical limit, they can either aggregate or agglomerate depending on the number and packing created by the strong bonds between the NPs involved. Agglomeration takes place with weaker bond interaction between different aggregates or primary particles. [96]

There are several stages in nanoparticle formation with underlying mechanisms, especially nucleation and growth. These mechanisms allow greater flexibility and control that determine the composition and properties of nanoparticles used for different fabrication and applications.

1.5.1 Metal Nanoparticles

With continuous development and discovery of new insights into nanotechnology, noble metal nanoparticles, especially gold and silver nanoparticles, continue to attract attention.[97] This was attributed to their fascinating optical properties that can be tuned based on their size, shape, surface chemistry, and aggregation status. Due to these properties, they exhibit quantised electrical and optical properties, which, expectedly, significantly impact their physicochemical properties. Hence, they are exploited for sensing, drug deliveries, diagnosis, and imaging. [98–101]

Gold nanoparticles exhibit excellent plasmonic properties with an extremely high extinction coefficient that allows visual observation at low nano and picomolar concentrations compared to organic dyes that require micromolar concentrations or more to achieve. Apart from this, being a nanoparticle, their high surface area to volume ratio also confers them a high surface energy and can strongly adsorb thiol, halides, and organic molecules with significant impact on their surface properties. [102]

Due to this, one of the primary applications is label-free colourimetric analysis. The change in their optical properties alone or conjugated with other molecules can be used to identify, detect, and quantify different biological samples, such as protein, DNA, and carbohydrates. [103, 104]

Generally, colloidal suspension is thermodynamically unstable and tends to flocculate; hence, it is important to monitor and control each of the experimental stages to achieve a sensible outcome.

To prevent this aggregation, positively or negatively charged small molecules that induce electrostatic stabilisation are used. Hence, a good understanding of the stability and kinetics of the aggregation process is needed. These can be detected and characterised using DLS and UV-vis spectroscopic techniques. Also, as the gold nanoparticles increase in size, scattering of electromagnetic radiation dominates with significant differences in their LSPR peaks. This property has also been used to determine where their application is well suited. [105, 106] Therefore, individual spherical gold nanoparticle colloids can be tuned with LSPR peaks in the visible region at 510 nm for 10 nm gold to around 580 nm for up to 100 nm gold nanoparticles. Hence, the ratio of absorption to scattering increases with reduced

particle size compared to increased scattering for larger-sized particles. [107] In this research, we will concentrate only on *in vitro* studies.

Gold nanoparticles have been used for several in vitro studies, especially in sensing applications using LSPR, which depend majorly on changes in the refractive index of the surroundings. This creates a plasmonic shift in its wavelength when gold nanoparticles are bound to other molecules or when free. Here, a red shift indicates a longer wavelength or increased refractive index when molecules are adsorbed to the nanoparticle's surface. However, a blue shift indicates a shorter wavelength, especially when the nanoparticle is free or attached to an electronegative element (e.g. fluorine) [37]. Therefore, a change in the local environment could easily be detected as a function of the plasmonic shifts specific for each properly functionalised gold nanoparticle. It is also important to note that the optical properties of gold nanoparticles or nanostructure in different sensing applications are not only based on localised surface plasmon resonance. Others are also based on Rayleigh scattering, surface-enhanced fluorescence, and Surface-enhanced Raman scattering (SERS).

1.5.2 Plasmonic Response of Gold and Silver Nanoparticles

The optical response of nanoparticles (especially silver and gold NPs) differs depending on their type, size, and bioconjugation. Generally, the electronic transition of the transition metal conforms with the Madelung (or Janet or Klechkowsky) rule where the order of degenerates orbital is filled and determined by the sum of the principal quantum number (n) and the azimuthal quantum number (l). Additionally, orbitals are filled following the order of increasing (n+l) value. When different orbitals have the same (n+l) value, the one with the lower n is considered first. With this convention, transition metals have completely filled d-orbitals, and their metallic properties are due to the single-filled s-subshell orbitals. Despite similar configurations, the optical properties of gold and silver atoms are exceptions due to their $5d \rightarrow 6s$ and $4d \rightarrow 5s$ transitions, respectively.[108] Due to the high atomic number of gold nanoparticles, there is a strong electrostatic interaction between the electrons and the positively charged core, which includes relativistic effects. This interaction significantly impacts their absorption properties, requiring higher excitation energy for it to occur. Consequently, the intraband energy transitions of the nanoparticles play a crucial role in their electronic transitions. The intraband energy transition refers to the

amount of energy an electron requires to transition from one energy level to the other (often to the higher energy level) within the same band, unlike in interband energy transition, which involves energy transfer within different bands. Specifically, gold and silver nanoparticles have different intraband energy transitions, with Ag having almost twice the value of the intraband energy transition of gold nanoparticles (2.4 eV for Au and 4 eV for Ag). This plays a crucial role in the optical properties and the electronic behaviours of the metal NPs during their interactions with the electromagnetic spectrum. Hence, the plasmonic response of gold nanoparticles is usually dampened during their intraband transition under visible light. At the same time, this is not the case for silver nanoparticles, which are free from this effect or losses. Although reports have also emerged on damping mechanisms for lower-sized (20 nm) silver nanoparticles [109] Apart from this, silver nanoparticles have also been shown to have an inherent advantage due to their higher theoretical refractive index, which makes them a better choice for biosensing applications compared to gold nanoparticles, even though both silver and gold nanoparticles have sensitive spectra responses to their environment. [110–112]

1.5.3 Effect of Interparticle Distance of Nanoparticles on their Plasmonic Response

Interparticle distance is between individual metal nanoparticles (e.g., gold NPs) and other surrounding metal nanoparticles in a colloidal system. It is an essential factor in biosensing applications, where its state can affect the sensitivity and impact the plasmonic properties of the NPs based on interactions with other particles or analytes. With this property, the colour and plasmonic properties of NPs can easily be affected upon aggregation (e.g., during conjugation) and dispersion (free state). These aggregations are reported to induce plasmonic coupling, especially when their interparticle distances are less than 2.5 times their overall diameter. Hence, a red-shifted plasmonic peak associated with longitudinal resonance in the electromagnetic spectrum is expected. [113, 114] Therefore, controlling the interparticle distance is essential in maintaining the physicochemical properties of metal nanoparticles for several sensing applications (Figure 3).

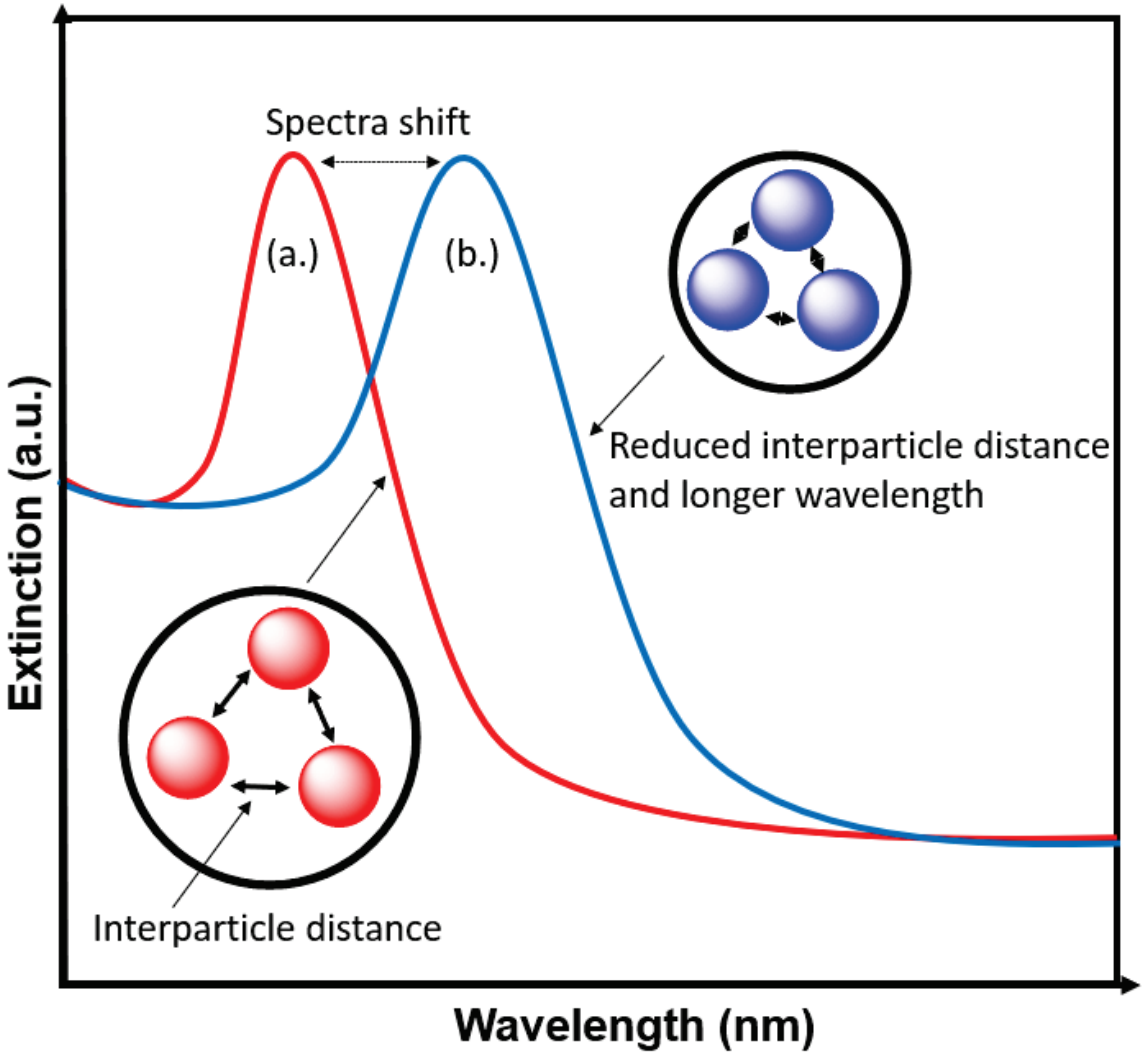

Figure 3: Schematic illustrating how changes in interparticle distance affect the absorption spectra and the stability of nanoparticles in a colloidal system. (a.) Depicts the absorption spectrum when the nanoparticles are well stabilised and without aggregation. Spectrum (b.) Depicts the absorption spectrum of nanoparticles after reduced interparticle distance, creating longer wavelength due to aggregation.

The following are ways in which the interparticle distance affects the sensitivity of gold nanoparticles in biosensing and how this can be explored for sensing applications:

1. Plasmonic biosensing:

In biosensing applications using the aggregation method, the challenge in reproducibility of the readout during bioconjugation with analytes occurs due to inconsistent interparticle distance and number of nanoparticles per cluster. Hence, interparticle distance is one of the most portent parameters that affect and influence the nature of aggregation-based biosensing applications at a fast, low cost, and small sample volume with improved sensitivities.

2. In optical biosensing, the interparticle distance of gold nanoparticles is reported to affect their sensitivities. For example, the change in the interparticle distance of the dimer of fabricated gold nanoparticles is shown to affect their refractive index sensitivity. [115] In addition, inconsistent interparticle distance and the number of NPs per cluster could lead to problems with reproducibility. [116]

3. Bioimaging:

Adjusting the interparticle distance for different nanostructures has proved vital in several medical fields, especially bioimaging. This offers the possibility of improving sensitivity, specificity, speed, contrast, resolution, and penetration depth. [117]

4. Signal enhancement

The gap distance created between dimers and trimers can influence their signal enhancement in surface-enhanced Raman spectroscopy (SERS) [118]. Hence, controlling this distance is important to improve the sensitivities of plasmonically coupled nano-entities.

5. As the distance between closely packed nanoparticle arrays increases, the plasmonic coupling among them weakens. Initially, the plasmonic band exhibits a red shift due to their close interactions. However, as the nanoparticles move further apart, this coupling diminishes, causing a blue shift in the plasmonic band, indicating a rise in energy levels. Conversely, when the interparticle distance decreases, the stronger coupling leads to a significant enhancement in signal strength, amplifying the collective resonant behaviour of the nanoparticles. [119]

1.5.4 Challenges Associated with the Aggregation of Nanoparticles

Surfactants stabilise colloidal suspensions, either during or after their synthesis, to prevent unwanted aggregations.[120] Fabricating patterned surfaces suitable for reversible attachment of these nanoparticles presents many challenges that hinder their effectiveness in various applications.

For instance, surface functionalisation is often used to improve the stability of nanoparticles and reduce aggregation. This process involves attaching different functional groups to the surfaces of the nanoparticles to enhance their dispersion, stability, and compatibility. However, uneven coatings can create areas with varying charge density, promoting unwanted aggregation instead of preventing it.

Moreover, the stability of these functional groups may be compromised under unfavourable conditions, leading to additional instability and irreversible aggregation. Apart from this, when NPs are deposited onto a surface, the van der Waals interaction can reduce interparticle distance, favouring the attractive force against the repulsive force. Apart from this, the tendency of nanoparticles to favour the minimum amount of energy during their stability appears to be one of the contributing factors to favour aggregation. Additionally, the shape, size, structure, composition, nature of the adsorbed layer, and the ionic environment can significantly influence the stability of the nanoparticles. Addressing these concerns is essential to fully utilise gold and silver nanoparticles in various fields, such as biomedicine, sensing, and materials engineering. [121] Drying of nanoparticles involves a physical and chemical process of isolating the nanoparticles from the aqueous or solvated environment, leading to irreversible aggregation or the possibility to re-disperse the nanoparticles. [122] Methods to immobilise these nanoparticles involve extensive silanisation, covalent immobilisation and varying temperatures. [123–125] The current methods offer very little or no opportunity to reuse the surface of the hydroxyl-terminated or silane-modified glass substrate after the nanoparticles have dried and aggregated. Allowing nanoparticles to dry on glass surfaces is wasteful, environmentally unfriendly, and presents a pollution challenge for the scientific community, where the repeated use of sensors is crucial.

Therefore, this research will focus on developing engineered surfaces that enable the reversible attachment of these nanoparticles.

1.6 Surface Energy of Nanoparticles

The surface energy of a material is the extra energy present at the surface compared to the total bulk of the material. This excess energy is due to the high surface-to-volume ratio and the concentration of the electron cloud at the surface or tip of the nanoparticles, which influences their physicochemical properties. This phenomenon is size-dependent and is affected by the kinetics and the thermodynamics of the nanoparticles during interaction with their environment. [126–128] It is a distinctive characteristic of nanoparticles (NPs) that is critical in their use. This energy tends to increase as the surface area of the NPs becomes larger or the size of the nanoparticles becomes reduced. [129] Due to the high

surface energy, NPs are often unstable or metastable. Managing this energy is essential during their synthesis and storage. By decreasing the particle size to nanoscale proportions, surface area and surface energy can be increased seven-fold.[130] Such an increase in surface properties leads to a reduction in bond length and changes in lattice properties as the atoms on the surface experience inward forces. These are significant points to consider in the application and handling of NPs. [131, 132]

1.7 Chemical Properties

The surface chemistry and properties of gold nanoparticles play essential roles in several functionalisation strategies. The surface of the nanoparticles can easily be conjugated with compatible and different moieties or functional groups. This can be used for several therapeutic purposes, including self-assembly monolayer and drug delivery.

Since its first breakthrough as a method for functionalising gold nanoparticles, gold-sulphur conjugation methods have continued to gain attention. [133] The Ag-S bond, with a bond strength of 45 kcal/mol (1/2 C-C bond of ~83 kcal/mol), ensures that the nanoparticles are anchored to the surface of the nanoparticles via several bonds.

The stability of these gold-sulphur bonds has been shown to depend on whether the thiol molecules form monodentate, bidentate, or tridentate ligands with the gold nanoparticles with the multidentate interaction with higher stability, especially against oxidised desorption at physiological conditions. When used with silane of interest, the density of the monolayer can easily be altered based on the concentration and the scope of the research. For this research, 0.5 mM of gold colloids were functionalised with a 50 mM concentration of PFDT using a fluorous-functionalised surface as an anchor in a non-covalent and reversible interaction. The degree of the surface ligands was analysed using UV-vis to evaluate the plasmonic shift or scanning electron microscope (SEM) to observe the surface morphology and quantify the surface density of the gold nanoparticles. Other analytical tools that can be used are zetasizer, via the dynamic light scattering technique and thermographic analysis (TGA).

1.8 Why should we aim to Synthesise Monodispersed Nanoparticles?

The mode of synthesis of nanoparticles influences their stability and distribution in colloidal systems. Hence, the distribution of these nanoparticles is vital for tailored applications. Monodispersed gold nanoparticles are shown to be desirable in biomedical applications due to sharp peaks and tunable LSPR when coupled with light. Consequently, higher performance and unique properties have been reported to be associated with gold nanoparticles with less than 5% size variation (SD < 5.0%) compared to the polydisperse AuNP. These properties are desirable, especially when their size, morphology, surface chemistry, and optical properties can be controlled. These controlled distributions afford them critical properties with invaluable applications in biomedicine, sensing, and bioimaging. Hence, this is crucial in designing a research-based colourimetric protocol using gold nanoparticles. (Figure 4) Monodispersed gold nanoparticles are desirable for efficient and tailored sensing applications, achieving higher sensitivity and a lower limit of detection (LOD).[134–136]

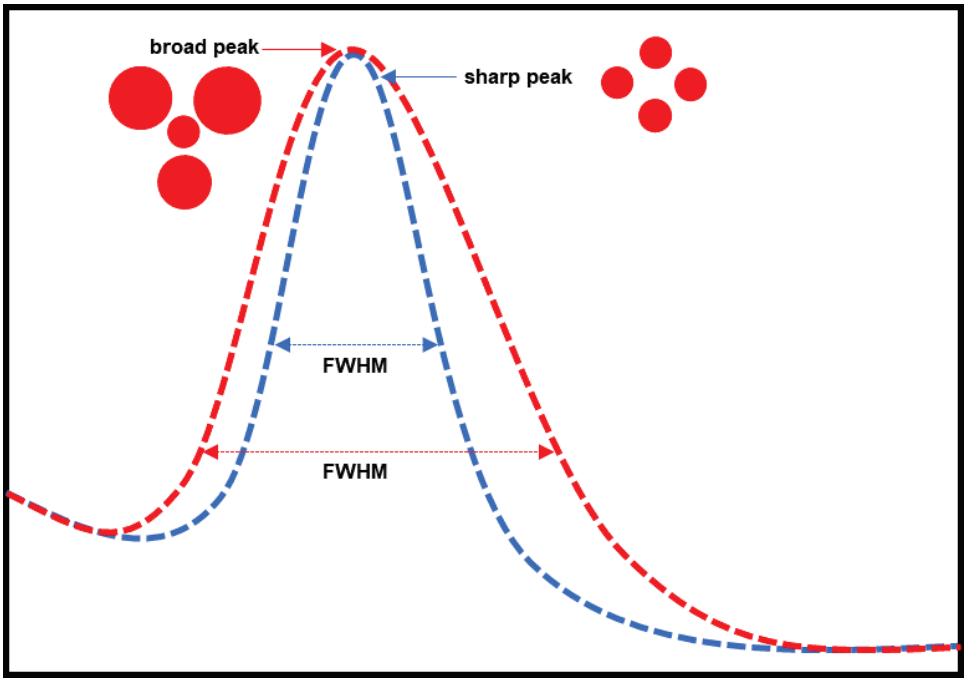

Figure 4: Schematics illustrating the concept of narrow and width size of colloids in colloidal systems. A narrow full-width half maximum (FWHM) indicates likely monodispersed AuNPs in the colloidal system (blue), and higher values indicate likely polydispersity of AuNPs in the colloidal system (red).

Hence, nanoparticles' size and interparticle distance significantly affect their plasmonic peak, which varies during sensing applications.[137, 138] Reports of

synthesised monodispersed nanoparticles have been put forward using different surfactants. [83, 84]. However, using the fluorous effect, careful selection of the surfactant or stabiliser was essential to meet the immobilisation needs of this research.

1.9 Metal Nanoparticles in Colourimetric Sensing

Noble metals are preferred for biosensing due to their optical properties, stability, and easy functionalisation with other materials. [141] While design rules for surface-based plasmonic sensors are established, knowledge of sensors based on nanoparticle aggregation is limited. This is because control over interparticle distances, number of nanoparticles per cluster, and mutual orientations is lacking, blurring the readout.

Colorimetric sensing, especially for gold nanoparticles, has several advantages over spectral sensors in mass testing. These advantages include facile fabrication, low cost, fast readout, and societal acceptance. Furthermore, the untrained human eye can complete the readout without medical assistance, making it a convenient tool for mass testing. Conversely, spectral sensors are difficult to implement as a mass testing method since they usually require sophisticated optical readouts, such as spectrophotometers and data processing, and are operated by expert personnel.

Therefore, optical geometric parameters that depend on nanoparticles' size, shape and interparticle distance are needed to enable fast and reliable readout without the need for a trained eye, computer vision or experts.

Current research by Montaño-Priede *et al.*, 2023 shows that the size, shape and interparticle distance are influential in controlling the geometric parameters needed to maximise optical readout during the conjugation of nanoparticles (gold) with biomolecules without the reliance on spectral data. Apart from this, a comparison between experimental and simulated data showed that gold decahedron nanoparticles with 30 nm edge length are the best-performing due to their colour transition-enhancing (red-to-blue) morphology. Also, reducing the interparticle gap of nanoparticles from 12 nm to 6 nm was reported to give a 4-fold increase in response, while decreasing from 6 nm to 2 nm gives an additional 3-fold increase at varying nanoparticles per cluster, especially for 20 nm decahedron nanoparticles size. Hence, this method uses gold nanoparticles at

ultra-low concentrations to find applications in real-time refractive index measurements, Surface-enhanced Raman scattering (SER), and ELISA. [142]

1.10 Consideration for Blood Analysis

Blood is a complex mixture of cellular and molecular components, including proteins, lipids, carbohydrates, cells, platelets, and plasma. Many non-invasive protocols have been developed to detect and monitor different biomarkers in blood using specific biomarkers. [143, 144] Traditional methods involve multiple steps, including dilution, filtration, and centrifugation. These methods mitigate the matrix effect due to the complex nature of the blood. [145] Additionally, several methods employ sample pretreatment, [146–148] signal amplification [149], coupled immunoassay [150], extensive volume centrifugation using a microfluidic device [151], ELISA [152–154]. Hence, overcoming this barrier is crucial for the accurate and reliable performance of sensors required for point-of-care diagnosis (POC), which directly impacts the test's sensitivity, specificity, and variability. [155–157]

Despite the progress, these methods require sophisticated and expensive laboratory equipment and technical skills, which hinders their use in the efficient development of POC testing. Hence, creating new strategies to reduce this complexity or bypass the matrix effect is necessary to reduce the sample matrix effect, leading to reduced sensitivity, increased background noise, and inaccurate quantification. [158, 159] Surface modification is crucial for minimising the impact of blood's complex properties on the sensitivity, specificity, and variability of tests involving ligand interactions. This process can be customised independently or combined with other techniques to reduce or prevent the matrix effect. It is crucial to create an anti-biofouling surface that promotes effective interactions between analytes and the immobilised surface molecules while ensuring favourable non-specific interactions between the surface and various blood-associated molecules. A study conducted by Chen et al. (2021) explores the hydrophobic nature of a fluorinated layer by modifying the surfaces with fluorinated polymer brushes using activators regenerated by electron transfer atom transfer radical polymerisation (ARGET-ATRP) and thiol-epoxy click reactions. Fluorinated alkyl chains are applied by coating the surface with brominated polydopamine (PDA) and initiating ARGET-ATRP with glycidyl

methacrylate (GMA). This process results in low surface-free energy. The method demonstrated high hydrophobicity and reduced protein adsorption, indicating its potential as an antifouling coating. This research underscores the effectiveness of these modifications in addressing biofouling challenges and can be combined with other methods to achieve specific interactions. [160] Another study examined the in vitro surface modification of a poly (2-hydroxyethyl methacrylate) (pHEMA) hydrogel film to enhance its hydrophobic and anti-biofouling properties. The pHEMA film was modified by grafting perfluorooctanoyl chloride (F15) onto its surface through covalent bonding. This modification significantly improved the surface's hydrophobicity compared to the unmodified layer. Specifically, the water contact angle increased from 101.5° for the unmodified pHEMA film to 135.8° for the pHEMA-F15 film. The surface energy decreased from 45.07 mN/m for pHEMA to 13.32 mN/m for the modified film, creating a hydrophobic layer suitable for various medical applications. When evaluated, the pHEMA-F15 film demonstrated the potential to significantly reduce bovine serum albumin (BSA) protein adsorption compared to the unmodified pHEMA. This approach improves the elimination of unwanted molecules and aids in detecting and analysing molecules in blood and complex samples. It prevents non-specific protein adhesion on device surfaces and can be adapted independently or alongside other methods for medical diagnostics and research. [161] Such non-specific interactions can lead to thrombus formation or the failure of blood-contacting devices during their interactions with the blood, creating an aggregate of platelets and fibrin. In this case, anticoagulants and antiplatelet agents are commonly used to prevent or treat blood clotting. Modifying the surface with multiple coatings is beneficial to enhance the antifouling properties of blood-contacting devices, which is crucial for clinical and biomedical applications. This approach can create low surface energy (for hydrophobic surfaces) and improve stability and efficiency. Additionally, combining this method with localised surface plasmon resonance could offer further advantages for signal amplification due to the opportunities provided by the size and shape-dependent properties of the nanoparticles upon interactions with electromagnetic radiation. [162] Therefore, developing a refreshable hydrophobic surface, especially utilising the fluorous effect, is an essential protocol that can be explored. The fluorous effect is crucial for developing stable hydrophobic surfaces with low surface energy necessary for specific interactions. In the past, it has been utilised to create reversible

immobilisations and develop fluorous-directed architectures, particularly by the Clark group. [32, 163] This proposed method can potentially reduce or eliminate the matrix effect, which can adversely affect the performance of devices needed for various diagnostic applications. The knowledge from this approach is invaluable and can be tailored or utilised independently or with other surface chemistry techniques to improve overall results.

Specifically, the hydrophobic interaction and specificity created using the fluorous effect can be utilised to passivate the surface of these devices to create multiple or differential surface affinities adaptable for specific interactions, enabling researchers to customise their applications. This is especially valuable for critical clinical applications, including point-of-care diagnostics, where blood and analytes are required for analysis. Hence, customising this surface allows for a reliable strategy to overcome non-specific interactions associated with various devices used in blood analysis for the selective, specific, and reversible attachment of biomolecules or their related analytes.

For example, hydrophobic interactions or layers are key factors in protein (e.g. fibrinogen) adsorption to device surfaces, as they are energetically more favourable for proteins to adsorb. [164] Therefore, more proteins are readily adsorbed to the hydrophobic layer than the hydrophilic layer. By incorporating and conjugating perfluorinated molecules with analytes specific to proteins, carbohydrates, or other essential molecules, along with the necessary surface chemistry for fluorous interactions, we can enhance the functionality and performance of devices. This enhancement can significantly improve the efficiency of analytical devices used for blood-related diagnostics. However, further research is needed to evaluate the effectiveness of the fluorous effect in enhancing the efficiency of devices that utilise blood analytes or analysis.

1.11 Mechanisms of Nucleation of Nanoparticles

Nucleation is the initial step in the formation of nanoparticles. [165] It refers to the process by which small clusters of atoms or molecules (nuclei) form from a supersaturated solution or vapour. This rapid process shapes the size and properties of the nanoparticles (NPs) and requires high supersaturation levels. Understanding this critical stage is essential to controlling the NP dimensions and functionalities.

During the mechanisms, the nucleation stage initiates the formation of nanostructures (crystalline or amorphous) from the reaction phase (gas, plasma, liquid, solid). Here, crystals are formed from the solution, liquid, vapour, or solid, containing a small number of ions, atoms, or molecules where they arrange themselves in a characteristic pattern like a crystalline solid. From here, they form sites on their surface where additional particles are deposited to encourage further growth. Factors that can affect the nucleation stage are the ionic strength, temperature, colloidal volume, stoichiometry of reactants and the level of agitations.

Increasing the temperature of the reaction vessels lowers the critical supersaturation and increases the kinetic energy and, hence, the nucleation rate. So, efficient control of this stage is important in producing tailored NPs. Apart from this, the ionic strength affects the reactivity of the reactants (ions), the ionic double layer at the crystal interface and crystal growth and the subsequent adsorption of the ionic species on the nuclei and crystal growth. Also, careful agitation of the reaction vessels can induce nucleation or create a form of increased fluctuation that leads to nucleation by shear-induced nucleation or an increase in fluctuation. [166–169]

Apart from this, several theories have been proposed in support of the nucleation and growth mechanisms of NPs [170]

1. Lamer's mechanisms
2. Ostwald and Digestive Ripening
3. Finke-Watzky Two-Step Mechanism
4. Coalescence and Orientated Attachment
5. Intraparticle Growth

1. Lamer's mechanisms of nanoparticle synthesis

This stepwise process includes nucleation, growth, and ripening during NPs formation. Since its explanation by Lamer et al. in 1950, it is a widely accepted model for the formation of nanoparticles. [83][171, 172] It accounts for the stages in the formation where NPs come together to form small clusters or nuclei. These clusters serve as the template for adding other precursors to form the NPs of interest. There are three stages involved.

(I) A rapid increase in the concentration of free monomers in solution, (II) the monomer undergoes “burst-nucleation”, significantly reducing the concentration of free monomers in solution. The rate of this nucleation is described as “effectively infinite”, and after this point, there is almost no nucleation occurring due to the low concentration of monomers after this point; (III) following nucleation growth occurs under the control of the diffusion of the monomers through the solution. A good example is the growth of silver halides, which have been studied and follow this classical nucleation and growth. [173, 174]

1. A rapid increase in the concentration of free monomers in solution. Here, the concentration of the monomers increases to a critical supersaturation level (C_{min}) or concentration needed for nucleation to occur. [175]
2. These monomers undergo “burst nucleation”, which significantly reduces the concentration of free monomers in the solution. This process reduces or exhausts the concentration of the monomers, and the rate of this nucleation is described as “effectively infinite” after this point.
3. The reduced concentration of these monomers reflects the growth of the monomers controlled by diffusion of the monomers through the solution. Hence, the growth of the nanocrystals is a function of the reaction time and concentration of precursor atoms in the reaction mixture. [176–178]

LaMer and Dinegar also explain the correlation between the nucleation and growth of the generated nuclei for monodisperse particles in a homogeneous solution. Increased solute concentration up to a critical level (C_{crit}) from the system or external source encourages nucleation. [179] Depending on the supply rate and the amount of the solute or precursor consumed per time, this stage soon peaks (C_{max}). Once the peak is reached, the curve faces a downward trend due to increased consumption of the reactants for product formation and reaches the critical level again. This signifies the end of the nucleation stage, and stable nuclei are generated until the supersaturation stage is attained below the critical level without further re-nucleation. At this point, the growth stage ensues with a distinct difference between the nucleation and the growth stage and yields monodispersed particles. Therefore, since the final number of the dispersed particles is determined only in the nucleation stage and kept constant in the growth stage. Apart from this, the control of particle size is equivalent to the control of particle number. Hence, the nucleation stage creates an opportunity to control the size of the NPs in the reaction system. [180]. However, LaMer ‘s model

was created to measure the qualitative explanation of monodispersed particle formation and not for size control. Other models have been put forward to explain different phenomena of NPs growth and formation. [181]

2. **Ostwald ripening**

The mechanism of Ostwald ripening occurs due to dissimilarities in the solubility of NPs in solution. Due to the size of smaller NPs, they have a higher surface energy, which impacts their solubility in solution. When they interact, they are guided by thermodynamic factors that influence the further growth of larger NPs in solution. Unlike the Ostwald ripening, digestive ripening is also a process of colloidal synthesis for NPs formation. Here, the smaller particles, with high surface energy, grow instead of the larger ones because the larger particles re-dissolve into the solution depending on thermodynamic factors. The digestive ripening is used mainly for synthesising NPs with a narrow size distribution, which helps convert polydisperse nanoparticles into monodisperse nanoparticles. In contrast, the Ostwald ripening favours particle growth during synthesis.

3. Finke-Watzky Two-Step Mechanism

Unlike the classical nucleation theory, the Finke-Watzky two-step Mechanism describes the simultaneous nucleation and growth of NPs in the colloidal system. Although this has not been fully proven explicitly, it is still shown to follow the growth pattern in the classical nucleation framework. This model is used to synthesise the nanostructure of transition metals (especially Ir, Au, Ag, Pt, Rh, Pd, and Ni) and the protein aggregation process. [182]

4. Coalescence and orientated attachment

Except for the orientation created, these processes are similar. Here, NPs can come together to randomly form a larger particle when they coalesce compared to oriented attachment, where there is a pattern of crystallographic alignment of the attachment along planes.[183]

5. Intraparticle Growth

This process-specific growth of NPs arises due to instability in the surface energy of the NPs. It is reaction-specific (Figure 5) and can be affected by many factors, including the size, conjugation process and concentrations. [184–186]

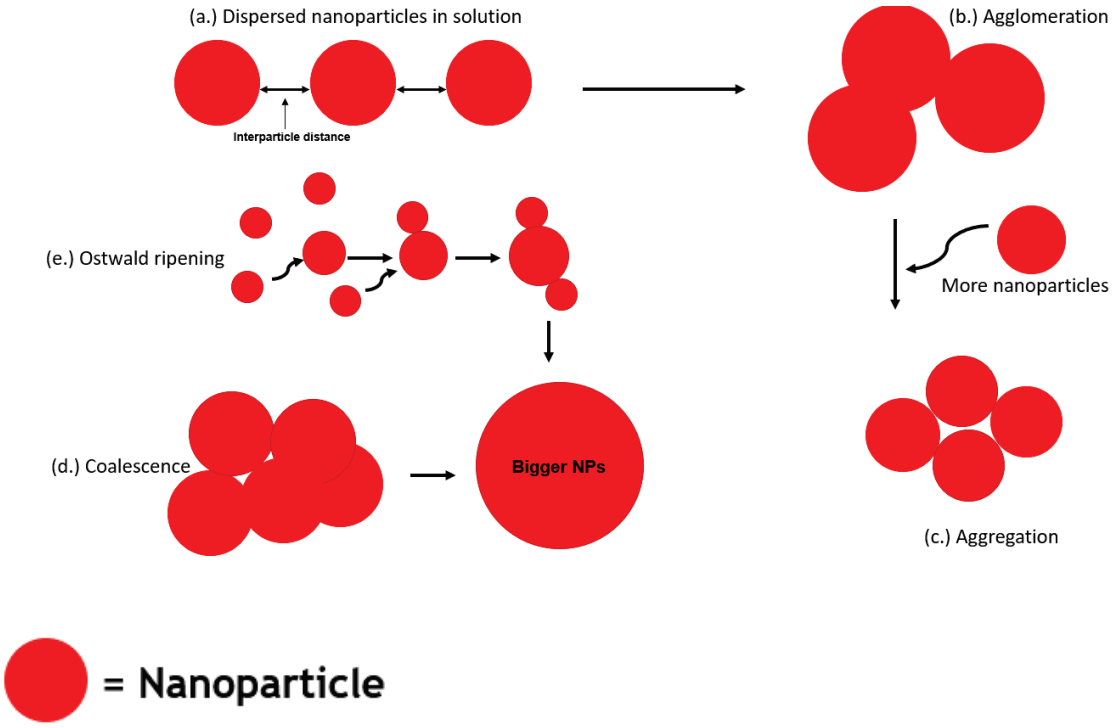

Figure 5: Schematics illustrating different stages affecting the size and stability of colloidal suspension. (a.) The nanoparticles are dispersed well in solution with adequate interparticle distance. (b.) Agglomeration of nanoparticles of bigger sizes is due to an unfavourable environment. This method creates tightly bound NPs. (c.) Particles aggregated due to a reduced interparticle distance. This method could be reversible under favourable conditions. (d.) The smaller nanoparticles merge to create a larger nanoparticle, reducing the number of particles (e.) In this case, larger particles grow at the expense of smaller ones in a dispersion.

1.12 Nanopatterns and their Applications

Recent advancements in creating colloidal nanoparticles have led to impressive developments in self-assembly applications, particularly on micro-patterned surfaces. The applications of this technique cut across several fields, including tissue engineering, biosensors, biochips, drug testing, optics, and fundamental research in molecular and cell biology.[187–189] However, nanoparticle immobilisation and self-assembly into controlled, nanometer-sized patterns is challenging due to factors like pattern size and the tendency of the nanoparticles to aggregate on the patterned surface. Achieving specific, controlled assemblies

of nanoparticles and the positioning from colloidal systems demand precise strategies.

Several methods exist for fixing nanoparticles in patterns, including single-layer electrostatic attachment of charged particles, multilayer electrostatic attachment, embedding within polymer brushes, and incorporation into sol-gel or polymer matrices. However, significant challenges need to be addressed to successfully immobilise gold nanoparticles over large, patterned areas. [190]

1. Controlled placement:

This is one of the most prominent challenges during the controlled immobilisation of nanoparticles on a functionalised surface or platform, especially at the nanoscale region. Hence, efficient functionalisation of the nanopattern surface for biorecognition purposes is essential.

2. Tendency for aggregation:

Because nanoparticles have a large surface area compared to their volume, they also have high surface energy and are very reactive. This makes them more likely to clump together. This clumping, or aggregation, is a significant problem as it can interfere with the precise placement of nanoparticles in the desired location.

3. Efficient surface modification

Ligand exchange is essential for creating surfaces that can chemically and easily interact with each other. If ligand exchange is inefficient during surface modification, it can block or slow down the precise placement of nanoparticles in their intended pattern.

4. Immobilisation techniques

Several methods have been created to attach nanoparticles to surfaces precisely. Yet, each method presents its difficulties. Hence, an immobilisation technique favours efficient ligand exchange, functionalisation, and proper orientation of the interacting functional groups is desirable for immobilisation in nanopatterns.

5. Nanopattern techniques

Creating nanopatterns with e-beam is costly, time-consuming, and complex, especially below a certain nanometer scale. Nanoparticles need optimal conditions for effective immobilisation; larger ones easily immobilise, but as size decreases, aggregation issues arise. Capillary force methods for nanopattern immobilisation present control challenges, particularly for particles under 30 nm.

1.13 Nanofabrication Techniques

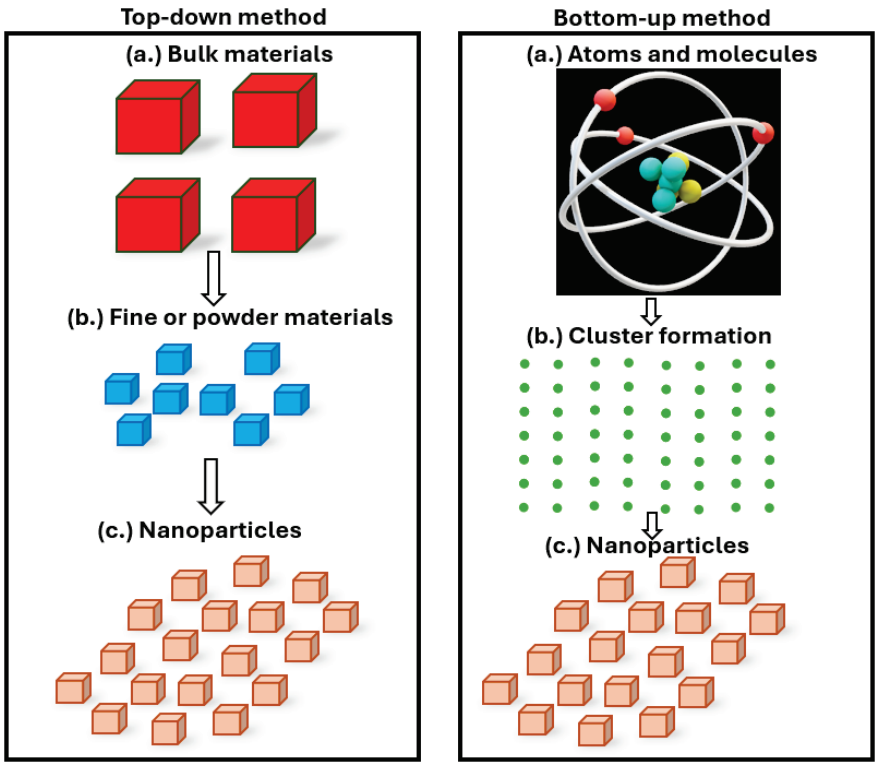

Figure 6: Schematic illustrating the top-down and bottom-up nanofabrication approaches to reduce the mass of bulk materials to produce fine particles down to the nanometer size (top-down method). (a.) The bulk materials are broken down into smaller pieces by different top-down methods to form fine materials (b.) The fine materials are further broken into the nanoparticles (c.) In the bottom-up method, various reduction methods and chemical vapour decomposition methods are used to produce nanoparticles. A similar process is followed in the bottom-up approach but from the smallest-sized material (c.).

Several techniques can be used to define and deposit engineered nanostructures. These can be broadly categorised as either top-down or bottom-up approaches.[191] Top-down approaches involve additive or subtractive methods to define nanostructures from their bulk materials, such as photolithography, scanning probe lithography, laser machining, soft lithography, nanocontact printing, nanosphere lithography, colloidal lithography, scanning probe lithography, ion implantation, diffusion, and deposition.[191–193] Despite its

numerous advantages, it is limited by cost (especially the lithographic process), hazardous materials, surface properties requirements, and longer etching times.[194, 195] On the other hand, the bottom-up approach provides the step-by-step assembly of atoms or molecules to achieve the desired nanostructures. It incorporates the direct synthesis of materials (**Error! Reference source not found.**). Examples include plasma arcing, chemical vapour deposition, metal-organic decomposition, laser pyrolysis, molecular beam epitaxy, sol-gel method, wet synthesis, and self-assembly processes. [196]

Using different top and bottom-up fabrication methods, nanomaterials can be precisely directed at specific areas of micro and nanopatterned materials to create a reconfigurable metasurface.

1.14 Microarrays

Microarray technology began in the 1980s and 1990s, when scientists first developed DNA microarrays to measure the activity of many genes at once. Since then, researchers have improved these methods to analyse gene activity, genetic differences, and protein interactions more efficiently. [197, 198]

DNA microarray technologies are powerful tools designed to detect and measure the expression of thousands of genes in a single experiment and are vital to studying mutation and other genomic features in biomedical and clinical research. Microarray platforms were initially designed to measure the transcriptional levels of RNA transcripts derived from thousands of genes among genomic sequences in a single experiment. This technology remains the basis for next-generation sequencing strategies using microarray spotting or light-directed chemical synthesis methods.

Apart from its limitations, which involve the need to pre-manufacture and transfer DNA for each spot (initially 450 μm), is costly, requires a large gap between each spot and involves cumbersome washing steps, microarray spotting has been used for over 20 years. However, recent advances in spotting devices create opportunities for smaller spot distances, and the length of DNA molecules is only limited by PCR (up to several kb).[199]

The light-directed chemical synthesis method was initially used to generate peptide arrays using photolabile groups with the aid of photolithography. Further improvement in this method showed that it is possible to create oligonucleotide

arrays via light synthesis to generate different DNA spots as many as 135,000 different spots, each measuring 35 μm × 35 μm, can fit on a single slide. Further improvements in spot size down to 5 μm have been reported in the literature [200][201] This method is cumbersome, costly, time-consuming, and requires several photolithographic masks to create the desired array. Different protocols have also been developed to address these. [202–207] Since its development, several research have reported them to study different gene expression signatures in tumours, disease progression, cellular response to stimuli, and drug target identification.[208–210]

Using a multi-stage approach, the microarray design has recently gone beyond use in gene expression analysis approaches to other research areas. Notable among these is the detection of Single Nucleotide polymorphism (SNPs) of the genome, methylation error, and alternative RNA splicing. [211–214] However, due to the need to create detection platforms with high accuracy and low cost, other high-quality microarray tools with standardised protocols have emerged to accurately detect and measure analytes of interest with powerful computational output. However, most are non-specific [215], non-repeatable, costly [216], and lack the desired efficiency. [217, 218]

Exploiting microarray for expression profiling is based on two fundamental principles.

1. In many gene pools, the change in expression occurs due to the alteration in the abundance of the cognate mRNA. Apart from this, posttranscriptional factors can also affect gene expression but are not generally amenable to microarray analysis.

2. Only the DNA strands with complementary sequences can hybridise with another DNA to form a stable, double-stranded molecule.

Therefore, using the property of this microarray by immobilising millions of single-stranded copies of a gene as individual array elements on a solid support surface. The incoming DNA is then incubated with mixture of labelled DNA molecules containing, in proportion, the representation of all the genes that are being expressed in each tissue sample. The amount of heteroduplex formed between the labelled or complementary molecules and the gene of interest can be used to estimate the relative transcript abundance level of each gene. From here, the gene expression pattern can be compared to other RNA abundance levels for thousands of genes in a single experiment. [219]

Based on the length and size of the length and size of the molecules, two types of microarrays exist.

1. DNA microarray, printed on membrane or glass with large fragments of genes between 400-2,000 bp and usually synthesised by PCR amplification.

2. Oligonucleotide-based microarrays of smaller, short synthetic molecules between 20 bp. The design and production of oligonucleotide-based microarrays usually occur via specialised equipment that is not typically available to research laboratories. The in-depth analysis of this process is beyond the scope of this research, which aims to focus more on the DNA microarray.

According to the analysis by Deyholos *et al.*,2001, the design and production of DNA microarrays can be grouped into three stages:

1. DNA probe preparation is one of the most resource-intensive aspects of microarray production. This can be immobilised DNA produced with high throughput via PCR amplification or any other source.

2. Preparation of a suitable array substrate. Here, primers are designed while the concentration and type of probe available are estimated from electrophoresis and

3. Robotics deposit array elements on different supports, such as nylon or glass. The properties (e.g., hydrophobicity, rigidity, and porosity) of the surface where the probes are spotted are very important. [220–222]

1.15 Immobilisation Techniques

Immobilisation techniques are techniques designed for tailored applications in microarray development. The aim is to ensure overall efficiency while reducing costs to the minimum. These techniques can be divided into physical and chemical methods depending on the type of biomolecules or nanoparticles involved and their interactions or the immobilisation surface involved (Figure 7). Consequentially, several methods used for enzyme immobilisation can also be used or adapted for the immobilisation of nanomaterials or both simultaneously (in case of conjugation of the nanomaterials and enzyme) for enhanced signal and sensitivities. However, several conditions, including those that can maintain or support the stability of the biomolecules, their kinetics, and reaction mixture, are needed for efficient immobilisation stages on the substrate's surface and must be considered.[223–225]

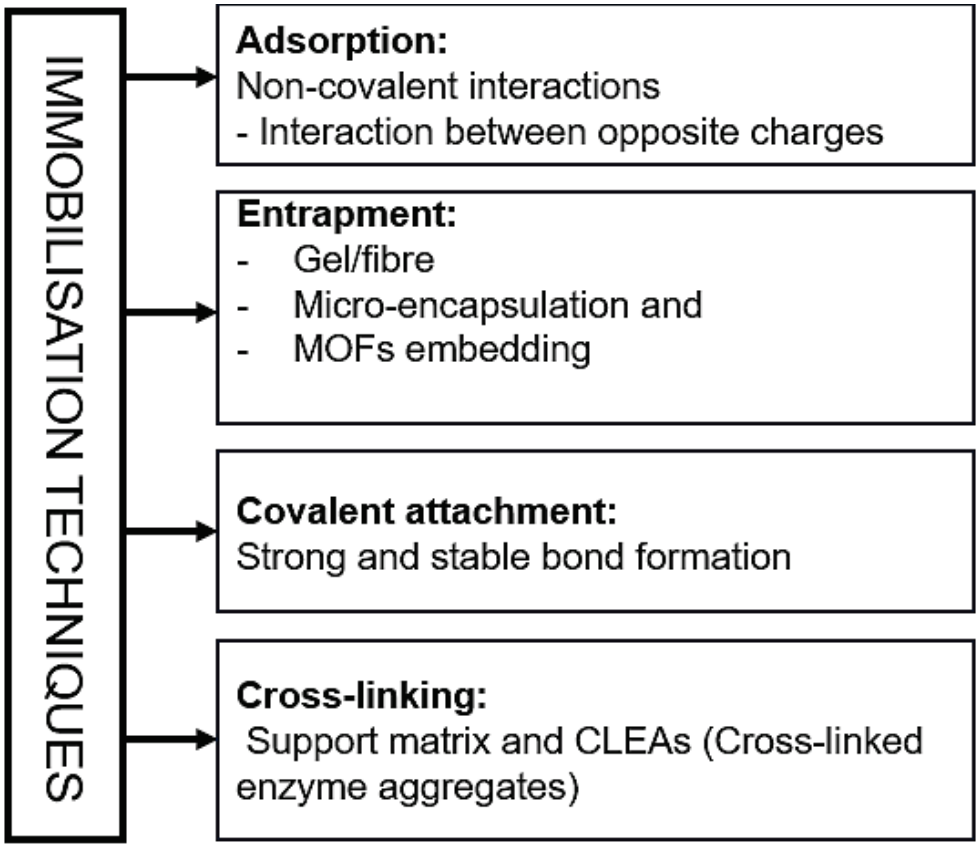

Figure 7: The diagram shows the various methods used to immobilise materials, which can be adapted based on the specific goals of each research study.

1.16 Support Materials for Reversible Attachment

Using compatible support materials during immobilisation is one of the most critical steps in achieving efficiency. [226] The following are the properties of the support materials:

1. Insoluble: This is important to ensure that the materials do not dissolve and participate in the reaction mixture during the Immobilisation process.

2. Mechanical strength: The surface needs this to withstand the different stages of the immobilisation process, including fabrication, if involved.

3. Non-biodegradable: The surface intended for the immobilisation process must retain its integrity. This prevents them from actively participating in the chemical reactions when not needed.

4. Reusability and inertness: The reaction surface must be inert to prevent unwanted side reactions of the reactant or products. Also, the surface reaction must be created to ensure that the bare surface can be reversible/re-produced for subsequent reactions. This is needed to manage the cost and wastage.

5. Specificity: The essence of most immobilisation is to ensure specific interactions that ensure the biomolecules of interest can be detected, identified, and

immobilised using the right chemical or physical interactions. Therefore, high specificity is desirable in biosensing applications.

6. Ultraclean surface: The substrate or support materials must be adequately cleaned to prevent hindrance to the reaction mechanism and

7. Biocompatibility: Biocompatibility of biomolecules is necessary; just like in the 'lock and key' hypothesis, the interacting molecules or surfaces must be recognisable via the head group or specific functional group of interest to trap the incoming molecules.

These properties have also been applied to enzyme immobilisation. Unlike enzymes, which are biological catalysts and are subjected to several alterations in their activity, specificity, and stability upon immobilisation or anchor to solid support, using MNPs creates a better opportunity to explore their optical, catalytic, and magnetic properties while preventing unwanted aggregation and facilitating their recovery or re-use. In addition to the stated above, the efficiency of the immobilisation depends on the overall properties of the reacting species and their environment, including the pH, temperature, ionic strength and ratio of the reactants or products formed. Therefore, depending on the aim, several immobilisation techniques have been reported.

1.17 Self-Assembly Monolayer

The term 'self-assembly monolayer' refers to a single layer of molecules on a surface formed by self-packing. [227] With this phenomenon, several supramolecular interactions can be created with unique properties tailored for significant biomolecular engineering and nanotechnology applications. This is a fundamental phenomenon in biology where biomolecules, especially proteins, peptides, and DNA, spontaneously organise themselves into complex and functional architecture. Due to these important spontaneous assemblies, the inherent properties of different molecules (DNA) or nanoparticles (gold and silver) can be tuned to serve specific functions where they can open exciting opportunities in sensing, diagnostics, biomaterials, bioelectronics, drug delivery, catalysis, molecular recognition, [223, 226] and nanocomposite with unprecedented control towards precision and specificity.

Recently, interest has grown in various fields due to the versatility of self-assembled molecules, which surpass barriers in molecular recognition

architecture, thus reducing costs and enhancing scalability and overall efficiency. Despite this gain, several challenges have been reported to reduce this phenomenon, which distorts their applicability in several biomedical fields.

Due to the high surface energy of nanoparticles, there is a tendency for uncontrolled aggregation, polydispersity, and a lack of directional interactions due to constant Brownian motion; it is, therefore, challenging to achieve self-assembly and specific structural interactions for intended applications. Apart from this, the contribution and balance of different interacting forces, including van der Waals, dipole-dipole, and other non-covalent or covalent interactions, are a few challenges that make precise self-assembling of these nanoparticles difficult. In addition, the size, shape, functional groups, solvation, concentration, and immediate environment of the nanoparticles are other major contributing factors that can hinder the success of self-assembly monolayer formation. [228]

1.17.1 Physical Adsorption

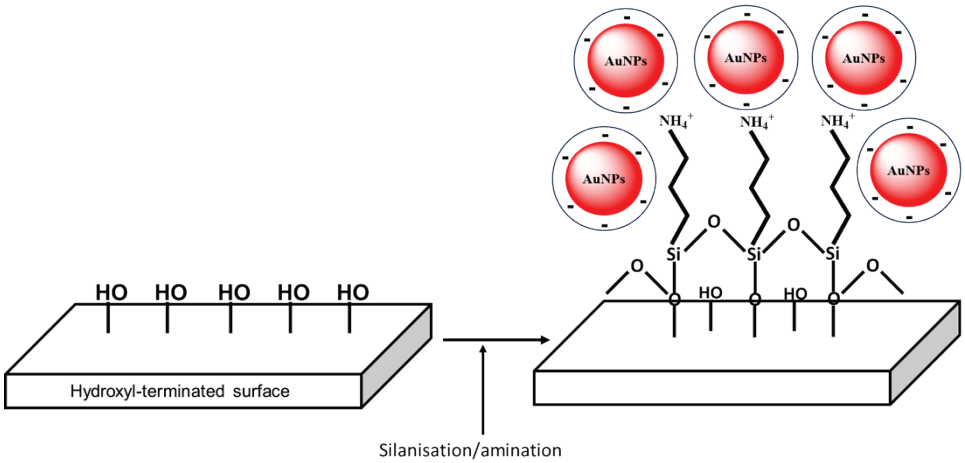

Figure 8: Schematics illustrating the non-covalent attachment of molecules on the glass surface. The hydroxyl-terminated layer of the glass is explored to create a self-assembly layer suitable for interaction with the amine functional group. This creates a template for ionic interactions in the presence of opposite charges.

This is the most common and simplest method of immobilising biomolecules or nanoparticles (also between the bioreceptor and the substrate). It is one of the most essential components to consider during the immobilisation of biomolecules due to the cost involved at this stage. Here, the substrate can be charged to favour ionic interactions or uncharged to create weaker bond interactions, including hydrogen bonds, van der Waals, hydrophilic and hydrophobic interactions, which favours immobilisation or SAM formation (Figure 8). Although this interaction is non-specific, it is fast, simple, and direct.[229, 230] However, the major

drawbacks to this method include random orientation, desorption, crowding effect, sensitivities to Ph, poor reproducibility, and limited applicability.[231] [232] For example, electrostatic interactions using charged SAM with amine functional and negatively charged carboxyl groups have been reported. [233] Also, a study showed that single use of charged molecules (i.e., amine-, epoxy- or aldehyde-silane) does not give the best SAM, but when synergistically combined with other charged molecules at specific ratios. However, combining different functional groups to aid the overall reaction conditions, including stability, is desirable. Using physical adsorption techniques, MNPs can be used for colourimetric sensing either alone or to enhance signals when conjugated to other molecules, e.g., enzymes or proteins. For citrate-coated gold nanoparticles, the extra carboxylic group can be electrostatically immobilised with functional groups, including amine. [234]

1.17.2 Chemical Attachment

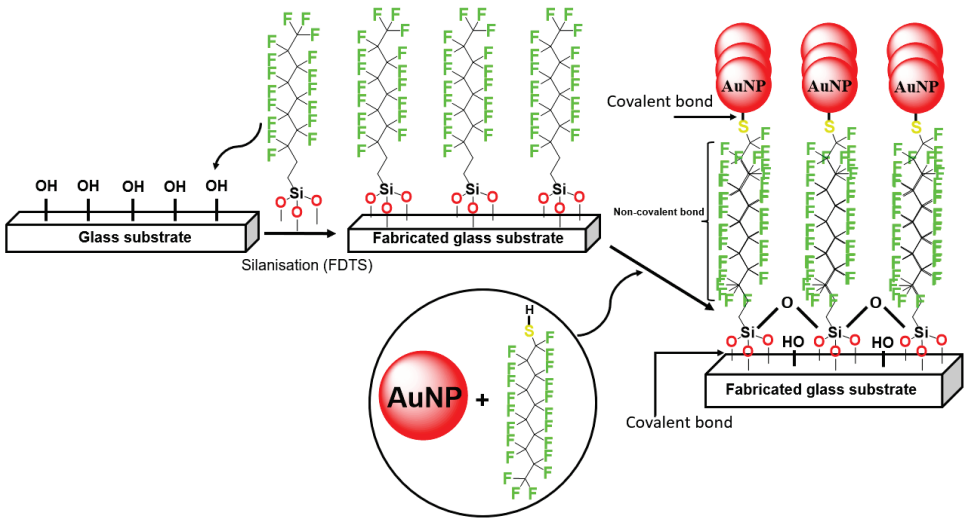

Figure 9: The schematics illustrate the chemical attachment of molecules on the glass surface. In this method, the chemical attachment between thiol and gold nanoparticles is an ideal example where covalent interaction can be explored. Furthermore, a hydroxyl-terminated surface is well-suited for the self-assembly of silane monolayers.

This approach strengthens the process, solving issues of desorption and instability often seen in physical adsorption.[235] It can involve chemisorption or firmly attaching biomolecules like proteins using specific functional groups. These include carboxylic (-COOH), amine (-NH2), hydroxyl (-OH), or sulfhydryl (-SH) groups and can come from aldehyde, epoxy, silanes, or isothiocyanates, among

others. These groups help anchor molecules in place through silanisation or similar methods. The binding can occur through a chemical reaction that either donates or accepts electrons.

Covalent attachment is an example of a chemical method of immobilisation. This method leads to an even distribution of probes on a surface, enhancing reliability and consistency. This method could be direct immobilisation, direct immobilisation after surface modification, and/or indirect (use of cross-linkers). Some copolymers such as molecules such as poly (glycidyl methacrylate-co-methyl acrylate) (P(GMA-co-MA)) and poly (styrene-co-maleic anhydride) (PSMA) can easily attract electrons on their own, and this favours their interactions with other molecules without the need for any modification. Research shows that P (GMA-co-MA) has a ring-shaped epoxide that can easily react with the amine functional group of biomolecules, making them invaluable for direct immobilisation technique. [236–238] Conversely, indirect attachment involves surface functionalisation of the surface or biomolecules of interest to introduce functional interest groups.

Gold nanoparticles have become popular in colourimetric and biosensing because they can be used alone or combined with other molecules to boost sensitivity in identification, detection, and separation processes. Using EDC as a cross-linker, extensive research has gone into EDC (1-Ethyl-3-(3-dimethylaminopropyl) carbodiimide) and its ability to link up with amines and form a bond between a solid surface and a biomolecule of interest, by activating the carboxylic acid group on nanoparticles. These activated groups then react with primary amines. Adding sulfo-NHS (N-hydroxy-succinimide) from an active ester compound speeds up this process and creates stronger, more stable bonds for later reactions. This method is often used when attaching gold nanoparticles to antibodies. The research by Mimari et al. (2021) [158] and colleagues describes a reliable method to attach citrate-coated gold nanoparticles (NPs) to plastic surfaces, which then allows for the addition of various biomolecules at a high concentration. The technique uses the strong bond between gold and sulphur-containing thiol groups, commonly utilised in developing functional surfaces (Figure 9). Furthermore, bare gold nanoparticles can be modified by attaching polyethene glycol (PEG) to the thiols (creating PEG-SH). This reduces unintended reactions due to PEG's water-attracting properties, enhancing biocompatibility. The modified gold

nanoparticles also have additional carboxylic acid groups that can interact with different substances of interest. [240–242]

Consequently, hybrid nanomaterials could also be created by attaching amino-functionalised gold nanoparticles, about 5 nm, onto graphene oxide sheets. This was achieved through a straightforward chemical reaction that forms a covalent bond between the molecules. This method opens the door for the development of new graphene-based hybrid nanomaterials.[243] Other functional groups used to form covalent immobilisation are maleimide and mercapto silane, which have improved efficiency. In addition, the combination of physical adsorption and covalent immobilisation can also be explored. Therefore, using covalent immobilisation offers several benefits compared to physical adsorption methods. These include high efficiency, enhanced specificity, cost-effectiveness, and increased stability.

1.17.3 Avidin/Streptavidin-biotin Interaction

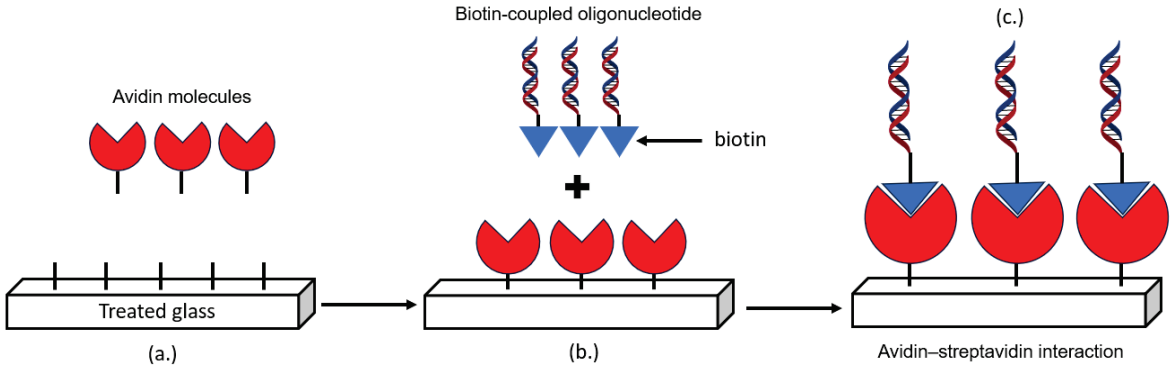

Figure 10: Schematics illustrating the avidin-biotin interactions during immobilisation. (a.) Illustrates the introduction and self-assembly of avidin on the treated glass surface. (b.) Interaction between the modified oligonucleotide and self-assembled avidin. (c.) Specific non-covalent interaction between avidin and biotin.

Avidin/streptavidin-biotin interaction is one of the most specific and stable non-covalent interactions, approximately 10^3 to 10^6 times higher than an antigen-antibody interaction (Figure 10). Avidin (PI = 10, originally derived from the eggs of aves, reptiles, and amphibians) is a basic tetrameric glycoprotein (70 KDa) with four identical subunits and terminal N-acetyl glucosamine and mannose moieties, where each unit can bind to biotin (Vitamin B_7) with high specificity and affinity (K_d = 10^{-15} M). This complex interaction involves biotin binding to the tetrameric avidin/streptavidin molecule with four binding sites. Compared to other covalent and non-covalent interactions, the binding affinity (K_d = 10^{-15} M) of

avidin/streptavidin to biotin during reaction provides desirable advantages such as amplifying weak signals, efficient operation, and high stability. It enables the use of highly diluted primary antibodies. Also, streptavidin is usually preferred against avidin because of its small isoelectric point (pI = 5) compared to Avidin (pI = 10.5). [244, 245] Avidin-biotin interactions have been used in several immobilisation protocols. [246, 247][156] Wang *et al.*, 2020 also described the use of biotin in novel biosensors. Here, a gold nanoparticles-decorated graphene field-effect transistor (AuNP-GFET) was used for detecting biotinylated macromolecules consisting of protein (protein A) and nucleotide at an approximately 0.4 pM sensitivity and high specificity. The specificity and applicability were later confirmed using real and synthetic samples and its ability to detect biomarkers of interest.

1.18 Concept of Multiplexing

Multiplexing is a powerful concept in biosensing microarrays, where multiple analytes can be detected simultaneously in a single sample. [248, 249] This allows the diagnosis of many diseases to be dramatically improved using a small number of samples at a reduced cost, time, and possibly technical know-how. Hence, this can be used to analyse samples to generate more information and interpret analytes.

One critical point in developing multiplexed biosensors is the immobilisation of receptors on the sensor or surface. Several protocols, including optimisation, biofouling, and affinity, have been designed to overcome these challenges and prevent cross-reactivity and lack of specificity among the analytes. [250–253]

A few of the challenges and progress that have been points of focus in the past include:

1. Optimisation of sensor surface: Developing optimised sensors consisting of specific materials that prevent cross-reactivity and biofouling improves the performance of multiplexing platforms or surfaces. For example, graphene oxide is reportedly used as a modified surface alone or with other specific groups that can reduce non-specific binding. [254]

2. Adoption of different detection methods: Combining different detection methods or methods of interactions, including optical, electrochemical, and

magnetic detection methods between the surface and the analytes, can reduce cross-reactivity and improve the specificity of the biosensor. [255, 256]

3. Use of affinity agent:

To improve the specificity and affinity of the multiplexing platforms, new affinity agents, including aptamers and molecularly imprinted polymers, are developed to improve the presence of affinity agents necessary to enhance specificity and affinity with the target analyte, prevent cross-reaction, and improve the sensitivity of the biosensor in question. [257]

4. Improved technology: The advent of continuously improved technology has been used to create advanced multiplexing technology, including nanoswitches and microfluidics, with enhanced sensitivity and specificity during the detection of multiple target analytes using a single sample. [258]

5. Improved quality control system: A quality control system that can improve and enhance the quality and reliability of the data produced from the multiplexed reaction in biosensors is essential. A combination of parameters, including positive and negative controls, is also essential.

Even though many proposed methods are used to improve the reliability of these biosensors with multiplexing functions, new technologies are currently being put forward to improve the existing ones to simplify the working principles of these sensors further.

Therefore, selecting the best immobilisation method for the multiplexed interactions requires several considerations, including specificity, selectivity, cost, stability, and the overall intention of the applications.[259, 260]

This introduction and review provide an overview of the progress made and the challenges commonly faced in designing and developing microarrays for the reversible attachment of nanomaterials. These challenges include issues related to surface chemistry, stability, the specificity of binding interactions, and the repeatability of the protocols.

1.19 Research Objectives

A clear understanding of these challenges is essential for creating surfaces that can effectively facilitate the reversible assembly of various nanomaterials, including DNA and metal nanoparticles (MNPs). The ability to develop protocols

that can overcome the challenges and direct this assembly process is crucial for many applications, including sensing, drug delivery, microarray designs, and nanotechnology. Hence, the objectives of this research are:

1. To immobilise fluorous-modified oligonucleotides (DNA) on a fluorous patterned surface in a repeatable manner (3 times).
2. To investigate how the number of fluorine atoms incorporated in fluorous-modified oligonucleotides affects the strength of immobilised oligonucleotides.
3. To direct the reversible and switchable immobilisation of gold and silver nanoparticles on micro-patterned surfaces (800 μm) for at least 10 times on the same engineered surface using the fluorous effect.
4. To direct the re-usable immobilisation of gold nanoparticles on a sub-500 nm fluorous patterned surface with the hope of immobilising single nanoparticles onto a sub-100 nm fluorous patterned surface using the fluorous effect.

Chapter 2

2.1 Materials and Methods

This chapter gives an overview of the materials used for this research, including the fabrication steps at the James Watt Nanofabrication Centre (JWNC), the other experimental stages carried out at the Rankine building, and finally, the Advance Research Centre (ARC), University of Glasgow.

2.2 Materials

Except stated otherwise, all chemicals listed in (Table 1) were used without further purifications from the manufacturer.

Table 1: List of chemicals used in this research and their sources.

Name	Source
Perfluorodecanethiol (PFDT, 97%),	Gelest, Inc. (Sigma Aldrich)
Trisodium citrate dihydrate ($Na_3C_6H_5O_7 \cdot 2H_2O$, ≥ 99.0%)	Merck
Gold (III) chloride trihydrate (≥99.9%)	Sigma-Aldrich
1H,1H,2H,2H-heptadecafluorotrimethoxylsilane	Gelest, Inc. (Also from TCI and Sigma Aldrich)
Citrate- coated gold colloids (20 nm and 40 nm)	Sigma-Aldrich
Citrate-coated silver colloids (40 nm)	Sigma-Aldrich
n-Decyltrimethoxylsilane	Gelest, Inc.
S1805 and S1818 positive resists	Shiply
Polymethyl methacrylate, PMMA	All resist
Silver nitrate	Sigma-Aldrich
Sodium hydroxide (>99.0%),	Sigma-Aldrich
Hydroxylamine hydrochloride (HH, 99.999%),	Sigma-Aldrich
Silver nitrate (>99%),	Sigma-Aldrich
Glass (borosilicate)	Pi-kem
Acetone	Sigma-Aldrich
Ethanol (99.96%)	VWR chemicals
Methanol	Honeywell chemical
Isopropanol	Sigma-Aldrich
H_2O (MilliQ)	Milli-Q purification system
RO water	JWNC
Phosphate saline buffer	Sigma-Aldrich
MIBK (methyl isobutyl ketone)	Merch chemical
Microposit MF CD-26	Shiply

H_2O refers to high-purity water with conductivity of 2 μS cm−1 and resistivity of 18.2 MΩ·cm at 25 °C obtained from a Milli-Q purification system.

2.3 Methods

2.3.1 Surface Cleaning and Functionalisation (SAMs)

a. Glass substrates are widely used due to their stability, inertness, and low autofluorescence. In addition to this, their chemistry supports the chemical modification of silanes and permits several modifications.
In this research, 500 μm-thick borosilicate glass wafers (pi-kem) were scribed into 4 square centimetres. The substrate was thoroughly cleaned by ultrasonication in acetone, methanol, and isopropanol for 3 min each. The cleaned sample was activated using O_2 plasma (PlasmaFab 505) set at 150 Watts for 3 min.
b. The surface required to immobilise DNA was silanised using two-layer self-assembled functionalisation with nDTS and FDTS.
c. The substrate required for the immobilisation of metal nanoparticles (MNPs) had its surface functionalised using a single-layer silane deposition with FDTS only.

2.3.2 Resist Spinning (EBL)

Electron beam lithography was used to create the required nanopatterns. To achieve this, a bilayer of poly-methyl methacrylate (PMMA) consisting of 4.0% dilution of PMMA (2010) in anisole was spun on the surface at 5000 r.p.m for 60 seconds to give a resulting resist layer of 100 nm, baked at 180 °C for 15 seconds to evaporate the trapped solvent. This process was repeated using another layer of 2.5 % solution of PMMA (2041) to produce a second layer with a thickness of 40 nm. This arrangement ensures that a good undercut profile and improved resolution were made after the development. Consequently, the sample for the immobilisation of the metal nanoparticles (MNP) was spun at 4000 r.p.m. each for 60 seconds and cured at 180 °C intervals (for each PMMA layer).

2.3.3 Charge Conduction Layer for Ebeam Samples (DNA and Nanoparticles)

Vacuum deposition for surface metallisation is a technique where metal is heated in a vacuum until it evaporates. The vaporised metals are later condensed on the surface of the metal to form a thin metal layer. The thin conduction layer of metal, such as Aluminium or Tin, is needed to dissipate charges when the surface is exposed to a stream of electrons. For the fabrication of the substrate used for DNA attachment, a 30 nm aluminium layer was deposited on a glass substrate at a rate of 0.3 nm/s using the Plassys MEB 4005 e-beam evaporation system. Subsequently, a 20 nm aluminium layer was evaporated onto the sample at 0.5 nm/s with a Plassys IV to act as a conduction layer for the nanoparticle immobilisation.

2.3.4 Pattern Design for E-Beam Lithography (DNAs and Metal Nanoparticles)

Photolithography and e-beam lithography (EBL) are two common methods to transfer molecular patterns to desired surfaces using light and electron beams, respectively. Unlike photolithography, which is limited by the wavelength of light, e-beam lithography provides greater resolution with improved fidelity at the nanometer scale region. Patterns were designed to fabricate a sample for the immobilisation of oligonucleotide, using an L-edit CAD software from Tanner Research Inc. The design was exported as a graphical data system (GDS) file with a multilayer pattern. Layout Beamer (GenlSys Gmbh.) was used to extract each layer from the designed GDS file to generate a corresponding file with a defined resolution in GPF format. From this, each GPF file was opened as a cjob file using MobaXterm software, where the substrate size and exposure parameters were defined (Table 2). In the final stage, the cjob file was transferred to the EBPG machine for writing at the JWNC. An appropriate dose test was done to determine the optimum exposure to create the patterns. [261, 262]

Table 2: Parameters for electron beam lithography (EBL) on engineered surfaces used to immobilise DNA and nanoparticles, developed using the Raith EBPG instrument.

a. Oligonucleotide sample	**Parameters**
Beam current	180.6 nA
Dose	390 μC/cm^2
Step size	50 nm
Aperture	300 μm
Beam diameter	82 nm
b. Nanoparticles sample	
Beam Current	2 nA
Dose	800 μC/cm^2
Step size	2 nm
Mainfield Resolution	1 nm

2.3.5 Pattern Design using Photolithography

Photolithography is a light-based technology that transfers patterns from a mask to a substrate by illuminating it with a light source, such as UV radiation. [263] To achieve this, light-sensitive photoresists (positive or negative) spun on the sample's surface are subjected to structural evolution after light irradiation. The mask creates a transparent and opaque layer where the desired patterns are transferred during irradiation. The transparent area of the mask allows light to penetrate the positive photoresist, where the areas undergo structural evolution and become soluble. Unlike the positive photoresist, the photo-reactive regions of the negative photoresist become insoluble or solidify upon irradiation with light, while the unexposed area becomes soluble. [264] In this research, photolithography was performed to create sensing (where the fluorous molecules are attached) and non-sensing (where the non-fluorous molecules are attached) regions on the sample. The cured wafer was exposed for 6.5 sec. using photolithography (SUSS Microtec, MA6) with a 5'-chrome photomask (JD Photodata) featuring an array of 50 μm squares and 800 μm circles for 6.5 sec. each.

(a.) For the micropatterned surface used for the oligonucleotide immobilisation, S1818 resist (Shiply) was spun at 4,000 r.p.m. for 30 s and baked at 115 °C for 3 minutes to create a thick positive resist layer used for the microarray experiments.

(b.) S1805 resist (Shiply) was also spun at 4,000 r.p.m. for 30 seconds and baked at 115 °C for 3 minutes to create a thick positive resist layer to immobilise nanoparticles (micro and nano-patterns).

2.3.6 Sample Development (Photolithography)

The sample was developed using a mixture of RO and Microposit developer (Shiply, USA) (1:1) for 40 seconds, rinsed with excess RO water and dried under a stream of Nitrogen. The developed sample was checked under the microscope to ensure adequately developed samples (Figure 111). The excess underdeveloped resist was removed using low-oxygen plasma treatment (80 W, 30 s). The sample with well-developed features was used for the next stage of the experiment, while the bad samples were discarded.

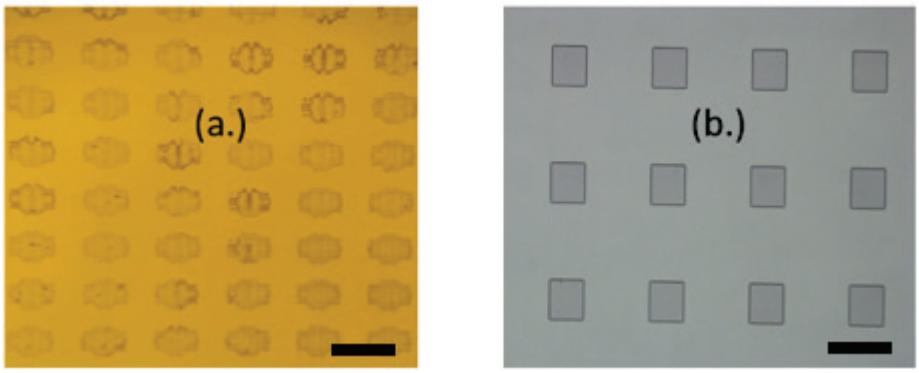

Figure 11: The patterns created from the developed sample are as follows: (a) The sample was of poor quality, not well-defined, and does not reflect the specification of the designed mask used during photolithography. Hence, it was not used for the subsequent fabrication stage. (b) The sample meets the necessary standards for the subsequent fabrication stage after development. 20x magnification, scale bar = 50 µm.

2.3.7 E-beam Sample Development (ODNs)

The charge-conducting aluminium layer was first removed using Microposit CD- 26 developer (Shiply, USA), rinsed in excess RO water, and dried in a stream of Nitrogen for the sample prepared for the oligonucleotide immobilisation. The cleaned sample was developed using 2.5:1 IPA: MIBK at 23 °C for 45 seconds while the remaining sample was rinsed with excess IPA for 1 minute. The (Methyl isobutyl ketone) MIBK: IPA is a high-resolution positive developer used to dissolve positive tone resist selectively (PMMA) exposed via electron beam lithography, leaving behind the desired pattern. The MIBK is a strong ketonic compound that

can dissolve PMMA with high resolution, shorter development time, and high sensitivity. IPA solvent is used to control the rate of the development of the PMMA. The excess PMMA sample was removed and cleaned using an oxygen plasma asher at 80 W for 30 seconds. [265–267]

2.3.8 E-beam Sample Development (Metal Nanoparticles)

Nanopatterns with size ranges 20 nm, 40 nm, 100 nm, and 500 nm were created using e-beam lithography (Reith). The aluminium layer was removed using CD26 for 1 min, as initially used in the previous protocol (Figure 12). The resulting substrate was developed using MIBK: IPA solution (2.5:1) for 1 min, rinsed in excess IPA for 1 min. and cleaned with a stream of nitrogen gas before use. The sample was ashered in flood of oxygen at 100 W for 2 mins., to remove excess impurities and activate the surface. The cleaned sample was silanised using vacuum silanisation with 20 uL FDTS solution for at least 2 hrs. The remaining PMMA layer was subjected to two-lift-off processes.

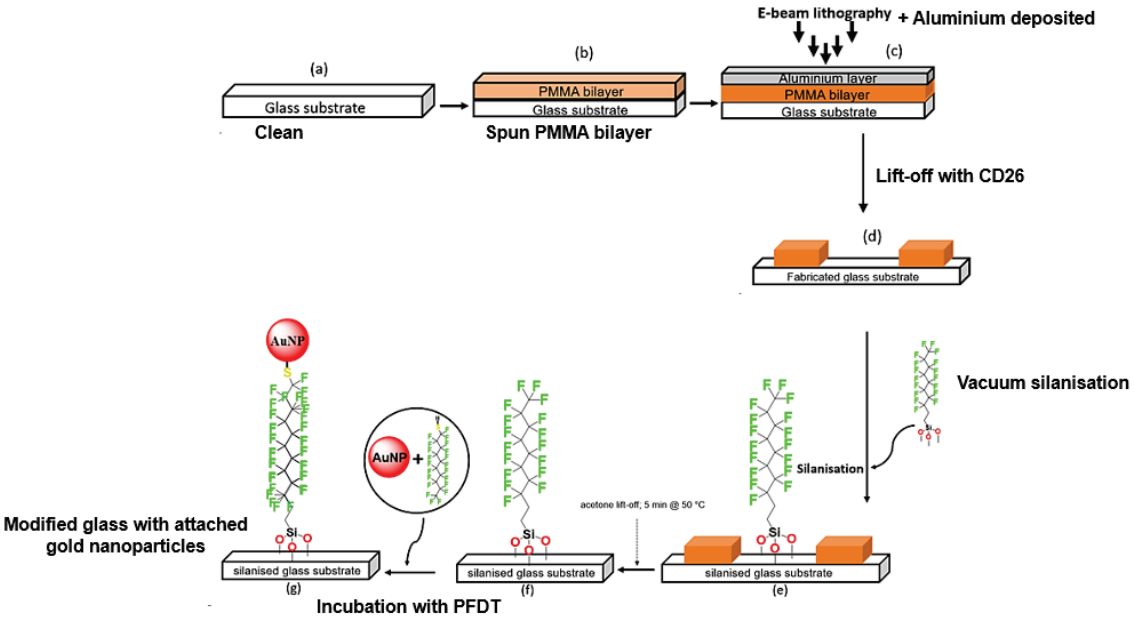

Figure 12: Diagram illustrating the stages in the e-beam process and the attachment of gold nanoparticles in an ethanolic solution of PFDT to produce fluorous-fluorous interactions.

2.3.8.1 Acetone lift-off

Conventionally, acetone has been used effectively to lift off PMMA. The current research used a 5-minute lift-off in acetone at 50 °C to remove the excess PMMA after silanisation.

2.3.8.2 Methanol Cleaning/Lift-off

Methanol can also be used to initiate the lift-off process, although it works slower than other conventional methods, including acetone. Consequently, it is not often used for this process. In this explorative instance, methanol sonication was applied for 5 minutes to clean the patterned surface, followed by a three-minute rinse in IPA.

2.3.9 Sample Sputtering

Sputtering is one of the physical vapour deposition methods used to create a thin metal film. In sputtering, a thin film of various materials is generated through plasma near the surface of the target or the materials. The positively charged energetic ions generated near the surface collide with the negatively charged materials where their atoms are ejected or sputtered on the substrate. This is unlike in evaporation, where the materials are heated to their vaporisation point, and the resulting vapour condenses onto a substrate to form a thin film. In this research, a 5 nm thin Au/Pd layer was sputtered on the sample before Scanning Electron Microscopy.

2.3.10 Silanisation and Surface Wettability

Silanisation of the fabricated surface was done using three different approaches (Figure 13):

(a.) Gas silanisation (90 ° C)

(b.) Gas silanisation (vacuum)

(c.) Liquid silanisation

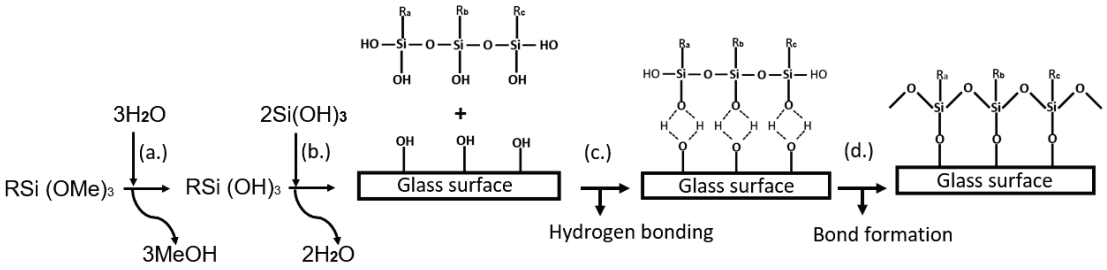

Figure 13: Schematics illustrating silanisation stages. (a.) The hydrolysis of the three labile silane groups in the presence of a hydroxyl group (b). The condensation of the silane group with subsequent water loss (c.) Hydrogen bond formation between the free hydroxyl group (d.) Drying and the removal of water with covalent bond formation.

The ultra-clean wafer was used to immobilise the ODNs. In this research, 20 µL silane was incubated at 90 °C while the MNPs were silanised under vacuum in a desiccator containing 200 µL of 1H,1H,2H,2H-heptafluorotrimethoxylsilane for 2 hrs. Before use, the silanised wafer containing resist was further cleaned with acetone, methanol, isopropanol, and nitrogen gas.

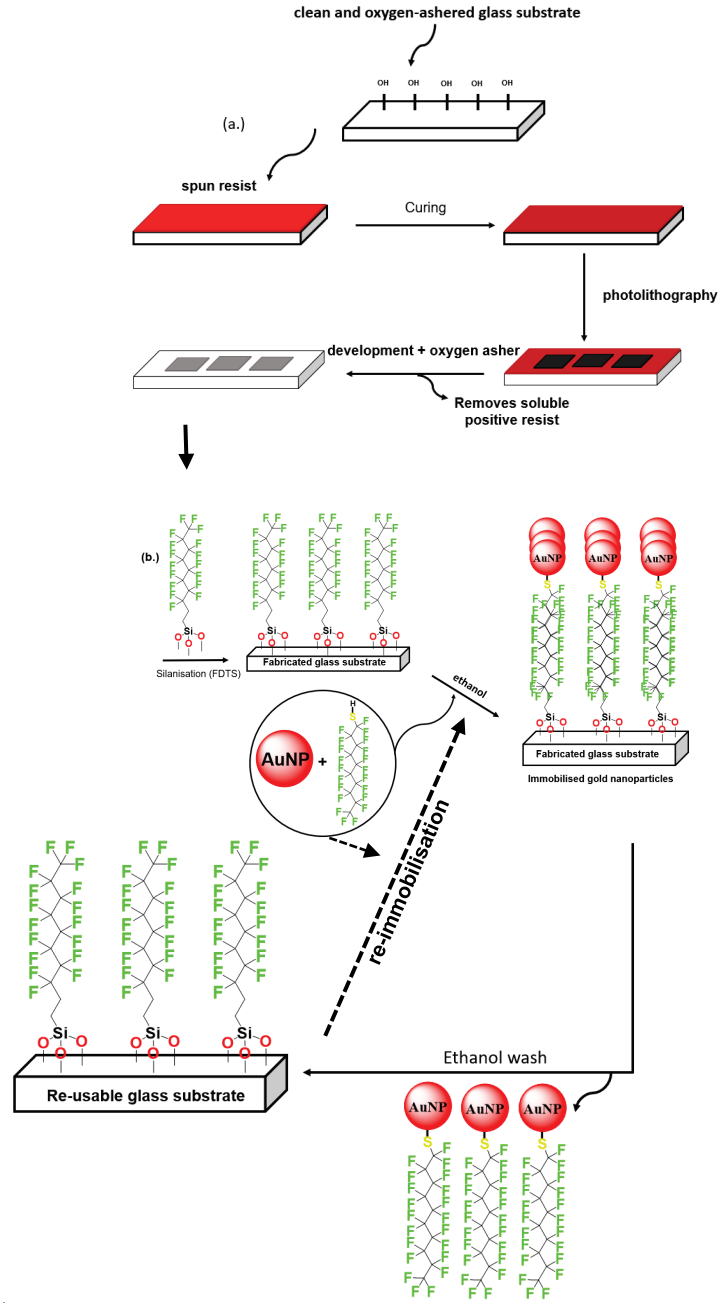

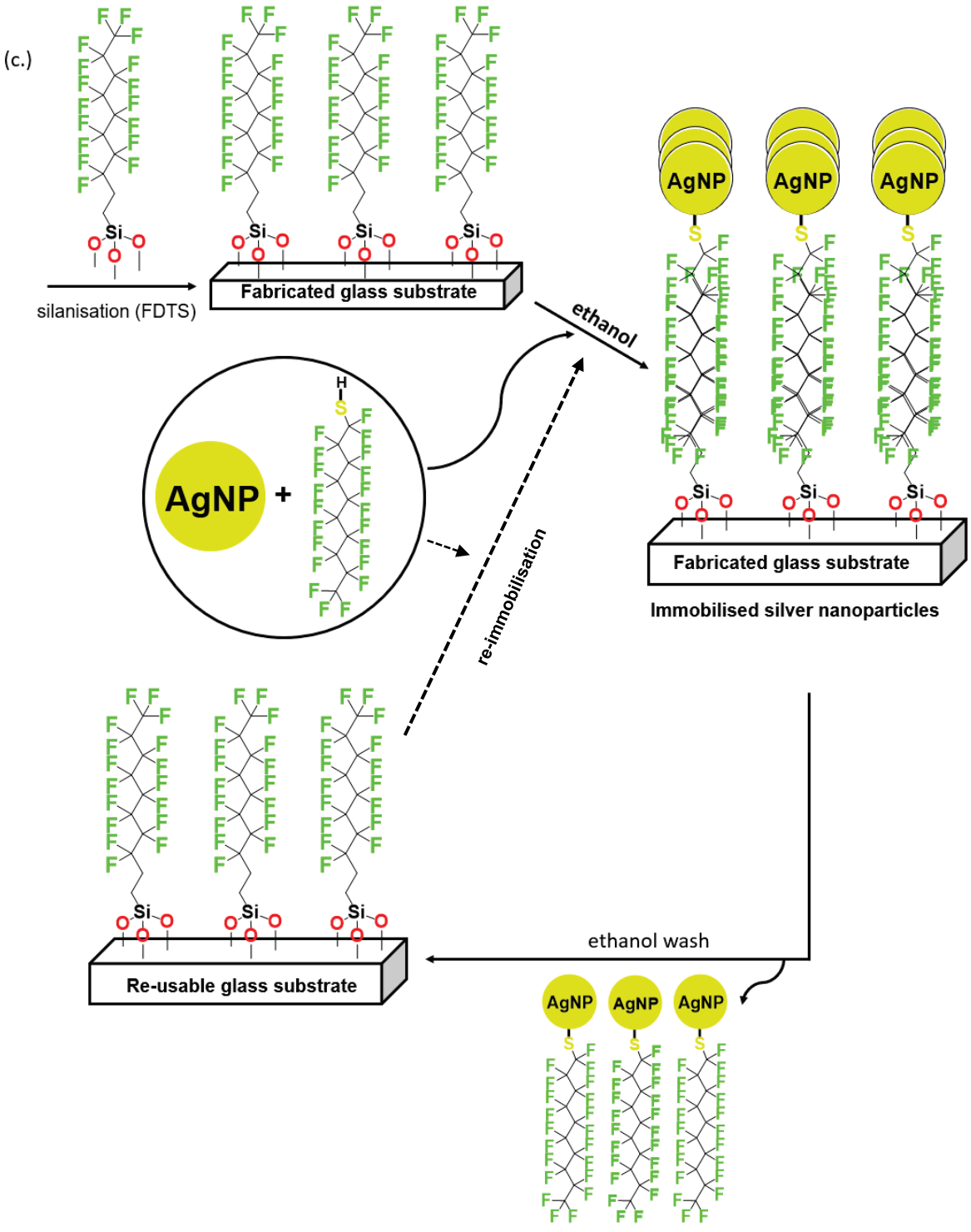

Figure 14: Diagram showing the (a.) Fabrication of glass substrate (50 µm and 800 µm sizes) using photolithography (b.) Reversible immobilisation of the gold nanoparticles shows the immobilisation of thiol -modified gold nanoparticles on the FDT-modified glass. This platform creates an opportunity for re-immobilisation after the first wash step (c.) Reversible immobilisation of the silver nanoparticles on the patterned surface using the fluorous effect.

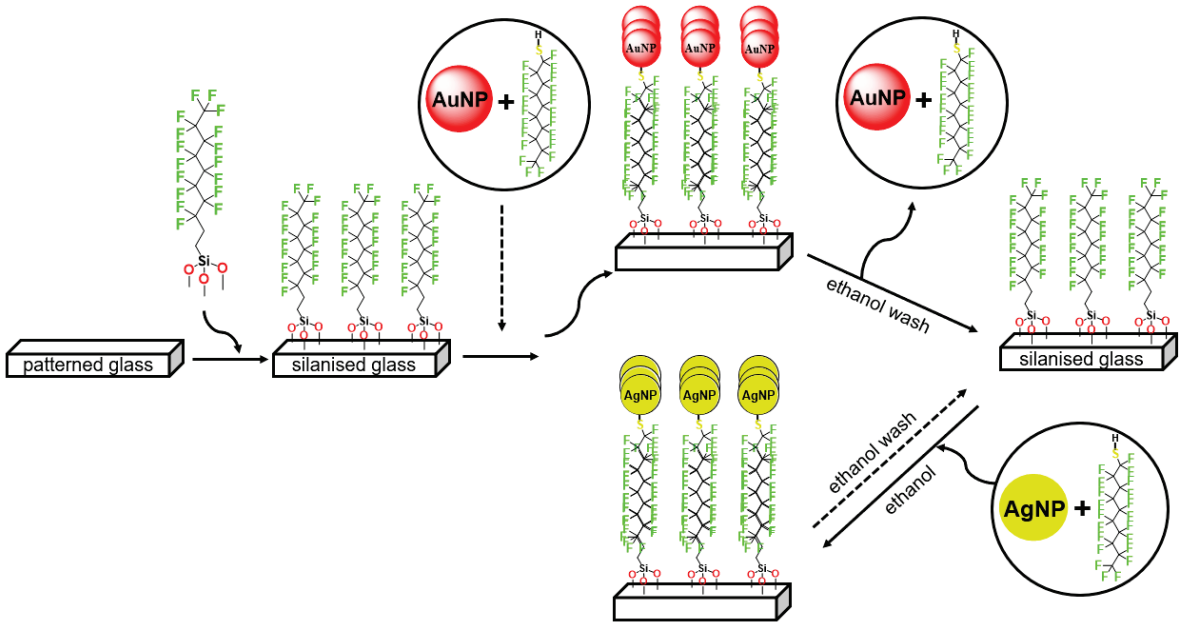

Figure 15: Diagram showing the 'switchable' patterned surface for reversible immobilisation of gold and silver nanoparticles. Using this method, it was possible to use different NPs (gold and silver) on the same patterned surface.

In general, silanisation is a low-cost, covalent process that modifies a hydroxyl-terminated surface (e.g., glass) by applying a thin silane layer. This process involves several steps (Figure 13) that ensure proper adhesion and coverage and help create a self-assembly monolayer of molecules that bridge the functionalised surface and the oligonucleotide or nanoparticles. The concentration and reaction conditions are crucial in making the desired layer. To ensure the efficiency of adhesion, bond formation, and impact homogeneity, the surface of the glass must be thoroughly cleaned with appropriate solvents to expose the free hydroxyl layer of the glass samples or any other oxide surface involved.

The following conventional steps have been reported as stages involved during liquid silanisation.[268–270]

1. Hydrolysis: The three labile alkoxyl groups are hydrolysed and converted to silanol groups (SiOH) in the presence of water or appropriate solvents

2. Condensation and hydrogen bonding: The functional groups of the silanol group are condensed with water loss. Here, they form hydrogen bonds with the surface hydroxide groups while the siloxane (Si–O-Si) network is formed from the remaining silanol group.

3. Bond formation (Drying): This stage drives off water to complete the covalent bond formation among the compatible moieties. The last step creates a

close-packed and well-organised molecular film. In general, the concentration of the silane and the reaction time may affect the eventual bond formation here. Consequently, the same procedure can be repeated and reproduced using the gas silanisation method. This process offers advantages to producing a thin self-assembly monolayer with improved surface properties, less contamination, less time, reproducibility, and stability.[271, 272]

For the immobilisation of oligonucleotides, silanisation was performed to effect the chemical interaction between the glass surface and n-decyltimethoxysilane (nDTS), which acts as the non-sensing region. At the same time, the second fluorosilane (FDTS) creates the self-assembled layer for the sensing region, where the fluorous-fluorous interaction occurs. This research used gas silanisation for all photolithography and nanoparticle immobilisation experiments. Liquid silanisation was used for silanisation using the e-beam sample (DNA).

Three silanisation methods were used:

a. Vacuum-Mediated Gas silanisation:

Here, the same 20 µL sample was incubated with the ultraclean borosilicate glass and subjected to at least 1 hr silanisation under vacuum. This process creates both sensing and non-sensing regions, which are used for the immobilisation stage and prevention of non-specific interactions, respectively.

b. Gas silanisation (90 ^{O}C):

For this gas phase silanisation protocol, 20 uL of n-decyltrimethoxysilane (n-DTS, Gelest) was incubated with the cleaned 4 cm^2 glass samples in the oven at 90 ºC oven for 1hr (Figure 13b). The sample was sequentially cleaned in acetone, methanol, and IPA for 3 minutes and dried with a stream of nitrogen gas.

c. Liquid silanisation:

Here, 1 % (v/v) FDTS was dissolved in toluene and incubated with ultra-cleaned samples for 1hr. The sample was sequentially cleaned with excess toluene and dried in a stream of nitrogen gas before the next stage.

2.4 DNA Modifications and Immobilisation

2.4.1 Modification of Oligonucleotides (ODNs)

ODNs purchased from Integrated DNA Technologies (IDT), USA, were fluorous modified by Dr. Jamie M. Withers and Dr. Andrea Sender from Prof. Glenn A. Burley of the Burley group at the University of Strathclyde using phosphoramidite chemistry and purified with high-performance liquid chromatography (HPLC). Phosphoramidite chemistry was used due to its simplicity, ability to synthesise large oligonucleotide volumes, and ease of modification. [273, 274] The remaining fluorescently labelled complementary oligonucleotides were purchased from the IDT.

Several protocols have been used in microarray designs, including physical adsorption, covalent interaction, and streptavidin/biotin interaction. [274]. In this research, 1 μM aqueous solution (12 uL) of fluorous tagged ODNs was carefully spotted on the silanised surface, covered with a clean glass slide, and incubated in a humidity chamber for 2 hrs at RT. The sample with the immobilised ODNs was rinsed with DI water before hybridisation.

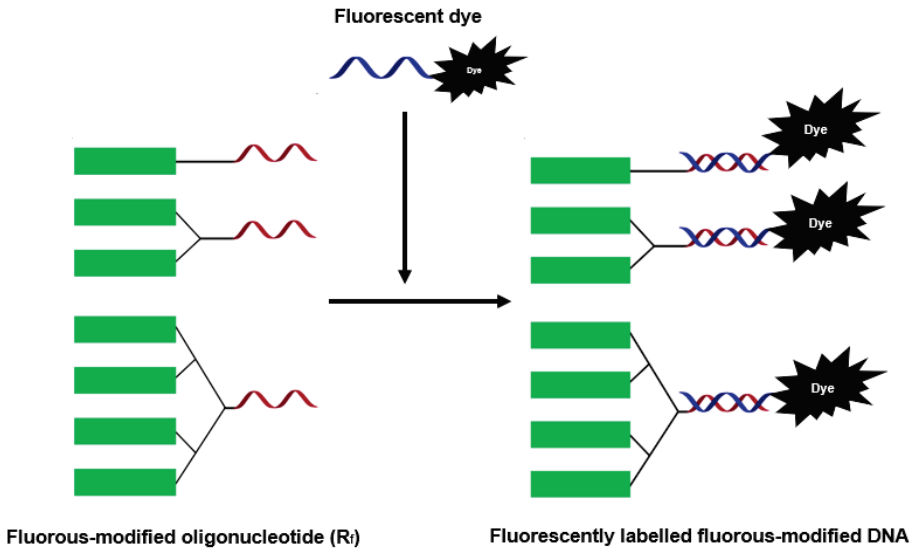

Figure 16: Schematics illustrating the interaction between fluorous-modified single-stranded DNA (green) with different branch systems and dye-modified (blue) oligonucleotides with varying systems of branch (Dyes used are TAMRA and Alexa -fluor).

a. For single ODN immobilisation, the complementary ODNs were fluorescently labelled with TAMRA dyes (Figure 16).

b. For multiplex immobilisation, complementary TAMRA and Alexa-fluor dyes attached via the 5'end of the nucleobase were used.

2.4.2 Dilution and Determination of ODNs Concentration

In line with the instructions from the manufacturers, all ODNs were re-suspended in nuclease-free water to produce a final concentration of 100 µM. Aliquots from this were mixed and diluted in clean Eppendorf tubes before use. At the same time, the concentration of the single-stranded oligonucleotides was determined using a Nanodrop Spectrophotometer (ND-1000, Thermo Fisher), built with a capacity to measure nucleic acid concentration with high accuracy and reproducibility.
The concentration of the ODN was calculated using the Beer-Lambert equation from the absorbance measured at 260 nm. The final concentration of ODNs used for this experiment was 1 µM, while each measurement was carried out with 1.5 µl aliquots. The final solution was stored at -20 ˚C before use.

$$A = \varepsilon c l \qquad \text{equation (1)}$$

Where:

A = Measured absorbance,

ε = Molar extinction coefficient ($M^{-1}cm^{-1}$)

c = Concentration (mol/L), and

l = Path length (cm)

2.4.3 Immobilisation of ODNs on Fluorous-Modified Glass

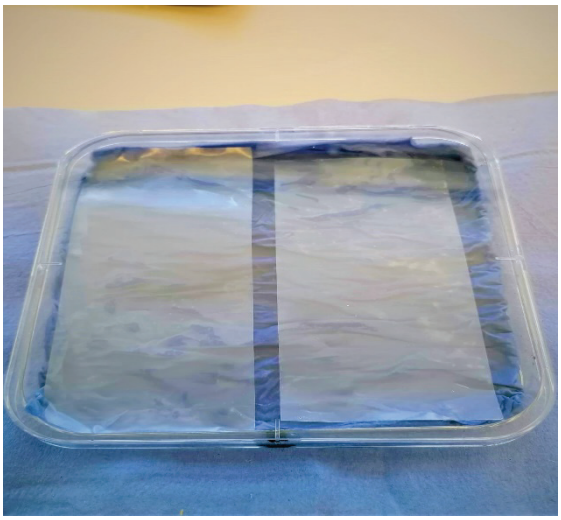

Figure 17: Shows a plastic incubation chamber (12 cm x 12 cm) prepared with wet (using water) tissue paper and parafilm (on top) during the immobilisation and hybridisation of DNA experiments. This environment was made humid to prevent unwanted drying of the droplets. In addition, the chamber was covered with aluminium foil during the hybridisation stage to avoid the direct effect of light on the attached fluorophores.

1 µM aqueous solution (12 uL) of the fluorous tagged ODNs was carefully spotted on the cleaned silanised surface, covered with a glass slide, and incubated in a humidity chamber for 2 hrs at RT (Figure 17). The sample with the immobilised ODNs was rinsed with DI water before hybridisation. For the multiplex immobilisation, 12 uL of each of the different fluorous modified oligonucleotides (weakest and strongest strand) were spotted and incubated for 2 hrs at RT.

2.4.4 Hybridisation of ODNs

To take advantage of the molecular recognition property of DNA, the surface with the already immobilised oligonucleotide was rinsed with excess solvent to remove the non-specifically bound or unbound ODNs from the surface.

a. 1µM (12 uL) of 16-mer complementary oligonucleotide (GCA GGA CAT CAC AAA T or CTG CTA TCT ATC TGC A), modified at the 5-end was spotted directly at the already immobilised oligonucleotides on the surface of the glass substrate. The sample was incubated at RT and covered with aluminium foil to prevent direct light interference for 1 hr.
b. For the multiplex immobilisation, the same concentration and volume of oligonucleotide were used for each fluorescently tagged oligonucleotide (TAMARA and Alexa). The sample was incubated like in (a) above.

2.4.5 Removal of attached DNA from the Fluorous Immobilised Surface

(a.) After 1 hr incubation, the sample mix was rinsed in Phosphate Buffered Saline (PBS), (pH=7) followed by washing in a solution containing methanol: buffer (PBS) mixture between (10 % - 80 %) in an ultrasonic bath for 2-3 minutes. The sample was rinsed in DI water, and the surface was dried under a stream of nitrogen gas. The sample was then imaged using the fluorescent microscope.

(b.) For the multiplex, the sample was rinsed in PBS buffer (pH=7) after hybridisation in a 5 ml solution consisting of methanol: buffer (PBS) mixture from 0-60% in a water bath for 2-3 minutes.

The treated sample was rinsed in DI water, dried with a stream of nitrogen, and imaged using Axio Observer Z1 (Zeiss, Germany) with 20x magnification, NA 0.4 and 1.0 sec exposure time. The grey 8-bit scale image captured was analysed using ImageJ software, where the difference in sample region and background were

captured and normalised to give the actual quantitative measurement. The final data was average triplicate data expressed as mean ± SD.

2.5 Immobilisation of Metal Nanoparticles (MNPs)

2.5.1 Synthesis of Silver Nanoparticles (AgNPs)

Initially, the synthesis of citrate-coated, KI-assisted silver nanoparticles was done using the method by Tao et al. (2013) with slight modifications. [275]

a. Briefly, 1ml of an aqueous solution of sodium citrate (1 wt. %) and 0.25 mL of the aqueous solution of $AgNO_3$ (1 wt. %) were premixed and added to 1.25 ml of MilliQ water, incubated under stirring and room temperature for 5 mins. The resulting mixture was injected into a boiling solution (47.5 mL) after adding 50 uL of Ascorbic acid for 1 min. The colour of the reaction changed from colourless to yellow and was sustained during the reaction boiling and stirring at 400 r.p.m. for 0.5 - 1hr at 200 °C.

b. Briefly, 1 ml of an aqueous solution of sodium citrate (1 wt. %) and 0.25 mL of the aqueous solution of $AgNO_3$ (1wt. %) were premixed and added to 1.25 ml of MilliQ water, incubated under stirring and room temperature for 5 min. The mixture was injected into a boiling solution (47.5 ml) after adding 50 uL of Ascorbic acid for 1 min. The colour of the reaction changed from colourless to yellow and was sustained during boiling and stirring at 400 r.p.m for 10 min at 200 °C.

c. Here, 50 uL (0.4 mM) of aqueous solution of Ascorbic acid (AA) 0.4 mM was added to 47.5 mL of boiling water in a clean beaker and boiled for 1 min. A pre-mixed mixture (5 minutes stirring) consisting of 1 ml solution of sodium citrate (1 wt. %) and 0.25 ml of silver nitrate (1 wt. %), and 0.0016 mM of potassium iodide was injected into the boiling solution of ascorbic acid just after 1 minutes. The colour of the solution changed from colourless to yellow, and it was boiled further for 1 hr with continuous stirring, indicating the formation of silver nanoparticles.

d. To synthesise quasi-spherical AgNPs, a modified method by Leopold and Lendl. was used. A 90 ml solution of HH (0.017 M) and sodium hydroxide (0.033 M) in H_2O was freshly prepared.10 ml of 0.01 M silver nitrate solution was injected into the reaction mixture, stirring at 5,000 r.p.m. for 20 min. The colour of the final colloidal suspension was orange-brown. All NPs were used as-prepared for the

subsequent immobilisation reaction. The remaining solution was stored at 4°C before use.

2.5.2 Synthesis of AuNPs

This research utilised three different methods to synthesise gold nanoparticles of various sizes.

a. Turkevich method:

The Standard Turkevich method was used to synthesise sub-20 nm gold nanoparticles by injecting 5 ml of a 5 mM solution of sodium citrate into a boiling 495 ml solution of gold chloride (0.0985 g). Within 10 minutes, the gradual colour change was observed from light yellow to colourless, which turned grey to grey-bluish, blue, and purple, and finally to ruby red, indicating the formation of gold nanoparticles. The synthesised sample was stored at 4 °C before use.

b. Modified Turkevich method:

Quasi-spherical colloidal AuNPs were synthesised using a previously reported citrate-mediated protocol with slight modifications. Briefly, 50 ml of freshly prepared 0.25 mM gold (III) chloride trihydrate solution was heated to boiling in a 250 ml Erlenmeyer flask. 2 ml of trisodium citrate dihydrate (34 mM) was injected into the boiling solution under vigorous stirring at 550 r.p.m. which was kept for 3 min. The reaction was monitored by observing colour changes from pale yellow to colourless, purple, and red. The reaction was stopped once there was no visible colour change and then cooled to room temperature.

c. Reversed Turkevich method:

For the larger gold nanoparticles (beyond 55 nm), the reversed Turkevich method was adopted. In this method, a 150 ml solution containing 2.2 mM sodium citrate was heated to boiling in a clean Erlenmeyer mask. 1ml solution containing 25 mM gold (III) chloride trihydrate was injected under vigorous stirring at 1000 r.p.m. After the colour change from colourless to red, the solution was cooled to 90°C and stirred for an additional 30 min. before adding another 1ml of gold (III) chloride trihydrate solution (25 mM). The final mixture was further stirred for an additional 30 min. and brought to room temperature before use while the

remaining solution was stored at 4°C.All NPs were used as prepared for the subsequent immobilisation reaction (**calculation in Appendix 1**).

2.6 Immobilisation of Metal Nanoparticles

The substrate with the fluorous patterns was cleaned, modified, and incubated following the fabrication design and silanisation.

2.6.1 Drop-casting method (50 µm)

We began the immobilisation of these nanoparticles using ordered citrate-gold nanoparticles from Maersk. This method aimed to see the immobilisation pattern of the nanoparticles on the fluorous-modified surface. In this method, the citrate layer of the gold nanoparticles was removed by centrifugation and concentrated to 0.5 mM. In contrast, 10 uL of the functionalised gold nanoparticles was spotted on a clean, fluorous-patterned surface and allowed to dry at RT using the 50 µm micropattern arrays.

2.6.2 Cover slip method (50 µm)

In this method, 30 uL of the already functionalised 0.5 mM gold nanoparticles were spotted on the fluorous modified surface, protected with a cover slip for 1 hr. before characterisation.

2.6.3 Hexane-ethanol method (50 µm)

In this method, the fluorous-modified glass substrate was immersed in an already functionalised 0.5 mM gold nanoparticle solution containing a hexane-ethanol mixture (1:2) for 48 hours. The sample was thoroughly rinsed in distilled water and allowed to dry before characterisation.

2.6.4 Immersion method (800 µm)

A clean, silanised borosilicate glass sample measuring 2 cm x 2 cm and 800 µm thick was incubated in 3 mL of ethanol containing 1.33% perfluorodecanethiol (PFDT). The mixture was stirred for at least 2 hours. Following this, 2 mL of as-synthesised gold/silver nanoparticles (NPs) were added to achieve instant immobilisation.

Image and video recordings of the immobilisation process and solvent exchange were captured using the EVOS microscope (EVOS FL Auto2, Invitrogen, Thermo Fisher Scientific).

2.7 Stability of Gold Nanoparticles in a Colloidal System using Perfluorodecanethiol (PFDT)

To evaluate the stability and efficiency of PFDT in stabilising gold nanoparticles, 2 mL of sub-20 nm gold nanoparticles were incubated with a 3 ml ethanolic solution consisting of 30 uL of PFDT. The sample was allowed to stand for 12 months (without stirring), and measurements were taken at the beginning and end of the incubation period.

2.8 'Switchable' Modified Surface for Immobilisation

To create a re-usable surface where gold and silver nanoparticles can be used interchangeably without the visible loss of functionalities after washing, an 800 µm-size lithographically patterned surface was used as in Figure 14. Briefly, 2 mL of gold nanoparticles were incubated and immobilised on the surface for 2 hrs, and solvent exchange was achieved using sodium citrate solution followed by spectra acquisition. The sample was sonicated in ethanol to remove the immobilised sample. The same sample and spots were re-incubated and immobilised with silver nanoparticles for at least four (4) cycles.

2.9 Solvent Exchange/ Wash Steps (MNPs)

Solvent exchange of immobilised NPs (in solution) was carefully carried out in 0.5 mM sodium citrate solution three (3) times the volume of the incubating mixture to obtain a clear solution with distinct surface immobilisation of MNPs in the fluorous regions.

2.10 Sample Recovery (Silver Nanoparticles)

An immobilised silver nanoparticle sample was used to estimate the amount of silver nanoparticles. In a typical 800 µm pattern (30 fluorous patterned circles) with immobilised silver nanoparticles, solvent exchange was done using 0.5 mM sodium

citrate. At the same time, the sample was re-dispersed in a 2 mL solution of sodium citrate. The absorbance or transmission was monitored using UV-vis spectroscopy.

2.11 Immersion method (20 nm, 40 nm, 100 nm and 500 nm Nanopatterns)

To direct the immobilisation of gold nanoparticles into the nanopatterns, several protocols were considered for proof of concept.

2.11.1 Protocol 1

The cleaned and silanised substrate was incubated in a 3ml ethanolic solution containing 30 uL PFDT via a one-pot protocol. The resulting sample, containing 55 nm gold nanoparticles, was left undisturbed overnight before solvent exchange in a 0.5 mM sodium citrate solution. The sample was allowed to dry at room temperature before surface characterisation using the SEM.

Density (g/mL) = mass (mg) / volume (mL) equation (2)

Using 30 uL (0.03 mL) or 0.04 mg/mL of PFDT with 1.389 g/mL at RT.

2.11.2 Protocol 2

The cleaned and silanised substrate was incubated with functionalised 55 nm gold nanoparticles and allowed to stay undisturbed overnight. The solvent exchange was done using a 0.5 mM sodium citrate solution, and the sample was also allowed to dry at room temperature before surface characterisation using the SEM.

2.11.3 Protocol 3:

Cleaned and silanised substrate was incubated in a mixture containing 30 uL PFDT and 3 ml ethanol. The substrate was allowed to mix for 2 hrs while 55 nm gold nanoparticles were added immediately. The mixture was stirred overnight before exchanging the solvent in 0.5 mM sodium citrate solution. The sample was allowed to dry at room temperature before surface characterisation using the SEM.

2.11.4 Protocol 4:

The sample was incubated for 48 hrs with functionalised gold nanoparticles with continuous stirring for 2 hrs.

2.12 Statistical analysis

Statistical analysis was done using the OriginPro software (Version 2023b, OriginLab Corporation, Northampton, MA, USA). ImageJ v1.53e [276] was used to analyse fluorescent data of the immobilised DNA and the nanoparticles from SEM micrographs. The steps for ImageJ analysis and nanoparticle counting are outlined below. We used triplicate measurements with the standard deviation, which provided us with 95% confidence intervals. Additionally, the margin of error was also applied to estimate the data variability (equation 3) using :

$$z * S.D/\sqrt{n}. \qquad \text{equation (3)}$$

Where n is the sample size and z is the z-score at a specified confidence level. Estimating the variability was necessary to quantify uncertainty, assess the reliability of results, and make informed decisions based on the data.

2.12.1 Fluorescent Data Analysis

(a.) The fluorescent image is extracted and converted to an 8-bit grey scale system

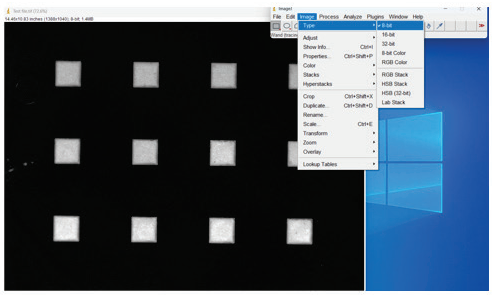

(b.) Each square (fluorescent region) is manually measured against the black background (non-fluorescent region).

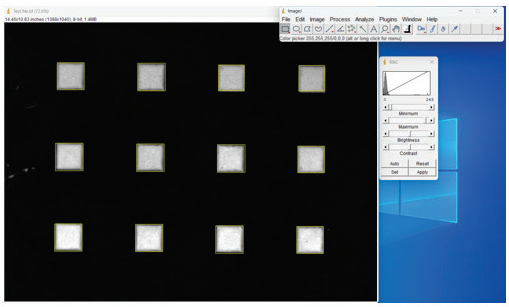

(c.) The image was measured using the in-built measurement system from image J.

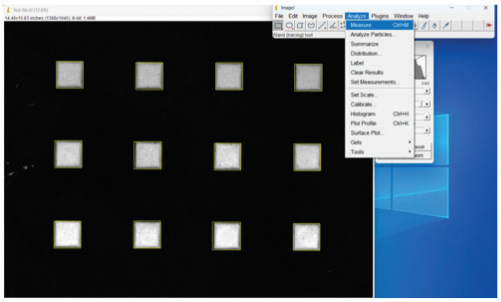

(d.) Measurement data are generated for the squares.

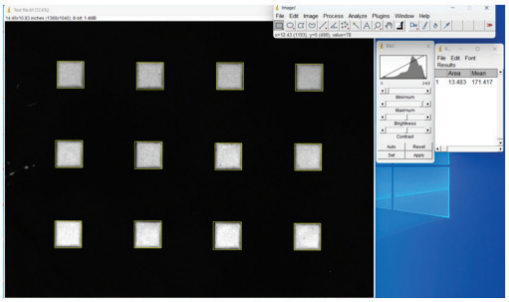

(e.) The inverse of the whole image is selected to capture or measure the non-fluorescent region (black background).

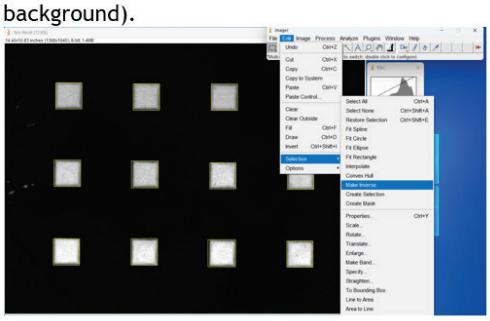

(f.) The difference between the background and the fluorescent data was calculated and expressed as Mean ± SD.

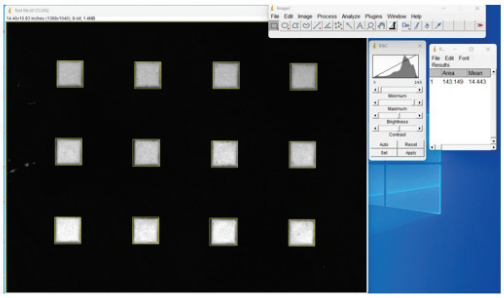

Figure 18: Step-by-step method for the estimation of fluorescent data from the immobilised DNA. Where necessary, a margin of error was also used to check for data variability among the triplicate values.

2.12.2 Nanoparticles Counting and Analysis

(a) Open SEM micrograph containing the imaged surface with the NPs.

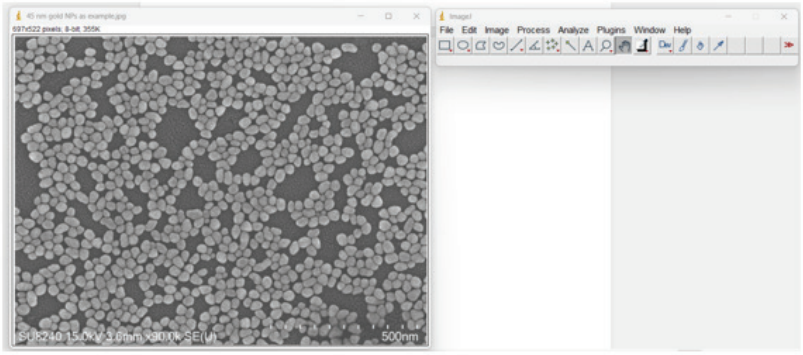

(b.) Set the scale by opening the initial scale and removing the default values.

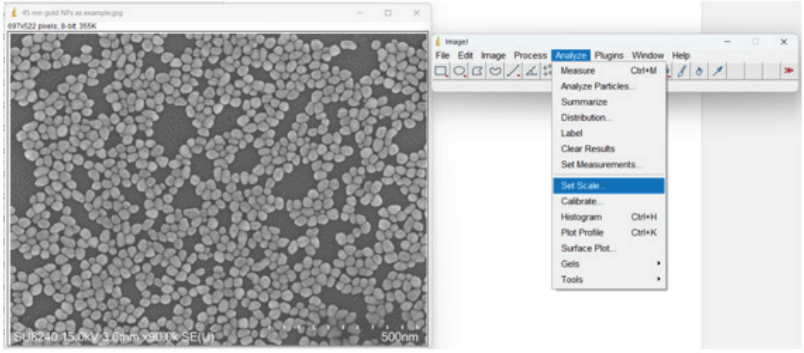

(c.) Remove the initial scale.

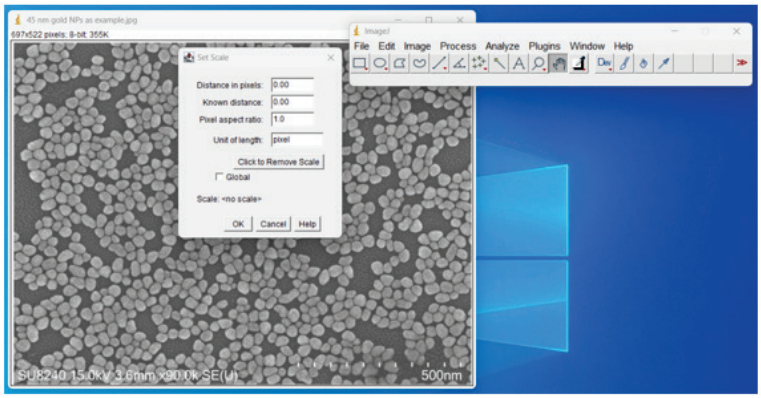

(d.) Calibrate the scale and image to reflect the 500 nm.

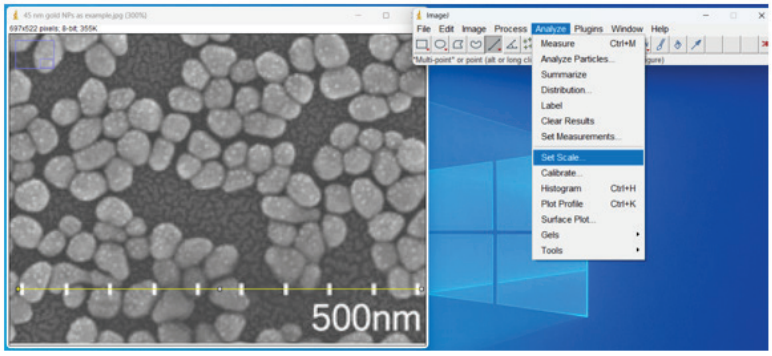

(e.) Calibrate the image to reflect the required scale (500 nm).

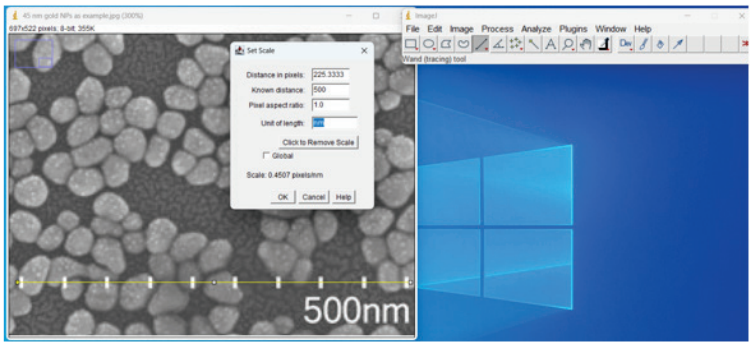

(f.) The image is calibrated and ready for size measurement.

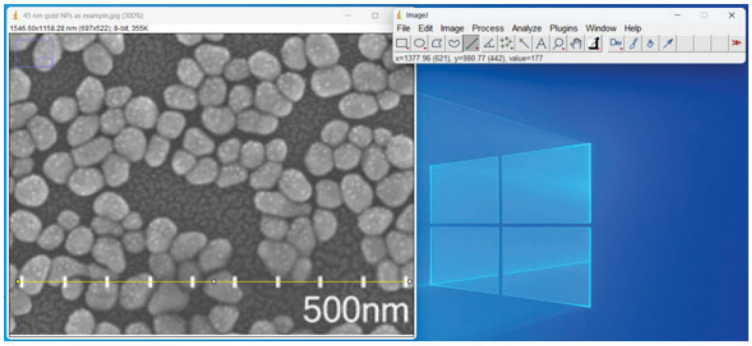

(g.) The image was subjected to thresholding to improve the detection of nanoparticles from non-nanoparticles on the SEM micrograph.

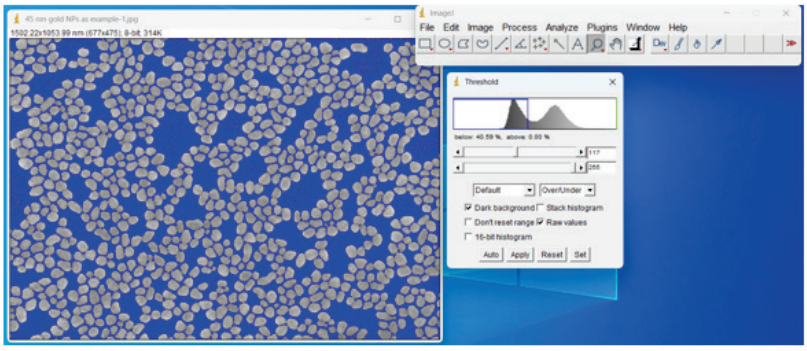

(h.) Analyse particles to obtain the areas of each nanoparticle.

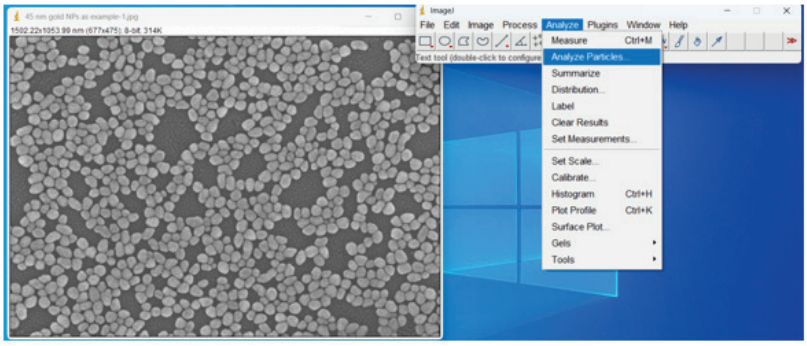

(i.) The required parameters were selected.

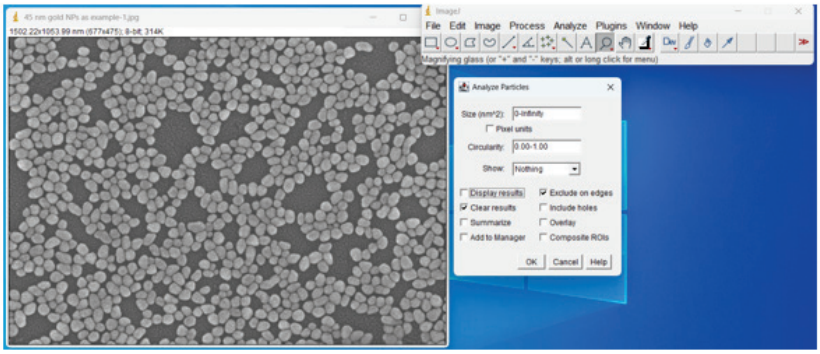

(j.) Analyse particles to obtain the areas, $A = \pi r^2$ of each nanoparticle.

The diameter of each NP is obtained from Diameter = 2 x radius.

Figure 19: A step-by-step method adopted to estimate the size of nanoparticles after immobilisation. (a-g).

2.12.3 Spectra Data Analysis

To ensure consistency and comparability, all spectroscopic data generated during this study were normalised using the OriginPro software (Version 2023b, OriginLab Corporation, Northampton, MA, USA) package, which scaled the values from 0 to 1. Additionally, unless stated otherwise, all ultraviolet (UV) graphs presented in this report were fitted using the Lorentzian function after normalisation to enhance the clarity and precision of the graphical representations of the data.

(a.) Data is acquired through the UV-visible spectrophotometer within a desirable range.

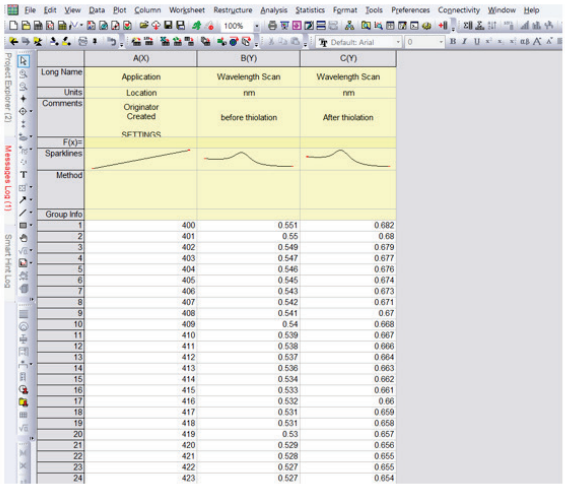

(b.) The wavelength data range is selected

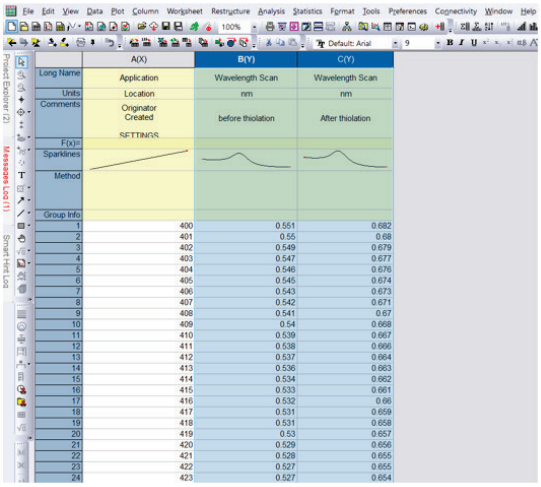

(c.) The selected data is normalised to keep within (0-1) range.

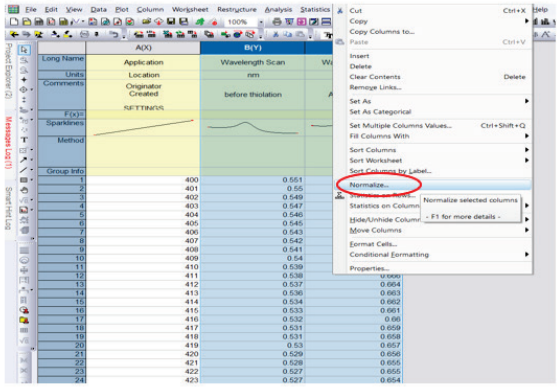

(d.) The normalised data are kept within the 0-1 range.

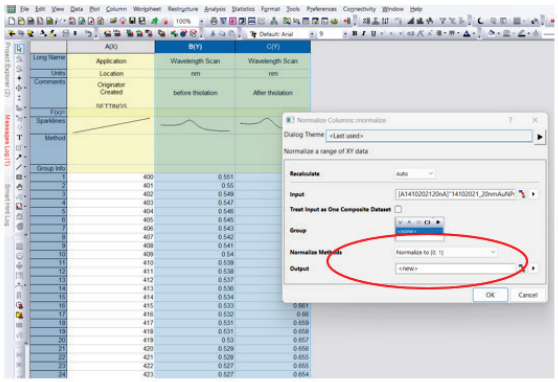

(e.) Raw and normalised data.

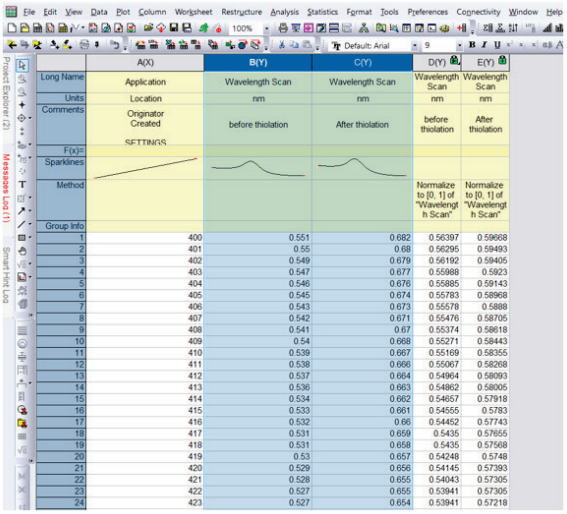

	A(X)	B(Y)	C(Y)	D(Y)	E(Y)
Long Name	Application	Wavelength Scan	Wavelength Scan	Wavelength Scan	Wavelength Scan
Units	Location	nm	nm	nm	nm
Comments	Originator Created SETTINGS	before thiolation	After thiolation	before thiolation	After thiolation
F(x)=					
Sparklines					
Method				Normalize to [0, 1] of "Wavelength Scan"	Normalize to [0, 1] of "Wavelength Scan"
Group Info					
1	400	0.551	0.682	0.56397	0.59668
2	401	0.55	0.68	0.56295	0.59493
3	402	0.549	0.679	0.56192	0.59405
4	403	0.547	0.677	0.55988	0.5923
5	404	0.546	0.676	0.55885	0.59143
6	405	0.545	0.674	0.55783	0.58968
7	406	0.543	0.673	0.55578	0.5888
8	407	0.542	0.671	0.55476	0.58705
9	408	0.541	0.67	0.55374	0.58618
10	409	0.54	0.668	0.55271	0.58443
11	410	0.539	0.667	0.55169	0.58355
12	411	0.538	0.666	0.55067	0.58268
13	412	0.537	0.664	0.54964	0.58093
14	413	0.536	0.663	0.54862	0.58005
15	414	0.534	0.662	0.54657	0.57918
16	415	0.533	0.661	0.54555	0.5783
17	416	0.532	0.66	0.54452	0.57743
18	417	0.531	0.659	0.5435	0.57655
19	418	0.531	0.658	0.5435	0.57568
20	419	0.53	0.657	0.54248	0.5748
21	420	0.529	0.656	0.54145	0.57393
22	421	0.528	0.655	0.54043	0.57305
23	422	0.527	0.655	0.53941	0.57305
24	423	0.527	0.654	0.53941	0.57218

(f.) Normalised data is selected for analysis.

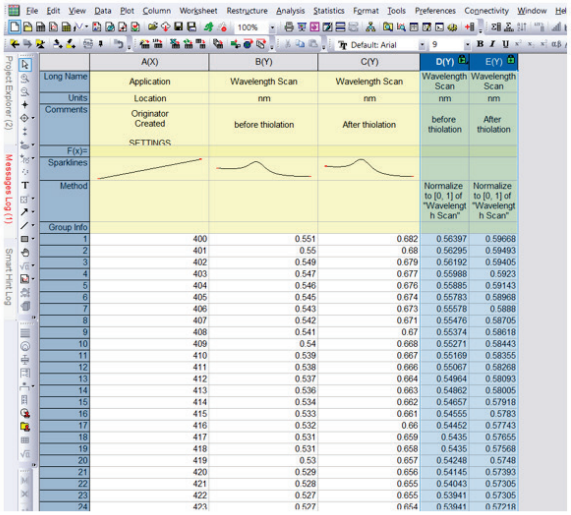

	A(X)	B(Y)	C(Y)	D(Y)	E(Y)
Long Name	Application	Wavelength Scan	Wavelength Scan	Wavelength Scan	Wavelength Scan
Units	Location	nm	nm	nm	nm
Comments	Originator Created SETTINGS	before thiolation	After thiolation	before thiolation	After thiolation
F(x)=					
Sparklines					
Method				Normalize to [0, 1] of "Wavelength Scan"	Normalize to [0, 1] of "Wavelength Scan"
Group Info					
1	400	0.551	0.682	0.56397	0.59668
2	401	0.55	0.68	0.56295	0.59493
3	402	0.549	0.679	0.56192	0.59405
4	403	0.547	0.677	0.55988	0.5923
5	404	0.546	0.676	0.55885	0.59143
6	405	0.545	0.674	0.55783	0.58968
7	406	0.543	0.673	0.55578	0.5888
8	407	0.542	0.671	0.55476	0.58705
9	408	0.541	0.67	0.55374	0.58618
10	409	0.54	0.668	0.55271	0.58443
11	410	0.539	0.667	0.55169	0.58355
12	411	0.538	0.666	0.55067	0.58268
13	412	0.537	0.664	0.54964	0.58093
14	413	0.536	0.663	0.54862	0.58005
15	414	0.534	0.662	0.54657	0.57918
16	415	0.533	0.661	0.54555	0.5783
17	416	0.532	0.66	0.54452	0.57743
18	417	0.531	0.659	0.5435	0.57655
19	418	0.531	0.658	0.5435	0.57568
20	419	0.53	0.657	0.54248	0.5748
21	420	0.529	0.656	0.54145	0.57393
22	421	0.528	0.655	0.54043	0.57305
23	422	0.527	0.655	0.53941	0.57305
24	423	0.527	0.654	0.53941	0.57218

(g.) A line graph was used to estimate the relationship between the absorbance and the wavelength.

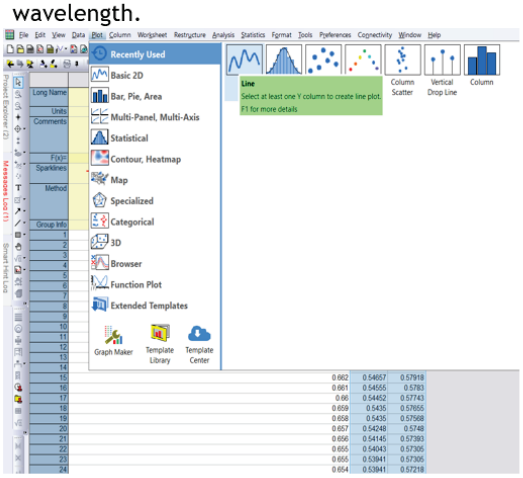

(h.) Graph generated from normalised data.

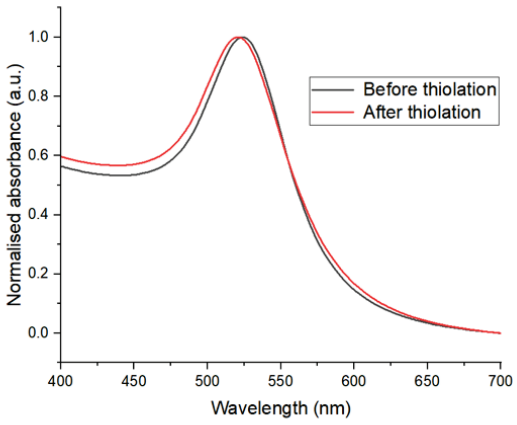

(i.) Graph was subjected to (where applicable) non-linear curve fit function.

(j.) Graph was fitted using an in-built Lorentzian function (where applicable) from the OriginPro.

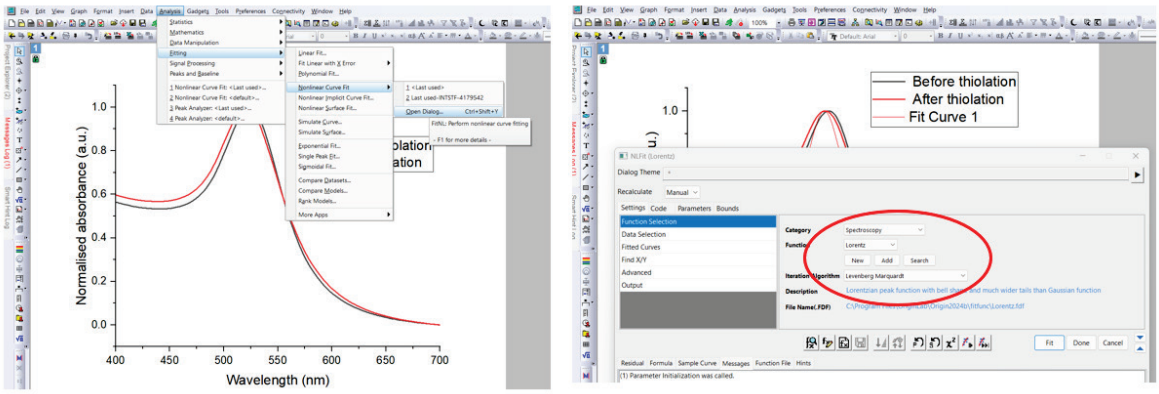

Figure 20: A step-by-step method adopted to estimate the absorption spectrum of nanoparticles (a-j).

2.12.4 Zeta and DLS analysis

The Zeta potential and DLS data were generated automatically by the Malvern analytical instrument during the triplicate data acquisitions and used without further manipulations. [277]

2.13 Characterisation Tools and Techniques

2.13.1 UV-visible Spectroscopy

UV-visible spectroscopy is a straightforward, non-invasive, and non-destructive analytical method. It measures the interaction between samples and light in the UV-visible regions to provide information about the electronic and chemical composition of matter at specific concentrations. [278] This is based on the principle that electrons are promoted to higher or excited states from their ground state upon interaction and energy absorption in the UV-visible regions. These transitions could be π to π, where electrons in the π-bond (bonding molecular orbital) are excited to a π* (anti-bonding molecular orbital). This type of transition is common in molecules with conjugated π-systems. Another type of transition is n to π, where non-bonding electrons (n) on atoms such as oxygen, nitrogen, or sulphur are excited to a π* orbital. The σ to σ transition occurs when electrons in a σ-bond (single bond, bonding molecular orbital) are excited to a σ* (anti-bonding molecular

orbital). This transition requires higher energy and typically occurs in the UV region. The last type of transition is n to σ, where non-bonding electrons are excited to a σ* orbital. This transition is less common but can be observed in molecules with lone pairs of electrons. [279–283] In UV-visible spectroscopy, the absorbed photon is used to determine the wavelength (absorbance or transmission) of light absorbed or transmitted by the molecule. This is based on the difference in energy between the ground state and the excited state of the molecule. Additionally, the ratio of the intensity of incident light to transmitted light can be related to the absorbance, A, at a specific wavelength (equation 4). Absorbance is defined as the negative base 10 logarithm of the transmission (equation 5). With this method, the intensity of light across the visible spectrum can be compared using the Beer-Lambert law, where the absorbance, the absorptivity ε(λ), and the length of the light path (l) are related to their concentrations (c) upon interaction with light. This property is, therefore, used in identifying and analysing the molecules.

Transmission = T =

wavelength of I_S (wavelength) / wavelength of I_O equation (4)

$A = - \log_{10} (T) = \log$ [wavelength of Io/wavelength of Is] equation (5)

Where I_O and I_S are the intensity of light that passes before and after the sample is introduced. [284]

The spectroscopic properties showing the surface plasmon peak of the synthesised and immobilised AuNPs or AgNPs were collected using the Ultrospec 9000 and Nikon Microscope (LV-TV) connected to StellerNet Tungsten Halogen Lamps in the UV-NIR range, respectively.

For the synthesised NPs, 200 uL of the sample was diluted to 2 ml to make a dilution factor 10 before data was collected within the 300-900 nm wavelength range using a cuvette of 1 cm path length. At the same time, the optical properties of the immobilised NPs on the patterned surface were collected using a Nikon Microscope. The spectra data were analysed with OriginPro 2023 software (Origin Lab Corporation). Unless stated otherwise, all real-time LSPR data during the reversible immobilisation of the nanoparticles were taken in triplicate at room temperature.

2.13.2 Contact Angle

In general, the contact angle instrument measures the contact between the surface of the solid and the liquid droplet. The working principle behind the Kruss goniometer involves the analysis of the shape of the liquid and the behaviour of the liquid droplet on the surface of the solid with a characteristic interface between the solid and the liquid droplet. Here, the contact angle is measured as an angle between the droplet and the surface of the solid using an inbuilt image processing algorithm to capture and analyse the images at various stages in which the liquid was added, allows to spread and at equilibrium. Lightning conditions, sample preparation, and calibration levels of the instrument have an impact on the result. Hence, care must be taken in image acquisition. This surface characterisation method finds applications in several fields, including surface chemistry, material science, and biotechnology, where understanding the type and nature of interactions between molecules and supports is vital to various discoveries. [285]

In this research, we monitored the wetting properties of the surface after silanisation by measuring the contact angle using a 5 µl RO water (18.2 MΩ cm) with the sessile drop method on the glass surface and immediately measuring the tangent of the water droplet with the silanised (FDTS and nDTS) glass using the DSA25 goniometer (Kruss). Here, an average of 3 measurements at room temperature was used to confirm the change in surface hydrophobicity. A bare, non-silanised glass sample was used to monitor and control this modification stage.

2.13.3 The Double Layer Theory

The double-layer theory was reported over 150 years ago by Helmholtz [286] and subsequently modified by Guoy-Chapman and Stern. [287–289] The double layer theory is an essential concept in colloidal science. According to the DLVO theory, it visualises the ionic environment in the vicinity of any charged colloids and its interaction with the colloidal environment in a sequence of steps. [290] The double-layer theory can be described in two ways. The first involves the effect of the positive ions (counter-ions) on negatively charged colloidal particles. The presence of negatively charged NPs causes the initial attraction of a positively

charged firm layer of counter-ions to the surface of the particles. This layer is also referred to as the stern layer. From here, further addition of positive charges causes repulsion of the excess positive charges by the initially deployed positive charges that make up the counter ions. Subsequently, the presence of the initial positive charges causes the attraction of other negative charges (co-ions) in the colloidal system. The movement of these mixed ions creates a diffuse layer of counter ions, which decreases with distance from the surface of the negative charges until an equilibrium is reached, unlike the concentration of the co-ions, which increases with the distance. This same scenario plays out for positively charged colloids. According to DLVO theory, the diffuse layer can be visualised as a charged atmosphere surrounding a colloid. The density of this charged layer at any distance is equal to the differential value between the two charges at that point. It is larger near the colloids and decreases with the distance depending on their concentration. The combination of the attached counter-ion on the stern layer and the mobile region of the diffuse layer is known as the double layer. [291] Between the stern and the diffuse layer is an imaginary line called the slip pane representing the ZP, whose exact position remains contentious among researchers. [292–295] Hence, the double layer helps to neutralise the charged colloids, creating electrokinetic potential between their surface and the surrounding medium. Other factors that can affect the double layer are the ionic strength or pH of the medium, the concentration of any additives, and temperature. [296] It has been estimated that the thickness of the double layer is defined by the Debye length (1/K), which is a function of the ionic strength and the general properties of the solution (i.e., ionic valency, temperature, and the ion concentration in the bulk solution) and not on any property of the charged surface. [297] Therefore, the relationship between the electric double layer and concentration is characterised by the thickness of the double layer (Debye length) being inversely related to the ionic concentration. Higher concentrations lead to a compressed double layer, increased ionic screening, and lower zeta potential. Understanding this relationship is critical for applications in electrochemistry, colloidal stability, and surface interactions, as it affects the behaviour of charged surfaces in various environments.

2.13.4 DLVO Theory

The DLVO theory was postulated by Boris Derjaguin, Lev Landau, Evert Verwey, and Theodoor Overbeek. The DLVO theory describes the balance of force between charged surfaces interacting through a medium (Figure 21). It accounts for the relationship between attractive and repulsive forces, with Van der Waals and electric double-layer forces identified as the independent forces that influence the interactions between two particles at a specified distance. [298, 299]

1. Van der Waals: These forces arise from the interaction between electron clouds of particles. They are the primary source of minimum potential energy curves where the particles are close to each other due to the strong force of attraction.

2. The electric double layer described by the double layer theory:

When two particles come close together in a colloidal system at room temperature, their ionic atmosphere begins to overlap, and repulsive forces develop due to electrical double-layer forces. These forces (from the double layer theory) arise due to the interaction between charged particles and the ions from the surrounding system. This interaction simultaneously takes place in the presence of van der Waals forces. The stability would be sustained if the repulsive force exceeds the attractive van der Waals forces. Therefore, the electrical double layer forces are responsible for the repulsive domain between the local maximum (corresponding to the barrier that prevents sticking together of particles) and the secondary minimum (favours coalescing of particles) in the potential energy curve. Hence, when the colloidal particles become energetic (from Brownian motion), they can overcome these repulsive forces, creating a zero-surface energy where, at any distance between the particles, the energy of attraction over the repulsive energy prevails, causing colloidal instability or flocculation. [206–208]

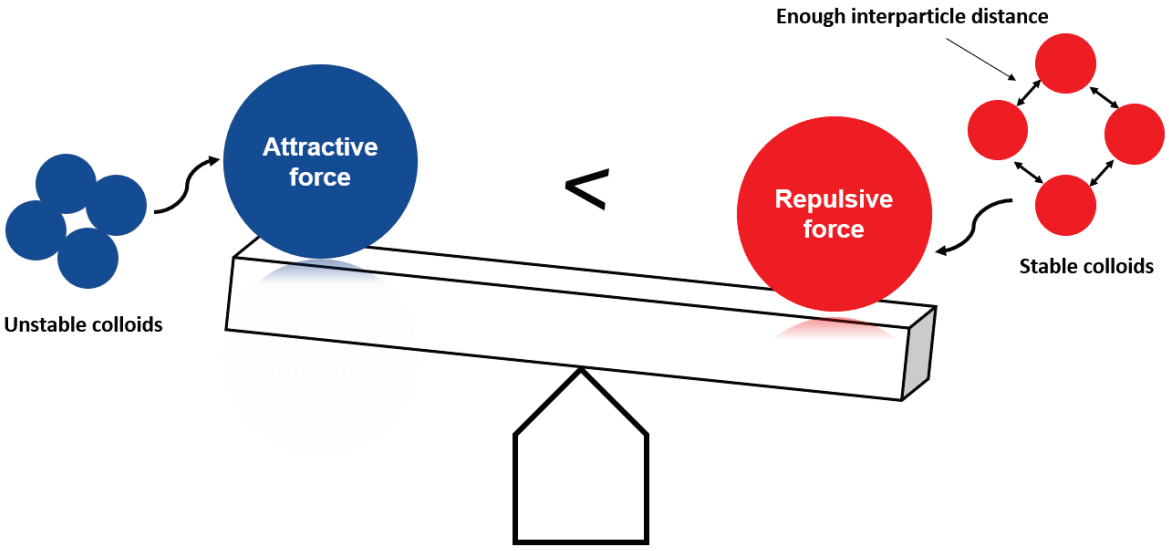

Figure 21: This diagram illustrates the balance of forces during the interaction of nanoparticles in a colloidal system. A reduced interparticle distance increases the tendency for aggregation within the colloidal system (blue). Conversely, a sufficient repulsive force is crucial for maintaining this distance (red). Aggregating in the colloidal system occurs when the attractive force outweighs the repulsive force.

The DLVO theory is a valuable model that explains the interactions of colloidal systems. However, this has limitations, and alternative hypotheses have also been proposed to explain these limitations where the DLVO theory cannot be applied. [303, 304]

The DLVO theory could not explain the following colloidal system, so alternative systems have been proposed.

1. Colloidal systems with short-range attraction and long-range repulsion

In this system, stability should be sustained once the repulsive force exceeds the attractive van der Waals forces. However, it was reported from experiments that systems that exhibit phase separation can create aggregation. Hence, an alternative theory is needed to explain the results.[305]

2. Colloidal system with non-DLVO forces: Unlike the DLVO theory, which assumes that van der Waals and electric double layer forces are the only forces in a colloidal stability system. However, other factors such as hydrophobic interaction, steric repulsion, and specific ion effects have also been identified to play roles in colloidal stability. Therefore, the DLVO theory can act as a guide to understanding colloidal stability but is not sufficient to explain complex colloidal systems. Therefore, alternative theories are needed to describe complex colloidal systems.

3. Electrostatic stabilisation: This theory proposes steric repulsion, which arises from the combined effect of steric hindrance, and electrostatic repulsion occurs due to the adsorption of polymers or surfactants to the surface of particles, contributes to the stability of a colloidal system.
4. Consistent alternatives to DLVO theory: This theory proposes that interactions from infinity to contact could be drawn from their models, including the low potential (LP) model, the co-ion exclusion (CX) model, and the constant potential (CP) model. [306]

2.13.5 Dynamic Light Scattering (DLS)

Dynamic Light Scattering (DLS), otherwise known as photon correlation spectroscopy [211] or quasi-elastic light scattering [308] is a non-invasive analytical method used to determine the hydrodynamic size distribution profile of small particles in suspension based on the time-dependent Brownian motion of the suspended particles with respect to scattered light. [309] Particles in solution do not exist alone but with different surface charges that maintain their stability, impact surface characterisation, and functionalisation for several biomedical applications.
Depending on the scattering angle (θ) and the observation time (t), Tyndall effect (scattering) and Brownian motion are the two common modes that colloidal suspension can be subjected to for analysis. Due to this, the information acquired from the scattering experiment can be static (Static Light Scattering), where the time-averaged scattering intensity is measured at various scattering angles or by Dynamic Light Scattering (DLS), in which the time dependence of the intensity is measured. The SLS can only estimate the particle size distribution of colloidal suspension when they are in the same range as the wavelength (λ) of light or at least greater than λ/20. In contrast, the DLS can measure the particle size distribution profile of particles much smaller than the wavelength of light. [310, 311]

2.13.5.1 Principle

The principle behind DLS is based on the ability of the dispersed colloidal particles to scatter incident light proportional to the 6^{th} power of their radii.[312]

Since colloidal particles are always in constant random and translational movement due to Brownian motion, increasing concentration and path length affects their speed and interparticle distance. [313]

2.13.5.2 Sample Concentration

An ideal concentration of colloidal samples is difficult to ascertain for the DLS analysis. A high sample concentration leads to multiple scattering, where the scattered light from one particle can interact with other particles before reaching the detector. Here, the intensity of interaction or scattering will be lost before getting to the detector, which can tentatively affect the size of the resulting measurements or cause further agglomeration. At the same time, very diluted samples may be unsuitable for the analysis. Other parameters such as sample preparation, scattering angle, volume of sample, contamination, laser power, and detector sensitivities can also affect the output of the generated data. [314–316] However, using too much diluted concentration may not be enough to generate the minimum count rate for the scattered light required to proceed with the measurement.

During DLS measurement, the suspended NPs are illuminated by a monochromatic laser at a specific angle while its scattering intensity is collected with a photon detector. Since the scattered intensity is time-dependent, the fluctuation of the intensity is affected by the diffusion rate of the particles. From here, the autocorrelation function is used to capture the fluctuation of the scattered intensity per time using a logarithmic function. [317] DLS measurement is useful for determining the range of sizes of nanoparticles synthesised, especially since this size can change depending on how they were synthesised.

In this research, the hydrodynamic size distribution of the NPs was measured using the zetasizer Nano series (Malvern Panalytical, 6.12). Here, 700 uL of each sample was laser-illuminated in a folded capillary cell while scattered light was collected at 90° with 30 measurements. All measurements were done in triplicate at 25°C.

2.13.5.3 Zeta Potential (ZP) Measurement

Nanotechnology has transformed many areas of science, such as biomedicine, pharmaceuticals, food, textiles, electronics, machinery, chemistry, and

biomedical engineering. This is because of the diverse uses of nanomaterials, which range in size from 1 to 100 nm. [318, 319] In colloidal chemistry, the properties of nanoparticles, especially their stability, are important for practical applications. The Zeta potential is one of the most crucial parameters used to analyse the stability of colloidal suspension. [320] ZP represents the potential difference at the slipping or share plane of suspended colloidal particles in solution under an electric field. It is also known as the electrokinetic potential between the electric double layer and the immediate surrounding charges around the slipping pane. As the size of the nanomaterials reduces from their bulk size, their surface area-to-volume ratio increases and impacts the distribution of their surface charge. Hence, this can induce either electrostatic repulsion or attraction among the charges. Depending on the coating or the stabilising materials on the surface of the nanoparticles, the surface charge can be positive or negative, with a high ZP equivalent to the stability of the colloidal system. Research has shown that ZP is crucial to determining colloids' stability and surface charge, including gold nanoparticles. Specifically, research shows that ZP above +30 mV or below -30 mV is likely to be stable for gold nanoparticles due to sufficient electrostatic repulsion. [321–324] Furthermore, a negative ZP has been associated with good stability in gold nanoparticle suspensions. Particle size is another factor that can influence the ZP of gold nanoparticles. [325–328] Additionally, ZP can act as an important indicator in interactions between NPs and biomolecules, with various applications.[329, 330] In summary, ZP analysis provides valuable insights into the surface charge and stability of nanoparticles in aqueous suspensions. In this study, the zeta potential of the NPs was determined using the same zetasizer at room temperature.

2.13.6 Resist Spinning /Spin Coating

This is a versatile and viable nanofabrication technique used to apply a thin layer of resist on substrates before pattern transfer. There are several methods used to achieve resist-spinning [331–334]

1. **Spin coating:**

Spin coating is a fast and easy method to apply a thin layer of uniform resist film on a flat or planar substrate. In this method, the resist is carefully dispensed on

the surface of the substrates. In contrast, the substrate is spun at a specific speed and time depending on the surface tension, rotation speed, drying rate, % of solids, and viscosity of the resist used. Apart from this, the thickness of the spin-coated film is inversely proportional to the square root of the angular velocity or the speed, w. The spin-coating method is appropriate only for flat surfaces, and over 90% of the resist applied is spun off the sample. For example, PMMA is a positively toned resist used in nanofabrication. PMMA can be used as a layer, alone or in combination with a copolymer, to produce the desired thickness. To produce a PMMA layer with high resolution and the desired profile, different bilayers of PMMA are used due to their differential dissolution rate during the development stage. A good undercut can be created from the first PMMA layer under the thicker, less sensitive PMMA during the development.

In addition, as the molecular weight of the resist increases, their sensitivity and rate of development reduce, with a lower molecular weight resist giving rise to higher sensitivity due to shorter polymer chains and less scission. Hence, a less concentrated developer is needed to make them soluble during the development. [239, 240]

2. **Dip coating**:

This simple, reliable, and robust industrial process is used to manufacture bulk products and specialised coatings in biomedical fields. It involves five basic steps: immersion, start-up, withdrawal, drying, and curing (optional).

In general, the substrate is submerged in the initial solution and then pulled out at a constant or control speed and evaporations to produce a thin film layer of desired property. The major drawbacks in this are the unbalanced coating and build-up during the coating process.

3. **Spray coating:**

In this method, substrates are aerosolised and sprayed through a nozzle that spreads across the entire surface of the substrates. Unlike in spin-coating technique, spray coating is suitable for coating a non-planner surface. In addition to this, high aspect ratio features such as pillars and deep trenches can be generated and uniformly coated on substrates at reduced sample amount. However, it is time and labour-intensive to generate thin film layer.

4. **Roll coating:**

This is a form of pre-metered coating in which the coating materials are applied to the surface of the substrates using pre-designed rollers. Like the other coating methods above, the coating thickness is also influenced by the roller's rotation speed and the coating fluid's rheological characteristics.

5. **Doctor blade coating:**

This technique generates a well-defined film thickness and works by placing a sharp blade at a fixed distance from the surface ready to be coated. This technique has minimal sample loss but takes time to optimise. [241, 242] In addition, coating methods for other materials are available depending on the desired needs.

2.13.7 Scanning Electron Microscope (SEM)

The scanning electron microscope is a valuable tool in topography measurement that uses a beam of highly energetic electrons to take a magnified image of an object with fine resolution using their interactions with the bombarding electrons in the sample. [339] A Scanning Electron Microscope (SU8200 series, HITACHI) with 0.8 nm resolution was used to characterise the morphology of the immobilised gold and silver NPs using the 5.0 KV electron beam with a 3.6 mm working distance. In this research, 100 uL of the colloidal samples were diluted in 1 mL of DI (except stated otherwise) and dried under ambient conditions. Particle count was analysed using image J.

2.13.8 Atomic Force Microscopy (AFM)

Atomic force microscopy (AFM) is a tunnelling microscope developed to overcome the basic drawbacks of the Scanning Tunnelling Microscope (STM). [340] The STM can only image conducting or semi-conducting samples, and they are often destroyed and non-reusable after processing before exposure to the electron beam from the STM. AFM provides highly detailed surface profiling of samples, including the topography and roughness on the nanometer scale.

The concept behind this involves measuring the intermolecular forces between the tips of the cantilever of the AFM and the surface of the sample as the tip of the AFM approaches the surface of the sample. Here, the deflection is monitored by the laser beam that reflects off the backside of the cantilever with a mounted

microscopic tip. Therefore, once the tip scans across the surface of the sample, the deflections across the surface due to these forces between the sample and the tips are measured using a position-sensitive photodiode detector that records these deflections, mathematically extrapolated and presented in the form of topological, mechanical, or electrical date. Examples of the forces that exist during the measurements include Van der Waal's, electrostatic, chemical, and steric forces.[341, 342]

With the inclusion of non-contact mode, there are two major modes in which the AFM operates - Contact and Tapping mode:

1. **The contact mode:** Here, the cantilever tip continues to contact the sample's surface. This mode improves the resolution, but the surface of the sample or the tip can easily be damaged.
2. **Non-contact mode:** Here, the tip of the cantilever oscillates near the surface of the sample without touching it, detecting the forces between the samples and the tips, creating a change in the cantilever's oscillation patterns. It is less invasive but more challenging regarding operations, sensitivities, and resolution.
3. **The Tapping mode:** In this mode, the cantilever tip occasionally taps lightly or gently on the sample's surface. This reduces the lateral forces and makes the cantilever tip soft enough to prevent damage to the sample. Hence, it is suitable for imaging fragile biological specimens or surfaces.

   Other modes of image generation, such as phase imaging, lateral force microscopy and force modulation mode, can be used to improve image acquisition using AFM. To reduce the risk of damage to the sample, the sample was imaged using Bruker AFM in tapping mode, while images were analysed using Nanoscope software 1.9 from Bruker (2017). The post-scanned images were processed by image flattening and cleaning to produce 2D and 3D output.

2.13.9 Contact Angle Measurement

Non-wetting surfaces are one of the critical targets in science, especially in surface chemistry, where their potential applications in self-cleaning, anti-fouling, anti-corrosion, and anti-adhesion are desirable. [343, 344] Hence, creating surfaces

that are hydrophobic, homophobic, or oleophobic is not an exception in the microarray industry, where self-assembly monolayers are desirable.

Using fluorous chemistry, where the perfluorinated thiol (PFDT) or silanes (FDTS and nDTS) act in the machinery that directs the attachment of ODNs, gold, or silver NPs to create ordered perfluorinated SAMs films with hydrophobic surface is embedded in the objectives of this research.

In this research, the wetting properties of the silanised sample were evaluated by depositing a 5 µL drop of RO water (18.2 MΩ cm) with the sessile drop method on the glass surface and immediately measuring the tangent of the water droplet with the silanised (FDTS and nDTS) glass surface. Subsequently, the contact angle was measured using a DSA25 goniometer (Kruss) with an integrated CCD camera. The contact angle measurements were carried out to monitor and compare the stage from hydrophilic to hydrophobic layer during surface functionalisation, with an average of triplicate data recorded for this experiment.

A surface contact angle greater than 90° signifies a hydrophobic layer or increased perfluorination. In comparison, a contact angle below 90° signifies hydrophilicity due to a free hydroxyl group on the hydroxy-terminated glass surface. This also agrees with earlier reports on fluorous effects on surfaces. [247–249] This surface characterisation method finds applications in several fields, including surface chemistry, material science, and biotechnology, where understanding the type and nature of interactions between molecules and supports is vital to various discoveries.[348]

2.14 Conclusion

This section focused on the techniques for immobilising oligonucleotides and metal nanoparticles on fluorous patterned surfaces using the fluorous effect. It also summarised the theoretical and practical methods that support each method.

Chapter 3

3.1 Repeatable and Selective Immobilisation of DNA using the Fluorous Effect

3.2 Introduction

The history, potentials, and limitations of microarray technology were discussed briefly in chapter one. It highlighted how this technology has evolved since its discovery and various applications. Microarray technology allows the simultaneous analysis of multiple genes and their targets, a crucial aspect of this method. This high-throughput method has great potential, making it an essential tool in gene expression profiling, mutation detection, genotyping, and other complex biomedical requirements. Despite its remarkable properties, the technology faces several limitations that require urgent attention to realise its full potential in various biomedical fields. One of the major challenges is the tendency for high background noise [349], which can compromise the accuracy of data interpretation. Low reproducibility is also a common issue in most reports from the literature. [350, 351] In addition, several factors can limit the widespread use of immobilisation experiments. Firstly, the costs associated with the experiment, the amount of time needed to conduct it, and the requirement of specialised equipment can be significant barriers. Furthermore, even if the experiment is successfully carried out, understanding the data it generates and interpreting it accurately can be challenging, which may impact its overall acceptance. [352] Many protocols have been proposed to address this challenge, either through improved sophistication with a high-cost impact (including polymerase chain reaction) or a trade-off between the two. [353–357] Therefore, it is desirable to develop a straightforward, sensitive, specific, and repeatable method.

3.2.1 Incorporation of Fluorous Tags for Microarray Applications

Central to the core of fluorous microarray technology is the fluorous phase interactions that can be applied for the reversible attachment of biomolecules in a highly uniform manner, leading to an increase in signal-to-noise ratios during detection. One of the most prominent applications of fluorous microarrays is diagnostic testing, where it can be used to detect disease biomarkers with higher

sensitivity. It is also widely used in genomics, proteomics, and drug discovery, where accurate and high-throughput screening of biomolecules is crucial.

Despite its promising applications, fluorous microarray technology is not without challenges. The synthesis and purification of fluorous-tagged biomolecules can be complex and costly, which limits the availability of ready-to-use fluorous reagents. Rigorous experimental conditions are also necessary to capture only the intended fluorous-tagged molecules on the microarray surface. Apart from this, there are technical challenges in fabricating the microarray itself. Creating a uniform fluorous surface with consistent functional groups across the entire substrate is essential for effectively immobilising biomolecules. Furthermore, the complexity of fluorous tagging and the unique properties of fluorous compounds can pose difficulties in the detection process.

Despite these challenges, a well-conjugated fluorous microarray can provide exceptional sensitivity and specificity, surpassing traditional microarray platforms. This makes it an essential tool for research and practical applications in clinical diagnostics and other biomedical applications.

To improve the specific interaction necessary for microarray applications, the oligonucleotides are conjugated with perfluorinated chains to impact the required hydrophobicity for specific interactions. Three distinct regions can be created from the alky chain (Figure 22):

1. The perfluorocarbon group, also known as R_f, where the inherent electronegativity of the perfluorinated chain is used for fluorous interactions.
2. The spacer
3. The organic group consisting of the interacting moieties (oligonucleotides).

In this research, the perfluorinated group creates fluorous tags or ponytails to encourage fluorous-fluorous interactions. As described in Chapter 1, the physicochemical properties of the fluorous tag are different from the rest of the hydrocarbon chain. Hence, there is a tendency for this perfluorinated region to be excluded from other aqueous and organic phases to
prevent unfavourable interactions. Therefore, exploring this property is the central focus of this research.

This section aims to address the following issues:

1. Determine if the fluorous effect is suitable to immobilise fluorous modified single-stranded oligonucleotide on fluorous modified support.
2. Compare the effect of incorporations of fluorine atoms on the size, length, branch system, and HEG linker of modified oligonucleotides.
3. Determine the repeatability of this method using the same protocol
4. Determine the suitability of the fluorous effect for multiplex applications

Table 3: List of oligonucleotides used for this research. The number of branches attached describes the modified oligonucleotides as 'mono, bis, and tetra. R_F was used to indicate the DNA attached to specific fluorous tags. The subscript indicates the chain length of the oligonucleotides.

Fluorous tags	Linker	DNA-LINKER-R_F	Sequence (5'-3')
Mono-C_4F_9	None	DNA-RF_4	TGC AGA TAG ATA GCA G
Mono-C_6F_{13}	None	DNA-RF_6	TGC AGA TAG ATA GCA G
Mono-C_4F_9	HEG	DNA-HEG-RF_4	TGC AGA TAG ATA GCA G
MonoC_6F_{13}	HEG	DNA-HEG-RF_6	TGC AGA TAG ATA GCA G
Tetra-C_8F_{17}	None	DNA-$(RF)_8$	TGC AGA TAG ATA GCA G
Bis-C_8F_{17}	None	DNA-$(RF_8)_2$	TGC AGA TAG ATA GCA G
Bis-C_8F_{17}	HEG	DNA-HEG-$(RF_8)_2$	ATT TGT GTA GTC CTG C
Tetra-C_8F_{17}	HEG	DNA-HEG-$(RF_8)_4$	ATT TGT GTA GTC CTG C
Mono-C_8-F_{17}	HEG	DNA-HEG-RF_8	TGC AGA TAG ATA GCA G

Complementary sequences:
1. 5'- CTG CTA TCT ATC TGC A-3'
2. 5'- GCA GGA CAT CAC AAA T-3'

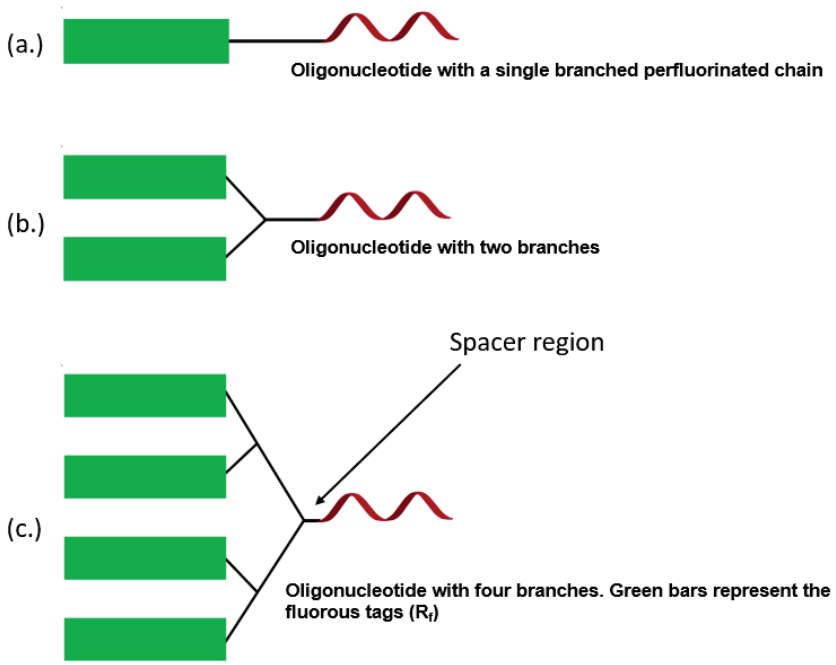

Figure 22: The schematics illustrate the evolution of the branching system in fluorous-modified oligonucleotides. (a) depicts the conjugation of an oligonucleotide with a single fluoro-alkyl chain. (b) demonstrates the conjugation of an oligonucleotide chain with two branches, each made of fluoroalkyl chains. (c) shows the conjugation of an oligonucleotide with four fluoroalkyl chains. The spacer region is included only in the tetra-branch system for illustrative purposes.

3.3 Results and Discussion

Microarray technology identifies and analyses multiple genes or oligonucleotides through various methods and designs, such as electrostatic adsorption, covalent interactions, and avidin-biotin interactions. These interactions are designed to create fast, stable, or reversible bonds. However, most immobilisation platforms are designed to provide maximum hybridisation signals, which could also result from unwanted interacting species rather than specific interactions. On the other hand, platforms like Polymerase Chain Reaction (PCR) (Figure 23), which are limited in their ability to amplify and detect multiple targets simultaneously, can be time-consuming, costly, and sensitive to variable conditions. [358]

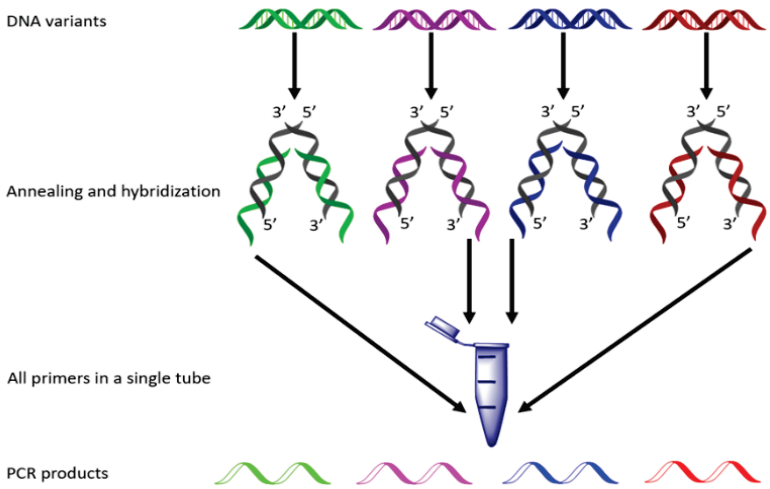

Figure 23: Schematics illustrating how PCR is adapted for DNA multiplexing.

Researchers have developed techniques to selectively localise fluorous-tagged molecules on surfaces or specific regions to create defined patterns or structures. These methods are attractive for applications in the microarray industry, where tailored surface properties are required. However, combining microarray design with other conjugation methods requires covalent interactions, which are difficult to achieve and involve multiple chemical steps. The protective functional group also offers little or no opportunity for reversible interactions. [359]

To address these issues, Pohl et al. (2005) demonstrated a highly specific fluorous affinity for synthetic carbohydrates tagged with a small-sized fluoroalkyl chain (C_8F_{17}) and fluoroalkyl-modified glass for microarray applications. This method has two advantages: Firstly, the perfluoroalkyl chain is chemically inert and compatible with a wide range of functional groups, and secondly, the fluorous tags allow for phase separation necessary for purification. [360] Additionally, the same fluorous effect can produce small-molecule microarrays with a multivalent display that mimics cell surface-bound compounds. [361] Other molecules, including proteins, have been isolated or purified using fluorous tags due to the specific affinity they confer.

In addition, researchers have demonstrated a new reversible immobilisation method onto defined patterns using the fluorous effect at a sub-micron resolution. [362] This opens new possibilities for creating supramolecular structures tailored for important biomedical applications. [363]

To expand the scope of this microarray design and its application, this chapter aims to demonstrate the repeatable immobilisation of fluorous modified 16-mer

oligonucleotide (Ta) on a 50 µm-sized lithographically fluorous patterned surface without losing functionality, using the fluorous effect. The idea is to address the methodological gap in DNA microarray studies. Traditional microarrays have limitations such as lack of repeatable self-recognition property, non-specific binding, loss of functional surface, and irreproducibility. [364] Therefore, using fluorous effect allows us to explore these interactions by comparing the strength of the modified oligonucleotides using their size, shape, HEG linker, and fluorous contents for suitable applications. [365, 366]

To overcome these limitations, researchers utilised the fluorous effect. This approach allows us to compare the modified oligonucleotides based on their size, shape, HEG linker, and fluorous contents. By doing so, we can better understand their interactions and identify suitable applications for these modified oligonucleotides. To achieve a specific interaction, creating an environment that distinguishes between hydrophilic and hydrophobic surfaces is essential, which is possible by utilising the fluorous effect. The first step in creating a hydrophobic surface involves coating a lithographically patterned hydrophilic glass surface with PEG silane to form a non-fluorous background. Next, the fluorous layer is created on the patterned surface (foreground) using FDTS. The decision to adopt PEG was based on its hydrophilic nature, wide usage as a passivation layer to prevent non-specific interactions of biomolecules on surfaces, and its ability to sterically prevent the binding of modified oligonucleotides to the non-fluorous regions. [367–369] With a low contact angle as low as 25.5° degree [370–372] we anticipated that this property would allow for an easy conjugation with the free hydroxyl group of the glass sample through a simple hydrogen bond. Hence, we anticipated that this would enable the distinction between the fluorous and non-fluorous regions and direct the immobilisation and hybridisation of incoming fluorous-modified oligonucleotides to the fluorous patterned regions instead of the background or non-fluorous regions. [373, 374] Despite using PEG, the expected result was not achieved even after different silanisation methods were explored before immobilisation and hybridisation. The inability to create a repeatable surface using PEG could be attributed to the complex nature and structural changes that occur when PEG is conjugated with other substrates or due to a general change in the assembly's architecture. [375] To replace the previous silane, nDTS was adopted to differentiate between the hydrophilic non-fluorous and hydrophobic fluorous layers.Therefore, we hypothesise that exploring the relationships

between the size, branch, and HEG linker could direct the specific interaction of these modified oligonucleotides on the fluorous patterned surface using the fluorous effect with the possibility of a simple methanol wash.

3.3.1 Comparison between PEG and Silane Self-Assembled Layer using Contact Angle

The surface properties were investigated to check the surface's wettability upon interaction with water using the static contact angle. [376, 377] Non-wetting surfaces are key targets in science, especially in surface chemistry, where their potential applications in self-cleaning, anti-fouling, anti-corrosion, and anti-adhesion are desirable.[378, 379] Quality check done on the silanised surface revealed the conversion of the surface properties from hydrophilic to hydrophobic SAM when passivated with a self-assembled layer of nDTS and FDTS layers (Figure 24). The results were far superior to those from PEGs, repeatable, and promising. Gas silanisation was adopted to create self-assemblies of nDTS (background), and FDTS (foreground) cured at 90 ºC.

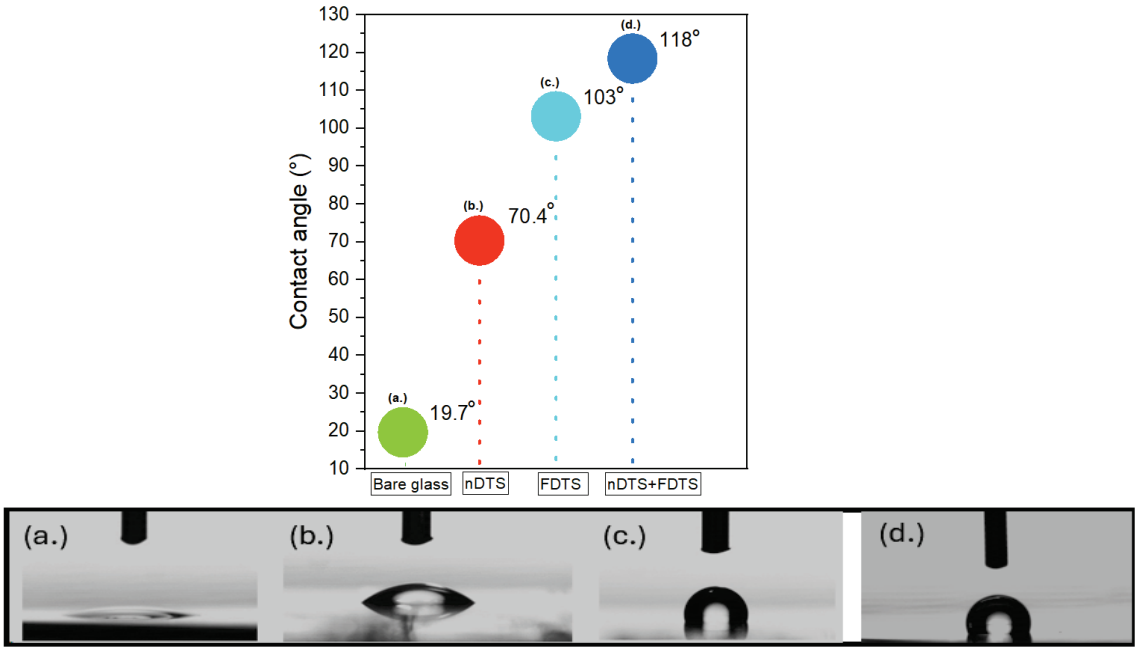

Figure 24: Silanisation stage indicating the switch from the hydrophilic (ordinary glass) to a hydrophobic surface (nDTS and FDTS). (a.) The hydroxyl-terminated surface is hydrophilic with a ca. 19.7 °± 2.0° contact angle (b.) The surface was silanised using nDTS to form a contact angle of 70.4°± 0.6° and below 90°(c.) Silanised surface in the presence of FDTS to create a silane-terminated perfluorinated surface with a contact angle above 90°, i.e. 103°± 1.44° confirming hydrophobic surface. (d.) The combined effect of nDTS and FDTS created a hydrophobic surface with a contact angle of ca. 118°±1.30°. Data were expressed as the mean ± standard deviation (SD) from triplicate measurements taken from different areas of the same surface.

The contact angle was measured using the 5 µL sessile drop method to evaluate the surface's hydrophobicity and hydrophilicity before and after silanisation (**Figure 24**) After the gas silanisation process, the surface's contact angle increased significantly from an initial 19.7 °± 2.0° (for bare glass) to 70.4°± 0.6°(for nDTS only). In contrast, the contact angle increased from 103° (for FDTS) to 118° (for nDTS + FDTS). The variability in these measurements was ±2.27° and ±1.39°, respectively, indicating a successful transition from a hydrophilic to a hydrophobic surface. This value aligns with similar reports in the literature, where a contact angle above 90 degrees is attributed to a hydrophobic surface. [380]

3.3.2 Comparison between the Length of Immobilised ODNs

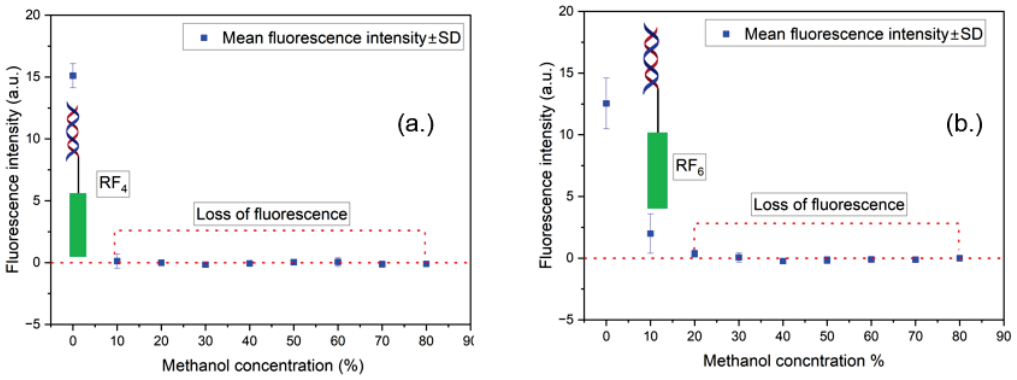

Figure 25: Effect of length on immobilisation and hybridisation of ODNs using fluorous support: (a) C_4F_9, (b) C_6F_{13}. The oligonucleotide (C_4) with a shorter chain length is reportedly weak and not suitable for most immobilisation experiments. Hence, it is easily stripped from the surface with a 10% methanol wash in this experiment. The C_6 is stronger and viable; thus, the required methanol concentration is 20%. The strength increases as the chain length increases.

This research hypothesises that exploring the relationships between the size, branch, and HEG linker could direct the specific interaction of these modified oligonucleotides on a 50 µm fluorous patterned surface using the fluorous effect with the possibility of a simple methanol wash. [381]

Firstly, we compared the length of modified oligonucleotides using the C_4 and C_6 carbon length without the HEG linker (Figure 25). Our findings suggest that longer oligonucleotides with more fluorine are more stable and require more solvent or methanol wash to dislodge the duplex DNA from the immobilised surface compared to shorter ones. This is consistent with previously reported immobilisation protocols where the length and density of the oligonucleotides used during immobilisation affect pre-synthesised complementary oligonucleotides' assembly and surface coverage. [382, 383] Research also

suggests that increasing the size or length of oligonucleotide chains can enhance the efficiency of hybridisation. This is because larger oligonucleotides provide more molecular recognition platforms and receptive contact areas for complementary oligonucleotides to bind to. Ultimately, this leads to the creation of an assembly with improved biorecognition specificity and fewer mismatches during oligonucleotide hybridisation. [384] Consequently, replacing the fluorine atoms with hydrogen atoms has a significant impact that improves the fluorous-fluorous interactions mong interacting moieties of the modified oligonucleotides. Our research showed that increasing the length of the chain leads to stronger non-covalent fluorous interaction due to the greater number of fluorine atoms promoting the fluorous effect. [385] Therefore, the methanol concentration required to strip the bound oligonucleotide (Figure 25) from the fluorous-modified surface increases as the length and the fluorous content increase, although with a similar fluorescent intensity. Specifically, 10% and 20% methanol concentrations were needed to strip the hybridised oligonucleotides C_4F_9 and C_6F_{13} from the patterned surface, respectively. Our research showed that increasing the chain length leads to stronger non-covalent fluorous interaction due to the increased number of fluorine atoms promoting the fluorous effect.

3.3.3 Introduction of HEG Linkers/Spacer in the Fluorous-Modified ODNs

Research shows that increasing the length of the modified oligonucleotide to a certain number of carbons could create unwanted interactions between the ODNs and the fluorous-modified surface. This is especially true when the oligonucleotide is near the modified patterned surface. [386] To avoid this, a spacer/linker was used to keep the modified oligonucleotide away from the patterned surface. This method reduces or eliminates the possibility of steric hindrance or overcrowding, particularly near the pattern's surface. [387] In this research, we adopted the use of a HEG linker within the fluorous-modified oligonucleotide (Figure 26) to achieve this. The HEG linker is a hydrophilic molecule that attaches to the modified oligonucleotide and acts as a spacer away from the surface of the modified glass.

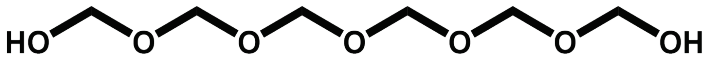

Figure 26: Hexamethylene glycol (HEG) used as a spacer 18.HEG has multiple hydroxyl groups that can also influence reactions.

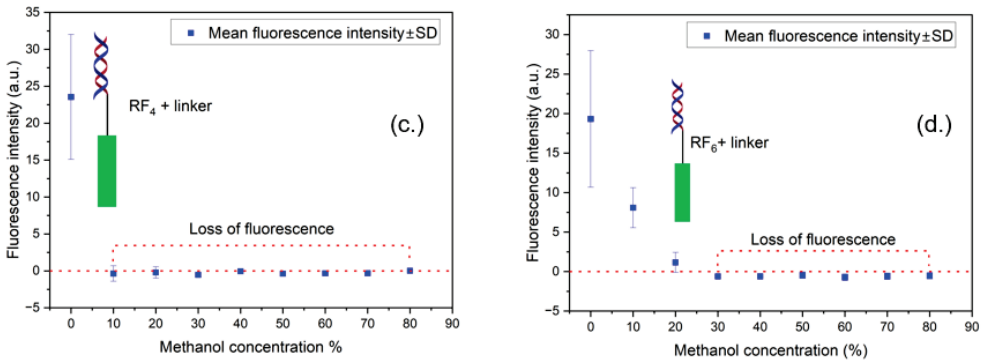

Figure 27: Effect of introducing HEG-linker in short oligonucleotides (C_4F_9 and C_6F_{13}). The introduction of the HEG linker suggests an improvement in the strength of hybridisation of the ODNs on the surface, with improved fluorescence intensity. However, the increased fluorescence intensity does not necessarily translate to strength for the C_4 (RF_4), unlike in the RF_6.

It has been reported that incorporating HEG linkers is essential to prevent unwanted interactions and steric hindrances and improve the accessibility of oligonucleotides during hybridisation. [388] Based on this, the two oligonucleotides (C_4F_9 and C_6F_{13}) were incorporated with a HEG linker (Figure 27) to evaluate if their presence could enhance hybridisation efficiency by preventing non-specific binding and improving accessibility to the bound oligonucleotide on the fluorous modified surface. Results showed that the average fluorescent intensity increased by a minimum of 54.39% (from 12.54 to 19.36 a.u.) due to substituting hydrogen atoms with fluorine atoms. Consequently, the amount of methanol needed to strip the duplex from the surface increased by 50% (from 20% to 30%).

This discovery suggests that incorporating fluorine atoms into the existing oligonucleotide chain can increase binding strength and improve hybridisation efficiency, which aligns with our hypothesis. Additionally, the presence of the HEG spacer contributes to the overall hybridisation efficiency due to the increased fluorescence intensity. This outcome suggests that there could be an improvement in hybridisation efficiency and a reduction in unwanted self-hybridisation among the self-assembled fluorous modified oligonucleotides on the patterned surface. However, it has been observed that the increased fluorescent intensity from the C_4 chain on microarrays may not necessarily be due to improved hybridisation efficiency but rather due to the increased surface density attributed to the size of the oligonucleotides. Consequently, the hybridised C_4F_9 ODNs were easily removable at 10% methanol wash, which supports our findings. This could be due to the size of the oligonucleotides, which have been reported to exhibit poor

hybridisation properties between C_2 and C_6 regions, thus limiting their viability for microarray applications. [389] Similar effects have been reported in the literature where hybridisation efficiency appears independent of the presence or absence of a spacer. [390–393]

3.3.4 Increased length of Oligonucleotides and the Incorporation of HEG linker

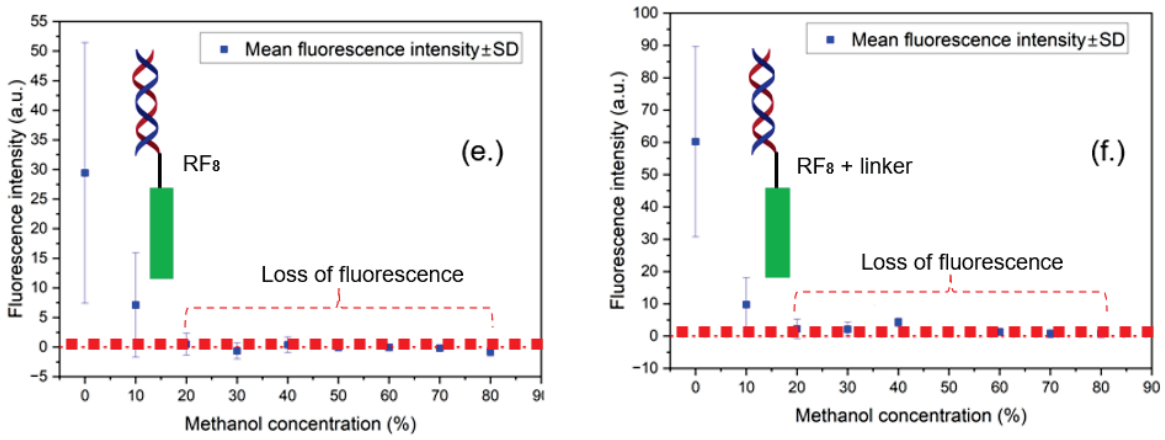

Figure 28: Effect of incorporating HEG linker with increased oligonucleotide length (C_8). Increasing the oligonucleotide length improved the hybridisation strength and the fluorescent intensity in (e.) and (f.).In addition, the fluorescent intensity was also approximately doubled from 29.2 to 60.2 a.u. from the previous chain length (C_8) without the HEG linker (e.).

In the earlier experiment, we studied the effect of increasing the length of the fluorous-bound oligonucleotides from C_4 to C_6. The results indicated that increasing the oligonucleotides' length and fluorine content improved their strength and hybridisation efficiency during interactions. In the current study (Figure 28), we increased the chain length from C_4 to C_8 and observed a 94.69% increase in fluorescence intensity without linkers. This outcome highlights the positive impact of increased perfluorination in the alkyl chain. Consequently, the methanol concentration required to remove the bound oligonucleotide from the hybridisation surface increased by 100% due to the combined presence of a linker and increased perfluorination against the C_4- No HEG chain.

Although the change in fluorescent intensity between the 10% and 80% washes does not show a significant difference due to variations among different concentrations and overlapping error bars (especially at the 10% wash), it appears that introducing a linker to the C_8 chain length improves the average fluorescent intensity from 29.4 to 60.2 a.u.(Figure 28), which represents a significant increase of 105 %. This showed that the presence of a linker in the single-stranded fluorous-

modified oligonucleotide chain could improve the hybridisation of the dye-modified oligonucleotides by preventing steric hindrance, improving accessibility between the fluorous-modified oligonucleotide and the surface or using other thermodynamically feasible methods to improve fluorescence intensity. This also aligns with previous research, which found that incorporating a linker improved the binding efficiency of oligonucleotides. [394–397]

This evidence supports the idea that increasing the perfluorinated alkyl chain length (with or without introducing a linker) can enhance the strength and efficiency of hybridisation. This conclusion is consistent with previous findings where introducing a spacer improved hybridisation efficiency. [398–401]

3.3.5 Introduction of the Two-branch system in Oligonucleotides

Table 4: The table shows the degree of variability from the mean value using triplicate measurements. High variability was noted at low methanol concentrations, which may be attributed to the viability and efficiency of each fluorous-modified spot in the microarray. In contrast, low variability at higher methanol concentrations is attributed to the efficiency of the wash step.

Methanol Wash (%)	0	10	20	30	40	50	60	70	80
Deviation $(RF_8)_2$	11.10	9.88	0.69	2.57	0.74	0.74	0.69	1.13	1.33
Deviation $(RF_8)_2$+Linker	15.03	7.86	4.78	0.83	1.08	1.07	0.39	0.37	1.00

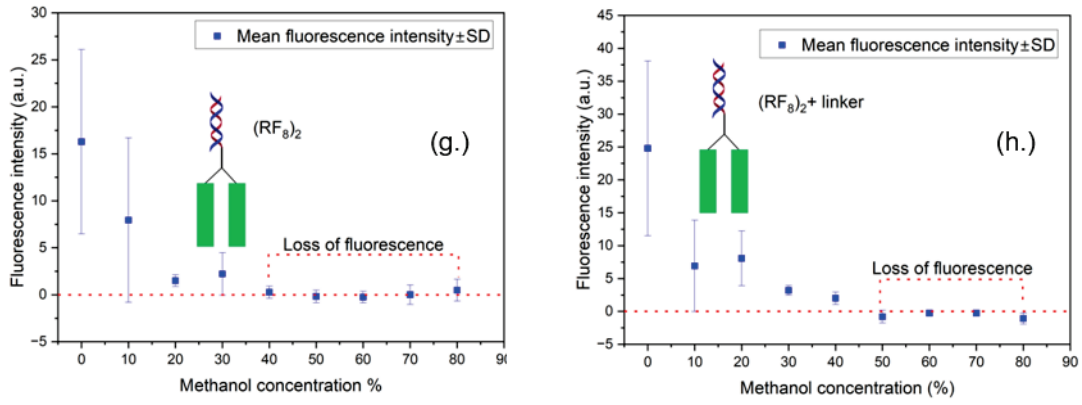

Figure 29: Comparison between two branch systems: (a) without an HEG-linker and (b) with an HEG-linker. The combined effect of the branch system and HEG linkers does not significantly affect the overall strength of the bound oligonucleotides. In this two-branch system, the HEG-linked oligonucleotide (h) washed off at 50% compared to the oligonucleotide without the linker, which washed off at 40%. However, the fluorescent intensity was reduced compared to (e) and (f).

Integrating a branch system during oligonucleotide immobilisation offers advantages such as increased oligonucleotide density [48], improved stability and hybridisation efficiency. We analysed the impact of the branch system on the fluorous effect by comparing the presence or absence of spacers or HEG linkers.

We aimed to understand how introducing branches affects the specificity, density, and pattern of hybridisation of fluorescently labelled complementary strands.
We also expect that this analysis will provide more insight into what factors influence the strength of oligonucleotide immobilisation using the fluorous effect. Is this interaction due to the length, fluorous content, the HEG linker, or all three? In our investigation, we introduced two branch systems, one with HEG linkers and one without (labelled as $(RF_8)_2$-HEG and $(RF_8)_2$-No HEG, respectively). Results from this immobilisation (Figure 29) showed that the size of the HEG-linked oligonucleotide directly impacted the amount of methanol needed to remove the immobilised duplex from the fluorous-modified surface. Specifically, for each carbon chain increase in the oligonucleotide size compared to the previous chain, there was a corresponding 100% increase in the required amount of methanol needed to strip, with a 400% increase observed as the carbon chain increased from C_4 to C_8 (Figure 29). This effect differed when oligonucleotides without the HEG linker were compared. In this case, as the oligonucleotide length increased from C_4 to C_8, the amount of methanol needed to dislodge it from the bound surface increased by 300% (Figure 29g). Additionally, incorporating HEG-linkers in the bis-oligonucleotide $(RF_8)_2$-HEG does not significantly improve results compared to simply increasing the number of oligonucleotide chains or branches from a single to a double-branch system across various percentages of methanol wash. The methanol concentration required to remove the bound oligonucleotides, ranging from 10% to 30%, seems statistically insignificant. This is indicated by the variations observed between the two branch systems, which suggest that the ease of removal from the fluorous patterned surface is similar after immobilisation.
Therefore, incorporating two branch systems does not appear to increase the strength of binding of the oligonucleotides across the wash data due to the variability observed between the two groups from 0 to 40%. Despite this, the impact of increasing the chain length, the branch system, and incorporating the HEG-linker in enhancing the self-assembly and molecular recognition properties of DNA using the fluorous effect needs to be further studied to ascertain the contributory factor of each variable incorporated.

3.3.6 Incorporating a Four-Branch System in Oligonucleotides

Table 5: The table shows the degree of variability from the mean value using triplicate measurements. High variability was noted at low methanol concentrations, which may be attributed to the viability and efficiency of each fluorous-modified spot in the microarray. In contrast, low variability at higher methanol concentrations is attributed to the efficiency of the wash step.

Methanol Wash (%)	0	10	20	30	40	50	60	70	80
Deviation $(RF_8)_4$	20.20	15.28	6.55	5.85	5.37	5.15	0.43	0.53	0.20
Deviation $(RF_8)_4$+ Linker	25.38	0.89	0.4	0.39	0.50	0.55	0.25	0.21	1.02

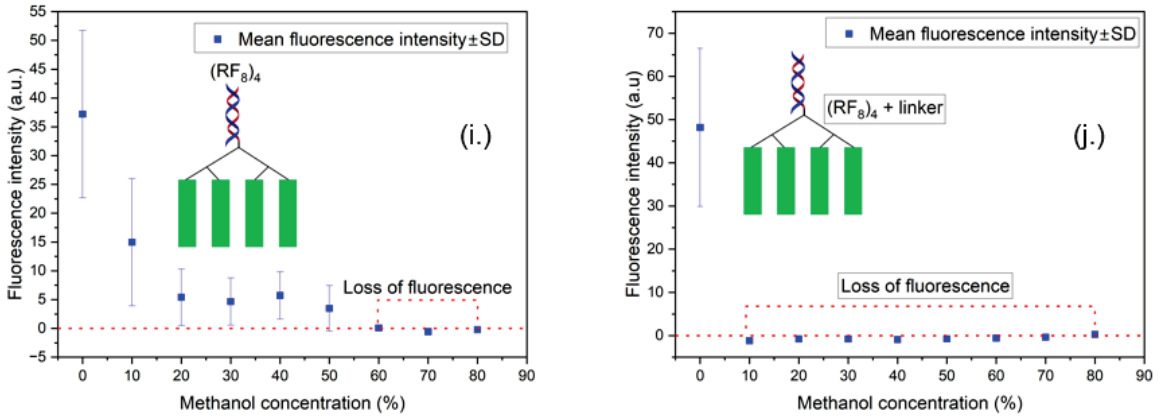

Figure 30: The effect of incorporating a four-branch system in HEG-linked and non-HEG-linked fluorous-modified oligonucleotides and their impact on the fluorous effect and incorporating a branch system beyond the two branches, as in (f.) above, appears to create an unfavourable condition for hybridisation efficiency.

Research suggests that probe density influences the efficiency of hybridisation. An optimal probe density can enhance hybridisation, leading to improved sensitivity. [402] However, excessively high probe density may reduce hybridisation efficiency.[403] We were curious about investigating this in relation to the use of the fluorous effect, so we compared the length, branch system, and introduction of the HEG linker using tetra-C_8F_{17} with four branch systems (with and without the HEG linker), as shown in Figure 30.

This comparison revealed that increasing the branch system from 1 to 4 enhanced hybridisation efficiency for single oligonucleotides lacking the HEG linker (tetra-C_8F_{17}). Specifically, for the four branch systems (tetra-C_8F_{17} - HEG and tetra-C_8F_{17}), the fluorescence intensity increased compared to the single and the bis-oligonucleotides, except for Figure 28. Interestingly, the amount of methanol required to dislodge the hybridised oligonucleotides increased to 60% from the initial 30% (representing 100%) against the single-chain oligonucleotide of similar length without any branch system (Figure 28). Surprisingly, increasing the number of branch systems up to four in the presence of HEG-linker (tetra-C_8F_{17} - HEG) did

not improve the strength of the fluorous interactions. Instead, its molecular recognition properties or hybridisation efficiency appeared to be negatively affected.

These results suggest that the density of hybridisation created by the increased number of branches could have created steric hindrance that appears to be thermodynamically unfavourable during hybridisation or interaction. To achieve favourable thermodynamics during this DNA immobilisation, the process should ideally have a negative change in Gibbs free energy (ΔG), driven by a combination of exothermic enthalpy changes (negative ΔH) and entropy changes (ΔS) that contribute positively to the spontaneity of the reaction. Hence, strong binding affinity, appropriate surface chemistry, and optimal environmental conditions ensure efficient and stable DNA immobilisation. [404–407]

This implies that the presence of the HEG spacer in the tetra-branch system does not favour efficient self-assembly of DNA using the fluorous compared to what was initially observed using the non-branched fluorous modified oligonucleotides with C_4, C_6, and C_8 carbon lengths. In addition, the strength of the tetra-C_8F_{17} - HEG appears similar to the C_4 (RF_4) oligonucleotides, suggesting this branch system's hybridisation pattern. This negative effect could also be attributed to the hydrophilic nature of the HEG, which could have interfered with the existing hydrophobic properties of the fluorous group created during the fluorous effect. Furthermore, the elevation pattern of the fluorous tagged oligonucleotide from the surface could have created an unfavourably dense environment that prevented efficient hybridisation. Therefore, the amount of methanol needed to strip the fluorescently bound oligonucleotides increases due to the improved strength created without introducing the branch system as the size increases. This observation aligns with earlier reports in the literature where bulky biomolecules were reported to increase the density of the immobilised biomolecules, causing changes in the thermodynamics of hybridisation. Consequently, adding these bulky molecules creates a gateway for poor control of the densely immobilised fluorous modified oligonucleotides, creating variations and selective hybridisation. [408–410] It is also essential to consider the orientation and concentration of available probes or fluorous-modified oligonucleotides when creating optimal interactions between immobilised oligonucleotides and their complementary strands.[411] This research found that the current concentration ratio of 1:1 between the fluorous modified bound oligonucleotide and the fluorescently labelled

oligonucleotides was sufficient to achieve the desired fluorous effect without any noticeable constraint. The hypothesis is that the improved fluorescent intensity is due to fluorous-fluorous interactions between the modified oligonucleotides. This increase in intensity aligns with other reports where increased fluorescent intensity is associated with increased hybridisation efficiency.[412–417]

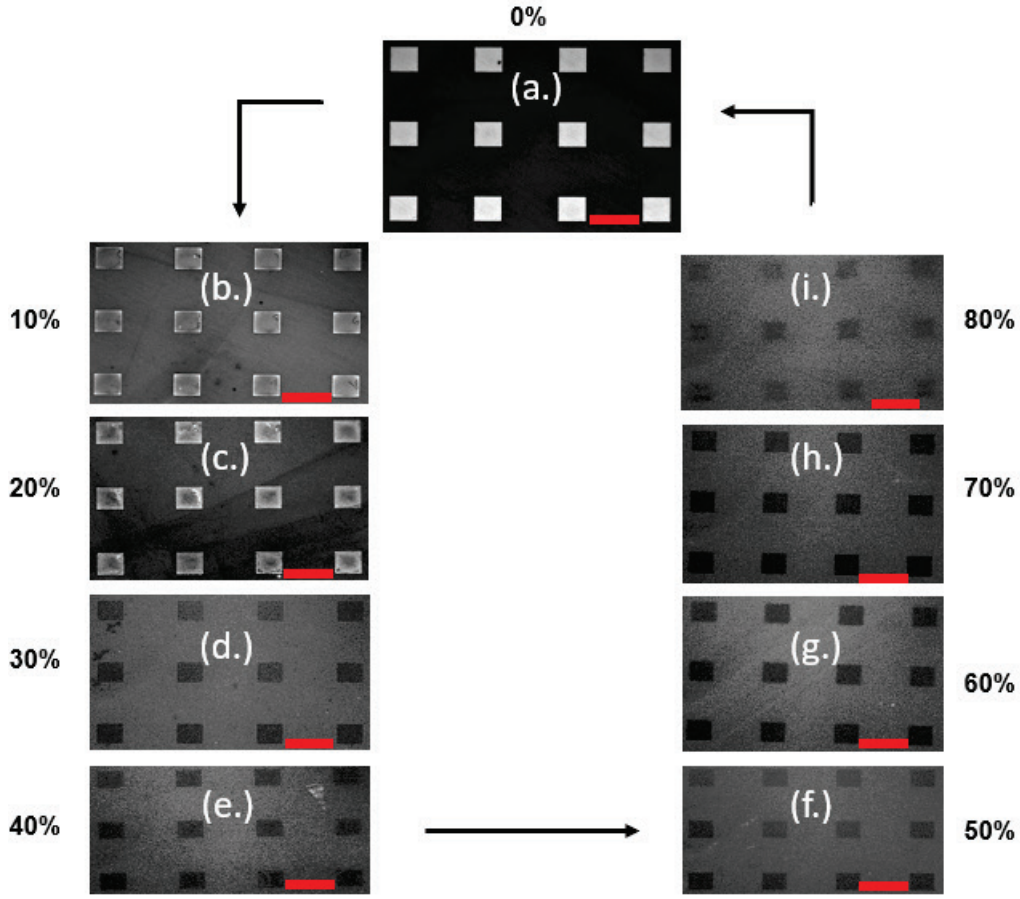

Figure 31: The fluorescent microscopy images display the hybridisation of fluorescently labelled oligonucleotides on a fluorous-patterned surface immobilised with fluorous-modified oligonucleotides (depicted as white squares). 0% represents the first stage without methanol wash, while the range of 10% to 80% represents the concentration of methanol used during the washing step. As the concentration of methanol increases, the fluorescent area (white squares) is removed from the patterned areas. Scale bar (red) = 50 µm; mag. = 20x.

3.3.7 DNA Multiplexing Utilising the Fluorous Effect

Multiplexing is the technique employed to detect multiple targets or analytes within a single experiment simultaneously. [406] This allows the possibility to improve the diagnosis of many diseases using a small number of samples at a reduced cost, time, and technical know-how. Hence, this can be used to analyse small samples to generate more information and make informed interpretations of the analytes. Due to the possibility of this high throughput, there has been an increasing trend in its adoption and modification in several practical applications,

including PCR. Despite the versatile nature of this method, it is susceptible to multiple challenges, including optimisation, sensitivity, cross-reactivity, contamination, and complex data interpretations. To address this challenge, many protocols have been put forward through improved sophistication with high-cost impact or trade-offs between the two. [418–422] Therefore, it is desirable to use a simple method that is affordable, specific, and sensitive for applications in the microarray industry.

Unlike immobilisation using a single oligonucleotide, controlling the cross-reactivity and non-specific binding events becomes crucial when multiple DNA sequences are immobilised simultaneously. These events can lead to false positive signals and compromise the accuracy of the results. Therefore, it is essential to optimise the conditions to minimise non-specific binding events and maintain the sensitivity and specificity of the detection process. [423]

Another significant challenge involves achieving uniform and reproducible immobilisation across different DNA sequences within the multiplexing setup. Variations in immobilisation efficiency can impact the reliability and comparability of the results obtained from different DNA targets. As a result, it is crucial to ensure that the immobilisation conditions are optimised to facilitate efficient and uniform immobilisation of all DNA targets. [424–426]

Furthermore, the simultaneous immobilisation of multiple DNA sequences may lead to competition for binding sites or interfere with the spatial arrangement of the immobilised molecules. Therefore, precise optimisation is necessary to ensure efficient and independent immobilisation of each DNA target. This optimisation will minimise interference between the multiple immobilisation processes and facilitate simultaneous detection of all DNA targets. [427]

It is important to overcome the challenges to fully realise the potential of this technology in applications such as high-throughput genetic analysis, diagnostics, and personalised medicine. By addressing these challenges, we can develop more reliable and robust methods for immobilising multiplex DNA, which can be used in various applications, including the isolation and identification of PCR products.

In this research, we utilised the fluorous effect and selected oligonucleotides based on their strengths and the initial immobilisation patterns (Figure 25-Figure 30). The oligonucleotides were conjugated with TAMRA and Alexa-fluor dyes for easy identification of the strands during fluorescent microscopy. Labelling the oligonucleotides with specific fluorescent dyes enables the parallel detection of

multiple targets, increasing the efficiency and throughput of genetic analysis. Different dyes also facilitate the discrimination of individual targets, allowing us to obtain a comprehensive and detailed view of the type of oligonucleotides and their pattern of interactions in the sample. Additionally, using different dyes minimises the potential for signal crosstalk and experimental variability, resulting in improved data quality and reliability.

3.3.8 Comparison of labelled Oligonucleotides using TAMRA and Alex Fluor dyes.

Following the previous outcome, where the fluorous effect was utilised to create a repeatable attachment of various modified oligonucleotides, the strength of these oligonucleotides was compared based on their length, fluorous content, number of branches, and HEG linker. Our research revealed that the fluorous content significantly impacts the strength of the attached oligonucleotide. Extending the length of the oligonucleotide or adding more branches can enhance its strength. Our research indicates that increasing the fluorous content in the oligonucleotide is the most effective method for improving its stability, particularly when no additional spacer, such as a HEG linker, is used. The hydrophobicity and fluorous effect of the oligonucleotide increase with its fluorous content, leading to enhanced stability and strength. Additionally, we noted that as the fluorous content increased, the amount of methanol needed to remove the hybridised duplex from surfaces also increased. Based on this information, we further evaluated how the strength of the oligonucleotide could influence the selective removal of different fluorous tagged oligonucleotides using different branches from the lithographically fluorous-patterned surface (**Table 6**).

This research aimed to develop a simple proof-of-concept that would allow for easy immobilisation, hybridisation, and selective removal of duplex DNA on solid support using the fluorous effect.

Table 6: Displays the two oligonucleotides: one with the strongest hybridisation strength, conjugated with the TAMRA dye, and the other with the weakest, conjugated with the Alexa dye, utilising the fluorous effect.

Modified strand	Standard Sequence (5' - 3')	Complementary strand/Dye	Number of branches
C_8F_{17}-C_2H_4 -ALEXA	TGC AGA TAG ATA GCA G	CTG CTA TCT ATC TGC A	1
$(C_8F_{17}$-$(C_2H_4)_4$-TAMARA	ATT TGT GAT GTC CTG C	GCA GGA CAT CAC AAA T	4

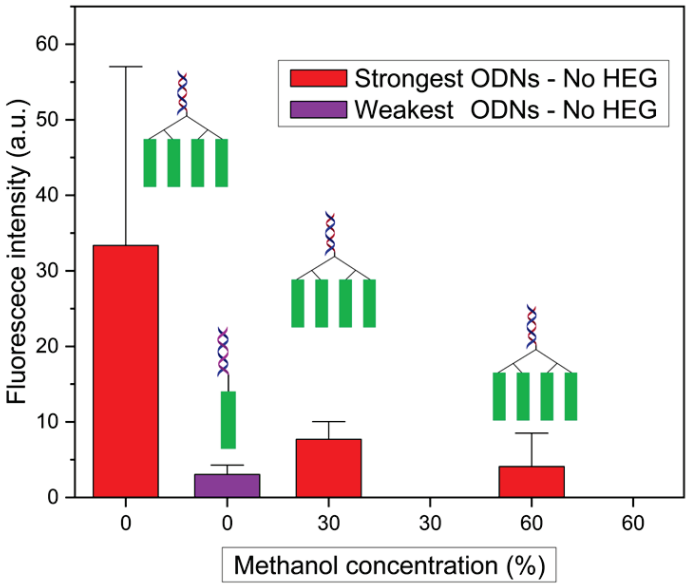

Figure 32: Shows the removal of mono-C_8F_{17} and tetra-C_8F_{17} fluorous-modified ODNs during multiplexing at various methanol concentrations. Complete removal of the weakest oligonucleotide (mono-C_8F_{17}) was witnessed at 60%. Data is expressed as mean ± SD of triplicate values.

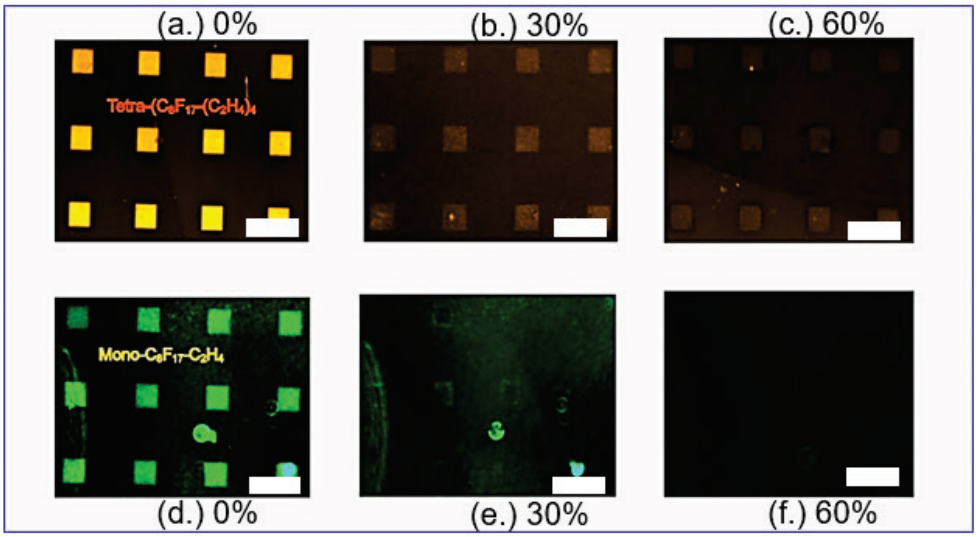

Figure 33: Fluorescent images showing the selective removal of hybridised ODNs on the fluorous-modified surface based on their strength using methanol wash. Oligonucleotide modified with TAMRA dye is depicted with a-c and has more strength of immobilisation. In comparison, the oligonucleotide conjugated with the Alexa Fluor 488 dye is depicted in Figure d-f and has less immobilisation stability or strength. Mag.= 20x; Scale bar = 50 µm

The four-branched oligonucleotides (mono-C_8F_{17}) and single-stranded oligonucleotides (tetra- C_8F_{17}) were simultaneously spotted on a fluorous-modified surface using the same technique described earlier.

Based on the results obtained, the average fluorescence intensity of the tetra-C_8F_{17}, the strongest fluorous-tagged oligonucleotide, was at least 5.69 times higher compared to the single fluorous-tagged oligonucleotide (mono-C_8F_{17}) before methanol treatment (Figure 32-Figure 33). This increase in fluorescence intensity was attributed to an increased oligonucleotide density per region when the two oligonucleotides were immobilised on the same fluorous modified surface during multiplexing, unlike when they were spotted individually.

This increase could also be attributed to the spectra overlap between the excited and emitted spectra of the two dyes, creating a cross-talk between detection channels. Specifically, the overlap between the excited spectra of the TAMRA dye attached to the strongest complementary ODN and the emitted spectra of the Alexa Fluor 488 dye attached to the weakest could be a contributing factor to the overall intensity.[428] We believe this overlap may have also contributed to the overall fluorescent intensity associated with the most effective ODNs. (Figure 34). This observation aligns with a previously reported protocol showing that the presence of fluorines influences the outcome of hybridisation. [429]

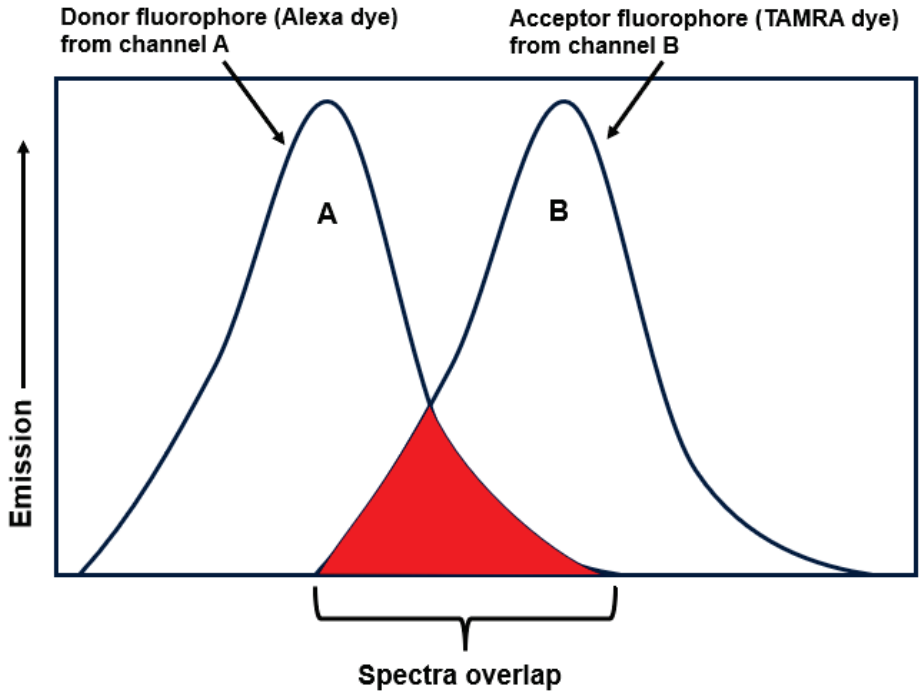

Figure 34: The schematics illustrate the excitation profile between two dyes (Alexa fluor and TAMRA), with a hypothetic overlap between the emitted spectra from the donor (Alexa dye) and the excited spectra from the acceptor (TAMRA dye).

From the previous experiment, it's important to note that the fluorescent intensity of the mono oligonucleotide is at least twice as high when it is hybridised alone compared to when it is hybridised during the multiplexing method. This observation suggests increased competition between the two dissimilar strands during the hybridisation stages when subjected to this protocol. The improved fluorescence intensity from the tetra ODNs can be attributed to a high number of fluorine atoms per carbon length compared to the mono-C_8F_{17} oligonucleotides. In addition, the number of branch systems introduced creates more per fluorination that favours the improved strength of immobilisation. Similarly, the overall fluorescence intensity of the tetra-C_8F_{17} oligonucleotides reduces slightly using the multiplexing approach compared to when it was hybridised alone, suggesting the presence of competition between the two fluorous-immobilised oligonucleotides during the immobilisation process.

It's also interesting to note that a 30% methanol wash was enough to strip the weaker mono-C_8F_{17} from the fluorous modified surface in the multiplex system while the branched oligonucleotides (tetra-C_8F_{17}7) remain hybridised, although with a significant loss of intensity. This affirms our interpretation of what influences the strength of the oligonucleotides using the fluorous effect. Consequently, a 60% methanol solution was enough to strip off completely the weakly bound oligonucleotide (mono-C_8F_{17}). In contrast, the strongly bound oligonucleotide remained on the surface of the patterned surface, although with a significant loss of fluorescence intensity. The reason behind this could be attributed to the strong fluorous-fluorous interaction between the fluorous-modified oligonucleotides and the stronger fluorescently labelled tetra-C_8F_{17}7 oligonucleotides compared to the mono-C_8F_{17} (Figure 33). Therefore, our research further establishes the influence of the fluorous effect in improving the binding strength of oligonucleotides of various shapes and lengths. It can easily control, immobilise, hybridise, and influence the selective removal of oligonucleotides from microarray surfaces with many similar or different fluorescently tagged oligonucleotides. This is particularly interesting in the microarray industry, where the cost, resources, specificity, and repeatability of experiments for various applications are a few of the key challenges hindering its success and miniaturisation. [430, 431] Our current protocol is simple, repeatable, and cost-effective. It could be tailored to address the issues associated with higher probe density and selective removal of hybridised duplex ODNs in microarray

platforms. This protocol also offers opportunities to develop miniaturised and adaptable detection technologies for prognosis, diagnosis, and monitoring. This protocol also offers opportunities to develop miniaturised and adaptable detection technologies for prognosis, diagnosis, and monitoring. [432, 433]

3.4 Conclusion

Microarray technology has evolved from a primary gene expression analysis platform to a highly advanced, efficient, personalised tool for various biomedical applications. However, despite this progress, problems such as specificity, sensitivity, reproducibility, signal interference, and complex designs continue to be persistent challenges that hinder its full potential and applicability. [434–437] We achieved this by using the fluorous effect to compare the length, fluorous content, branch system, and the introduction of a spacer (HEG-linker). Our findings show that hybridisation efficiency can be improved by increasing the perfluorination level, either by increasing the oligonucleotide length or by introducing a branch system. Our method also compared the relationship between the fluorine content and the branch system using mono-C_8F_{17} and tetra-C_8F_{17}, respectively. This research revealed that increasing the fluorine content creates stronger and stably hybridised oligonucleotides with high fluorescent intensity and overall hybridisation efficiency compared to using oligonucleotides with lesser fluorine contents or non-branched fluorous-modified oligonucleotides (with or without HEG-linker). Furthermore, a simple methanol wash was sufficient to strip and selectively remove the desired oligonucleotide from the duplex, depending on their strength and partition coefficient, without requiring multiple solvent washes or strict temperature control. Moreover, incorporating HEG-linkers in the RF_6 and the RF_8 probes enhanced the fluorescent intensity and hybridisation efficiency using the fluorous effect. This was evident in the methanol concentration needed to strip the oligonucleotides from the fluorous patterned surface. We assume this was possible due to the favourable thermodynamics of the interaction created by the fluorous effect in the presence of the linker, which facilitates accessibility between the fluorous modified oligonucleotides and the fluorescently labelled oligonucleotides. However, this works better for single and bis-oligonucleotides. Unlike the single oligonucleotide chain, incorporating a HEG linker in the tetra-C_8F_{17} branch system appears to reduce the fluorescent intensity and hybridisation

efficiency, which may be attributed to steric hindrance, the hydrophilicity of the incorporated HEG, or the generally unfavourable thermodynamics of the interactions with the branch system. Our assumption was supported by the fact that using the branch system alone (especially the tetra-C_8F_{17}) without the HEG-linker showed improved stability and required 60% methanol concentration to strip from the fluorous-modified surface. This was attributed to the absence of the linker to create an unfavourable interaction as the number of the branch sytem moved from -bis to the -tetra system.

While incorporating a branch system enhances the fluorescent intensity, it does not necessarily translate to improved hybridisation efficiency, as a low-concentration methanol wash can easily remove the tetra-branch system. Hence, incorporating a HEG linker in the branch system reduces the overall stability and hybridisation efficiency of the tetra-C_8F_{17}.

While our method is exploratory and qualitative, and currently focuses on 16-mer oligonucleotides, it remains repeatable—though there is some variability in the repeatability of the immobilised DNA. This variability could stem from several factors, such as the efficiency of individual spots on the array and the kinetics of the interactions. Overall, our approach is specific, sensitive, and cost-effective. However, using sophisticated tools (e.g., the SPR tool), additional quantitative experiments are recommended to understand better the binding mode and general kinetics of each oligonucleotide. In the future, we believe that the specific non-covalent interactions created by the fluorous effect will continue to deserve attention and further exploration. Therefore, incorporating fluorous tags can facilitate self-assembly and direct delivery, enhancing sensitivity for various applications.

3.5 Future Work

The recent research findings underscore the importance and effectiveness of the fluorous effect in designing and implementing microarrays. Although still in its early stages, this innovative method shows great promise for use in a wide range of biomedical applications where precise and reversible immobilisation is crucial for the self-assembly of molecules. Moreover, it is recommended to employ sensitive techniques, such as surface plasmon resonance or biolayer interferometry (BLI) tools, to monitor the real-time kinetic binding of the

oligonucleotides. Both surface plasmon resonance (SPR) and bio-layer interferometry (BLI) are powerful techniques for analysing binding kinetics, but they operate on different principles and have unique advantages and limitations. SPR is often preferred for its high sensitivity and detailed kinetic analysis, while BLI offers a more straightforward and cost-effective approach for real-time monitoring of molecular interactions. These approaches can offer improved detection, measurement, and quantification of the oligonucleotides with reference to the change in their binding kinetics. Furthermore, this method can be integrated with the polymerase chain reaction (PCR) technique to accurately quantify and identify the number and hybridised and unhybridised oligonucleotides. Other techniques can also be adapted to optimise this method for various applications.

Chapter 4

4.1 Reversible Immobilisation of Gold and Silver Nanoparticles on Engineered Surface

4.1.1 Results and Discussions

This section utilised the fluorous effect to reversibly immobilise MNPs (gold and silver) onto a micropatterned fluorous surface. By taking advantage of the fluorous effect, the MNPs were efficiently and effectively anchored to the surface, allowing for precise control and manipulation in subsequent experimental procedures. This method demonstrated the fluorous surface's versatility in accommodating diverse nanoparticles and showcased the potential for tailored surface modifications for specific applications. The reversible immobilisation of MNPs opens avenues for further exploration in nanotechnology and surface science, offering promising prospects for advanced material design and manipulation.

4.1.2 Immobilisation of Gold Nanoparticles on Modified Surface

Initially, a proof-of-concept immobilisation procedure was developed to deposit fluorous-functionalised citrate-coated gold NPs on a micro-patterned surface. The motivation was to use the fluorous effect to create a simple method capable of reversible attachment of functionalised 20 nm gold nanoparticles for reconfigurable metasurface. Our previous research reported the functionalisation of 20 nm gold nanoparticles in a water-based environment using perfluorodecanethiol (PFDT). This method was simple and repeatable and can be explored to immobilise gold or silver nanoparticles on fluorous-modified surfaces to the nanoscale level. [438]

With this method, we attempted the initial immobilisation of thiol-modified, citrate-coated 20 nm gold nanoparticles on a lithographically (50 μm) patterned fluorinated surface using the fluorous effect. The results obtained from this method are specific and repeatable but not reversible due to the initial challenge of using a two-step approach involving water-based thiol-functionalisation of gold nanoparticles using a 10-carbon perfluorodecanethiol (PFDT) and the attachment of the functionalised gold nanoparticles on the fluorous-patterned surface (Figure

35). The idea was to take advantage of the non-covalent interaction between the perfluorinated alkyl chain and the fluorous-modified metasurface in creating specific interactions using the fluorous effect.

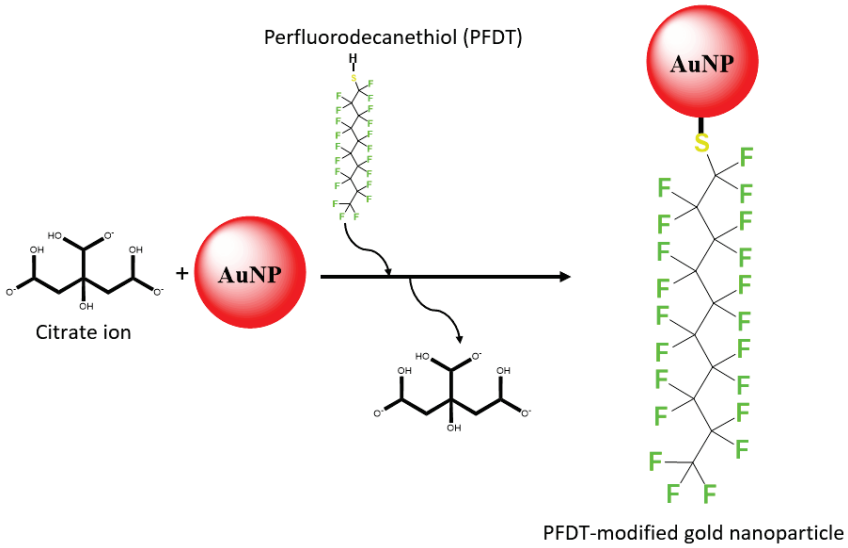

Figure 35: Schematics illustrating the ligand exchange between citrate-coated gold nanoparticles and perfluorodecanethiol (PFDT) before and after functionalisation. Initially, the citrate-coated gold nanoparticles are replaced by thiol-coated perfluorodecanethiol, forming a thiol-sulphur covalent bond.

Upon functionalisation, the LSPR peak change of the 20 nm gold nanoparticles was evaluated using UV-visible spectroscopy (Figure 36). The results revealed a peak absorption shift from 523.5 nm to 520.5 nm after modification with perfluorodecanethiol, resulting in a 3 nm blue-shifted absorption maximum. There was also a slight widening of the peak after the thiolation without a corresponding visible change in the colour of the gold nanoparticles. This may be attributed to the transient change during the interaction of the gold nanoparticles with the sulphur atoms attached to the fluorine-rich perfluorodecanethiol. These shifts also align with previous predictions due to the electron-withdrawing properties of fluorine atoms attached to the carbon chains of the perfluorodecanethiol. [439-441]

The stability of the gold nanoparticles is crucial before and after the ligand exchange protocol. Therefore, the analysis of the surface charge of the nanoparticles using the zeta potential showed a negative charge distribution (-25 mV±10 mV) (Figure 37) along the plane of the nanoparticles attributed to the presence of a negatively charged citrate layer before ligand exchange. This value is similar to the ZP for bare gold nanoparticles reported in the literature. [442] In the same context, the zeta potential of the functionalised gold nanoparticles increases upon ligand exchange and simultaneous conjugation of

perfluorodecanethiol (PFDT) in a simple water-based environment (-39.60 mV ±14.8 mV) (Figure 37). PFDT is, itself, a net zero-charged molecule but with high perfluorination. Due to this high fluorine content and an unusually high hydrophobicity, the van der Waals interactions are created with an overall negative charge. In this case, a high deviation of the zeta potential is attributed to the measurement capacity of the Malvern instrument using the M3-PALS (mixed-mode measurement) method. [443]

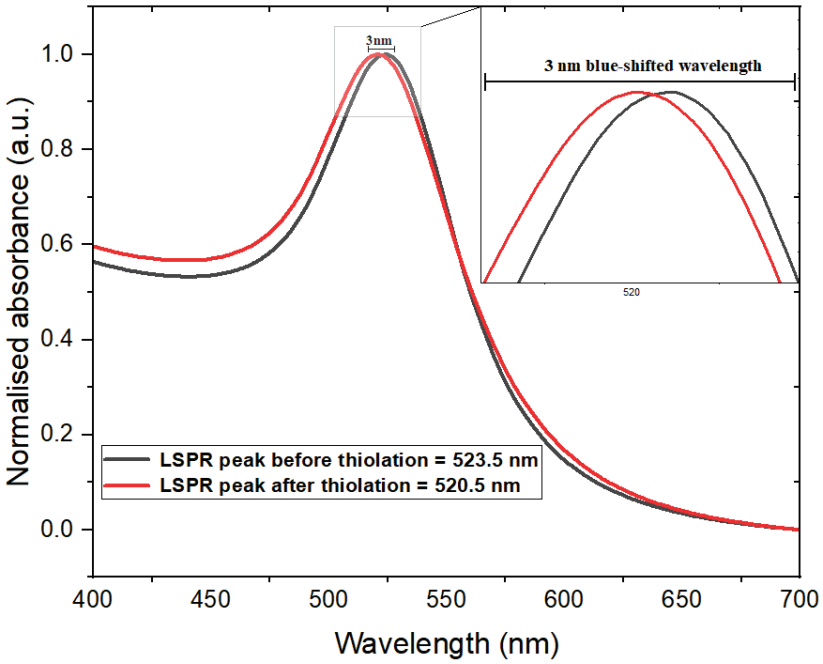

Figure 36: UV-vis spectra of the 20 nm gold nanoparticles showing the absorption maxima at 520.5 nm and 523.5 nm before and after modification with perfluorodecanethiol (PFDT). The graph was plotted without fitting.

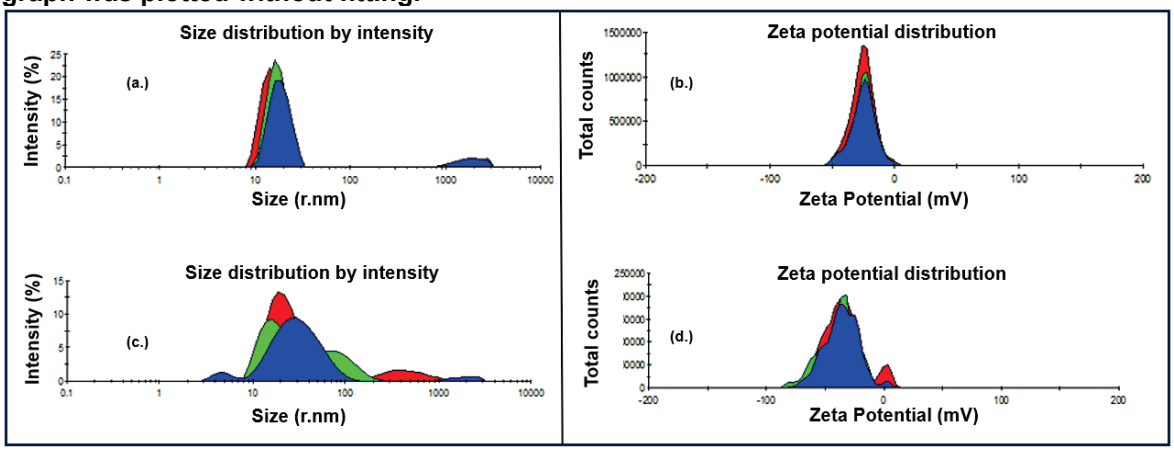

Figure 37: DLS and Zeta size measurement of 20 nm gold nanoparticles before (a and b) and after thiolation (c and d). The hydrodynamic size shows the distribution of the NPs in the colloidal system. In (a.), the size distribution was narrow before the colloidal system was concentrated, decanted and functionalised with the PFDT.(b.)The Zeta potential appeared more stable due to the sufficient stability of the colloidal system by the citrate layer. (c.)The hydrodynamic size distribution of the colloidal gold nanoparticles becomes broader during the transient conjugation stage without any corresponding visible colour change or aggregation. (d.) The zeta potential showed improved stability after functionalisation with PFDT.

4.1.3 Binding Mode of Citrate with Gold Nanoparticles

As explained in the previous chapter of this report, efficient ligand exchange and functionalisation are essential to ensure good molecules self-assembling on patterned surfaces. It is vital to delve into the brief details of the citrate-coated gold nanoparticles and how the presence and arrangement of citrate ions on the surface can influence ligand exchange.

Citrate-coated gold nanoparticles are stabilised by the negatively charged citrate anions, which serve as reducing and stabilising agents to prevent unwanted aggregation by enabling a favourable distance between adjacent ions by repulsive forces. To functionalise the gold nanoparticles, the citrate layers are usually removed mostly by different rounds of centrifugation and eventually re-dispersed in a preferred solvent, mostly distilled water. Similarly, several functionalisation techniques can be used to displace the citrate ion and conjugate it with gold nanoparticles. The scope of this write-up will be limited to thiol functionalisation and the displacement of the citrate anions only.

Recent research has shown that thiol plays a crucial role in displacing citrate anion to form a covalently bonded Au-S. [444–446] This result was expected, as the energy of association between gold and sulphur is about 40 kcal/mol, compared to 2 kcal/mol for Au-Citrate. [447, 448] This finding underscores the significance of our research in understanding the complex processes involved in the synthesis and modification of citrate-stabilised gold nanoparticles. The intermediates produced during the synthesis of citrate-stabilised gold nanoparticles using the Turkevich method are reported to hinder effective functionalisation. The trisodium citrate dihydrate, which serves as the reducing and the stabilising agent, is initially oxidised to produce unstable acid dicarboxy acetone, which, in the presence of more tetra chloroauric acid gold chloride, is further oxidised to form acetoacetate [449] In addition to this, the acetoacetate produced can be further oxidised to form acetone and acetate [450–454] This interference creates obstacles that prevent the accessibility and conjugation of thiol to the surface of gold nanoparticles, even at higher-than-normal thiol concentrations. These obstacles are caused by steric and chelating hindrances that hinder the desorption and availability of the surface to other ions. As a result, it has been observed that thiol co-adsorption with other molecules in the reaction mixture is the norm rather

than direct conjugation of thiol to the surface of the gold nanoparticles. This was confirmed using various molecular spectroscopy techniques to monitor the different stages of functionalisation, rather than using ordinary UV-vis spectroscopy that only checks changes in particle aggregation, which could be due to changes in the inter-particle distance among several particles in the reaction mixture. [455]

Various modes of citrate binding to AuNPs have been proposed and discussed. At a neutral pH, the surface of gold nanoparticles is surrounded by monodentate citrate, with only a *syn* conformation. This means that the monosodium citrate is adsorbed in a bridge pattern that enables interaction with each other to produce a dangling citrate. For example, preabsorbed citrate anions are not readily displaced using alkyl or arylthiols during functionalisation, and the hydrogen-bonded dihydrogen citrate species and the thiols are coadsorbed instead of via ligand exchange. Additionally, it was reported that the ligand exchange does not readily occur between the citrate anion and the thiol, but acetoacetate, which is an oxidative product of the citrate. [456] It was also reported that using 1H-NMR and ATR-FTIR data, the spectrum of a synthesised solution of gold nanoparticles after synthesis was broader and less intense compared to pure sodium citrate since they are adsorbed to the surface. Hence, as the concentration of the monodentate-bound citrate species is reduced during functionalisation, the conformation (of the citrate) creates a more tightly bound dicarboxylate bridging form that favours co-adsorption. [457]

However, under alkaline conditions, the solution becomes less protonated, and the monodentate citrate ion is converted to tri-sodium citrate (TSC), which can undergo tetradentate coordination when bound to the hydroxyl and carboxyl groups on the surface. Thus, when synthesising gold nanoparticles (AuNPs) using citrate, binding citrate ions to the gold surface plays a vital role in reducing and stabilising the nanoparticles, influencing their properties. Specifically, gold nanoparticles have different crystal facets (Au (100), Au (111), and Au (110)) whose properties affect the properties and the shape of the nanoparticles upon interactions with citrate (with multiple functional groups). The binding of the citrate is most favoured to the Au (111) facet due to their low surface energy requirement, most stable configuration with a well-ordered layer exhibiting $(4 \times 2\sqrt{3})$ symmetry on Au (111) between citrate and the Au atoms compared to the Au (110) and Au (100) with less optimal geometry. This binding conformation

between citrate ions and gold atoms prevents aggregation and promotes the growth of spherical nanoparticles, which are commonly observed in citrate-stabilized AuNP syntheses. [458–460] This phenomenon has been confirmed using thermogravimetric analysis (TGA) of dried AuNPs. [461] Hence, the increase in pH from a nearly neutral state to an alkaline state creates a repulsive interaction between the tetradentate coordination of the citrate layer.

During the centrifugation and re-dispersion of gold nanoparticles in solution, ionic strength or pH alterations typically occur. These changes can affect citrate availability on the surface of the gold nanoparticles before or during thiol functionalisation. In this research, 20 nm gold nanoparticles were functionalised, resulting in a 3 nm blue shift in the absorption maximum after ligand exchange. This shift was attributed to the combined effects of the surface properties of the gold nanoparticles during ligand exchange and the electron-withdrawing characteristics of the fluorine atoms incorporated in perfluorodecanethiol. [462–466] Further insight was also given from a similar experiment using gold nanoparticles synthesised with the Turkevich method. It was observed that the coordination state of citrate around the gold nanoparticles depended on the protonation state of the citrate, with the lower pH (less than 6.8) preferred for bidentate bridge coordination with the central carboxylate being dominant compared to the terminal carboxylates bound to the gold nanoparticles at higher pH (more than 6.8). Surprisingly, only a chloride-rich solution was shown to favour monodentate binding. While these interactions are pH-dependent, it is also important to note that this coordination is susceptible to the ageing and microenvironment of the synthesised colloids. [467]

4.1.4 Attachment of Functionalised 20 nm Gold Nanoparticles

In the earlier part of this chapter, we discussed how 20 nm gold nanoparticles were functionalised with PFDT. This section explores the use of the fluorous effect to promote the self-assembly of these thiol-coated gold nanoparticles. To achieve this, we employed three different approaches, continuously fine-tuning our methods to reach the goals of this research.

4.1.4.1 Drop-Cast/Evaporation-Induced Method

4.1.4.1.1 Scanning Electron Microscopy of Immobilised Gold Nanoparticles

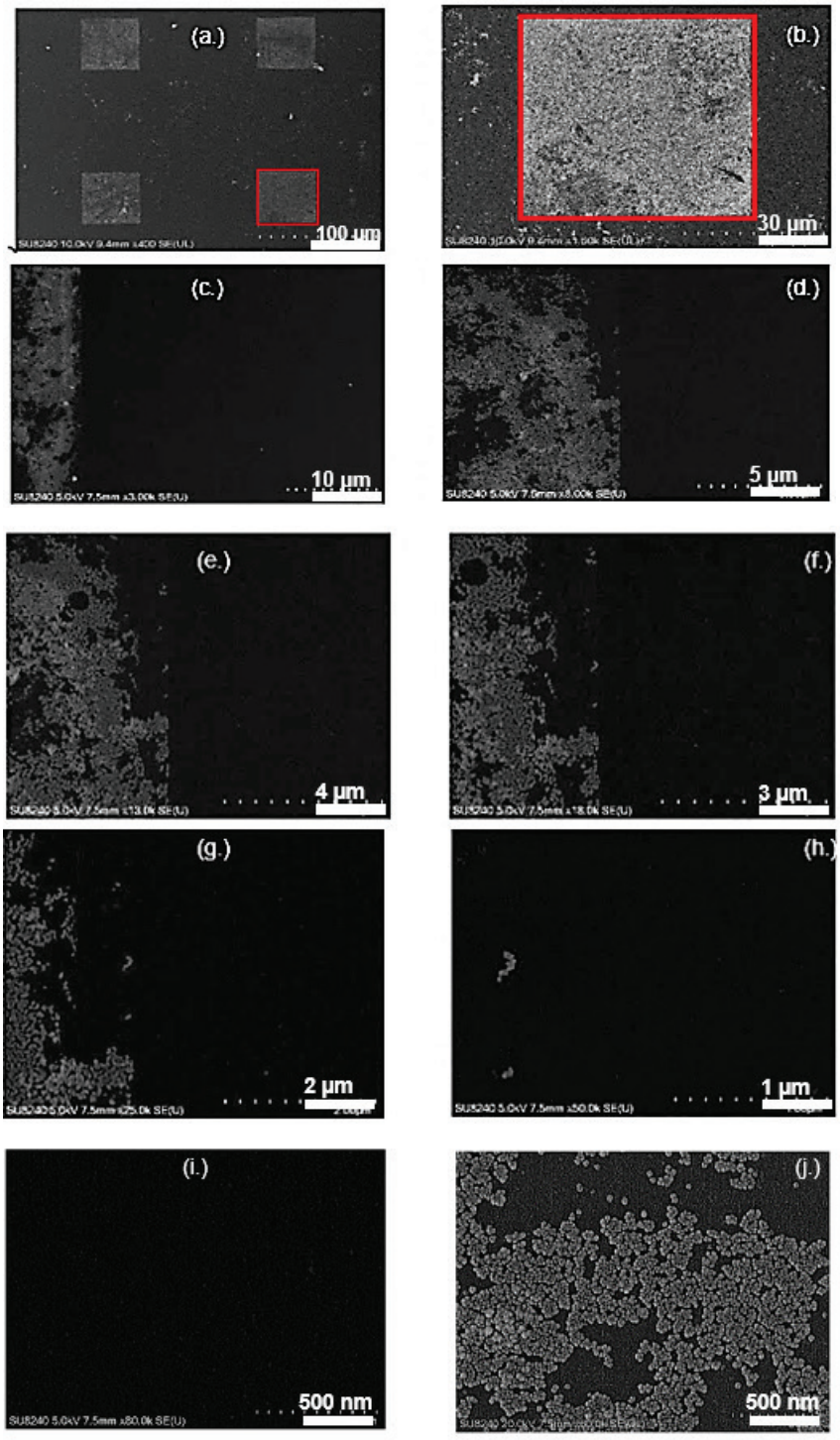

Figure 38: This micrograph from a scanning electron microscope shows gold nanoparticles attached to a fluorous modified surface. Fluorous region in red square. Image (a.) shows the initial immobilisation of PFDT-coated gold nanoparticles on the fluorous patterned layer (four squares), showing distinct fluorous from the non-fluorous layer. Image (b.) shows the enlarged view of one of the squares immobilised with PFDT-coated gold nanoparticles. Image (c-h) shows the clear non-fluorous region separated from the fluorous region at different magnifications, indicating the absence of gold nanoparticles in the non-fluorous region as it is zoomed towards the fluorous-modified region. Images (i. and j.) depict the non-fluorous region (i.) at 500 nm magnification and the fluorous region with immobilised gold nanoparticles (j.) at the same magnification.

The first method involves drop-casting the thiol-functionalised gold nanoparticles on the fluorous modified surface (Figure 39).

In this method, using 30 uL thiol-modified gold nanoparticles on the fluorous-modified was enough to attach the gold nanoparticles within 10-30 minutes. The results obtained using the SEM (Figure 38) showed that directed immobilisation of the NPs can be achieved using the fluorous effect. This created our first proof-of-concept design, where functionalised 20 nm gold nanoparticles can be immobilised on a micro-patterned surface. Many protocols have been developed to attach nanoparticles from colloidal suspension on a solid support. However, the unwanted drying of dissolved particles from a colloidal suspension is one of the major challenges in attaching these nanoparticles to a glass substrate, creating a phenomenon known as the 'coffee ring' effect. The coffee ring effect is frequently observed when a liquid or colloidal solution containing suspended particles evaporates, leaving behind a circular or ring-like deposit on a surface along the perimeter of the drop. This property is attributed to the interactions between gravity, viscourse force and surface tension. [468] The mechanism behind this occurs due to the pinning of the contact line of the droplets as the droplets evaporate, creating an outward flow of the solute from the centre to the edge of the pinned line. This creates concentrated and accumulated nanoparticles along the perimeter of the semi-spherical shape of the droplets after the completed evaporation. [469] In addition, the surface energy, size of the droplets, dispersed or aggregated state of the colloidal system [470] and wettability (hydrophobicity or hydrophilicity) of the surface play essential roles in determining the pattern of the coffee ring, if at all. [471] This effect is significant in various scientific and industrial applications, including inkjet printing, coating processes, diagnostics, and nanoparticle self-assembly. Several methods have also been put forward to reduce or prevent this coffee-ring challenge, including surface acoustic waves (SAWs) [472], using a hydrophobic surface with low contact angle hysteresis, induced oscillations of the contact line or electrowetting. [473–477] Therefore, it is essential to develop a surface-engineered platform that can effectively address various challenges, such as the coffee ring effect, to attach nanoparticles needed for different sensing capabilities and assays. Their sensitivities and specific interactions with other biomolecules are particularly of great interest for colourimetric assays.[478]

Hence, using the fluorous effect, the coffee ring process is minimal or absent from the engineered fluorous patterned region after the attachments and analysis using the SEM with a distinct fluorous region compared to the non-fluorous regions. [479, 480]

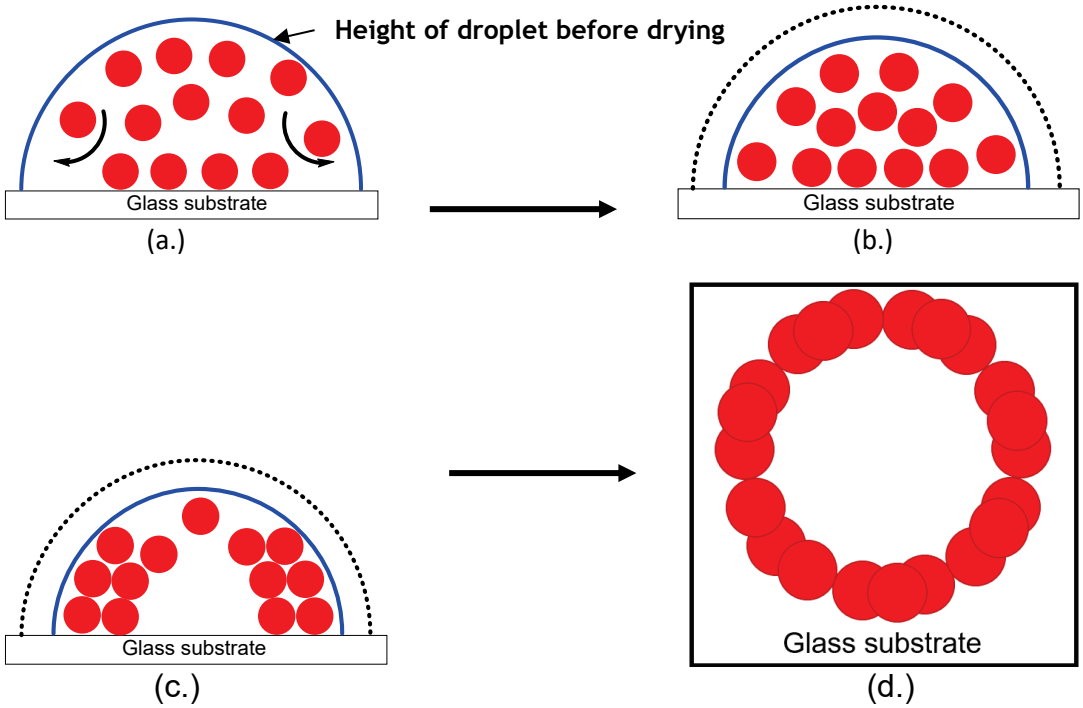

Figure 39: Schematics depicting the coffee ring effect before and after drying of nanoparticles on the flat metallic surface using gold nanoparticles. (a.) Depicts the initial deposition of gold colloids at room temperature. The black arrow shows the direction of movement of NPs during evaporation. This creates a drying effect that is easily visible at the edge of the drying liquid. (b. and c.) . (d.) The aerial view of a coffee ring formed during surface immobilisation. This is the final stage when the NPs dried on the glass surface, where the interparticle distance is lost, and the NPs stick to each other along the edge of the dried droplet. Hence, preventing this common challenge was central to each protocol developed for this research.

4.1.4.2 Cover Slip Method

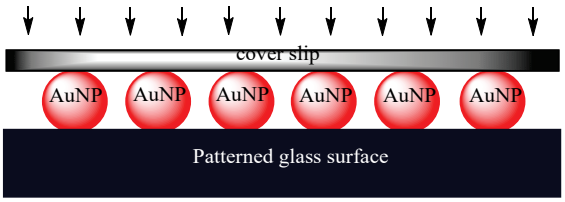

Figure 40: Schematics illustrating the control of evaporation using the coverslip method. In this method, placing a coverslip on the surface of the liquid helps to slow down unwanted evaporation. The sample was allowed to immobilise within 15 hrs and rinsed with distilled water to prevent visible drying before surface characterisation.

To overcome the challenge in the previous method, where direct exposure to the atmosphere interfered with the droplet volume on the modified surface at room temperature during the immobilisation stage, leading to unwanted evaporation (Figure 39), a coverslip was used as a protective layer to control the evaporation rate using the already thiol-functionalised gold nanoparticles (Figure 40). This method creates an improved attachment on the surface that can distinguish between the fluorous modified surface and the bare glass surface. This was possible due to the controlled evaporation rate in the presence of the coverslip for 15 hrs.

4.1.4.2.1 Atomic Force Microscopy (AFM)

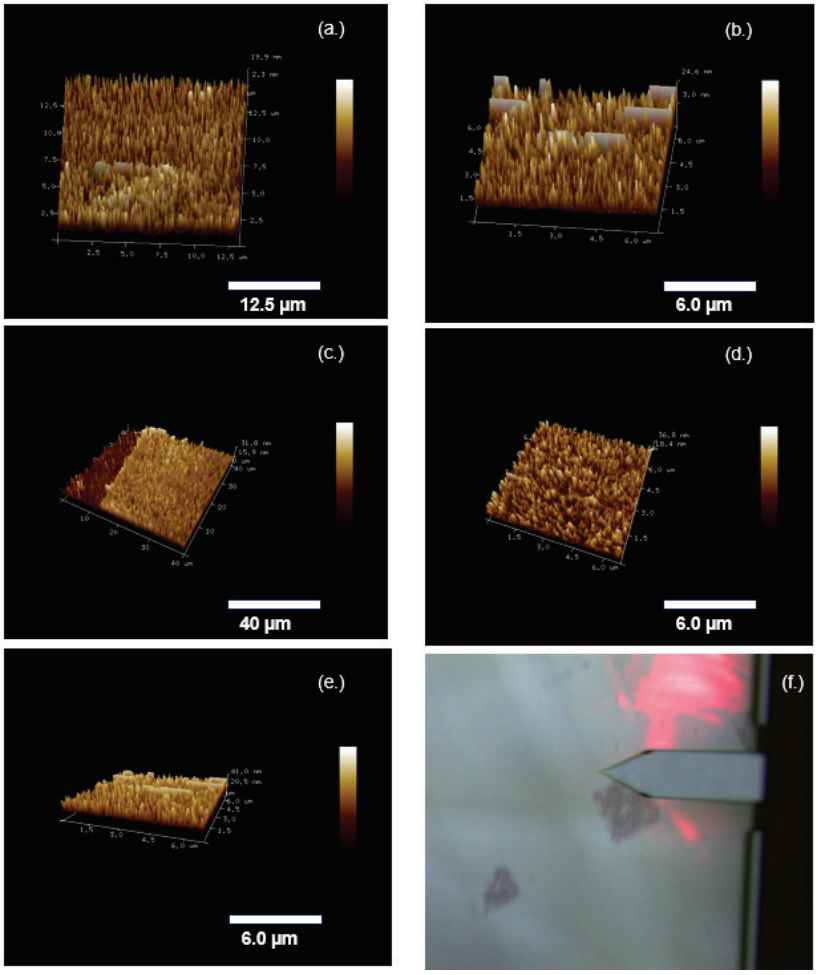

Figure 41: AFM images across five sample areas showing the attached gold nanoparticles using the coverslip methods. Each image represents a different region of the immobilised gold nanoparticles on the patterned surface. Image (a.) This was imaged on a 12.5 µm-sized region with a total nanoparticle height of 19.9 nm (b.) The image was taken across a 6 µm length with a total height of 24.6 nm (c.) The image was taken across a 40 µm length of the sample surface spanning the fluorous and the non-fluorous region with a total height of 31.8 nm (d.) This region was imaged across 6 µm length with a height of 18.4 and a total height of 36.8 nm. (e.) This region was imaged at 6 µm with a total height of 20 nm and 41 nm. The total height may be attributed to artefacts, aggregated sample region or any other unwanted contaminants on the immobilised sample (f.) Photographic evidence from the AFM video during scanning of the surface. The average sub-height and total height recorded from the images were 12.02 ± 8.71 nm and 30.82 ± 8.64 nm, respectively. Images were processed using the Nanoscope software. Scale bar = various.

One of the drawbacks of using the SEM is the tendency to damage the sample during processing, especially sputtering. Characterisation using the AFM affords us additional opportunities for further surface characterisation. The surface topography revealed that the gold nanoparticles are tightly packed and can be self-directed by controlling the evaporation stage. Although this method is still prone to unwanted aggregation (better than evaporation-induced), it further affirms our hypothesis that the functionalised gold nanoparticles can be self-directed on the fluorous patterned surface. Specifically, scanning along the different fluorous patterned regions of the immobilised gold nanoparticles, the height of the immobilised gold nanoparticles was revealed to range from 19.9 nm – 41(Figure 41). In addition, the C_{sp^3}–C_{sp^3} bond length is estimated to be equivalent to 1.76 nm for a 10-carbon perfluorodecanethiol. [481, 482] Immobilisation of the functionalised gold nanoparticles with an average peak size of 20.5 nm is equivalent to 22.26 nm. This value falls within the ones obtained from AFM and strongly suggests the attachment of 20 nm gold nanoparticles on the fluorous modified surface. To gain a deeper understanding of the nanoparticles, it is crucial to conduct further characterisation. Techniques such as X-ray Photoelectron Spectroscopy (XPS) and Surface Plasmon Resonance (SPR) will provide valuable insights into the elemental composition of the nanoparticles as well as the nature of their binding interactions. Utilising these methods will allow for a comprehensive analysis of how the nanoparticles interact at the molecular level, enhancing our overall knowledge of their properties and potential applications.

4.1.4.3 Attachment of Gold Nanoparticles using Hexane-Ethanol Mixture (48 hrs)

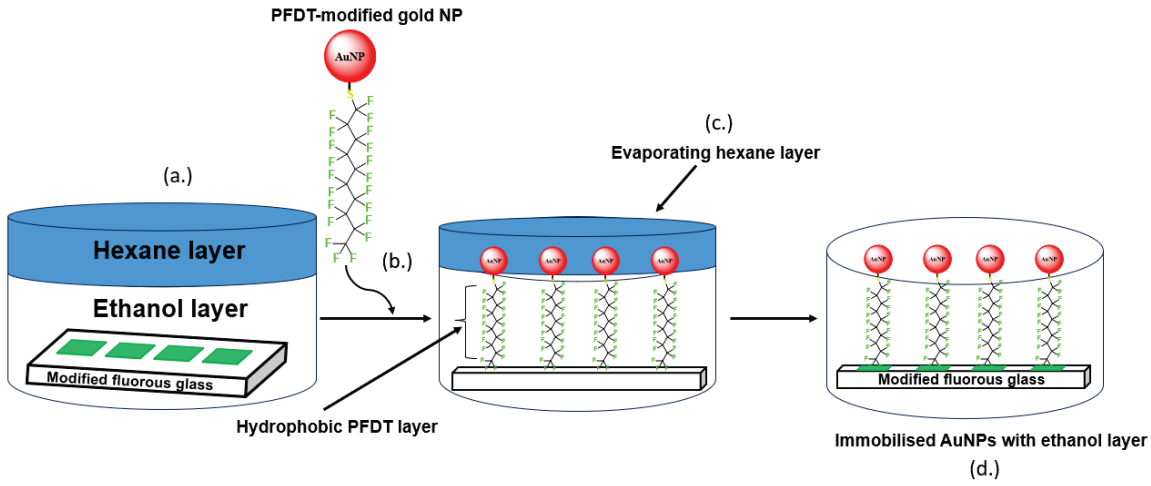

Figure 42: Schematics illustrating the attachment of gold nanoparticles in hexane: ethanol mixture. (a.) Fluorous-modified glass substrate (green squares) is immersed in a hexane-ethanol mixture. (b.) PFDT-modified gold nanoparticles are introduced into the mixture and allowed to stand for 48 hrs. (c.) This enables the hexane to evaporate and simultaneously allows the fluorous effect between the surface and the PFDT on the modified glass surface. (d.) After 48 hrs, the glass substrate is removed from the solution, allowed to dry and imaged using AFM (Figure 44) and SEM (Figure 45).

Nanoparticles can spontaneously assemble to form 2D or 3D structures tailored for various applications. However, traditional methods of achieving this are limited. They require a hydrophobic and efficient ligand exchange to functionalise the nanoparticles, making them less efficient. [483] An alternative approach to this challenge is using an air/solvent interface between two liquids. [484] Exploring the low surface tension of the nanoparticles, they can be attracted to the hydrophobic fluorous layer while simultaneously trapped between the air/solvent interface (Figure 42). This method also allows for controlled evaporations and gold nanoparticles in place. Immersing the fluorous modified layer in 0.5 mM gold nanoparticles in a mixture containing hexane-ethanol mixture (1:2) for 48 hours was enough to encourage the formation of a self-assembled layer (Figure 43). In this method, the tendency of the NPs to segregate into interfaces was due to their ability to overcome the thermodynamic and kinetic barriers created by the constant negative free Gibbs energy. [485–487] This Gibbs free energy was tuned by creating hydrophobic support to the fluorous layer. In addition, the phase separation using ethanol and hexane mixture ensures favourable interaction between the PFDT chain and the hydrophobic layer. At the same time, the gold nanoparticles surface is suspended at the interface of the mixture. Unlike the

Langmuir method for SAM, which requires the transfer of the monolayer from the air-water interface onto the substrate, this method can potentially attach self-assembled nanoparticles directly on the modified surface without transferring the SAM formed from the air-solution interface to another solid layer. [488] However, there is a tendency for nanoparticle aggregation, especially when hexane in the mixture evaporates. Apart from this, the total coverage was still poor [57, 58] and the safety concerns of using hexane [491] as the solvent rendered this method unsuitable for this research compared to the coverslip method.

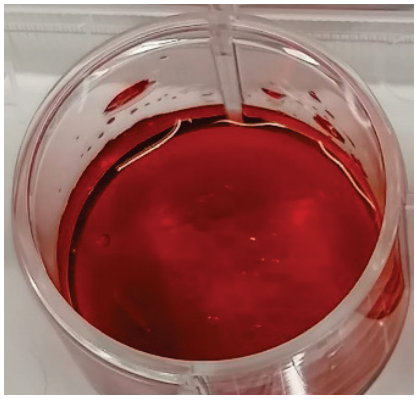

Figure 43: The image depicts the fluorous-modified glass substrate immersed in a hexane-ethanol mixture during the immobilisation of thiol-modified AuNPs.

4.1.4.3.1 Atomic Force Microscopy

Surface coverage examination across and around the edge of the sample with immobilised gold nanoparticles was measured using Atomic Force Microscopy (AFM). The result revealed nanoparticle heights of 15.4 nm, 28.1 nm, 33.0 nm, and 37.5 nm, with sub-heights ranging from 7.7 nm to 18.7 nm, respectively (Figure 44). These measurements indicate that gold nanoparticles within the 20 nm range are attached and likely present, particularly when estimated from the sub-heights across all the samples analysed. However, sizes above 30 nm were also found. We attributed this to unwanted aggregation due to evaporation during processing.

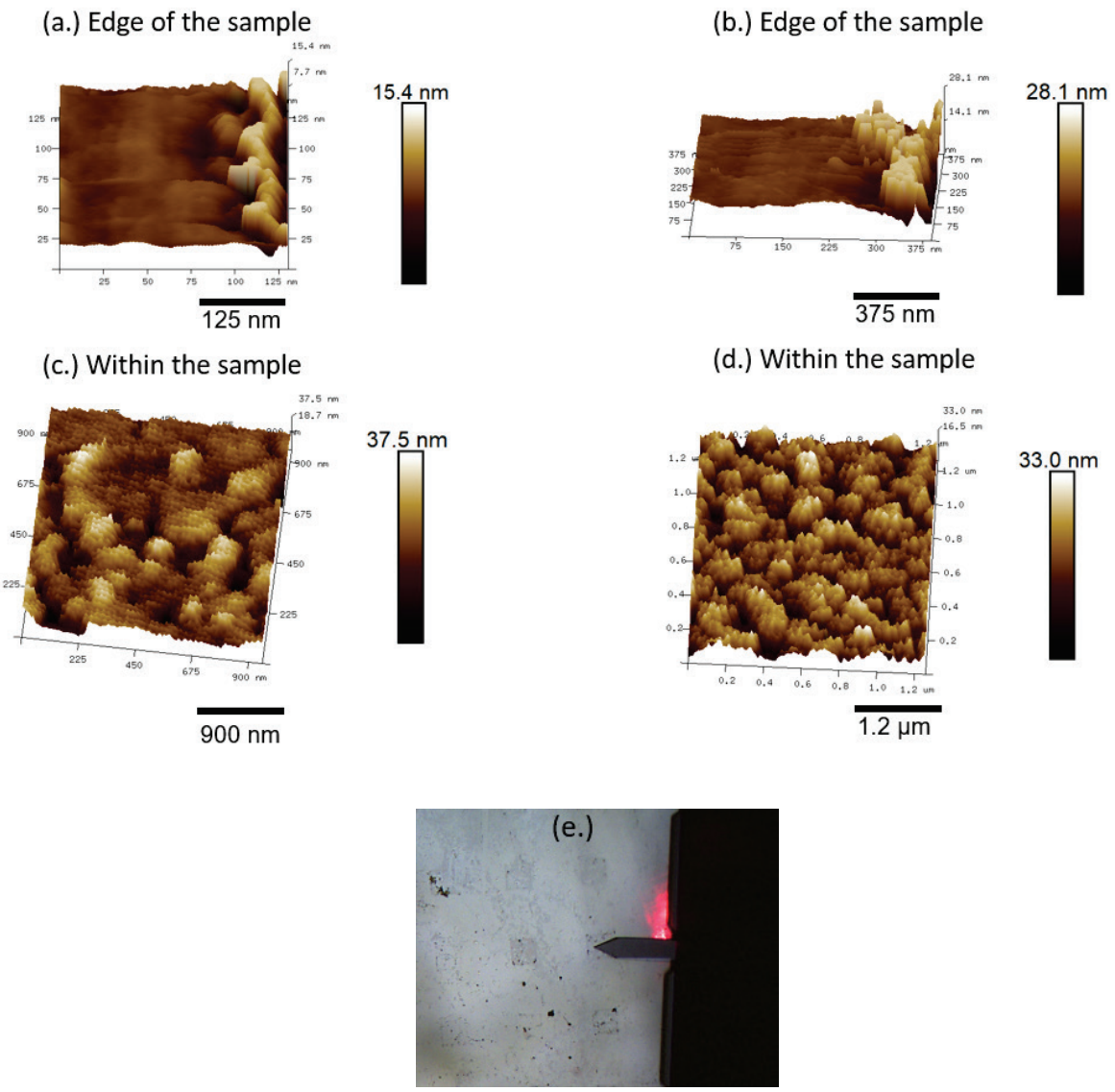

Figure 44: AFM images across four sample areas showing the attached gold nanoparticles using hexane-ethanol immersion for 48 hrs. Each image represents a different region of the immobilised gold nanoparticles on the patterned surface. Image (a.) This was imaged on a 125 nm-sized region spanning the fluorous and the non-fluorous region with a total nanoparticle height of 15.4 nm (b.) The image was taken across a 375 nm length spanning the fluorous and the non-fluorous region with a total height of 28.1 nm (c.) The image was taken within a 900 nm length of the sample surface with a sub-height of 18.7 nm and a total height of 37.5 nm (d.) This region was imaged within 1.2 µm length with a sub-height of 16.5 nm and a total height of 33 nm. (e.) Photographic evidence from the AFM video during scanning of the surface. The average sub-height and total height recorded from the images were 14.18 ± 4.89 nm and 28.50 ± 9.54 nm, respectively. Images were processed using the Nanoscope software. Scale bar = various.

4.1.4.3.2 Surface characterisation using the SEM from (hexane-ethanol)

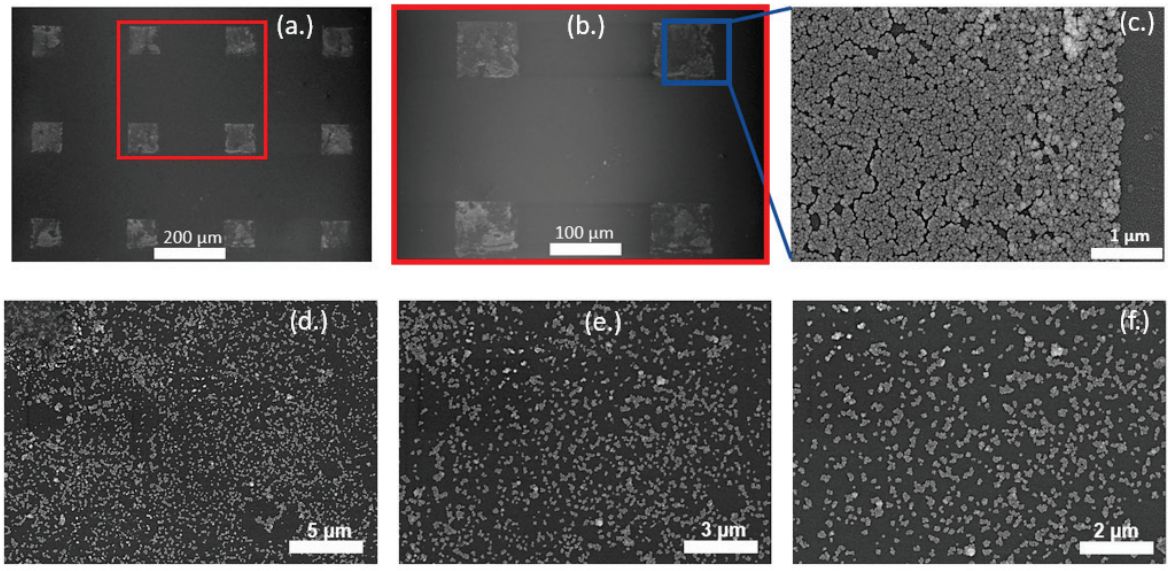

Figure 45: The SEM micrograph shows gold nanoparticles attached to distinct fluorous and non-fluorous layers. Using the Hexane-ethanol method, figure (a) displays the immobilised gold nanoparticles on the fluorous-patterned surface, with 12 squares showing distinct fluorous and non-fluorous regions. Micrograph image (b) shows an inset from (a). Image (c) was captured at 1 µm to highlight the fluorous region from the non-fluorous regions. Samples were also imaged at (d) 5 µm, (e) 3 µm, and (f) 2 µm. Various scale bars.

The surface characteristics of the immobilised gold nanoparticles were performed using SEM. Details from the micrographs revealed the presence of attached gold nanoparticles across the surface, with a distinct fluorous layer from the non-fluorous background. Like previous proof-of-concept methods using the fluorous effect, a uniform layer of fluorous-modified gold nanoparticles can be achieved using this phase separation method. This further suggests that incorporating this method with fluorous effect could direct the immobilisation of gold nanoparticles onto fluorous patterned areas (Figure 45). However, this was not the case compared to the topographical SEM image pattern analysed on bare, non-functionalised glass (Figure 46), which showed the distribution pattern of the unmodified nanoparticles on bare glass surfaces with characteristic closed-packed random interactions among the nanoparticles. This was also attributed to the inability of the unmodified nanoparticles to form any association or bonds with the non-fluorous bare environment. Hence, they form chains of protective layers to favour only fluorinated interactions. However, the tendency to aggregate continues to emerge as one of the significant challenges that requires further optimisation.

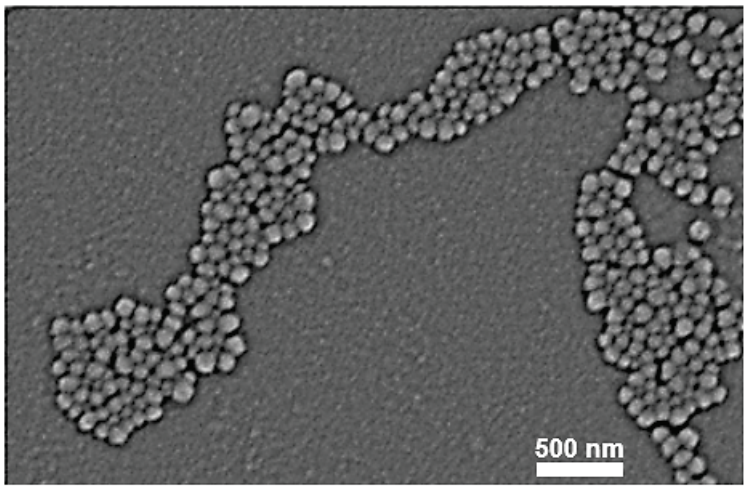

Figure 46: SEM micrograph of dry non-functionalised gold nanoparticles on bare glass surface. The characteristic chain formation was evident after drying on this bare surface.

To satisfy our curiosity in this research on the possibility of fluorinated gold nanoparticles to form a self-assembly monolayer on the lithographically designed fluorinated layer, Atomic Force Microscopy (Bruker instrument, tapping mode) was used to capture the height and 3D images of the resulting surface obtained via the evaporation-induced (without coverslip) using OTESPA 3 probe at the James Watt Nanofabrication Centre (JWNC). Even though the processed image showed promising applications, unwanted aggregation created due to the coffee ring effect appears to create a mix of monolayers and multilayers due to unwanted aggregations on different regions of the patterned surface during processing. To solve this unintended consequence, the cover slip method enabled even distribution of the solution on the surface. The result obtained from this method using AFM revealed that a self-assembly monolayer of functionalised gold nanoparticles on the patterned surface can be achieved with improved coverage and reduced aggregations (Figure 40 and Figure 44). However, a trade-off between the coverage and the colour intensity obtained from the immobilised gold nanoparticles must be balanced accordingly. Due to this, the intensity or colouration of the immobilised layer appears brighter from the surface obtained using the evaporation-induced method than other methods. Therefore, the number of nanoparticles attached is directly proportional to the air exposure level and the concentration of nanoparticles per mL. This technique of immobilisation using thiol-conjugated gold nanoparticles is consistent with what has been described in existing literature. [492–496]

4.1.5 Preliminary Findings

1. This study revealed for the first time that thiolated gold nanoparticles can be assembled on lithographically patterned surfaces using the fluorous effect.
2. Various characterisation techniques, including SEM, AFM, and Zetasizer analysis, revealed that the thiolated gold nanoparticles with hydrophobic f-alkyl chains exhibited height behaviour similar to that of a monolayer.

Despite the repeatability of these methods, a significant limitation arises from the tendency of the colloidal suspension to form unwanted aggregates, primarily due to evaporation. To address this issue, the objectives of this research included further optimising the immobilisation of gold and silver nanoparticles in solution using a reversible "one-pot" immobilisation approach.

The methods were varied to ensure the following:

a. Ligand exchange occurs between the gold or silver nanoparticles and PFDT.

b. Simultaneous immobilisation and self-assembly of the gold or silver nanoparticles on the fluorous-modified micro-patterned surface take place through a three-step approach that includes fabrication, silanisation, and reversible self-assembly of metal nanoparticles (MNPs). These methods were also tested for other pattern sizes below 50 µm (see Appendix 2).

4.1.6 Reversible Attachments of 15 nm Gold Nanoparticles using the Fluorous Effect

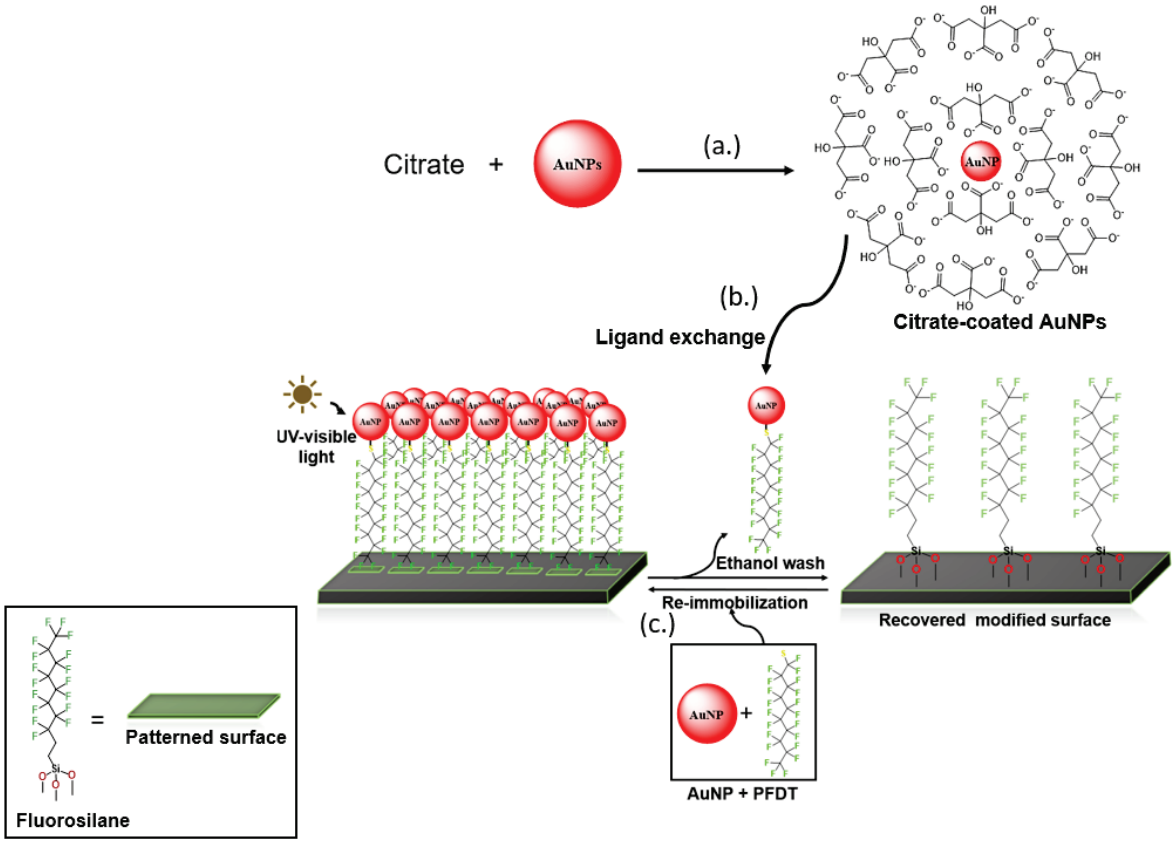

Figure 47: Shows a schematic representation of the reversible immobilisation of gold nanoparticles on fluorous-modified surfaces. In (a.), the gold Nps is coated with sodium citrate to confer electrostatic stability to the NPs in the colloidal system. (b.) Ligand exchange occurs between the citrate layer and the sulphur, creating a gold-sulphur bond via covalent interaction. This critical step creates thiol-functionalised gold NPs for onward immobilisation on the fluorous-patterned surface. (c.) Re-immobilisation of the functionalised AuNPs after incubating the patterned surface in the colloidal mixture of the PFDT and the AuNPs.

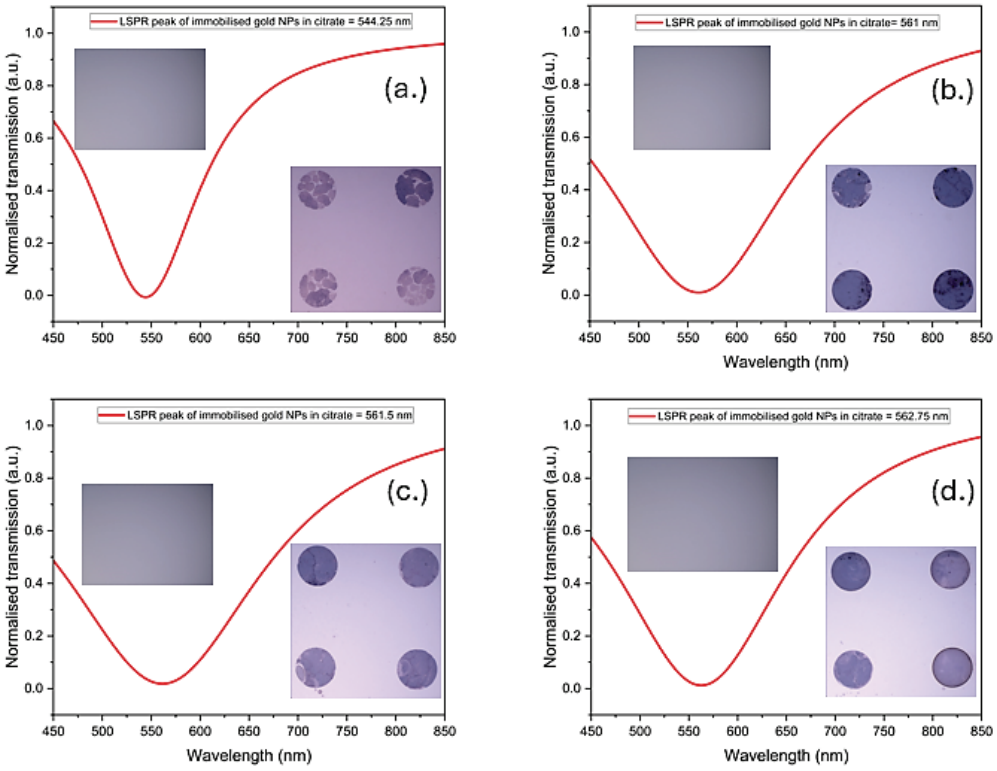

Figure 48: The figure illustrates the LSPR peak and optical image showing the reversible attachment of sub-20 nm gold NPs using the fluorous effect. (a.) Illustrates the initial immobilisation of the gold NPs on a fluorous-patterned surface with a distinct fluorous layer (circle) from the non-fluorous layer (other areas). The blank image shows the recovered (refreshed) surface after ethanol wash, regenerating the surface in the process (b.) Shows the newly immobilised gold NPs on the refreshed or recovered surface (from (a.)). The same cycle continues for images (c and d), where the recovered surface (blank image) serves as the template for the next immobilisation stage. Scale bar: 800 µm. Mag. = 20x.

Creating a reconfigurable and refreshable metasurface with unique colourimetric properties of metal NPs is necessary to detect and monitor plasmonic spectra change in real-time. This offers several advantages, including tunability, adaptability, and multiplexing capability. Achieving this requires the control of many factors, including concentration, aggregation, and immobilisation rate. Despite the different methods of conjugation of nanoparticles to control and direct immobilisation of NPs on surfaces, one of the significant challenges is the inability to regenerate the surface of the nanoparticles for another incoming molecule, which remains a concern. [497] In the previous experiment, we succeeded in functionalising 20 nm gold nanoparticles using perfluorodecanethiol in a water-based environment. This section aims to attach the functionalised gold nanoparticles synthesised via the Turkevich method to create a plasmonic metasurface whose surface can be refreshed multiple times using the fluorous effect (Figure 47 and Figure 48).To achieve this, the stability of the NPs must be

monitored and tailored to the assembly and the disassembly of the NPS on the fluorous modified surface using the fluorous effect. [498–500] Therefore, we explored our hypothesis on the reversible assembly of different sizes of MNPs using the fluorous effect, starting from the synthesised sub-20 nm gold nanoparticles. The result obtained showed that the spectra data of the immobilised gold nanoparticle can be acquired in a repeatable and reversible manner using this simple method. Also, the absorption peak of the dispersed colloids shifted to the longer wavelength after attachment to the fluorous patterned surface, indicating the presence of larger assembled nanoparticles. This was predicted due to the reduced interparticle distance among the nanoparticles as they were directed to the fluorous-patterned surface by the fluorous effect. [501] This aligns with previous findings, which showed that decreasing the distance between nanoparticles enhances their coupling effects. [502] The plasmonic response was predicted to be influenced by the size, shape, and refractive index of the surrounding environment on the fluorous-modified micro-patterned surface. [503–505] Following the successful attachment of the nanoparticles, we achieved the first reversible immobilisation with a simple solvent wash using ethanol. This method holds significant potential in creating simple reconfigurable metasurfaces tailored for many biomedical applications. [74, 75]

4.1.7 Solvent Choice to Strip Bound Nanoparticles on the Fluorous-Modified Surface

As part of this research objectives to ensure safe and common laboratory solvents with minimal or no risk, we carefully considered the choice of solvent to remove the required nanoparticles from the fluorous modified surface. After evaluating various options, water was the safest solvent due to its non-toxic and non-flammable nature. This method showed potential when combined with sonication to remove the bound nanoparticles from the non-fluorous region and some visibly unbound nanoparticles from the fluorous regions or areas close to the fluorous regions. However, this washing method did not guarantee 100 % efficiency, as many patches of bound nanoparticles were still present. Unlike using hexafluoroisopropanol (HFIP), tetrafluoromethane (CF_4), perfluorooctane, and PFOS, which are not environmentally safe, ethanol was the ideal laboratory solvent for stripping the already attached gold nanoparticles via the non-covalent interaction on the modified surface. [508–510]

4.1.8 Re-Immobilisation of Gold Nanoparticles using the Fluorous Effect

After the ethanol wash, an attempt was made to re-immobilise the nanoparticles by exchanging the solvent with distilled water and sonication. The goal was to remove excess non-immobilised nanoparticles from the non-fluorous regions. However, this method was inefficient in removing the nanoparticles from this region. The hydrophilic nature of the non-fluorous region facilitates the formation of multiple hydrogen bonds between the surface's hydroxyl groups and incoming water molecules. A 0.5 mM sodium citrate solution was used carefully to address this issue. Gentle cleaning of the non-fluorous region effectively removed the remaining or non-specifically bound gold nanoparticles from this area and directed them to the fluorous region. The success of this method can be attributed to the deprotonation state of the carboxylic acid group attached to the citrate ions, which can exist in either a monodentate, bidentate, or tridentate conformation (or dynamic equilibrium) upon dissociation in solution. This process creates a negatively charged group that is essential for electrostatic interactions. As a result, we believe this facilitated the re-direction of the remaining nanoparticles to the fluorous regions of the patterned surface. This method created electrostatic repulsion during the solvent exchange from the non-fluorous regions, resulting in an efficient solvent exchange and creating a distinct fluorous region from the non-fluorous region on the patterned sample.

4.1.9 Reversible Immobilisation of 45 nm Gold Nanoparticles using the Fluorous Effect in 800 µm Patterns

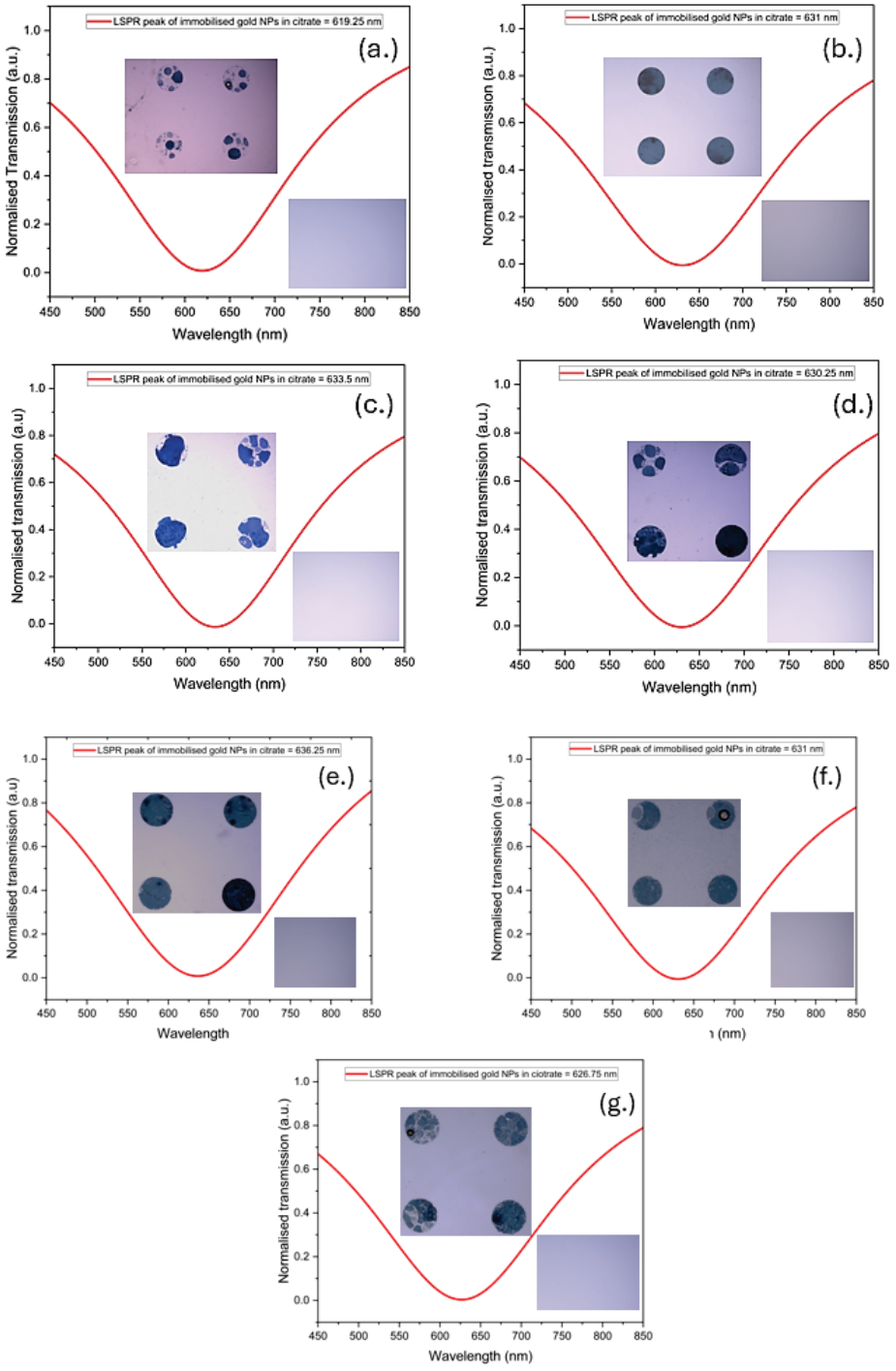

Figure 49: The figures illustrate the LSPR peaks and optical images showing the reversible attachment of 45 nm gold nanoparticles using the fluorous effect. (a.) The figure depicts the initial immobilisation of gold NPs on a fluorous-patterned surface with a distinct fluorous layer (circle) from the non-fluorous layer (other areas. The blank image (bottom-right) shows the recovered (refreshed) surface after ethanol wash, regenerating the surface in the process (b.) Shows the newly immobilised gold NPs on the refreshed or recovered surface (from (a.)). The same cycle continues for image (c-g), where the recovered surface (blank image) is a template for the next immobilisation stage. Scale bar: 800 µm. Mag. = 20x

Following the initial immobilisation of sub-20 nm gold nanoparticles on the fluorous patterned surface, the same procedure was employed to immobilise 45 nm gold nanoparticles synthesised through the modified Turkevich method. The rationale was to investigate the behaviour of larger gold nanoparticles on the fluorous patterned surface due to the extra signal amplification they offer during colourimetric applications. [511, 512]

As anticipated, the resulting UV-visible peak shifted to a longer wavelength than the initial value post-synthesis (Figure 49). [513]

4.1.10 Long-term Stability of Synthesised Gold Nanoparticles using Perfluorodecanethiol (PFDT)

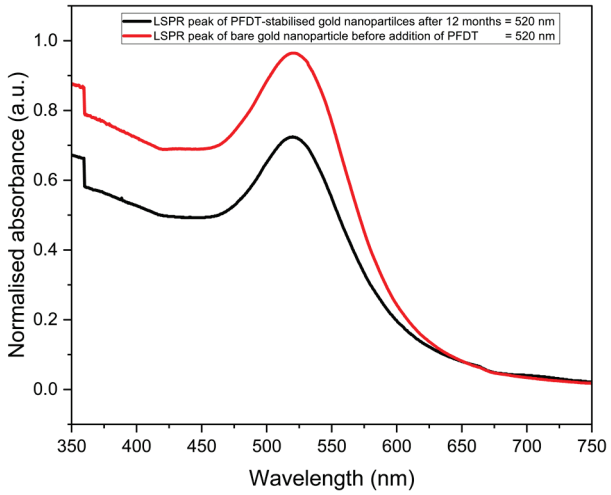

Figure 50: UV-visible spectroscopy depicting the stability of PFDT-stabilised gold nanoparticles in ethanol for 12 months. The spectrum (red) indicates the initial spectrum detail just after the introduction of the PFDT, while the second (black) line represents the spectrum detail after 12 months.

Gold NPs are commonly used for various applications due to their size-dependent sensitivity to their local environment. Hence, their stability for many experiments over an extended period is crucial for their reliability to guarantee consistent performance. Maintaining this stability over time is vital to preserving their size, shape, and surface characteristics, which are essential to their functionality. [514] To extend this research, it was found that incubation of the same amount of ethanolic PFDT with the synthesised gold nanoparticles showed no change in the absorption peak within 12 months (Figure 50). We believe this method can be

applied to other research requiring the long-term stability of MNPs for various applications.

4.1.11 Immobilisation of Silver Nanoparticles onto Micro-Patterns (800 µm)

Colourimetric analysis using silver NPs to create a reconfigurable metasurface offers more advantages than gold NPs. [515–519]
Silver nanoparticles tend to be more sensitive to plasmonic responses than gold because the conduction electrons on silver's surface are more responsive to electromagnetic fields. [520] This results in a stronger and sharper LSPR band, making AgNP nanoparticles extremely sensitive to changes in their surrounding environment compared to their gold counterparts. Additionally, the LSPR peak of silver nanoparticles is generally located at shorter wavelengths than gold, usually in the visible range, implying that a higher frequency (lower wavelengths) is needed to induce the resonance than gold NPs. [521]

Despite their superior sensitivities compared to the gold nanoparticles, they are prone to oxidation and unwanted reactions with their local environment, and these sensitivities must be carefully balanced. [522]

4.1.12 Initial Immobilisation with Citrate-Coated Silver Nanoparticles

To replicate the immobilisation process of gold nanoparticles, we followed our previously established protocol and synthesised citrate-coated silver nanoparticles using KI-assisted and non-KI-assisted synthesis routes. Adding KI enhanced the silver nanoparticles' sphericity, as uniformity and shape are crucial for their properties and applications in various fields. Based on the existing protocol, we anticipate this approach will yield a similar immobilisation pattern used to attach the citrate-coated gold nanoparticles. [523, 524]

4.1.12.1 Characterisation of Synthesised Silver Nanoparticles using UV-visible Spectroscopy

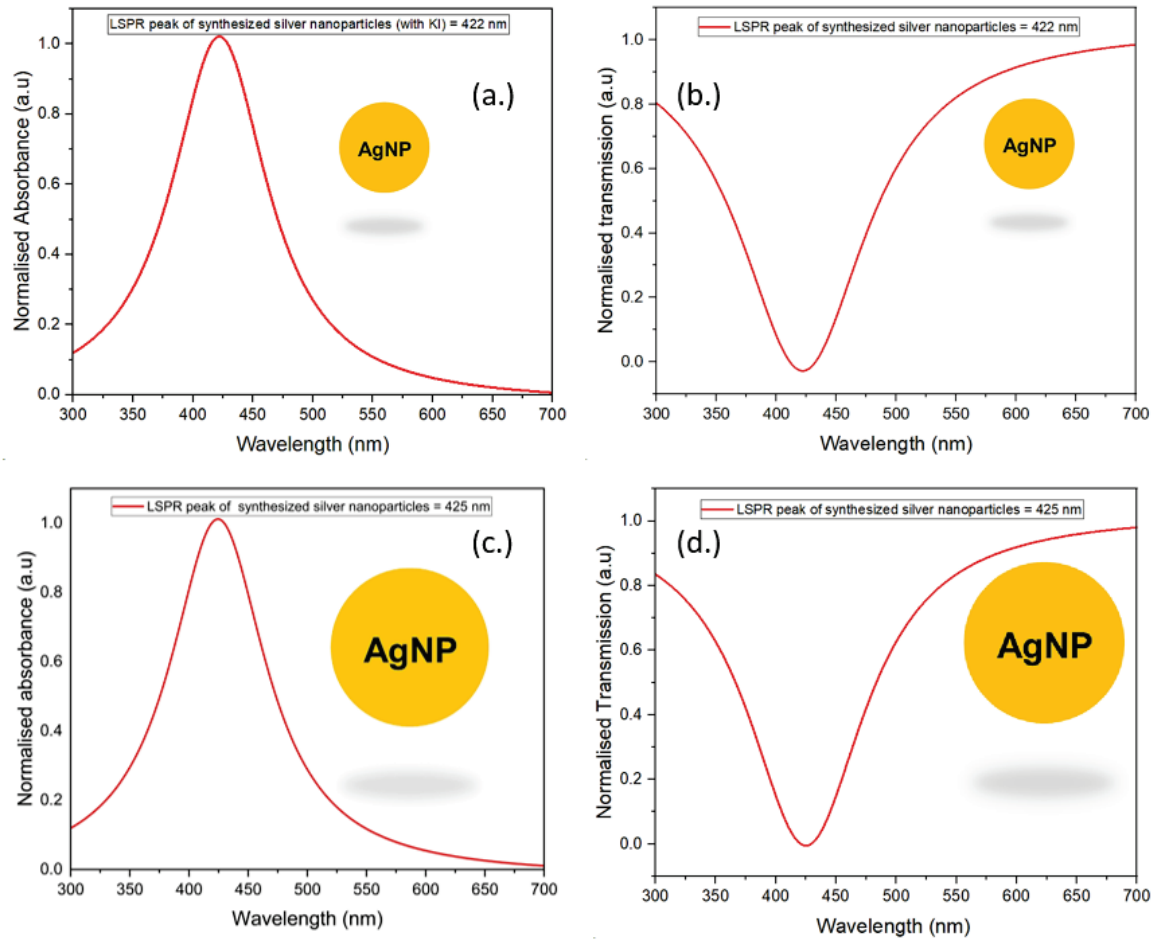

Figure 51: LSPR peaks of 40 and 51 nm of synthesised citrate-coated silver nanoparticles. (a. and b.) illustrates the absorption and transmission peaks of the KI-assisted citrate-coated silver nanoparticles, while c. and d. illustrates the absorption and transmission peaks of the citrate-coated silver nanoparticles, respectively.Dilution factor (DF) = 10. Narrow peaks were possible when estimating these synthesised silver NPs using these methods. However, the colour impact created using this method does not align with the goal of our research.

UV-vis spectroscopy was carried out to confirm the presence of silver nanoparticles and estimate their sizes upon interaction with light (Figure 51). The synthesised silver nanoparticles displayed absorbance peaks at 422 nm and 425 nm, respectively. These results are consistent with earlier reports in the literature. [525] The variation in the peaks of nanoparticles is due to their interaction with electromagnetic radiation in the UV-visible regions, which is dependent on their sizes. Moreover, the absorption peak of silver nanoparticles is typically lower than gold nanoparticles of similar sizes. This is because their d-electron energy levels are relatively higher compared to gold nanoparticles, requiring more energy (lower wavelength) to excite electrons to a higher level and absorb light. The

immobilisation of these nanoparticles using this synthesis method has shown great potential. However, the presence of unwanted black residues attached to the immobilised silver nanoparticles did not support the model of our research (Figure 52). This black residue could be attributed to the product generated by ligand exchange, an unwanted byproduct of reactions, and multilayer formation due to concentrations or time. Hence, this immobilisation pattern may be suitable for other applications, which may be further explored.

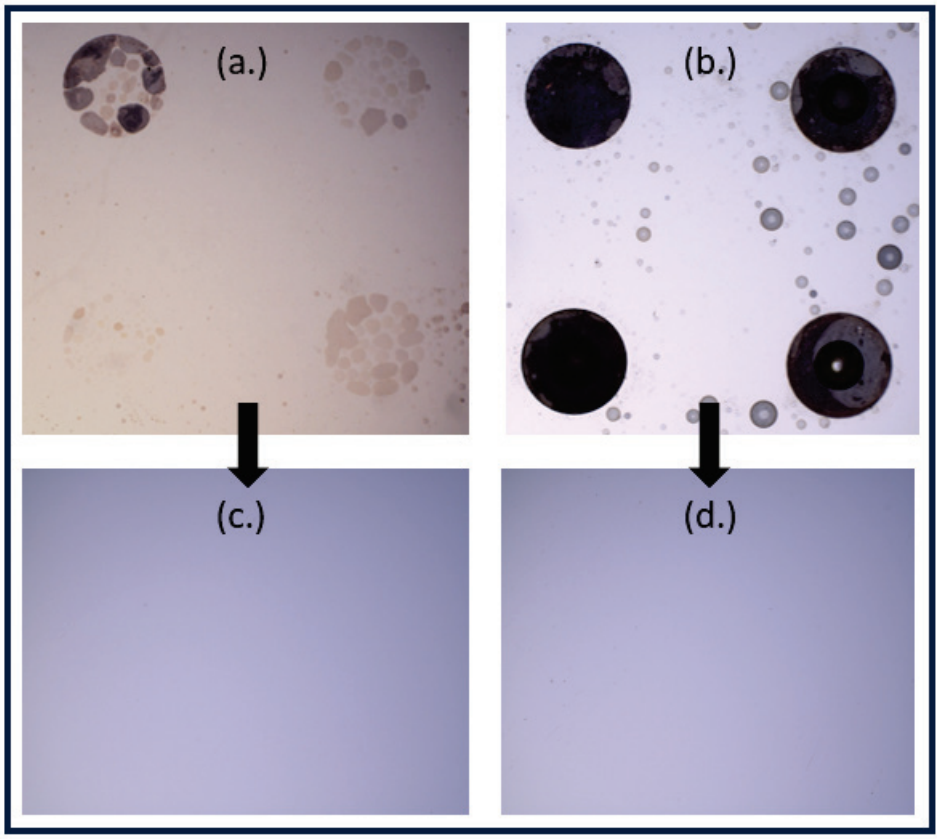

Figure 52: The image depicts silver nanoparticles attached to a fluorous-modified surface. The first image (a) shows 40 nm silver nanoparticles, while image (b) shows 51 nm silver nanoparticles. The colour of the nanoparticles turns black after the solvent exchange, and the surfaces can be refreshed (c. and d.) with a simple ethanol wash. Image scale bar = 800 µm; Mag. = 20x (a and b) and 4x Mag. (c and d); Dilution factor (DF) = 10.

4.1.12.2 Dynamic Light Scattering

Dynamic light scattering (DLS) is a commonly used technique to determine the hydrodynamic size of suspended nanoparticles in constant Brownian motion. [526] In this study, DLS was used to estimate the size of nanoparticles. The results showed that the sizes of the nanoparticles were 40 nm and 51 nm, respectively. Additionally, these sizes correspond to 422 nm and 425 nm absorption peaks in the UV-visible spectrum in Figure 51. The absorption peaks also increased with the size

of the nanoparticles. This correlation can be explained by the increasing tendency of the larger nanoparticles to scatter and absorb more light in the UV-vis region than the smaller ones. [527, 528]

4.1.13 Choice of Solvent for the Removal of the attached Silver Nanoparticles (Ki-Assisted)

Despite the challenge of immobilising the KI-assisted synthesised silver nanoparticles, sonication in ethanol was enough to wash and refresh the immobilised silver nanoparticles via non-covalent interactions. This further establishes the nature of the fluorous effect as a veritable method for reversible immobilisation (Figure 52).

4.1.14 Synthesis of Silver Nanoparticles using Hydroxylamine Hydrochloride (HH) Method

To overcome the challenge faced during the immobilisation of silver nanoparticles, a modified method proposed by Leopold and Lendl was utilised in an alkaline environment.[529, 530] In this method, hydroxylamine hydrochloride acts as a reducing agent, reducing silver nitrate and producing silver nanoparticles at room temperature. This method takes advantage of the chloride ions in the hydroxylamine hydrochloride, which can be adsorbed on the surface of the silver ion to stabilise it with less ambiguity. This is unlike the citrate-coated ions, which provide more robust electrostatic stabilisation and steric hindrance. [531, 532]
We believe this interaction pattern could significantly affect the kinetics and mode of interaction between these citrate-coated and chloride-coated silver nanoparticles on the PFDT-coated fluoros layer.

4.1.14.1 UV-visible spectroscopy

The absorption peak of the hydroxylamine hydrochloride-synthesised silver nanoparticles was investigated using UV-visible spectroscopy. The absorption spectra revealed a maximum extinction at 396.5 nm (Figure 53), indicative of the presence of silver nanoparticles. This also agrees with similar wavelength or silver nanoparticles using the same method in the literature. [533]

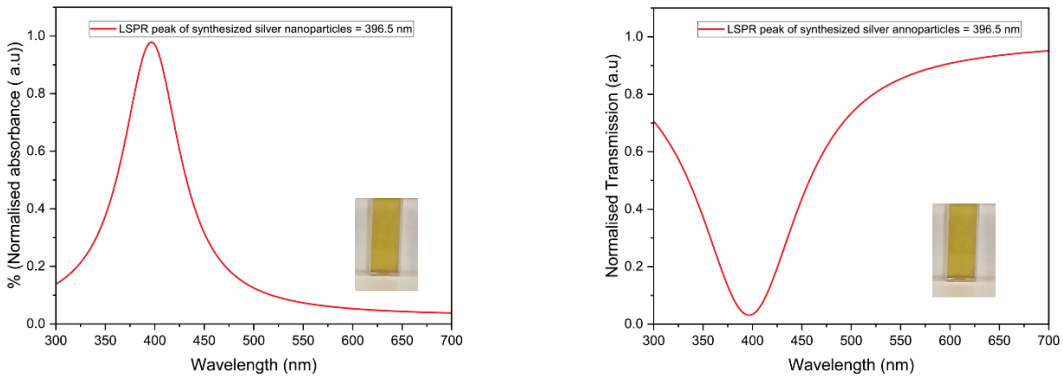

Figure 53: UV-vis spectra of silver nanoparticles synthesised with hydroxylamine hydrochloride: (a) Shows the LSPR peak of 396.5 nm during absorption. (b) LSPR peak of 396.5 nm during transmission. DF= 21x.

4.1.14.2 Dynamic Light Scattering (DLS) of the HH-synthesised Silver Nanoparticles

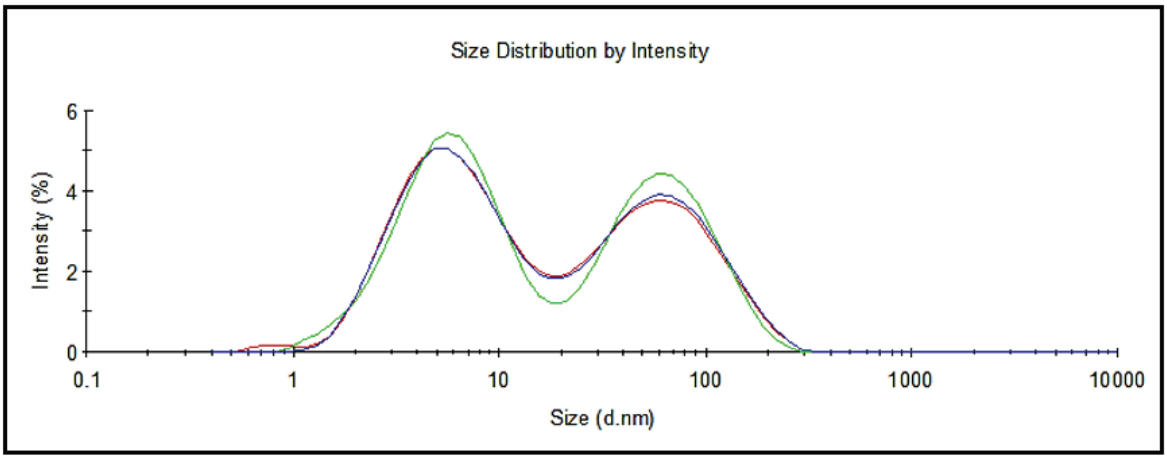

Figure 54: This shows the distribution of the synthesised silver nanoparticles using DLS measurements. The results indicate a bimodal hydrodynamic size distribution with distinct peaks.

The hydrodynamic size distribution of the colloidal suspension was measured in solution upon interaction with light using dynamic light scattering (DLS). This was carried out at a scattering angle of 90° with 30 measurements in triplicate. The DLS results revealed a bimodal size distribution of 52 nm and sub-10 nm nanoparticles, as indicated by the zeta sizes (Figure 54). These values are similar to the range obtained from the literature. [534] This results in a negatively charged outer chloride ion layer, similar to the negatively charged layer of the citrate-coated gold nanoparticles used to immobilise gold nanoparticles. [535]

4.1.14.3 Zeta Potential (ZP) of the HH-synthesised Silver Nanoparticles

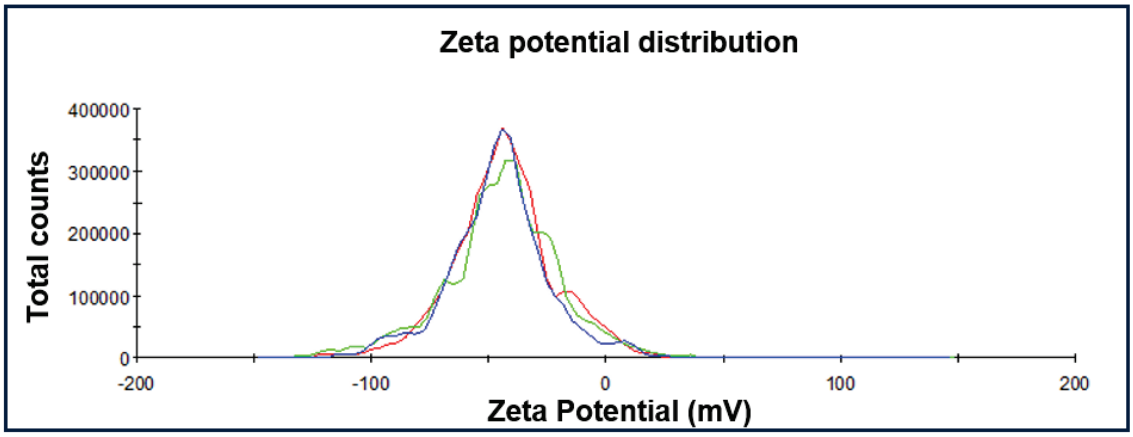

Figure 55: Zeta potential showing the extent of the surface coating of the synthesised silver nanoparticles. The ZP of - 44.50 mV indicates a stable colloidal system post-synthesis.

The zeta potential was used to measure the magnitude of particle charge surrounding the synthesised silver nanoparticles. The results indicate a negatively charged corona, stabilised by chloride ions. The negative zeta potential value of -44.50 mV confirms the presence of a negatively charged layer on the nanoparticles (Figure 55). This value range confirms the stability of the colloidal system, which is also in line with the previous report. [536]

4.1.14.4 Scanning Electron Microscopy (SEM)

Scanning Electron Microscopy was performed as described in Chapter 2. The morphological properties of the synthesised silver nanoparticles were imaged using a beam of highly energetic electrons from the SEM. Initial visual observation of the distributed nanoparticles showed quasispherical nanoparticles with an average size of 40 nm (Figure 56).

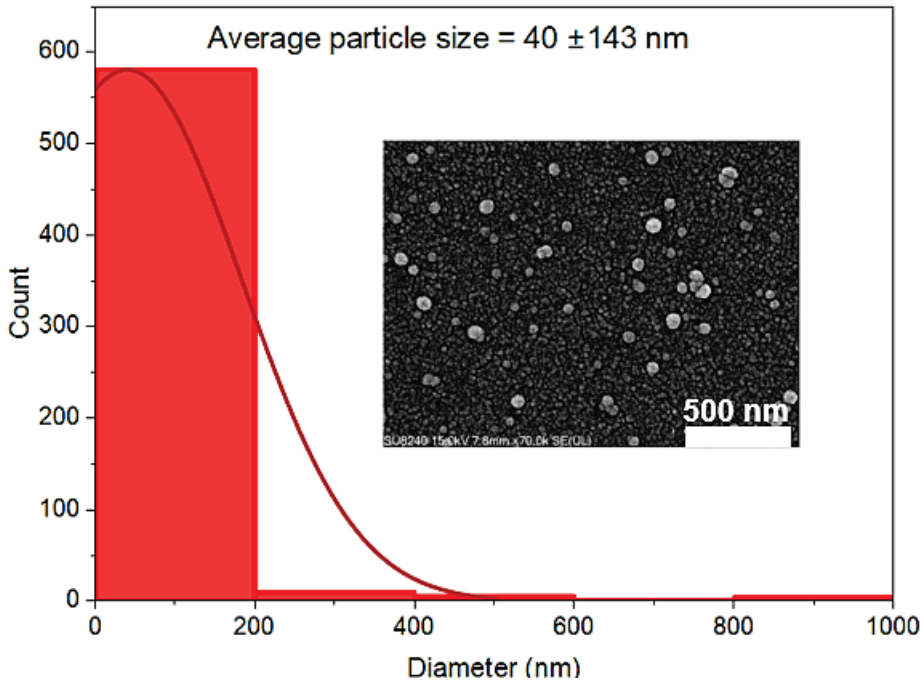

Figure 56: SEM micrograph showing the distribution of synthesised silver nanoparticles on bare glass surface. The average particle size estimated from ImageJ is 40 nm. The significant deviation could be attributed to aggregated NPs during drying. Scale bar = 500 nm

4.1.15 Reversible attachment of Silver Nanoparticles using the Fluorous Effect (HH method)

The current method utilised the fluorous effect to temporarily assemble silver nanoparticles in an ethanolic solution containing 0.04 mg/mL (30 µL) perfluorodecanethiol. The previous experiment using citrate-coated gold nanoparticles suggested that gold or silver nanoparticles were immobilised through a synchronous ligand exchange and self-assembly in a thermodynamically favoured reaction, feasible within two minutes. The results presented a distinct and preferential interaction between the PFDT-functionalised gold nanoparticles and the fluorous-modified layers (800 µm and 50 µm) using the fluorous effect. According to the current protocol, using silver nanoparticles synthesised with the Hydroxylamine hydrochloride(HH) method has shown that the negatively charged chloride surrounding the nanoparticles' outer coating significantly improves their stability and ligand exchange. This leads to the directed immobilisation of the nanoparticles in the fluorous regions of the patterns. In addition to this, the colour generation due to LSPR fits into this research. This research aimed to create reversible attachment of MNPs using the fluorous effect, with the ability for easy spectra data acquisition apparatus. The 50 µm patterns could not offer a convenient spectra data acquisition platform but were adequate for creating a reversible

immobilisation platform (appendix 2). Moreover, the initial size (50 µm) of the patterns in relation to their pitch (100 µm) was not suitable for the washing steps before the next immobilisation cycle. Therefore, we opted for a larger pattern size of 800 µm in subsequent experiments. The benefits of using larger circular-sized patterns are clear: they are easier to see and offer more flexibility for data acquisition using common laboratory equipment. With this method, we achieved reversible interaction of the thiol-modified silver nanoparticles with the fluorous-modified surface using the fluorous effect.

From these results, there was a large increase (red-shift) in the plasmonic shift of the immobilised silver nanoparticles on the 800 µm-size circular fluorous patterns compared to the initial **396.5** nm (dispersed state after synthesis) with an average LSPR peak of 463.5 nm ± 9.1 (Figure 57). This is attributed to the increased coverage of the fluorous patterned surface by the thiol-modified silver nanoparticles, creating enhanced neighbour-to-neighbour plasmonic coupling due to the reduced interparticle distance and efficient ligand exchange. This also aligns with the literature for different nanoparticles, where it was shown that plasmonic shift could increase as the interparticle distance reduces to at most 2.5 nm of the nanoparticle size [108] and is insignificant when this is more than 3.5 times the particle size. [538] This method (using the fluorous effect) is reversible, repeatable, and can easily acquire UV-visible data for at least ten times.

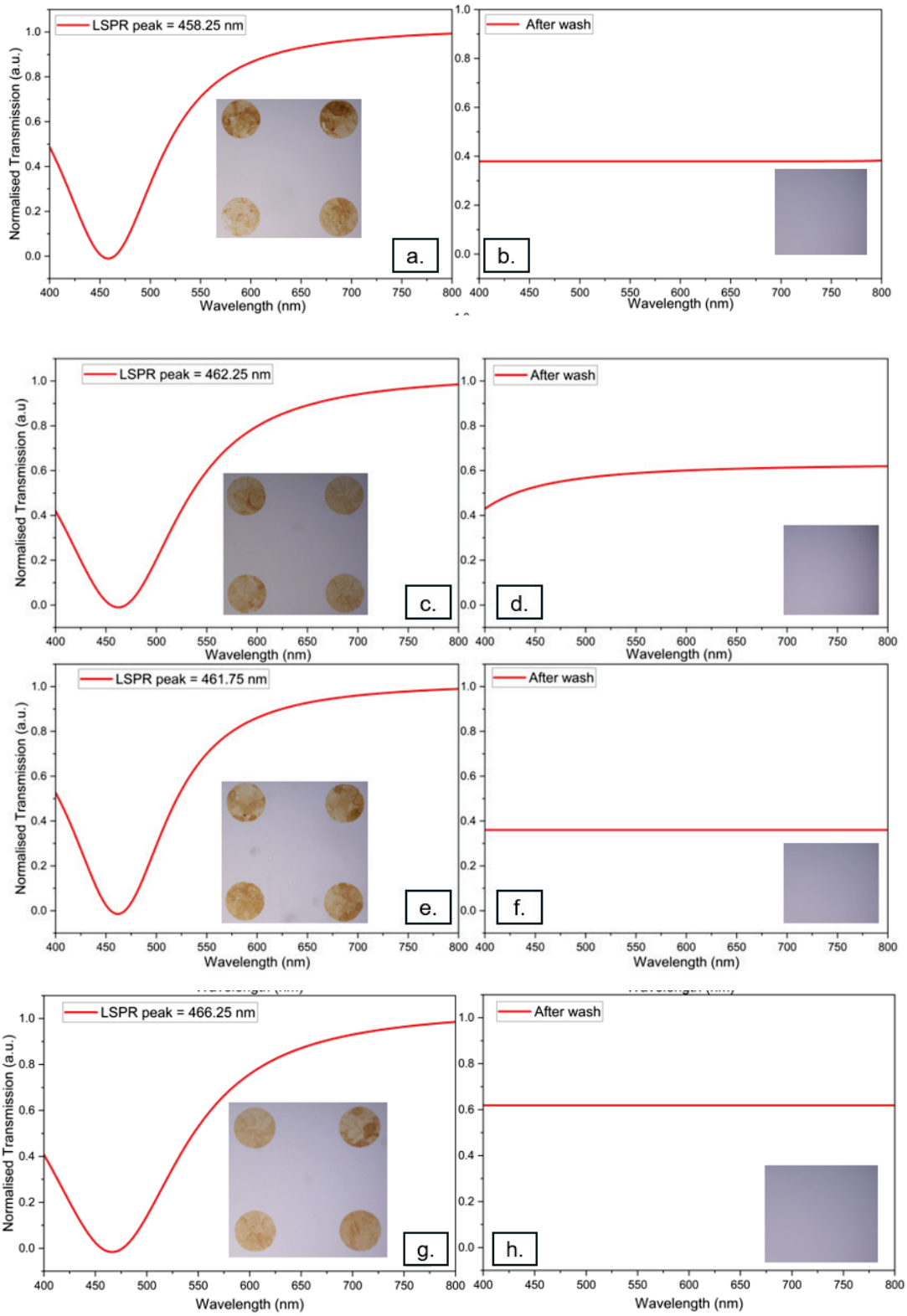

Figure 57: Spectra data and optical images showing the reversible attachment of silver nanoparticles using the fluorous effect. (a.) The figure depicts the initial immobilisation of silver NPs on a fluorous-patterned surface with a distinct fluorous layer (yellow circle) from the non-fluorous layer (other areas). (b.) The spectrum illustrates the results after a simple ethanol wash, regenerating the surface in the process (c.) This figure shows the second immobilisation of silver NPs after washing or regenerating the surface with ethanol wash from (b.).The silver was successfully re-immobilised for the third time, and the cycles of immobilisation and re-immobilisation continued up to the tenth time (d-h). Data is presented (only four of the ten data are presented in the graph) as the mean ± standard deviation of the measurements taken in triplicate. Scale bar: 800 µm; Mag. = 20x

4.1.16 Switchable or Reconfigurable Metasurface with Gold and Silver Nanoparticles

Recently, there has been a growing demand for multifunctional surfaces with tunable properties. [539, 540] Metamaterials and adaptive surfaces have gained attention due to their unique electromagnetic properties in recent decades. [541, 542] Once designed, they can be modified dynamically, enabling the metasurfaces to alternate between different states with unique optical properties. [543] This ability to switch states is often achieved using external stimuli, including electrical fields and temperature changes. Switchable metasurfaces facilitate reversible interactions, making them highly suitable for applications requiring non-permanent alterations.

One of the main issues with using silane-functionalised glass surfaces in various applications is that the siloxy bond formed between the silane molecules and the glass surface tends to become hydrolytically unstable over time due to temperature, moisture, and duration of use. [544] Hence, it is necessary to create a viable and repeatable surface that is simple, specific, reversible, switchable, and considerably less expensive protocol.

This section explores the possibility of immobilising different nanomaterials on the same modified surface at various times, offering the ability to 'switch' the passive surface when repeated immobilisation is needed for another incoming material.

By changing the refractive indices of certain materials, their chemical and electrochemical properties can be altered, allowing for dynamic control of their optical properties. Unlike active tunable metasurfaces, which can create reversible and rapid surface changes in response to external stimuli, this newly developed passive switchable surface can be used as a functional surface to attach different MNPs. [545] The results revealed that 45 nm and 52 nm gold and silver nanoparticles of different sizes can be interchangeably assembled on the same modified surface using a simple solvent wash. This outcome further supports our hypothesis that the fluorous-fluorous interaction is non-covalent and allows stripping off the required molecules or nanoparticles from the patterned surface using a suitable solvent, making the surface reusable for the next incoming

molecule (**Figure 58**). From the spectra acquired, there was a change in the LSPR peaks of the two nanoparticles to the longer wavelengths, indicating an increase in the size of the assembled nanoparticles on the fluorous patterned surface. Specifically, the average transmission peaks were 632.75 ± 4.5 and 455 ± 4.5 for gold and silver NPs, respectively. This was close to the initial data acquired during the reversible immobilisation of AuNPs or AgNPs on different pattern surfaces.

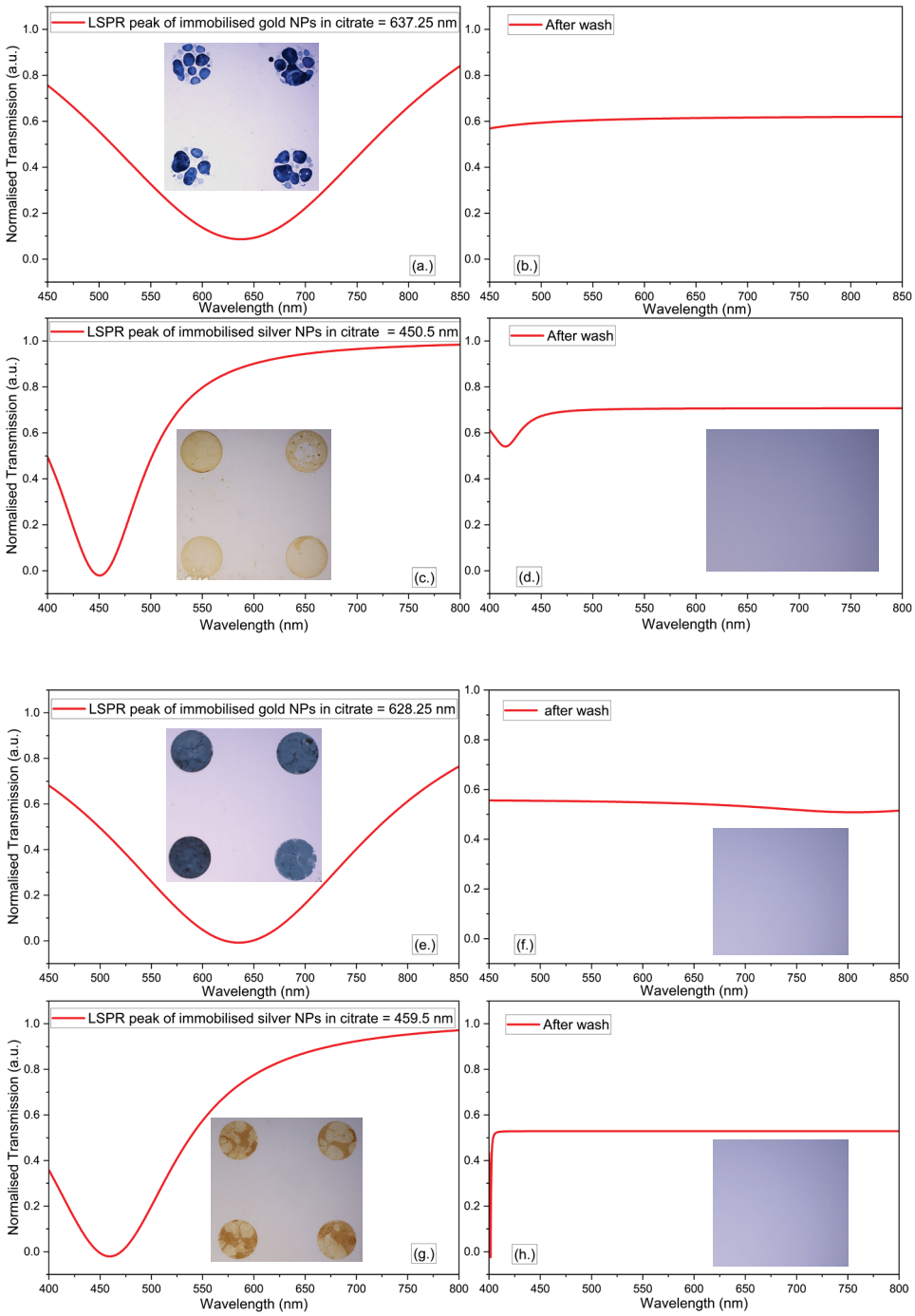

Figure 58: Spectra and optical images depicting the reversible and switchable immobilisation of gold and silver nanoparticles on the fluorous patterned surface (1st - 4th) with gold and silver nanoparticles using the fluorous effect. The average wavelength of the assembled AuNPs = 632.75 ± 4.5, while the average wavelength of the assembled silver NPs = 455 ± 4.5.

4.1.17 Recovery of Attached Silver Nanoparticles from the Fluorous-Modified Surface

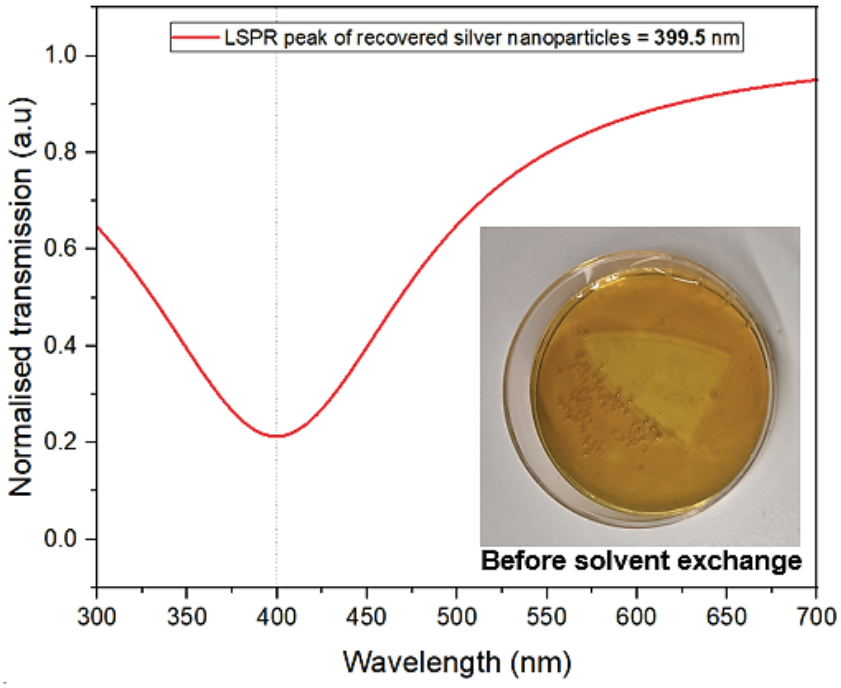

Figure 59: UV-visible spectrum of recovered silver nanoparticles from the fluorous modified surface. This method is a crude and direct way to test the recoverability of the immobilised nanoparticles on each fluorous-modified layer after carefully rinsed in citrate solution. This method also confirms the non-covalent nature of the interaction between fluorous-modified molecules during the fluorous effect.

Apart from the tendency for assembled nanoparticles to aggregate during their attachment, another notable challenge is the inability to recover the already attached materials, especially when the interaction occurs through covalent bonds. [546–549]

In this research, we achieved the reversible attachment of different nanoparticles by non-covalent interactions influenced by the fluorous effect. To satisfy our curiosity about the nature of the interaction, the assembled silver nanoparticles were recovered in 2 ml (0.5 mM) sodium citrate solution, followed by characterisation using UV-vis spectroscopy. The result showed no sign of aggregation from the initially immobilised nanoparticles on the fluorous functionalised surface (Figure 59). Apart from this, there was no significant change in the LSPR peak of the synthesised and recovered silver. However, further studies would be needed to substantiate the kinetics and mode of binding due to this effect.

4.1.18 Conclusion and Future Work

Using the fluorous effect to immobilise gold and silver nanoparticles on reconfigurable metasurfaces presents a promising opportunity to develop advanced optical materials. This innovative approach enables the precise assembly and dispersion of nanoparticles through non-covalent interactions, allowing for significant flexibility in design and application.

We have developed a new proof-of-concept protocol that comprehensively investigates the optical properties of metallic nanoparticles (MNPs) for use in reconfigurable metasurfaces. This method leverages the tunable properties of nanoparticles of various sizes when interacting with light, utilising a phenomenon known as localised surface plasmon resonance (LSPR). The ability to adjust the optical characteristics of nanoparticles allows for the creation of reusable multifunctional surfaces that can seamlessly switch between two different MNPs without causing any damage to the underlying substrate, making it particularly suitable for various biomedical applications, such as diagnostic imaging and targeted drug delivery.

This technique can yield specific, repeatable, reusable, and switchable surfaces with significant potential for applications in microarrays, drug delivery systems, and sensing. Furthermore, additional exploration of the kinetics of these interactions is necessary to thoroughly assess their suitability for a broader range of biomedical uses, ensuring that the technology can be effectively integrated into clinical practices and research settings. By advancing our understanding of these dynamics, we can enhance the performance and versatility of optical and fluorescently labelled materials using the fluorous effect to solve real-world applications.

Chapter 5

5.1 Immobilisation of Gold Nanoparticles on Fluorous Modified Nanopatterns

5.1.1 Introductions

Nanomaterials (NMs) are popular candidates in several applications, including diagnostics and therapeutics.[550, 551] In particular, smart nanoplatforms are being developed for enhanced precision and effectiveness across multiple applications.[552–555]

For example, adaptive or reconfigurable metasurfaces offer specialised properties that can dynamically change the electromagnetic properties of materials in real-time upon interaction with external stimuli or signals. Pattern definition by lithography and metallisation through metal deposition or evaporation are the usual techniques for [556, 557] manufacturing this surface. However, these methods face challenges with scalability and precise geometric control. Due to the limitations associated with top-down nanofabrication methods, bottom-up nanofabrication has become a popular alternative to creating self-assembly monolayers.[558]

Bottom-up nanofabrication techniques have emerged as promising methods for reversible fabrication processes suitable for various applications. This approach involves the self-assembly and precise organisation of nanoscale structures, resulting in tailored platforms capable of switchable functionalities with a high degree of control and precision and paving the way for advanced functional materials and devices.[557] [559] A promising area of research is the controlled and reversible attachment of gold nanoparticles onto patterned surfaces while maintaining precise control over their spatial arrangement. [560]

Nanopatterning using nanofabrication techniques (e.g. EBL) offers an avenue to direct precise control and spatial arrangement of nanoparticles, enabling the creation of structured surfaces with enhanced properties and functions. Despite these fabrication methods, many challenges persist, including scalability and spatial definition of patterns. [561–565]. Despite advances, immobilisation on nanopatterned surfaces often leads to nanoparticle aggregation, detachment, or oxidation, impairing their performance. [566]

To address the challenges, especially with the assembly of nanoparticles, it is necessary to improve their surface chemistry and functionalisation. This can be done using electrostatic or covalent interactions to direct them towards a nanopatterned surface. Covalent interactions can create strong and stable bonds without the opportunity for reversible interactions, which can make substrate regeneration difficult. Additionally, covalent interaction can lead to unwanted aggregation if not well controlled. [567] Hence, facile and simple methods of attachment that are specific, sensitive, and reversible are needed. This technique, if achieved, holds significant applications in manipulating the spatial arrangement of gold nanoparticles to harness their colourimetric properties via localised surface plasmon resonance (LSPR). This property makes them excellent candidates for surface-enhanced Raman spectroscopy (SERS), biosensing, and plasmonic device applications. In addition, these applications can be extended to catalysis, drug delivery and energy conversion systems. [568] [569]

In the earlier chapter, the fluorous effect was used to immobilise metal nanoparticles on the fluorous functionalised micro-patterned surfaces in a reversible manner. This section aims to direct the precise and reversible immobilisation of these nanoparticles onto a fluorous-modified nano-patterned surface using the fluorous effect to attach individual nanoparticles at exact locations without aggregation.

5.2 Results and Discussion

5.2.1 Synthesis and Characterisation of Gold Nanoparticles

Gold nanoparticles were synthesised using three different methods: Turkevich, modified Turkevich, and inverse Turkevich. [570, 571] One significant advantage of using the Turkevich method is the ability to tune the size of the nanoparticles synthesised by varying the molar ratios of the reactants (sodium citrate and gold chlorate) while ensuring a complete reduction of the gold chloride to gold nanoparticles. [572] Our goal was to synthesise gold nanoparticles of different sizes and evaluate how the particle size distribution to nanopattern size ratio could affect the precise immobilisation of these nanoparticles on the fluorous nanopattern regions. As explained in Chapter One, using the classical Turkevich/Frens method, gold nanoparticles within the range of 30 nm can be synthesised based on the reductive ability of the citrate on gold chloride to

produce gold nanoparticles. [573] However, as size increases, synthesised gold nanoparticles tend to assume irregular, non-spherical shapes with increasing tendencies to create broader peaks in the UV-Vis spectrum. [574] This is attributed to multiple factors, including the molar ratio of gold to citrate, pH, and temperature. [575] However, creating larger, uniformly sized nanoparticles is essential for medical applications. [576–581]

Over the past few decades, extensive research has focused on how noble metal nanoparticles such as gold (Au), silver (Ag), and copper (Cu) interact with electromagnetic radiation through LSPR with varying sensitivity and with respect to their shape, dimensions, and dielectric properties.[582–584]

This sensitivity is crucial in research studies where interactions between nanoparticles and analytes cause visible colour changes in the colloidal system. This property is important, especially when the naked eye can detect such changes. [585–588]

Adapting the size of gold or silver nanoparticles to achieve specific outcomes depends on the unique requirements of each research project. Factors such as optical properties, ease of functionalisation, stability, compatibility with research objectives, sensitivity, and safety are critical considerations in this research.

Previous research reported the use of nanoparticle sizes suitable for different applications.

Smaller nanoparticles (15-20 nm) are excellent for highly sensitive biosensing and drug delivery due to their sharp LSPR peaks and ease of cellular uptake. Medium-sized nanoparticles (30-40 nm) are suitable for immunoassays, environmental sensing, and imaging due to their larger surface area and strong optical responses. Larger nanoparticles (50-60 nm) are ideal for therapeutic applications, cell labelling, and plasmonic sensors due to their enhanced light absorption and scattering properties.[589–591] Studies have shown that colourimetric analysis to detect metal nanoparticles requires particles ranging from 15-50 nm, while sizes of 6-35 nm and 12-30 nm are needed for biological molecule detection and cancer research for drug discovery, respectively.[592] Additionally, larger gold nanoparticles offer stronger light absorption and scattering, improving signal amplification, stability, and fractional change in local refractive indices.[593, 594] Specifically, it was also reported that as the cross-sectional area of nanoparticles increases from 10 nm to 80 nm, there is increased scattering with a five-order of magnitude compared to a typical dye. [595, 596] Therefore, using

larger NPs provides an extra opportunity for signal amplifications and overall efficiency during sensing applications. We synthesised and utilised gold nanoparticles measuring 45 nm and 55 nm in size, as these dimensions are particularly suitable for colourimetric applications. These nanoparticles exhibit enhanced capabilities in both scattering and absorbing light, making them highly effective for various analytical purposes. Their specific sizes allow for optimal performance in sensing applications, where precise changes in colour can indicate the presence or concentration of specific substances. This quality underscores their overall efficiency and versatility in laboratory settings.

Using the fluorous effect, this research investigated the reversible attachment of various sizes of gold and silver nanoparticles on fluorous patterned surfaces. This method allows us to select the appropriate NP size suitable for our designed metasurfaces.

5.2.1.1 UV-visible Spectroscopy

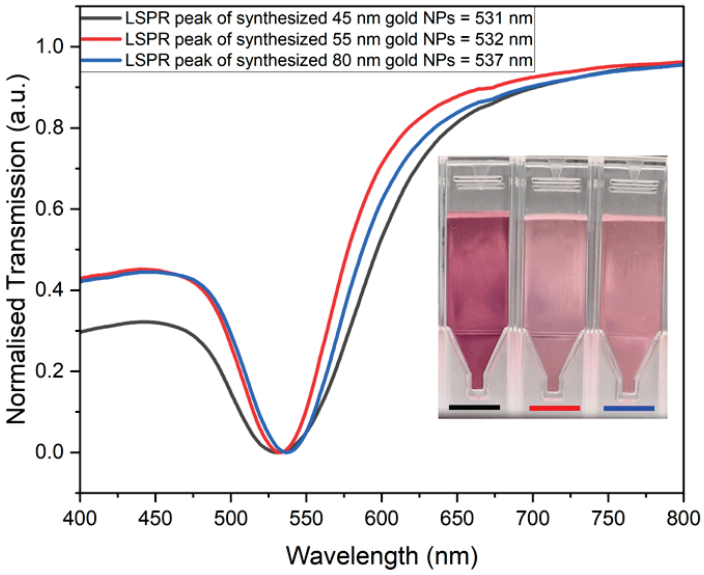

Figure 60: The LSPR absorption peaks of citrated-coated gold nanoparticles (45 nm, 55 nm, and 80 nm) were analysed using UV-visible spectroscopy. The results showed absorption maxima at 521 nm, 532 nm, and 537 nm, respectively, indicating that the absorption wavelength increases as the size of the nanoparticles increases (DF = 11).

This is a simple, fast, and non-invasive technique for measuring nanomaterials' size, concentration, and aggregation state. [597] UV-visible spectrophotometry revealed the characteristic maximum peak of 531 nm, 532 nm, and 537 nm with

narrow bandwidths, indicating the presence of gold nanoparticles size distribution for the 45 nm, 55 nm, and 80 nm gold nanoparticles, respectively (Figure 60). These findings are consistent with other reports using similar synthetic methods, especially where the size of the gold nanoparticles is accompanied by an increase in the absorption maxima due to absorption, scattering, or both. [598–603]

Also, the 80 nm gold nanoparticles were synthesised by the inverse Turkevich method. In this study, the molar ratio between the citrate and the gold chloride was varied to produce larger particle sizes with pre-determined sizes, thereby preventing further secondary nucleation during growth. This method generates monodispersed nanoparticles with controlled concentrations. [604] . This method further suggests that growth was accompanied by Lamer's mechanism, which outlines NP growth into an initial rapid focusing period characterised by increasing mean radius of the nanoparticles and subsequent defocusing period characterised by wider size distribution due to Ostwald ripening. The transition between these two stages is also primarily influenced by concentrations of the monomers at every point during the synthesis. Puntes *et al.* (2011) also give insights into this phenomenon during the synthesis of larger-sized nanoparticles. [605]

5.2.1.2 Dynamic Light Scattering (DLS)

Table 7: The synthesis of 80 nm gold nanoparticles was monitored using DLS measurements to track the different stages of the reaction. High transient instability was observed initially, but this stabilised as a more stabilising agent was available during the nanoparticle synthesis. This stabilisation was evidenced by the change in the PDI at the beginning, 15 minutes, and 30 minutes into the reaction.

Time (min)	Size (nm)	PDI (polydispersity index)
During synthesis	65	0.305
15	72	1.000
30	83	0.307

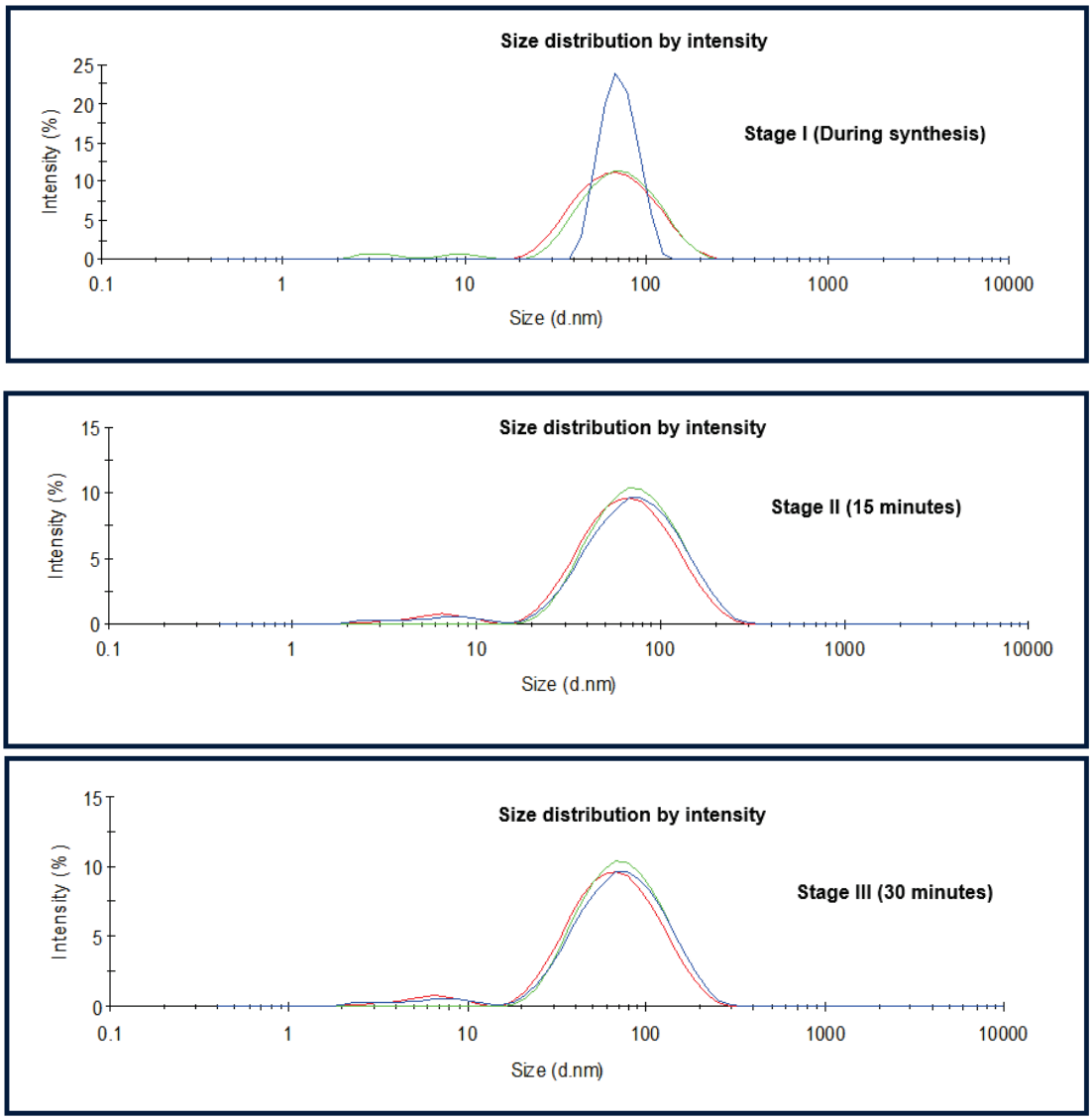

Figure 61: Stages during the synthesis of 80 nm gold nanoparticles monitored with DLS measurements. Stage I. showed high instability due to the delayed nucleation stage. Stage II. Showed initial stability and continuous growth of the NPs.Stage III. Showed continuous stabilisation by the sodium citrate.

Dynamic light scattering is a phenomenon which computes the interaction of the dispersed colloidal suspension in a constant brownian motion with white light. In this study, the hydrodynamic size distribution of the synthesised gold nanoparticles was analysed by measuring their mobility in the solution as they interacted with the beam of light.

In this research, we evaluated this finding using DLS to characterise each stage during nanoparticle synthesis. Our results revealed that the stage and concentration of the monomers in solution could affect the size and the distribution of the nanoparticles from the point of synthesis at 15 minutes to 30 minutes for the 80 nm gold nanoparticles (Figure 61). Specifically, in stage I, the

citrate concentration delayed the nucleation of the nanoparticles. Hence, there was no uniform growth of the nanoparticles, as this stage precedes the beginning of the stabilisation by the citrate ions. Thus, this stage is characterised by multiple non-uniform sizes. Additionally, the size of the nanoparticles continued to increase as the smaller gold atoms became incorporated on the surfaces of the larger gold nanoparticles. This was obvious from the broadened peak of the graph beyond the 100 nm mark (stage II) and the resulting PDI of 1 (Table 7). At 30 minutes, most nanoparticles are formed, coated with citrate, and with little or no further growth (stage III).

Table 8: Dynamic light scattering and the Zeta potential of synthesised gold nanoparticles. DLS was performed at a scattering angle of 90˚ using 30 measurements in triplicate. For the 80 nm size, the PDI continued to reduce after 30 min., showing enough stability by the citrate as the size continued to grow up to the supersaturation limit, where adequate stability was achieved without further noticeable growth. 45 and 55 nm sizes were also synthesised by varying the concentration ratio between the gold chloride and the sodium citrate.

Size	Zeta size (nm)	PDI	Zeta potential (mV)
45 nm	45.00	0.74	-37.30
55 nm	55.00	0.27	-39.20
80 nm	80.00	0.31	-41.00

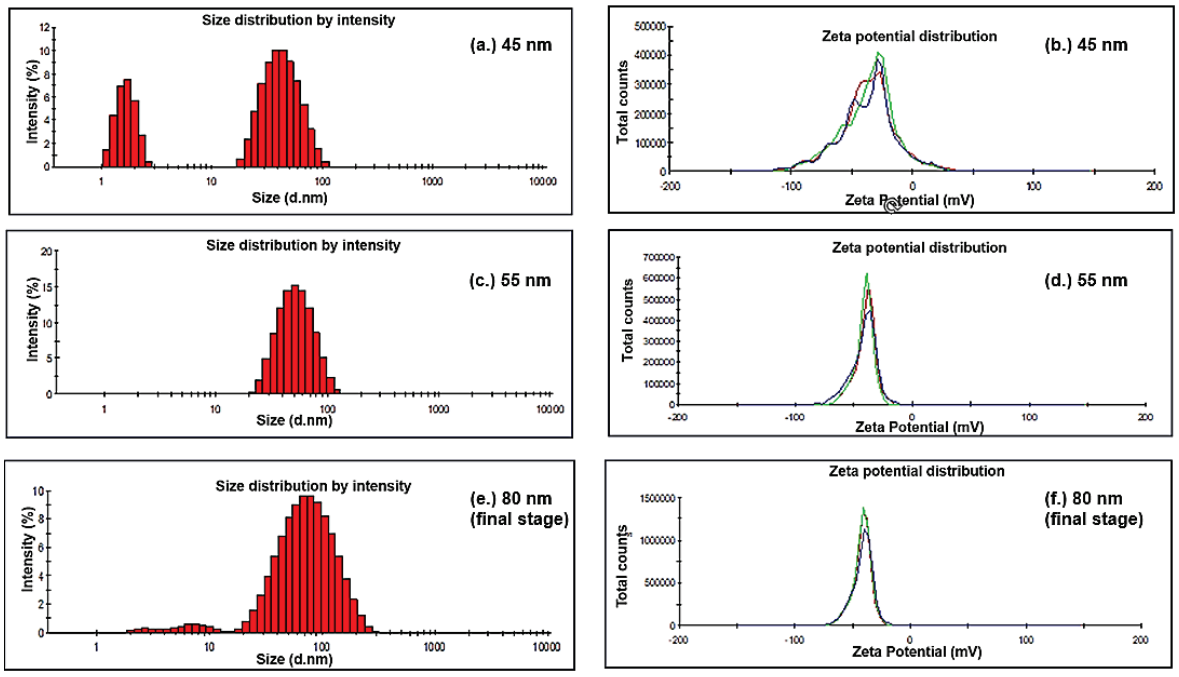

Figure 62: Size distribution of synthesised gold nanoparticles of different sizes from DLS (left) and zeta potential analysis (right) of the bare gold nanoparticles of various sizes (45 nm, 55 nm, and 80 nm). The (a.) 45 nm and the (e.) 80 nm showed a bimodal distribution of nanoparticles, especially around the sub-12 nm region, while the (b.) 55 nm was the most monodispersed among the three colloidal systems. The three nanoparticles (b, d, and f) also showed adequate stability higher than 30 mV after the synthesis.

Using several methods, nanoparticles of different sizes were evaluated for self-assembly in nanopatterns. The result revealed an average hydrodynamic size of 45 nm, 55 nm, and 80 nm with the lowest polydispersive index from the 55 nm gold nanoparticles (Table 8). The remaining nanoparticles were also monodispersed except for the sub-5 nm and sub-12 nm size distributions presented after the synthesis (Figure 62). This could be attributed to many factors, including incomplete coalescence of the seeds to form larger nanoparticles during the synthesis. In addition, the correlation between the electric potential and the electric double layer surrounding the surface of the nanoparticles can be interrogated for their colloidal stability using the zeta potential. The zeta potential of all the gold nanoparticles analysed revealed a well-stabilised colloidal system with a negative potential, indicating the presence of a negatively charged coating contributed from the citrate. These outcomes align with previous research on a similar synthesis route for citrate-coated gold nanoparticles.[606]

5.2.1.3 Scanning Electron Microscopy (SEM)

Scanning electron Microscopy was used to characterise the topography of the assembled gold nanoparticles onto the nanopatterns, as described in Chapter One. SEM micrograph of the 55 nm gold nanoparticles revealed a nanoparticle size of approximately 36 nm (Figure 63) lower than the value obtained from the DLS measurement. This was expected as the DLS measures the hydrodynamic size of the particles in colloidal solution while the characterisations using electron microscopy were carried out in a dried state after the sample was sputtered and processed before SEM imaging. [607] Hence, the loss of solvated layers during the characterisation by SEM appears to contribute to the reduction in the final size of the nanoparticles during the characterisation using SEM (Figure 64).

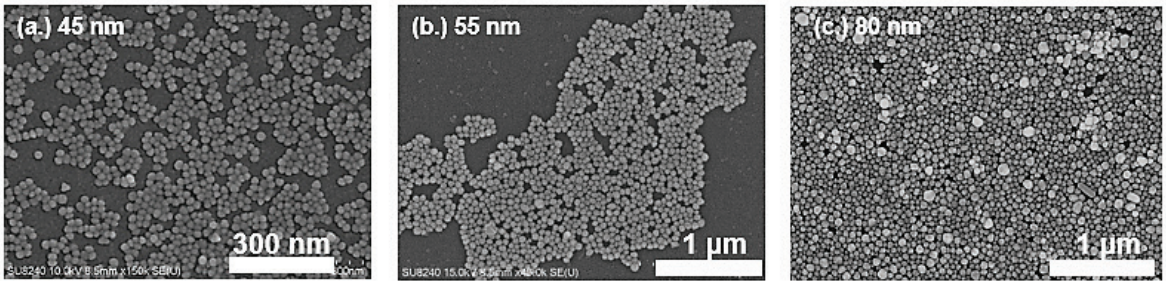

Figure 63: Scanning electron micrograph of bare (a.) 45 nm, (b.) 55 nm, and (c.) 80 nm gold-nanoparticles after synthesis on bare glass surface.

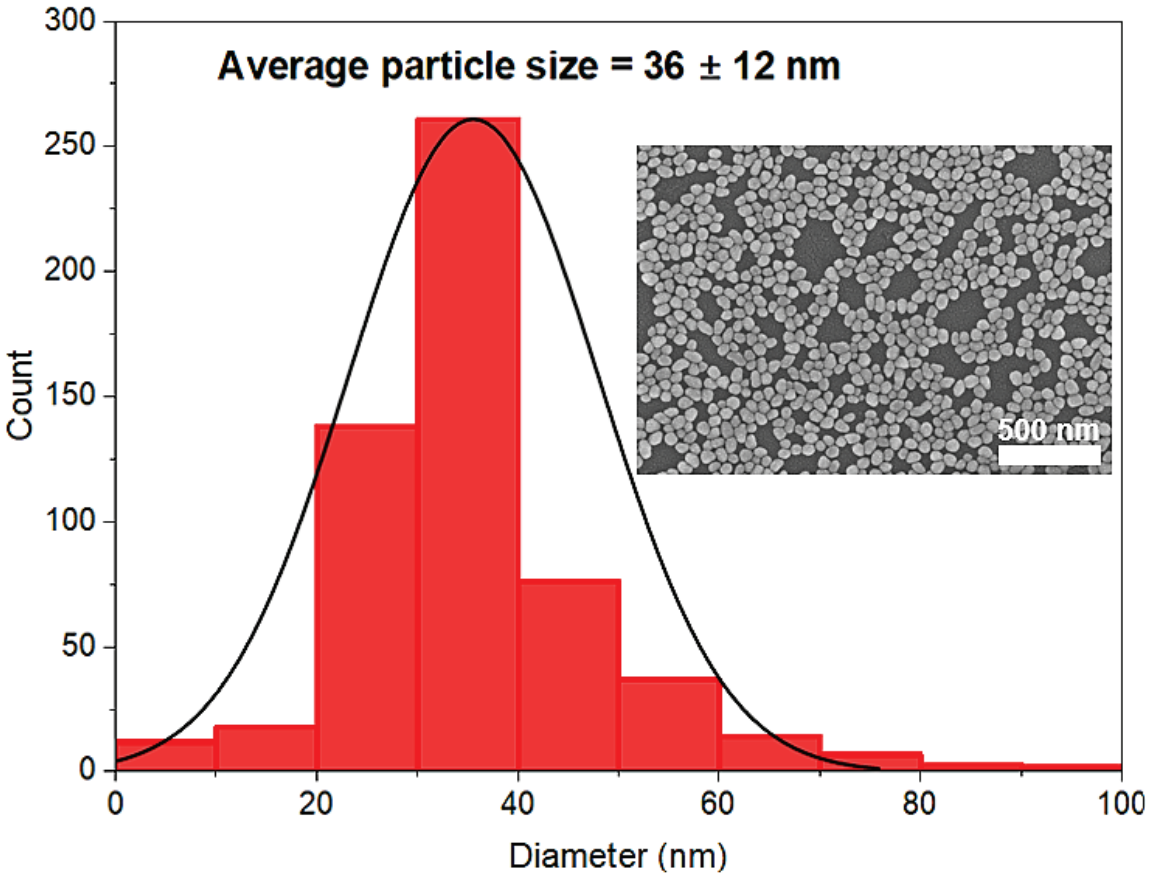

Figure 64: Size distribution of 55 nm gold nanoparticles (from average Zeta size) from SEM micrograph using ImageJ. The average nanoparticle size is approximately 36 nm.

5.3 Immobilisation of Gold Nanoparticles on the Nanopatterned Surface

In the previous experiment, we established a new proof of concept to immobilise gold and silver nanoparticles onto micro-patterns (800 µm and 50 µm). In the initial protocol, where we achieved reversible immobilisation of both gold and silver nanoparticles on micro-patterns (800 µm and 50 µm), we extended this method to immobilise 55 nm gold nanoparticles after unsuccessful attempts with the other two nanoparticles (45 nm and 80 nm) onto nanopatterned surfaces of the size range (20 nm, 40 nm, 100 nm and 500 nm). One of the challenges with immobilisation in a nanopattern includes the increased tendency of the nanoparticles to aggregate or change morphology as the size-to-particle ratio reduces or varies. [608] Apart from this, the concentration, solvent used, pH, and general environmental conditions must be well-tuned to achieve efficient immobilisation. [609] Despite these challenges, we successfully immobilised 55

nm gold nanoparticles onto a sub-500 nm nanopattern surface using the one-pot approach. This also suggests that the ‘one-pot’ immobilisation with the nanopattern approach was accompanied by simultaneous ligand exchange between the gold nanoparticles and the perfluorodecanethiol molecules, ensuring a thermodynamically feasible interaction to create a self-assembly monolayer (SAM). However, as the nanoparticles-to-pattern ratio reduces due to the size of the pattern (500 nm, 100 nm, 40 nm, and 20 nm), the tendency to create such reversible immobilisation using the same non-covalent interactions remains a challenge similar to what has been reported using a more complex protocol. [610] In the first instance, we attempted to use the smaller pattern that could direct the nanoparticles into the smallest region (20 nm size) of the pattern using the fluorous effect. This was a challenge as there was no feasible immobilisation of such using this simple protocol. This can be attributed to many factors, including the nanoparticle's size-to-pattern ratio, complexity due to e-beam lithography, failed ligand exchange, and concentration effect. With this challenge, our next idea was to focus on the larger particles with larger pattern sizes. Larger nanoparticles offer several advantages due to their ability to scatter light more efficiently, creating an amplified and stronger LSPR effect that could enhance the sensitivity. Apart from this, they are stable, less prone to aggregation, and have improved binding sites for ligand exchange.

5.3.1 One-pot Immobilisation of Gold Nanoparticles using Extended Methanol and IPA Sonication.

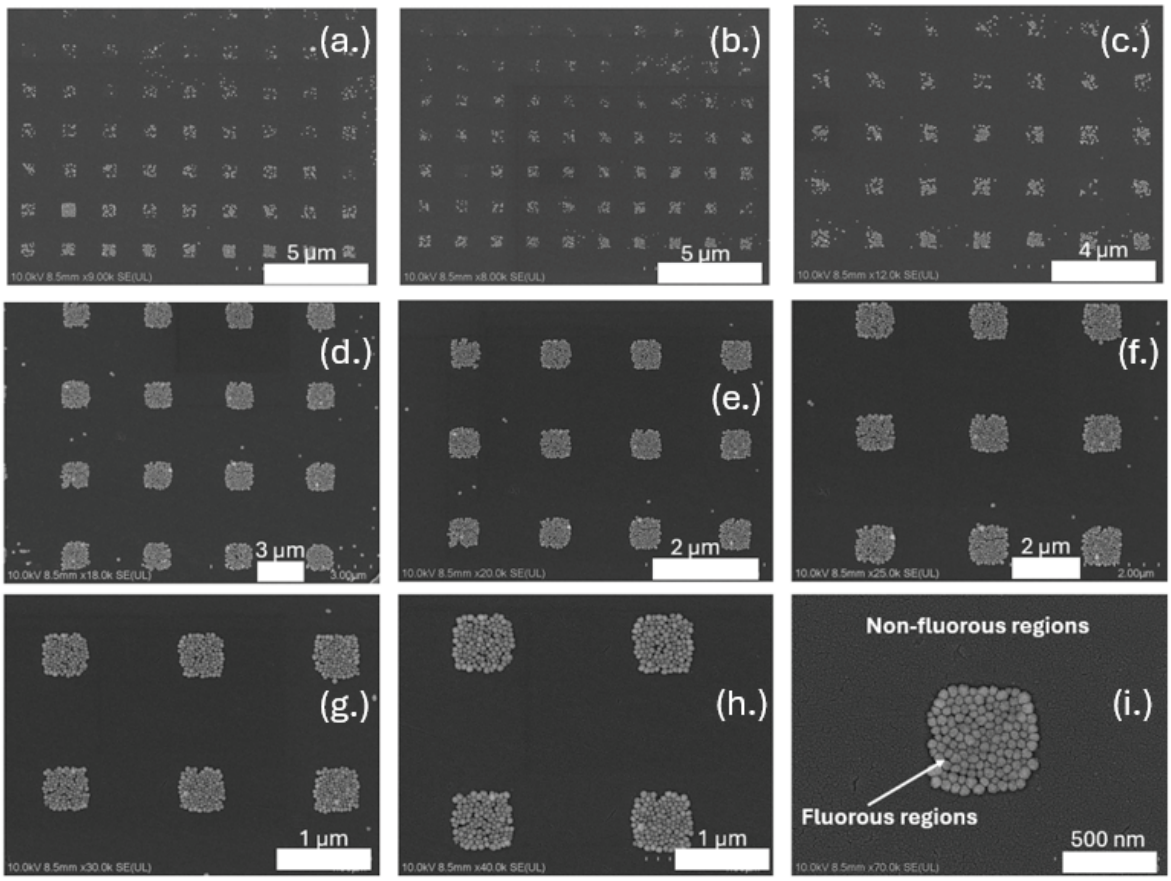

Figure 65: The figure illustrates the distribution of immobilised 55 nm gold nanoparticles across various EBL-patterned sizes, ranging from 5 µm to 500 nm. SEM micrographs (a), (b), and (c) display the immobilised gold nanoparticles on the 500 nm-sized nanopatterns, covering different regions of 5 µm, 5 µm, and 4 µm, respectively. Each micrograph shows distinct fluorous regions compared to the non-fluorous areas. Micrographs (d), (e), (f), (g), and (h) show the immobilised nanoparticles sized between 3 µm and 1 µm. The SEM micrograph (i) illustrates the immobilised gold nanoparticles arranged in a 500 nm pattern, highlighting the distinction between the fluorous and non-fluorous regions.

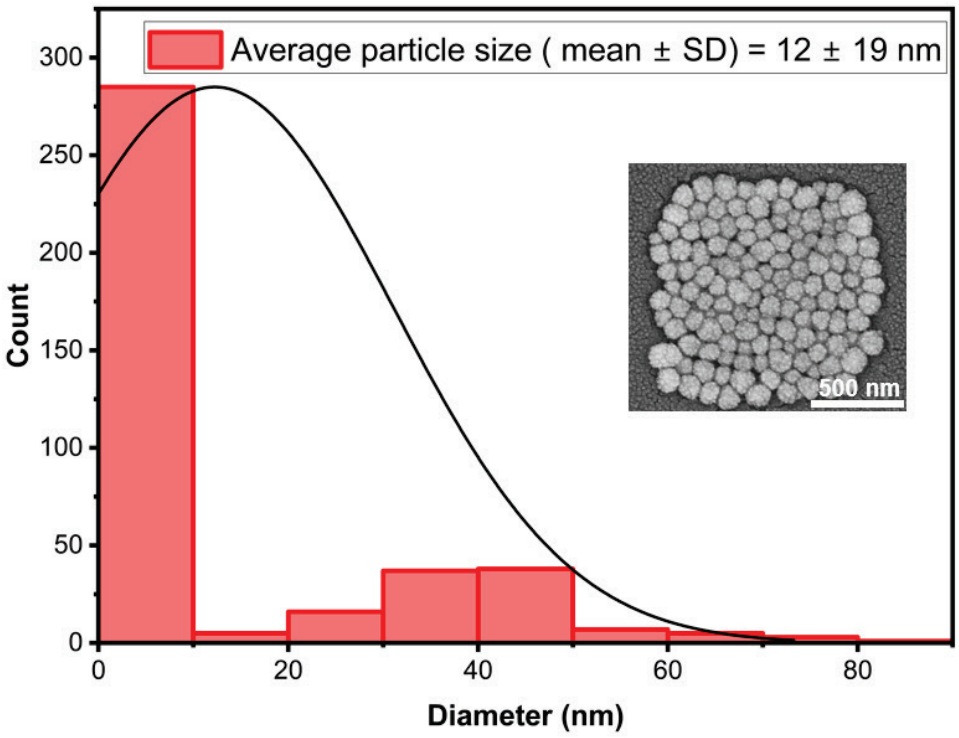

Figure 66: The figure shows the distribution of immobilised 55 nm gold nanoparticles on a patterned surface. ImageJ was used for size distribution analysis. This figure differs from Figure 64. The reason may be attributed to several factors highlighted in this thesis, including the selective immobilisation of functionalised NPs onto the modified nanopatterns.

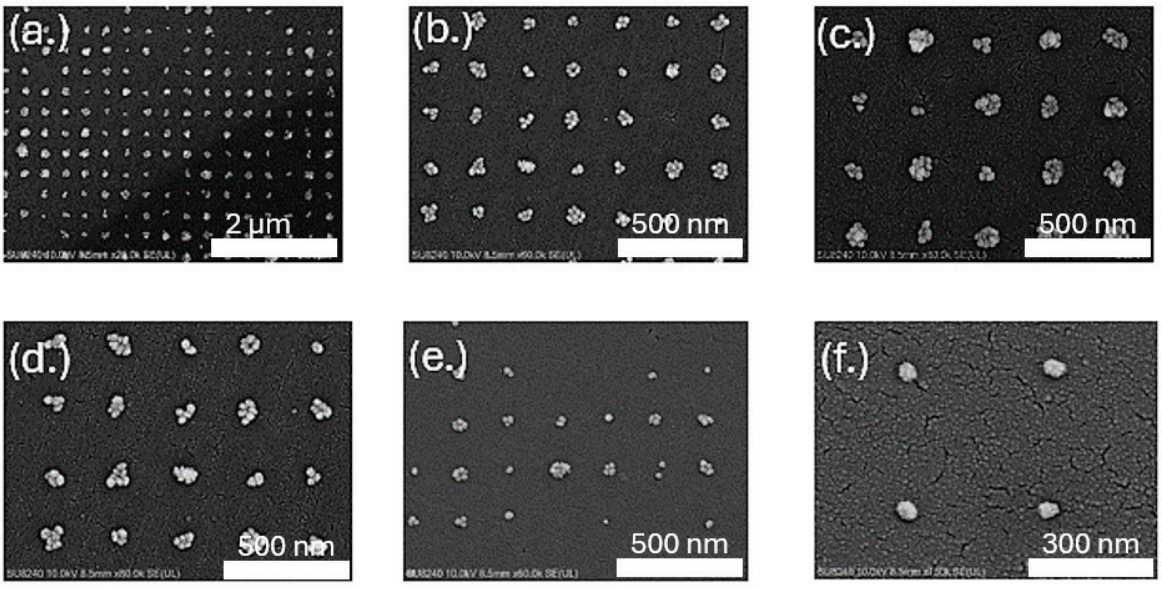

Figure 67: The SEM micrographs demonstrate the immobilisation of 55 nm gold nanoparticles on various regions of 100 nm-sized nanopatterns created through electron beam lithography using the fluorous effect. These images highlight the fluorous effect's capacity to selectively immobilise a small number of functionalised gold nanoparticles, ranging from 8 down to a single nanoparticle per region. Micrographs (a), (b), (c), and (d) display nanoparticle coverage across the entire nanopatterned surface. In contrast, micrographs (e) and (f) show a mix of nanoparticle counts, with numbers ranging from 1 to 5. Notably, micrograph (f) reveals the attachment of a single nanoparticle on a modified layer, although the repeatability and coverage was low at 100 nm. Various scale bars.

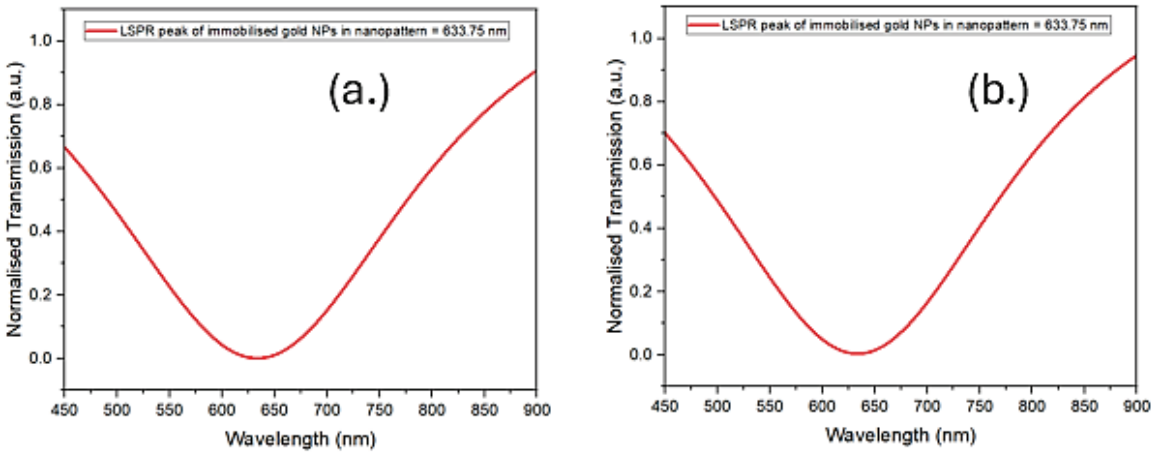

Figure 68: LSPR data of reversibly immobilised gold nanoparticles on 500 µm x 500 µm patterned surface using the fluorous effect. The first (a.) and second (b.) immobilisations showed the same absorption maxima of 633.75 nm, indicating the ability to repeat and reversibly immobilise the NPs on these fluorous-modified surfaces using the fluorous effect.

This approach reversibly immobilises 55 nm gold nanoparticles onto sub-500 nm patterns (Figure 65). To suit the objective of this design for sensing applications, it was possible to acquire real-time spectra information of the reversibly immobilised nanoparticles on the same patterned surface (Figure 68). This is the first time this simple method has been reported using the fluorous effect.

Furthermore, this protocol was extended to immobilise individual nanoparticles on the fabricated nanopatterns (Figure 67). This approach aimed to overcome the common barriers to the successful immobilisation of single particles by precisely controlling the spatial arrangement of individual nanoparticles on the desired surface. This arrangement allows for the creation of nanostructures with tailored properties useful for biosensing, electrical, and optical applications.[611–613] This method also used the fluorous effect to immobilise nanoparticles arranged in ones, twos, threes, and multiple arrangements of up to 8 nanoparticles per region. This further confirms our hypothesis that the fluorous effect can direct the immobilisation of nanoparticles onto fluorous-modified surfaces to form an organised, self-assembled monolayer suitable for various applications.

Although challenges such as incomplete coverage arise during the immobilisation of these nanoparticles on other areas of the fluorous-modified nanopatterned surface using this method (Figure 67), this could be attributed to several factors, including incomplete ligand exchange or unsustainable van der Waal's interactions as the particle immobilisation moves from esembling to single nanoparticles immobilisation, and solution concentrations among other reasons. In addition to

these, no or incomplete coverage could arise due to several factors, including changes in immobilisation kinetics, temperature, surface energy heterogeneity, inefficient surface chemistry and differences in topography [614–616] Therefore, tuning the concentrations of the particles and ensuring a proper solvent exchange after immobilisation appears to be one of the critical points to prevent disruption of non-covalent interactions, encourage stability, and ensure continuous immobilisation of the nanoparticles within such critical nanoscale limits. Expectedly, the incomplete removal of resist using this method remains challenging (Figure 69). Hence, further research will be needed to optimise this method and explore its potential for molecular trapping or other biomedical applications.[617–619]

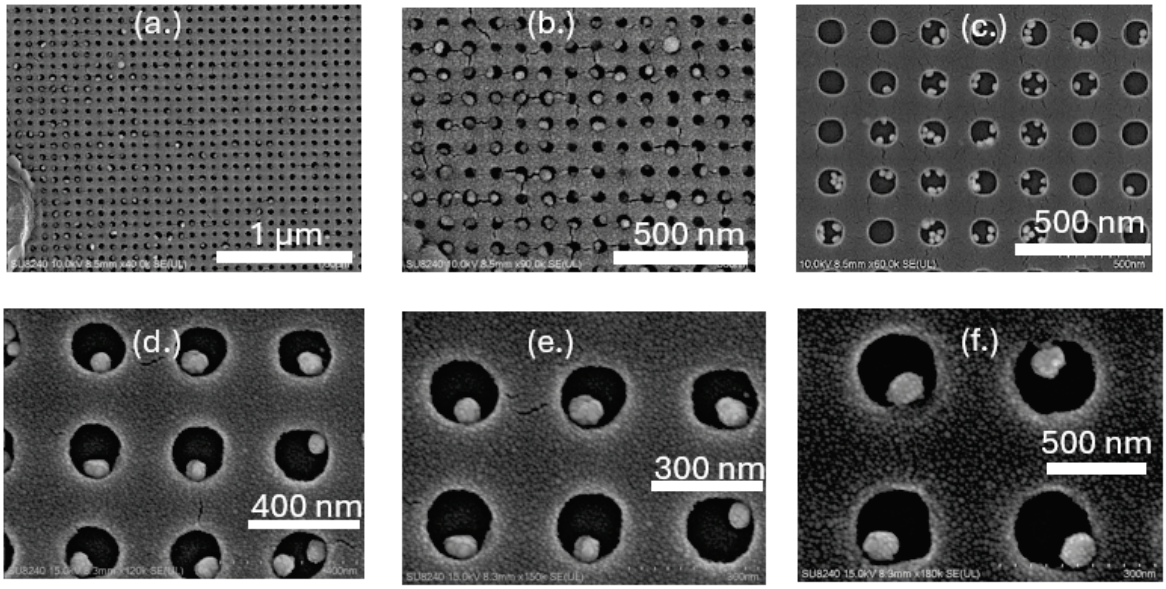

Figure 69: The SEM micrograph illustrates the immobilisation of gold nanoparticles on a 100 nm nanopattern size. The challenge with the incomplete removal of resist remains a hindrance in this method (a-c). This method can also immobilise individual NPs (d., e., and f.) but requires further optimisation. Therefore, it could be adapted for other similar research.

5.3.2 One-Pot Immobilisation using pre-Functionalised Gold Nanoparticles with Acetone-Lift off (with unwanted drying)

In the previous sections, we used the fluorous effect to selectively immobilise gold nanoparticles in sub-500 nm nanopatterns. The current section aims to create reaction dynamics to improve ligand exchange, surface coverage, and efficient immobilisation. Technically, the route of this immobilisation would be achieved with efficient ligand exchange in such a way that citrate is displaced by sulphur to generate a stable gold-sulphur bond, creating thiol-coated gold nanoparticles,

with simultaneous or phase-induced immobilisation, depending on the thermodynamics of the reactions.[620] With this in mind, 55 nm gold nanoparticles were pre-functionalised using our previous water-based protocol for 20 nm gold nanoparticles and introduced into the reaction mixture. [621] These results further supported our assumptions that efficient ligand exchange is critical in immobilising these nanoparticles onto nanopatterns. Using acetone as the preferred solvent for lift-off, the surface of the 500 µm x 500 µm layer was covered, creating a distinct fluorous from the non-fluorous background. It could also be used to immobilise single particles using well-controlled conditions. Compared with the earlier surface, this method creates more sample coverage and is promising for single-particle immobilisation due to better ligand exchange during functionalisation (Figure 70). While this method shows potential and could be applied to other applications with no need for reversible immobilisation, the effect created through drying does not entirely align with our goal to create a reversible surface in a solution. Hence, further optimisation was needed.

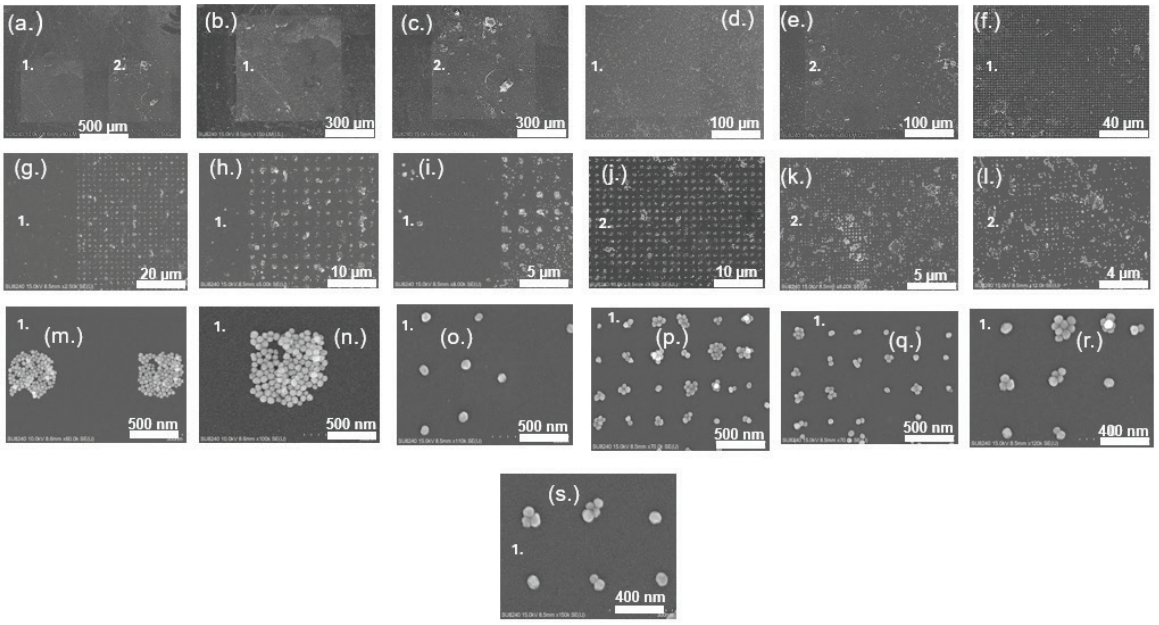

Figure 70: The SEM micrographs (a) to (s) show the immobilisation of 55 nm gold nanoparticles on a sub-500 nm fluorous-modified surface using the acetone-lifted-off method with drying. In Figure (a), patterns (1) and (2) represent two different regions from a 500 µm by 500 µm fluorous patterned surface, each with 500 nm and 100 nm size, respectively. (b.), (d.) and (f.) represent an enlarged 500 nm pattern size from (1.) at 300, 100 and 40 µm magnifications. g., h. and i. represent the immobilised AuNPs on a patterned 500 nm sized surface showing the non-fluorous from the fluorous regions at 20, 10 and 5 µm, respectively. (m.), (n.), (i.,) and (p.,) show the immobilised nanoparticles in the nanometer range on the same region of the pattern. Likewise, (c.) and (e.) represent an enlarged 100 nm pattern size from (2.) at 300 and 100 µm magnifications.(j.),(k.), and (l.) represent the central region of the immobilised AuNPs on a 100 µm patterned surface from (2), at 10, 5 and 4 µm magnifications respectively. This study highlighted the significance of efficient ligand exchange, the influence of drying during immobilisation, and the need for optimisation without surface drying using the fluorous effect.

5.3.3 One-Pot Immobilisation of Gold Nanoparticles with Acetone Lift-Off (No Drying)

Efficient immobilisation is encouraged by optimum conditions that favour the interactions of multiple species during ligand exchange and self-assembly of individual atoms. In the current method, we attempted the "one-pot" synthesis approach using our previous protocol, which involved simultaneous ligand exchange without needing multiple steps or drying. Acetone is the gold standard for most PMMA-resist lift-offs, especially for surfaces fabricated using e-beam lithography. Our objective was to enhance the ligand exchange and improve the surface coverage at the nanoscale, which was previously inconsistent and not as effective as desired.

The results showed that ‘one-pot’ ligand exchange and simultaneous immobilisation are possible with the right thermodynamic conditions and appropriate concentrations. Furthermore, the nanoparticles were immobilised on the fluorous patterned region, distinct from the non-patterned regions. This revealed specific interactions due to fluorous effects. Again, this is the first time this has been reported in any research where simultaneous ligand exchange and immobilisation of metal nanoparticles takes place in a liquid environment, especially at the sub-500 nm scale. Comparatively, the outcome of the immobilisation achieved using this method shows improved surface coverage (Figure 71). Consequently, ensembling the nanoparticles was possible but challenging for single-particle immobilisation. This could be attributed to the nature of the non-covalent interaction and other conditions unfavourable to assembling single nanoparticles on fluorous patterned surfaces. Hence, improving several parameters could enhance the optimisation of this protocol, which could come with additional laborious steps.[622–624]

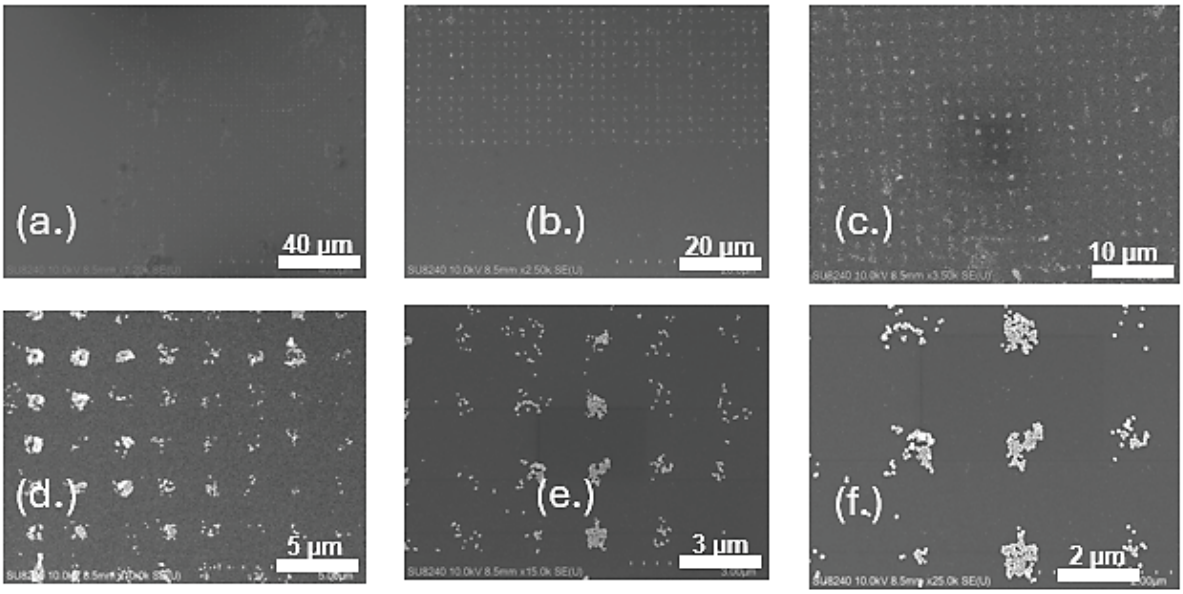

Figure 71: The images (a) through (f) show the immobilisation of 55 nm gold nanoparticles on an acetone-lifted off sub-500 nm fluorous modified surface without drying during the 'one-pot' incubation. This method is promising as it shows a distinct fluorous layer from the non-fluorous background and can be optimised for single-particle immobilisation.

Apart from this directed immobilisation, the fluorous effect can also form randomly self-assembled functionalised gold nanoparticles on a bare surface elf-assembled layer (appendix 3).

5.4 Conclusion and Future Work

In this thesis, we designed and investigated using a reconfigurable metasurface suitable for the reversible attachment of fluorous-tagged nanomaterials on a fluorous-modified surface without damaging the surface integrity using the fluorous effect. Initially, we explored using this method to immobilise fluorous-tagged DNA molecules with varying features such as length, number of fluorine atoms, HEG-linker, and branch system. The results revealed that perfluorinated tags could direct specific and repeatable interactions between fluorous-modified molecules using the fluorous effect. In addition, this method can be applied to selectively remove the immobilised DNA molecules based on their strengths. To demonstrate the simplicity and efficiency of this method, we successfully removed the immobilised fluorous-tagged DNA duplex from the solid support using a simple methanol wash. Using the fluorous effect, this outcome revealed specific, selective, and repeatable immobilisation of nanomaterials suitable for various microarray applications, including simplex and multiplex.

We extended this protocol to allow the reversible attachment of thiol-functionalized gold and silver nanoparticles. This method facilitates the switching of surface attachment between the two types of nanoparticles, allowing for the refreshing of the surface each time a new set of nanoparticles is introduced. This is of particular importance due to the colourimetric properties of the nanoparticles, which change based on their local environment, enabling real-time visual observation. Therefore, this method offers a cost-effective, environmentally friendly, and less complex alternative to traditional methods, making it useful in various fields.

Finally, we revealed that nanoparticle attachment on solid support can be achieved by controlling the number and aggregation state of the colloidal system. Using the same concept, we achieved the reversible attachment of gold and silver nanoparticles on micro-patterned (800 μm) surfaces. Using this method, it was also possible to reversibly immobilise 55 nm gold nanoparticles on fluorous modified nanopatterned (sub-500 nm) surfaces. The same process has a promising potential in the sub-100 nm region, providing an opportunity for single nanoparticle attachment.

This research also identified many challenges that can impede or ensure the successful immobilisation of these nanomaterials on engineered surfaces using the fluorous effect. These include:

1. The Nature of the Fluorous Effect

The fluorous effect is a non-covalent interaction between perfluorinated molecules or molecules with many fluorine atoms, fit enough to be termed fluorous. Due to these interactions, care must be taken during solvent exchange to prevent disruption of van der Waal's and other non-covalent interactions. This was informed because this interaction can be sustained when the drying method was adopted during one of the immobilisation protocols with late solvent exchange. Hence, we assume that this must have influenced the retention or disruption of these bonds and the stability of the functionalised nanoparticles during the immobilisation stage.

2. **The Concentration of the Metal Nanoparticles per ml of Colloids**

Using the fluorous effect, we successfully immobilised silver and gold nanoparticles due to the effective ligand exchange and subsequent or simultaneous immobilisation of the nanoparticles on a fluorous-modified surface at the microscale level. Varying the concentrations of colloidal mixtures improves immobilisation by reducing the nanoparticles per nm^2. However, challenges ensue once the size of the nanopattern reduces, especially in the sub-100 nm regions, where each nanopattern competes for millions of nanoparticles/mL. Therefore, maintaining a balance between the number of conjugated or bare nanoparticles and the size of the nanopattern at every stage of the immobilisation is integral to successful immobilisation. Therefore, careful introduction of colloidal suspension into the reaction mix is also paramount as this could create a settling effect that can cause multiple layers of nanoparticles at thermodynamic equilibrium.

3. **Efficient Salinisation**

Immobilisation will not occur without successful silanisation to create a self-assembly of the initial silanes on the glass or other surfaces. The vacuum silanisation method appears effective in creating a self-assembly of

perfluorosilane. However, we believe that other challenges highlighted above are inherent in hindering the immobilisation of the nanoparticles.

4. Size and Pattern Limitation

Using the fluorous effect, this thesis developed a protocol to reversibly immobile metal nanoparticles on micro (gold and silver) and nanopatterned surfaces (gold nanoparticles). While this new protocol is often easily reproducible and adaptable for the micropatterned surface, it is only reproducible in the sub-500 nm regions. Attempts to create immobilised nanoparticles in sub-100 nm size are feasible but proved difficult and hardly reversible with the current non-covalent interaction method using the fluorous effect. This could be attributed to several factors limiting the precise control and immobilisation of the nanoparticles, including the nature of the interactions, the concentration of the colloidal system, silanisation, nanofabrication methods or the environment in which the substrate was dispersed, inefficient ligand exchange and the tendency of aggregation, and random surface coverage. Further research to optimise the size-to-pattern ratio, especially the sub-100 nm, is essential to achieve reversible and repeatable immobilisation. Additionally, incubating the reaction mixture in a suitable solvent concentration is crucial.

5. Incubation time

Most self-assembly monolayer studies usually take place within seconds. The remaining incubation times are for bond re-ordering and stability. With our new protocol, we have been able to prove beyond reasonable doubt how this new protocol works using the fluorous effect, irrespective of the immobilisation or incubation time. Despite this success, further research still needs to be conducted to identify the nature of each interaction per time. This way, important information can be derived and tailored for specific applications. [625]

In the future, we plan to optimise and customise this method to create a suitable platform for various tailored applications requiring the reversible attachment of nanomaterials. This approach is promising and can adapted to different areas of research, including but not limited to:

a. Targeted Drug Delivery: This method can be adapted for the controlled release of drugs in a drug delivery system where therapeutic agents (such as nanoparticles loaded with drugs) can be attached to and detached from

specific sites in the body. This allows for precise control over the timing and location of drug release, improving treatment efficacy and reducing side effects. In regenerative medicine, these nanomaterials can be reversibly attached to scaffolds or implants to promote tissue regeneration. The nanomaterials can be removed once the healing is underway to prevent potential long-term side effects.

b. Advanced Electronics and Optoelectronics: In reconfigurable circuits, reversible immobilisation enables the dynamic reconfiguration of the electronic circuit at the nanoscale. Hence, optimising this method can create adaptive and reprogrammable electronic devices, enhancing their versatility and functionality. Also, in optical devices, nanomaterials with unique optical properties can be functionalised and reversibly attached to surfaces to create tunable optoelectronic devices. This can be used in dynamic displays, sensors, and communication systems.
c. Catalysis and Chemical Synthesis: One of the significant challenges of nanocatalysts is the inability to recover or reuse them after product formation. Creating a reversible reactor surface capable of easy removal and regeneration of the catalyst is desirable. This increases the efficiency and lifespan of catalytic processes in chemical manufacturing and environmental applications. Also, creating selective attachments and detachments of the nanomaterials with specific catalytic properties enables the selective activation of different reactions, improving the precision and yield of chemical synthesis.
d. Improved Microarray and Biosensor Technology: Reversible immobilisation is suitable for developing microarrays for high-throughput screening of biomolecules, such as DNA, proteins, and small molecules. This reduces costs and increases the efficiency of diagnostic and research applications. It is essential to create a refreshable surface for biosensors to enhance their sensitivity and selectivity. These nanomaterials can be detached, cleaned, and reattached, ensuring consistent performance and extending the sensor's lifespan.
e. Environmental Remediation: Functionalising nanomaterials designed to bind specific contaminants can be reversibly immobilised on surfaces deployed in water or soil. Once the pollutants are captured, the nanomaterials can be detached and regenerated for reuse, making the

process more sustainable and cost-effective. Reusable sensors can also be used to create sensors that can detect pollutants. Once a sensor's capacity is reached, the nanomaterials can be detached, cleaned, and reattached to restore sensor functionality.

References

1. Schena M, Shalon D, Davis RW, Brown PO (1995) Quantitative Monitoring of Gene Expression Patterns with a Complementary DNA Microarray. Science (1979) 270:467–470. https://doi.org/10.1126/SCIENCE.270.5235.467
2. Bumgarner R (2013) Overview of DNA Microarrays: Types, Applications, and Their Future. Curr Protoc Mol Biol 101:22.1.1-22.1.11. https://doi.org/10.1002/0471142727.MB2201S101
3. Barouki R, Kogevinas M, Audouze K, et al (2021) The COVID-19 pandemic and global environmental change: Emerging research needs. Environ Int 146:. https://doi.org/10.1016/j.envint.2020.106272
4. Boukoufi C, Boudier A, Lahouari S, et al (2023) Activity and reusability of immobilized gold nanoparticles for the catalysis of both oxidation and reduction reactions. Results Chem 5:100979. https://doi.org/10.1016/J.RECHEM.2023.100979
5. Tang L, Wang X, Guo B, et al (2013) Salt-triggered liquid phase separation and facile nanoprecipitation of aqueous colloidal gold dispersion in miscible biofluids for direct chromatographic measurement. RSC Adv 3:15875–15886. https://doi.org/10.1039/C3RA40676H
6. Nimse SB, Song K, Sonawane MD, et al (2014) Immobilization Techniques for Microarray: Challenges and Applications. Sensors 2014, Vol 14, Pages 22208-22229 14:22208–22229. https://doi.org/10.3390/S141222208
7. Forster A, Junger M (2022) Opportunities and challenges for commercializing microarray patches for vaccination from a MAP developer's perspective. Hum Vaccin Immunother 18:. https://doi.org/10.1080/21645515.2022.2050123
8. Bolon-Canedo V, Alonso-Betanzos A, Lopez-de-Ullibarri I, Cao R (2019) Challenges and Future Trends for Microarray Analysis. Methods Mol Biol 1986:283–293. https://doi.org/10.1007/978-1-4939-9442-7_14
9. Rahman M, Heng LY, Futra D, Ling TL (2017) Ultrasensitive Biosensor for the Detection of Vibrio cholerae DNA with Polystyrene-co-acrylic Acid Composite Nanospheres. Nanoscale Res Lett 12:1–12. https://doi.org/10.1186/S11671-017-2236-0
10. Zhang X, Xu W, Tan J, Zeng Y (2009) Stripping custom microRNA microarrays and the lessons learned about probe–slide interactions. Anal Biochem 386:222–227. https://doi.org/10.1016/J.AB.2008.12.008
11. Shaskolskiy B, Kandinov I, Kravtsov D, et al (2021) Hydrogel droplet microarray for genotyping antimicrobial resistance determinants in neisseria gonorrhoeae isolates. Polymers (Basel) 13:3889. https://doi.org/10.3390/POLYM13223889
12. Krämer SD, Wöhrle J, Meyer PA, et al (2019) How to copy and paste DNA microarrays. Scientific Reports 2019 9:1 9:1–10. https://doi.org/10.1038/s41598-019-50371-1
13. Gladysz JA, Jurisch M (2012) Structural, physical, and chemical properties of fluorous compounds. Top Curr Chem 308:1–24. https://doi.org/10.1007/128_2011_282
14. Barthel-Rosa LP, Gladysz JA (1999) Chemistry in fluorous media: a user's guide to practical considerations in the application of fluorous catalysts and reagents. Coord Chem Rev 190–192:587–605. https://doi.org/10.1016/S0010-8545(99)00102-2
15. Horváth IT, Rábai J (1994) Facile Catalyst Separation Without Water: Fluorous Biphase Hydroformylation of Olefins. Science (1979) 266:72–75. https://doi.org/10.1126/SCIENCE.266.5182.72

16. Gladysz JA, Curran DP (2002) Fluorous chemistry: from biphasic catalysis to a parallel chemical universe and beyond. Tetrahedron 58:3823–3825. https://doi.org/10.1016/S0040-4020(02)00222-3
17. Xu Z, Oleschuk RD (2014) A study of the methylene/perfluormethylene selectivity of porous polymer monolithic stationary phases exhibiting different fluorous/hydrophobic content. J Chromatogr A 1329:61–70. https://doi.org/10.1016/J.CHROMA.2013.12.032
18. Gladysz JA, Curran DP (2002) Fluorous chemistry: from biphasic catalysis to a parallel chemical universe and beyond. Tetrahedron 58:3823–3825. https://doi.org/10.1016/S0040-4020(02)00222-3
19. Shah P, Westwell AD (2007) The role of fluorine in medicinal chemistry. J Enzyme Inhib Med Chem 22:527–540. https://doi.org/10.1080/14756360701425014
20. Tian P, Feng C, Loh TP (2015) Rhodium-catalysed C(sp2)–C(sp2) bond formation via C–H/C–F activation. Nature Communications 2015 6:1 6:1–7. https://doi.org/10.1038/ncomms8472
21. Berger R, Resnati G, Metrangolo P, et al (2011) Organic fluorine compounds: a great opportunity for enhanced materials properties. Chem Soc Rev 40:3496–3508. https://doi.org/10.1039/C0CS00221F
22. Cametti M, Crousse B, Metrangolo P, et al (2011) The fluorous effect in biomolecular applications. Chem Soc Rev 41:31–42. https://doi.org/10.1039/C1CS15084G
23. Casa S, Henary M, Zhang W, et al (2021) Synthesis and Applications of Selected Fluorine-Containing Fluorophores. Molecules 2021, Vol 26, Page 1160 26:1160. https://doi.org/10.3390/MOLECULES26041160
24. Matsui M (2006) Fluorine-containing dyes. Functional Dyes 257–266. https://doi.org/10.1016/B978-044452176-7/50008-5
25. Tressaud A (2019) Fluorine, a key element for the 21st century. Fluorine 77–150. https://doi.org/10.1016/B978-0-12-812990-6.00002-7
26. Kirsch P (2005) Modern Fluoroorganic Chemistry: Synthesis, Reactivity, Applications. Modern Fluoroorganic Chemistry: Synthesis, Reactivity, Applications 1–308. https://doi.org/10.1002/352760393X
27. Budisa N, Kubyshkin V, Schulze-Makuch D (2014) Fluorine-Rich Planetary Environments as Possible Habitats for Life. Life : Open Access Journal 4:374. https://doi.org/10.3390/LIFE4030374
28. Krafft MP (2001) Fluorocarbons and fluorinated amphiphiles in drug delivery and biomedical research. Adv Drug Deliv Rev 47:209–228. https://doi.org/10.1016/S0169-409X(01)00107-7
29. Henary E, Casa S, Dost TL, et al (2024) The Role of Small Molecules Containing Fluorine Atoms in Medicine and Imaging Applications. Pharmaceuticals 2024, Vol 17, Page 281 17:281. https://doi.org/10.3390/PH17030281
30. Smart BE (2001) Fluorine substituent effects (on bioactivity). J Fluor Chem 109:3–11. https://doi.org/10.1016/S0022-1139(01)00375-X
31. Cavallo G, Metrangolo P, Milani R, et al (2016) The Halogen Bond. Chem Rev 116:2478–2601. https://doi.org/10.1021/ACS.CHEMREV.5B00484
32. Flynn GE, Withers JM, Macias G, et al (2017) Reversible DNA micro-patterning using the fluorous effect. Chemical Communications 53:3094–3097. https://doi.org/10.1039/C7CC00288B
33. Meanwell NA (2018) Fluorine and Fluorinated Motifs in the Design and Application of Bioisosteres for Drug Design. J Med Chem 61:5822–5880. https://doi.org/10.1021/acs.jmedchem.7b01788

34. Bassanini I, Galli C, Ferrandi EE, et al (2020) Perfluorinated Probes for Noncovalent Protein Recognition and Isolation. Bioconjug Chem 31:513–519. https://doi.org/10.1021/ACS.BIOCONJCHEM.9B00846
35. Neil E, Marsh G (2000) Towards the nonstick egg: Designing fluorous proteins. Chem Biol 7:R153–R157. https://doi.org/10.1016/S1074-5521(00)00139-3
36. Gerig JT (1994) Fluorine NMR of proteins. Prog Nucl Magn Reson Spectrosc 26:293–370. https://doi.org/10.1016/0079-6565(94)80009-X
37. O'Hagan D, Rzepa HS (1997) Some influences of fluorine in bioorganic chemistry. Chemical Communications 645–652. https://doi.org/10.1039/A604140J
38. Neil E, Marsh G (2000) Towards the nonstick egg: Designing fluorous proteins. Chem Biol 7:R153–R157. https://doi.org/10.1016/S1074-5521(00)00139-3
39. Zou J, Stammers AC, Taladriz-Sender A, et al (2023) Fluorous-Directed Assembly of DNA Origami Nanostructures. ACS Nano 17:752–759. https://doi.org/10.1021/acsnano.2c10727
40. Zou J, Stammers AC, Taladriz-Sender A, et al (2023) Fluorous-Directed Assembly of DNA Origami Nanostructures. ACS Nano 17:752–759. https://doi.org/10.1021/acsnano.2c10727
41. Flynn GE, Withers JM, Macias G, et al (2017) Reversible DNA micro-patterning using the fluorous effect. Chemical Communications 53:3094–3097. https://doi.org/10.1039/C7CC00288B
42. Bueno-Alejo CJ, Vega MS, Chaplin AK, et al (2022) Surface Passivation with a Perfluoroalkane Brush Improves the Precision of Single-Molecule Measurements. ACS Appl Mater Interfaces 14:49604–49616. https://doi.org/10.1021/acsami.2c16647
43. Brolo AG (2012) Plasmonics for future biosensors. Nature Photonics 2012 6:11 6:709–713. https://doi.org/10.1038/nphoton.2012.266
44. Daghestani HN, Day BW (2010) Theory and Applications of Surface Plasmon Resonance, Resonant Mirror, Resonant Waveguide Grating, and Dual Polarization Interferometry Biosensors. Sensors 2010, Vol 10, Pages 9630-9646 10:9630–9646. https://doi.org/10.3390/S101109630
45. Aftab M, Mansha MS, Iqbal T, Farooq M (2023) Surface Plasmon Excitation: Theory, Configurations, and Applications. Plasmonics 1:1–19.https://doi.org/10.1007/s11468-023-02095-2
46. Kretschmann E, Raether H (1968) Radiative Decay of Non Radiative Surface Plasmons Excited by Light. Zeitschrift fur Naturforschung - Section A Journal of Physical Sciences 23:2135–2136. https://doi.org/10.1016/0030-4018(72)90224-6
47. Otto A (1968) Excitation of nonradiative surface plasma waves in silver by the method of frustrated total reflection. Zeitschrift für Physik 216:398–410. https://doi.org/10.1007/BF01391532
48. Sharma AK, Jha R, Gupta BD (2007) Fiber-optic sensors based on surface plasmon resonance: A comprehensive review. IEEE Sens J 7:1118–1129. https://doi.org/10.1109/JSEN.2007.897946
49. Anh NH, Doan MQ, Dinh NX, et al (2022) Gold nanoparticle-based optical nanosensors for food and health safety monitoring: recent advances and future perspectives. RSC Adv 12:10950–10988. https://doi.org/10.1039/D1RA08311B
50. Wang C, Zhao XP, Xu QY, et al (2018) Importance of Hot Spots in Gold Nanostructures on Direct Plasmon-Enhanced Electrochemistry. ACS Appl Nano Mater 1:5805–5811. https://doi.org/10.1021/acsanm.8b01436
51. Anh NH, Doan MQ, Dinh NX, et al (2022) Gold nanoparticle-based optical nanosensors for food and health safety monitoring: recent advances and future perspectives. RSC Adv 12:10950–10988. https://doi.org/10.1039/D1RA08311B

52. He Z, Li F, Liu Y, et al (2020) Principle and Applications of the Coupling of Surface Plasmons and Excitons. Applied Sciences 2020, Vol 10, Page 1774 10:1774. https://doi.org/10.3390/APP10051774
53. Islam K, Alnuaimi A, Battal E, et al (2014) Effect of gold nanoparticles size on light scattering for thin film amorphous-silicon solar cells. Solar Energy 103:263–268. https://doi.org/10.1016/J.SOLENER.2014.02.023
54. Hosseini-Benhangi P, Tomlinson M, Asselin E, et al (2018) Nanoparticle Optical Properties: Size Dependence of a Single Gold Spherical Nanoparticle. J Phys Conf Ser 1083:012040. https://doi.org/10.1088/1742-6596/1083/1/012040
55. Wu JZ, Ghopry SA, Liu B, Shultz A (2023) Metallic and Non-Metallic Plasmonic Nanostructures for LSPR Sensors. Micromachines 2023, Vol 14, Page 1393 14:1393. https://doi.org/10.3390/MI14071393
56. Oka H, Ohdaira Y (2018) Simple model of saturable localised surface plasmon. Scientific Reports 2018 8:1 8:1–8. https://doi.org/10.1038/s41598-018-20880-6
57. Anik MI, Mahmud N, Masud A Al, Hasan M (2022) Gold nanoparticles (GNPs) in biomedical and clinical applications: A review. Nano Select 3:792–828. https://doi.org/10.1002/NANO.202100255
58. Gao Q, Zhang J, Gao J, et al (2021) Gold Nanoparticles in Cancer Theranostics. Front Bioeng Biotechnol 9:647905. https://doi.org/10.3389/fbioe.2021.647905
59. Anker JN, Hall WP, Lyandres O, et al (2008) Biosensing with plasmonic nanosensors. Nature Materials 2008 7:6 7:442–453. https://doi.org/10.1038/nmat2162
60. Liz-Marzán LM (2006) Tailoring surface plasmons through the morphology and assembly of metal nanoparticles. Langmuir 22:32–41. https://doi.org/10.1021/la0513353
61. Homola J (2006) Surface Plasmon Resonance Based Sensors. 4:. https://doi.org/10.1007/B100321
62. Cao X, Ye Y, Liu S (2011) Gold nanoparticle-based signal amplification for biosensing. Anal Biochem 417:1–16. https://doi.org/10.1016/J.AB.2011.05.027
63. Su V-C, Tsai DP, Chu CH, Sun G (2018) Advances in optical metasurfaces: fabrication and applications [Invited]. Optics Express, Vol 26, Issue 10, pp 13148-13182 26:13148–13182. https://doi.org/10.1364/OE.26.013148
64. Neshev D, Aharonovich I (2018) Optical metasurfaces: new generation building blocks for multi-functional optics. Light: Science & Applications 2018 7:1 7:1–5. https://doi.org/10.1038/s41377-018-0058-1
65. Ren MX, Wu W, Cai W, et al (2016) Reconfigurable metasurfaces that enable light polarization control by light. Light: Science & Applications 2017 6:6 6:e16254–e16254. https://doi.org/10.1038/lsa.2016.254
66. Sharma J, Imae T (2009) Recent Advances in Fabrication of Anisotropic Metallic Nanostructures. J Nanosci Nanotechnol 9:19–40. https://doi.org/10.1166/JNN.2009.J087
67. Barmparis GD, Lodziana Z, Lopez N, Remediakis IN (2015) Nanoparticle shapes by using Wulff constructions and first-principles calculations. Beilstein Journal of Nanotechnology 6:35 6:361–368. https://doi.org/10.3762/BJNANO.6.35
68. Neouze MA, Schubert U (2008) Surface modification and functionalization of metal and metal oxide nanoparticles by organic ligands. Monatsh Chem 139:183–195. https://doi.org/10.1007/s00706-007-0775-2
69. Barar J (2015) Bioimpacts of nanoparticle size: why it matters? Bioimpacts 5:113. https://doi.org/10.15171/BI.2015.23
70. Krpetić Ž, Guerrini L, Larmour IA, et al (2012) Importance of Nanoparticle Size in Colorimetric and SERS-Based Multimodal Trace Detection of Ni(II) Ions with

Functional Gold Nanoparticles. Small 8:707–714. https://doi.org/10.1002/SMLL.201101980
71. Han X, Xu K, Taratula O, Farsad K (2019) Applications of Nanoparticles in Biomedical Imaging. Nanoscale 11:799. https://doi.org/10.1039/C8NR07769J
72. Ankamwar B, Ankamwar B (2012) Size and Shape Effect on Biomedical Applications of Nanomaterials. Biomedical Engineering - Technical Applications in Medicine. https://doi.org/10.5772/46121
73. Dolai J, Mandal K, Jana NR (2021) Nanoparticle Size Effects in Biomedical Applications. ACS Appl Nano Mater 4:6471–6496. https://doi.org/10.1021/acsanm.1c00987
74. Kelly KL, Coronado E, Zhao LL, Schatz GC (2003) The optical properties of metal nanoparticles: The influence of size, shape, and dielectric environment. Journal of Physical Chemistry B 107:668–677. https://doi.org/10.1021/jp026731y
75. Saha K, Agasti SS, Kim C, et al (2012) Gold Nanoparticles in Chemical and Biological Sensing. Chem Rev 112:2739. https://doi.org/10.1021/CR2001178
76. Daniel M-C, Astruc D (2004) Gold Nanoparticles: Assembly, Supramolecular Chemistry, Quantum-Size-Related Properties, and Applications toward Biology, Catalysis, and Nanotechnology. https://doi.org/10.1021/CR030698
77. Xia Y, Xiong Y, Lim B, Skrabalak SE (2009) Shape-Controlled Synthesis of Metal Nanocrystals: Simple Chemistry Meets Complex Physics? Angewandte Chemie International Edition 48:60–103. https://doi.org/10.1002/ANIE.200802248
78. Chang CC, Chen CP, Wu TH, et al (2019) Gold Nanoparticle-Based Colorimetric Strategies for Chemical and Biological Sensing Applications. Nanomaterials 2019, Vol 9, Page 861 9:861. https://doi.org/10.3390/NANO9060861
79. Wu Y, Feng J, Hu G, et al (2023) Colorimetric Sensors for Chemical and Biological Sensing Applications. Sensors 2023, Vol 23, Page 2749 23:2749. https://doi.org/10.3390/S23052749
80. Cao T, Liu K, Lu L, et al (2019) Chalcogenide–gold dual-layers coupled to gold nanoparticles for reconfigurable perfect absorption. Nanoscale 11:20546–20553. https://doi.org/10.1039/C9NR04759J
81. Zhang Z, Zhao R, Cong M, Qiu J (2024) Developments of terahertz metasurface biosensors: A literature review. Nanotechnol Rev 13:. https://doi.org/10.1515/ntrev-2023-0182
82. Lewandowski W, Fruhnert M, Mieczkowski J, et al (2015) Dynamically self-assembled silver nanoparticles as a thermally tunable metamaterial. Nature Communications 2015 6:1 6:1–9. https://doi.org/10.1038/ncomms7590
83. López-Miranda JL, Molina GA, Esparza R, et al (2021) Green Synthesis of Homogeneous Gold Nanoparticles Using Sargassum spp. Extracts and Their Enhanced Catalytic Activity for Organic Dyes. Toxics 2021, Vol 9, Page 280 9:280. https://doi.org/10.3390/toxics9110280
84. Saladino GM, Vogt C, Li Y, et al (2021) Optical and X-ray Fluorescent Nanoparticles for Dual Mode Bioimaging. ACS Nano 15:5077–5085. https://doi.org/10.1021/acsnano.0c10127
85. Atzrodt J, Derdau V, Kerr W, Reid M (2017) Applications of hydrogen isotopes in the life sciences. Angewandte Chemie International Edition 1–26. https://doi.org/10.1002/anie.201704146
86. Tiwari PM, Vig K, Dennis VA, Singh SR (2011) Functionalized Gold Nanoparticles and Their Biomedical Applications. Nanomaterials 2011, Vol 1, Pages 31-63 1:31–63. https://doi.org/10.3390/NANO1010031
87. Kang H, Buchman JT, Rodriguez RS, et al (2019) Stabilization of Silver and Gold Nanoparticles: Preservation and Improvement of Plasmonic Functionalities. Chem Rev 119:664–699.https://doi.org/10.1021/acs.chemrev.8b00341

88. Wang Y, Van De Vyver S, Sharma KK, Román-Leshkov Y (2014) Insights into the stability of gold nanoparticles supported on metal oxides for the base-free oxidation of glucose to gluconic acid. Green Chemistry 16:719–726. https://doi.org/10.1039/C3GC41362D
89. Egorova EA, Van Rijt MMJ, Sommerdijk N, et al (2020) One Peptide for Them All: Gold Nanoparticles of Different Sizes Are Stabilized by a Common Peptide Amphiphile. ACS Nano 14:5874–5886. https://doi.org/10.1021/acsnano.0c01021
90. Onses MS, Liu CC, Thode CJ, Nealey PF (2012) Highly selective immobilization of au nanoparticles onto isolated and dense nanopatterns of poly(2-vinyl pyridine) brushes down to single-particle resolution. Langmuir 28:7299–7307. https://doi.org/10.1021/la300552w
91. Schaal PA, Simon U (2013) Guided immobilisation of single gold nanoparticles by chemical electron beam lithography. Beilstein Journal of Nanotechnology 4:39 4:336–344. https://doi.org/10.3762/BJNANO.4.39
92. Joó P, László-Nagy K (2004) Chapter 5 Colloidal systems; solid/liquid interfaces. Interface Science and Technology 3:99–140. https://doi.org/10.1016/S1573-4285(04)80059-0
93. Kolluru LP, Atre P, Rizvi SAA (2021) Characterization and Applications of Colloidal Systems as Versatile Drug Delivery Carriers for Parenteral Formulations. Pharmaceuticals 2021, Vol 14, Page 108 14:108. https://doi.org/10.3390/PH14020108
94. Becher P (1991) Review of: "Basic Principles of Colloid Science". D. H. Everett. Royal Society of Chemistry, London, pp. xv + 243. $ 19.50. J Dispers Sci Technol 12:107–108. https://doi.org/01932699108913109
95. Stetefeld J, McKenna SA, Patel TR (2016) Dynamic light scattering: a practical guide and applications in biomedical sciences. Biophys Rev 8:409–427. https://doi.org/10.1007/s12551-016-0218-6
96. Lochhead RY (2017) Basic Physical Sciences for the Formulation of Cosmetic Products. Cosmetic Science and Technology: Theoretical Principles and Applications 39–76. https://doi.org/10.1016/B978-0-12-802005-0.00003-3
97. Shrivastav AM, Cvelbar U, Abdulhalim I (2021) A comprehensive review on plasmonic-based biosensors used in viral diagnostics. Communications Biology 2021 4:1 4:1–12. https://doi.org/10.1038/s42003-020-01615-8
98. Ishida T, Yanaga Y, Yamada S, Takahashi Y (2021) A versatile method for surface functionalization and hydrophobization of gold nanoparticles. Appl Surf Sci 546:148932. https://doi.org/10.1016/J.APSUSC.2021.148932
99. Pamies R, Cifre JGH, Espín VF, et al (2014) Aggregation behaviour of gold nanoparticles in saline aqueous media. Journal of Nanoparticle Research 16:1–11. https://doi.org/10.1007/s11051-014-2376-4
100. Liu S, Zhu T, Hu R, Liu Z (2002) Evaporation-induced self-assembly of gold nanoparticles into a highly organized two-dimensional array. Physical Chemistry Chemical Physics 4:6059–6062. https://doi.org/10.1039/B208520H
101. Ou X, Liu Y, Zhang M, et al (2021) Plasmonic gold nanostructures for biosensing and bioimaging. Microchimica Acta 2021 188:9 188:1–15. https://doi.org/10.1007/S00604-021-04964-1
102. Liu B, Liu J (2019) Interface-Driven Hybrid Materials Based on DNA-Functionalized Gold Nanoparticles. Matter 1:825–847. https://doi.org/10.1016/j.matt.2019.08.008
103. Lee JH, Cho HY, Choi HK, et al (2018) Application of Gold Nanoparticle to Plasmonic Biosensors. International Journal of Molecular Sciences 2018, Vol 19, Page 2021 19:2021. https://doi.org/10.3390/IJMS19072021

104. Khaniani Y, Ma Y, Ghadiri M, et al (2022) A gold nanoparticle-protein G electrochemical affinity biosensor for the detection of SARS-CoV-2 antibodies: a surface modification approach. Scientific Reports 2022 12:1 12:1–12. https://doi.org/10.1038/s41598-022-17219-7
105. Eremina OE, Semenova AA, Sergeeva EA (2015) Plasmonic nanoparticles: Towards the fabrication of biosensors. IOP Conf Ser Mater Sci Eng 87:012009. https://doi.org/10.1088/1757-899X/87/1/012009
106. Calvo R, Thon A, Saad A, et al (2022) Size characterization of plasmonic nanoparticles with dark-field single particle spectrophotometry. Scientific Reports 2022 12:1 12:1–8. https://doi.org/10.1038/s41598-022-21649-8
107. Rosi NL, Mirkin CA (2005) Nanostructures in biodiagnostics. Chem Rev 105:1547–1562. https://doi.org/10.1021/cr030067f
108. Kolwas K, Derkachova A (2020) Impact of the Interband Transitions in Gold and Silver on the Dynamics of Propagating and Localized Surface Plasmons. Nanomaterials 2020, Vol 10, Page 1411 10:1411. https://doi.org/10.3390/NANO10071411
109. Lee C, Park Y, Park JY (2019) Hot electrons generated by intraband and interband transition detected using a plasmonic Cu/TiO2 nanodiode. RSC Adv 9:18371–18376. https://doi.org/10.1039/C9RA02601K
110. Lee C, Park Y, Park JY (2019) Hot electrons generated by intraband and interband transition detected using a plasmonic Cu/TiO2 nanodiode. RSC Adv 9:18371–18376. https://doi.org/10.1039/C9RA02601K
111. Lee KS, El-Sayed MA (2006) Gold and Silver Nanoparticles in Sensing and Imaging: Sensitivity of Plasmon Response to Size, Shape, and Metal Composition. Journal of Physical Chemistry B 110:19220–19225. https://doi.org/10.1021/JP062536Y
112. Loiseau A, Asila V, Boitel-Aullen G, et al (2019) Silver-Based Plasmonic Nanoparticles for and Their Use in Biosensing. Biosensors 2019, Vol 9, Page 78 9:78. https://doi.org/10.3390/BIOS9020078
113. Jain PK, El-Sayed MA (2010) Plasmonic coupling in noble metal nanostructures. Chem Phys Lett 487:153–164. https://doi.org/10.1016/J.CPLETT.2010.01.062
114. Gold E, Ferrari E (2023) Gold Nanoparticle-Based Plasmonic Biosensors. Biosensors 2023, Vol 13, Page 411 13:411. https://doi.org/10.3390/BIOS13030411
115. Semwal V, Jensen OR, Bang O, Janting J (2023) Investigation of Performance Parameters of Spherical Gold Nanoparticles in Localized Surface Plasmon Resonance Biosensing. Micromachines (Basel) 14:1717. https://doi.org/10.3390/MI14091717
116. Montaño-Priede JL, Sanromán-Iglesias M, Zabala N, et al (2023) Robust Rules for Optimal Colorimetric Sensing Based on Gold Nanoparticle Aggregation. ACS Sens 8:1827–1834. https://doi.org/10.1021/acssensors.3c00287
117. Si P, Razmi N, Nur O, et al (2021) Gold nanomaterials for optical biosensing and bioimaging. Nanoscale Adv 3:2679–2698. https://doi.org/10.1039/D0NA00961J
118. Arbuz A, Sultangaziyev A, Rapikov A, et al (2021) How gap distance between gold nanoparticles in dimers and trimers on metallic and non-metallic SERS substrates can impact signal enhancement. Nanoscale Adv 4:268–280. https://doi.org/10.1039/D1NA00114K
119. Borah R, Ninakanti R, Bals S, Verbruggen SW (2022) Plasmon resonance of gold and silver nanoparticle arrays in the Kretschmann (attenuated total reflectance) vs. direct incidence configuration. Scientific Reports 2022 12:1 12:1–19. https://doi.org/10.1038/s41598-022-20117-7
120. Suárez-López R, Puntes VF, Bastús NG, et al (2022) Nucleation and growth of gold nanoparticles in the presence of different surfactants. A dissipative particle

dynamics study. Scientific Reports 2022 12:1 12:1–12. https://doi.org/10.1038/s41598-022-18155-2

121. Hotze EM, Phenrat T, Lowry G V. (2010) Nanoparticle Aggregation: Challenges to Understanding Transport and Reactivity in the Environment. J Environ Qual 39:1909–1924. https://doi.org/10.2134/JEQ2009.0462
122. Zhao Y, Wang M, Liu Y, Cui H (2014) Redispersity/Solubility of Nanopowder in Solvents. Recent Pat Nanotechnol 8:18–30. https://doi.org/10.2174/1872210507999131128103202
123. Kameyama T, Ohno Y, Kurimoto T, et al (2010) Size control and immobilization of gold nanoparticles stabilized in an ionic liquid on glass substrates for plasmonic applications. Physical Chemistry Chemical Physics 12:1804–1811. https://doi.org/10.1039/B914230D
124. Seitz O, Chehimi MM, Cabet-Deliry E, et al (2003) Preparation and characterisation of gold nanoparticle assemblies on silanised glass plates. Colloids Surf A Physicochem Eng Asp 218:225–239. https://doi.org/10.1016/S0927-7757(02)00594-0
125. Weinrib H, Meiri A, Duadi H, Fixler D (2012) Uniformly Immobilizing Gold Nanorods on a Glass Substrate. J At Mol Phys 2012:683830. https://doi.org/10.1155/2012/683830
126. Vollath D, Fischer FD, Holec D (2018) Surface energy of nanoparticles – influence of particle size and structure. Beilstein Journal of Nanotechnology 9:211 9:2265–2276. https://doi.org/10.3762/BJNANO.9.211
127. Holec D, Dumitraschkewitz P, Vollath D, Fischer FD (2020) Surface Energy of Au Nanoparticles Depending on Their Size and Shape. Nanomaterials 2020, Vol 10, Page 484 10:484. https://doi.org/10.3390/NANO10030484
128. Ali S, Myasnichenko VS, Neyts EC (2015) Size-dependent strain and surface energies of gold nanoclusters. Physical Chemistry Chemical Physics 18:792–800. https://doi.org/10.1039/C5CP06153A
129. Holec D, Dumitraschkewitz P, Vollath D, Fischer FD (2020) Surface Energy of Au Nanoparticles Depending on Their Size and Shape. Nanomaterials 2020, Vol 10, Page 484 10:484. https://doi.org/10.3390/NANO10030484
130. Goldstein AN, Echer CM, Alivisatos AP (1992) Melting in Semiconductor Nanocrystals. Science (1979) 256:1425–1427. https://doi.org/10.1126/SCIENCE.256.5062.1425
131. Van Hove MA (1985) Low-energy electron diffraction — Experiment and theory. 517–522. https://doi.org/10.1007/BFB0108187
132. Van Hove MA (1985) Low-energy electron diffraction — Experiment and theory. 517–522. https://doi.org/10.1007/BFB0108187
133. Love JC, Estroff LA, Kriebel JK, et al (2005) Self-assembled monolayers of thiolates on metals as a form of nanotechnology. Chem Rev 105:1103–1169. https://doi.org/10.1021/cr0300789
134. Singh R (2019) Nanotechnology based therapeutic application in cancer diagnosis and therapy. 3 Biotech 2019 9:11 9:1–29. https://doi.org/10.1007/S13205-019-1940-0
135. Chang J, Zhang A, Huang Z, et al (2019) Monodisperse Au@Ag core-shell nanoprobes with ultrasensitive SERS-activity for rapid identification and Raman imaging of living cancer cells. Talanta 198:45–54. https://doi.org/10.1016/J.TALANTA.2019.01.085
136. Liu M, Guyot-Sionnest P, Lee TW, Gray SK (2007) Optical properties of rodlike and bipyramidal gold nanoparticles from three-dimensional computations. Phys Rev B Condens Matter Mater Phys 76:235428. https://doi.org/10.1103/PhysRevB.76.235428

137. Polte J, Ahner TT, Delissen F, et al (2010) Mechanism of gold nanoparticle formation in the classical citrate synthesis method derived from coupled in situ XANES and SAXS evaluation. J Am Chem Soc 132:1296–1301. https://doi.org/10.1021/ja906506j
138. Montaño-Priede JL, Sanromán-Iglesias M, Zabala N, et al (2023) Robust Rules for Optimal Colorimetric Sensing Based on Gold Nanoparticle Aggregation. ACS Sens 8:1827–1834.https://doi.org/10.1021/acssensors.3c00287
139. Figat AM, Bartosewicz B, Liszewska M, et al (2023) α-Amino Acids as Reducing and Capping Agents in Gold Nanoparticles Synthesis Using the Turkevich Method. Langmuir 39:8646–8657. https://doi.org/10.1021/acs.langmuir.3c00507
140. Tang J, Huang J, Man SQ (2013) Preparation of gold nanoparticles by surfactant-promoted reductive reaction without extra reducing agent. Spectrochim Acta A Mol Biomol Spectrosc 103:349–355. https://doi.org/10.1016/J.SAA.2012.10.049
141. Doe E, Hayth HL, Brumett R, Khisamutdinov EF (2023) Effective, Rapid, and Small-Scale Bioconjugation and Purification of "Clicked" Small-Molecule DNA Oligonucleotide for Nucleic Acid Nanoparticle Functionalization. International Journal of Molecular Sciences 2023, Vol 24, Page 4797 24:4797. https://doi.org/10.3390/IJMS24054797
142. Montaño-Priede JL, Sanromán-Iglesias M, Zabala N, et al (2023) Robust Rules for Optimal Colorimetric Sensing Based on Gold Nanoparticle Aggregation. ACS Sens 8:1827–1834. https://doi.org/10.1021/acssensors.3c00287
143. Stern E, Vacic A, Rajan NK, et al (2009) Label-free biomarker detection from whole blood. Nature Nanotechnology 2010 5:2 5:138–142. https://doi.org/10.1038/nnano.2009.353
144. Angioni D, Delrieu J, Hansson O, et al (2022) Blood Biomarkers from Research Use to Clinical Practice: What Must Be Done? A Report from the EU/US CTAD Task Force. Journal of Prevention of Alzheimer's Disease 9:569–579. https://doi.org/10.14283/jpad.2022.85
145. Chen D, Han W, Su X, et al (2017) Overcoming Sample Matrix Effect in Quantitative Blood Metabolomics Using Chemical Isotope Labeling Liquid Chromatography Mass Spectrometry. Anal Chem 89:9424–9431. https://doi.org/10.1021/acs.analchem.7b02240
146. Chiu ML, Lawi W, Snyder ST, et al (2010) Matrix Effects-A Challenge Toward Automation of Molecular Analysis. JALA - Journal of the Association for Laboratory Automation 15:233–242. https://doi.org/10.1016/j.jala.2010.02.001
147. Sia SK, Kricka LJ (2008) Microfluidics and point-of-care testing. Lab Chip 8:1982–1983. https://doi.org/10.1039/B817915H
148. Whitesides GM (2006) The origins and the future of microfluidics. Nature 2006 442:7101 442:368–373. https://doi.org/10.1038/nature05058
149. Wei Z-H, Xie L, Wang Y-J, et al (2023) Red Blood Cell Lysis Pretreatment Can Significantly Improve the Yield of Treponema pallidum DNA from Blood. Microbiol Spectr 11:e05198-22. https://doi.org/10.1128/SPECTRUM.05198-22
150. Soares RRG, Novo P, Azevedo AM, et al (2014) On-chip sample preparation and analyte quantification using a microfluidic aqueous two-phase extraction coupled with an immunoassay. Lab Chip 14:4284–4294. https://doi.org/10.1039/C4LC00695J
151. Amasia M, Madou M (2010) Large-Volume Centrifugal Microfluidic Device for Blood Plasma Separation. Bioanalysis 2:1701–1710. https://doi.org/10.4155/BIO.10.140
152. Sia SK, Linder V, Parviz BA, et al (2004) An Integrated Approach to a Portable and Low-Cost Immunoassay for Resource-Poor Settings. Angewandte Chemie International Edition 43:498–502. https://doi.org/10.1002/ANIE.200353016

153. Peruski AH, Peruski LF (2003) Immunological methods for detection and identification of infectious disease and biological warfare agents. Clin Diagn Lab Immunol 10:506–513. https://doi.org/10.1128/cdli.10.4.506-513.2003
154. Hinsberger M, Becker-Kettern J, Jürgens-Wemheuer WM, et al (2023) Development of an Enzyme-Linked Immunosorbent Assay (ELISA) for the Quantification of ARID1A in Tissue Lysates. Cancers (Basel) 15:4096. https://doi.org/10.3390/CANCERS15164096
155. Barbosa AI, Edwards AD, Reis NM (2021) Antibody Surface Coverage Drives Matrix Interference in Microfluidic Capillary Immunoassays. ACS Sens 6:2682–2690. https://doi.org/10.1021/acssensors.1c00704
156. Barbosa AI, Castanheira AP, Edwards AD, Reis NM (2014) A lab-in-a-briefcase for rapid prostate specific antigen (PSA) screening from whole blood. Lab Chip 14:2918–2928. https://doi.org/10.1039/C4LC00464G
157. Leeflang MMG, Allerberger F (2019) How to: evaluate a diagnostic test. Clinical Microbiology and Infection 25:54–59. https://doi.org/10.1016/j.cmi.2018.06.011
158. Clemente F, Antonacci A, Giardi MT, et al (2023) Last Trends in Point-of-Care (POC) Diagnostics for the Management of Hematological Indices in Home Care Patients. Biosensors (Basel) 13:345. https://doi.org/10.3390/BIOS13030345
159. Mahshid SS, Mahshid S, Vallée-Bélisle A, Kelley SO (2019) Peptide-Mediated Electrochemical Steric Hindrance Assay for One-Step Detection of HIV Antibodies. Anal Chem 91:4943–4947. https://doi.org/10.1021/acs.analchem.9b00648
160. Chen L, Li L, Zhao X, et al (2021) Construction of antifouling fluorinated polymer brush via activators regenerated by electron transfer ATRP and thiol-epoxy click reaction. React Funct Polym 165:104974. https://doi.org/10.1016/j.reactfunctpolym.2021.104974
161. Yao S, Yan H, Tian S, et al (2024) Anti-fouling coatings for blood-contacting devices. Smart Mater Med 5:166–180. https://doi.org/10.1016/J.SMAIM.2023.10.001
162. Wang Z, Paul S, Stein LH, et al (2022) Recent Developments in Blood-Compatible Superhydrophobic Surfaces. Polymers 2022, Vol 14, Page 1075 14:1075. https://doi.org/10.3390/polym14061075
163. Zou J, Stammers AC, Taladriz-Sender A, et al (2023) Fluorous-Directed Assembly of DNA Origami Nanostructures. ACS Nano 17:752–759. https://doi.org/10.1021/acsnano.2c10727
164. Jaffer IH, Fredenburgh JC, Hirsh J, Weitz JI (2015) Medical device-induced thrombosis: What causes it and how can we prevent it? Journal of Thrombosis and Haemostasis 13:S72–S81. https://doi.org/10.1111/jth.12961
165. Polte J, Erler R, Thünemann AF, et al (2010) Nucleation and growth of gold nanoparticles studied via in situ small angle X-ray scattering at millisecond time resolution. ACS Nano 4:1076–1082. https://doi.org/10.1021/nn901499c
166. Karatutlu A, Barhoum A, Sapelkin A (2018) Theories of nanoparticle and nanostructure formation in liquid phase. Emerging Applications of Nanoparticles and Architectural Nanostructures: Current Prospects and Future Trends 597–619. https://doi.org/10.1016/B978-0-323-51254-1.00020-8
167. (2020) The Handbook of Continuous Crystallization. The Handbook of Continuous Crystallization. https://doi.org/10.1039/9781788013581
168. Karatutlu A, Barhoum A, Sapelkin A (2018) Liquid-phase synthesis of nanoparticles and nanostructured materials. Emerging Applications of Nanoparticles and Architectural Nanostructures: Current Prospects and Future Trends 1–28. https://doi.org/10.1016/B978-0-323-51254-1.00001-4

169. Polte J (2015) Fundamental growth principles of colloidal metal nanoparticles – a new perspective. CrystEngComm 17:6809–6830. https://doi.org/10.1039/C5CE01014D
170. Thanh NTK, Maclean N, Mahiddine S (2014) Mechanisms of nucleation and growth of nanoparticles in solution. Chem Rev 114:7610–7630. https://doi.org/10.1021/cr400544s
171. Lamer VK, Dinegar RH (1950) Theory, Production and Mechanism of Formation of Monodispersed Hydrosols. J Am Chem Soc 72:4847–4854. https://doi.org/10.1021/ja01167a001
172. Whitehead CB, Özkar S, Finke RG (2021) LaMer's 1950 model of particle formation: a review and critical analysis of its classical nucleation and fluctuation theory basis, of competing models and mechanisms for phase-changes and particle formation, and then of its application to silver halide, semiconductor, metal, and metal-oxide nanoparticles. Mater Adv 2:186–235. https://doi.org/10.1039/D0MA00439A
173. Patakfalvi R, Papp S, Dékány I (2007) The kinetics of homogeneous nucleation of silver nanoparticles stabilized by polymers. Journal of Nanoparticle Research 9:353–364.https://doi.org/10.1007/S11051-006-9139-9
174. Sugimoto T (2007) Underlying mechanisms in size control of uniform nanoparticles. J Colloid Interface Sci 309:106–118. https://doi.org/10.1016/J.JCIS.2007.01.036
175. Vreeland EC, Watt J, Schober GB, et al (2015) Enhanced Nanoparticle Size Control by Extending LaMer's Mechanism. Chemistry of Materials 27:6059–6066. https://doi.org/10.1021/acs.chemmater.5b02510
176. Sugimoto T (2007) Underlying mechanisms in size control of uniform nanoparticles. J Colloid Interface Sci 309:106–118. https://doi.org/10.1016/J.JCIS.2007.01.036
177. Thanh NTK, Maclean N, Mahiddine S (2014) Mechanisms of nucleation and growth of nanoparticles in solution. Chem Rev 114:7610–7630. https://doi.org/10.1021/cr400544s
178. Jana S (2015) Advances in nanoscale alloys and intermetallics: low temperature solution chemistry synthesis and application in catalysis. Dalton Transactions 44:18692–18717. https://doi.org/10.1039/C5DT03699B
179. Sugimoto T (2007) Underlying mechanisms in size control of uniform nanoparticles. J Colloid Interface Sci 309:106–118. https://doi.org/10.1016/J.JCIS.2007.01.036
180. Sugimoto T (2007) Underlying mechanisms in size control of uniform nanoparticles. J Colloid Interface Sci 309:106–118. https://doi.org/10.1016/J.JCIS.2007.01.036
181. Becker R, Döring W (1935) Kinetische Behandlung der Keimbildung in übersättigten Dämpfen. Ann Phys 416:719–752. https://doi.org/10.1002/ANDP.19354160806
182. Perala SRK, Kumar S (2014) On the two-step mechanism for synthesis of transition-metal nanoparticles. Langmuir 30:12703–12711. https://doi.org/10.1021/la503199m
183. Niederberger M, Cölfen H (2006) Oriented attachment and mesocrystals: Non-classical crystallization mechanisms based on nanoparticle assembly. Physical Chemistry Chemical Physics 8:3271–3287. https://doi.org/10.1039/B604589H
184. Thanh NTK, Maclean N, Mahiddine S (2014) Mechanisms of nucleation and growth of nanoparticles in solution. Chem Rev 114:7610–7630. https://doi.org/10.1021/cr400544s
185. Peng X, Manna L, Yang W, et al (2000) Shape control of CdSe nanocrystals. Nature 2000 404:6773 404:59–61. https://doi.org/10.1038/35003535
186. Peng ZA, Peng X (2001) Formation of high-quality CdTe, CdSe, and CdS nanocrystals using CdO as precursor. J Am Chem Soc 123:183–184. https://doi.org/10.1021/ja003633m

187. Tran H, Ronaldson K, Bailey NA, et al (2014) Hierarchically ordered nanopatterns for spatial control of biomolecules. ACS Nano 8:11846–11853. https://doi.org/10.1021/nn505548n
188. Mendes PM, Yeung CL, Preece JA (2007) Bio-nanopatterning of Surfaces. Nanoscale Research Letters 2007 2:8 2:373–384. https://doi.org/10.1007/S11671-007-9083-3
189. Glotzer SC, Solomon MJ (2007) Anisotropy of building blocks and their assembly into complex structures. Nature Materials 2007 6:8 6:557–562. https://doi.org/10.1038/nmat1949
190. Schaal PA, Simon U (2013) Guided immobilisation of single gold nanoparticles by chemical electron beam lithography. Beilstein Journal of Nanotechnology 4:39 4:336–344. https://doi.org/10.3762/BJNANO.4.39
191. Bellah MM, Christensen SM, Iqbal SM (2012) Nanostructures for medical diagnostics. J Nanomater 2012:. https://doi.org/10.1155/2012/486301
192. Yu HD, Regulacio MD, Ye E, Han MY (2013) Chemical routes to top-down nanofabrication. Chem Soc Rev 42:6006–6018. https://doi.org/10.1039/C3CS60113G
193. Kumar S, Bhushan P, Bhattacharya S (2018) Fabrication of Nanostructures with Bottom-up Approach and Their Utility in Diagnostics, Therapeutics, and Others. Energy, Environment, and Sustainability 167–198. https://doi.org/10.1007/978-981-10-7751-7_8
194. Glangchai LC, Caldorera-Moore M, Shi L, Roy K (2008) Nanoimprint lithography based fabrication of shape-specific, enzymatically-triggered smart nanoparticles. Journal of Controlled Release 125:263–272. https://doi.org/10.1016/J.JCONREL.2007.10.021
195. Biswas A, Bayer IS, Biris AS, et al (2012) Advances in top–down and bottom–up surface nanofabrication: Techniques, applications & future prospects. Adv Colloid Interface Sci 170:2–27. https://doi.org/10.1016/J.CIS.2011.11.001
196. Kumar S, Bhushan P, Bhattacharya S (2018) Fabrication of Nanostructures with Bottom-up Approach and Their Utility in Diagnostics, Therapeutics, and Others. Energy, Environment, and Sustainability 167–198. https://doi.org/10.1007/978-981-10-7751-7_8
197. Schena M, Shalon D, Davis RW, Brown PO (1995) Quantitative Monitoring of Gene Expression Patterns with a Complementary DNA Microarray. Science (1979) 270:467–470. https://doi.org/10.1126/SCIENCE.270.5235.467
198. Southern EM (2001) DNA Microarrays. Methods Mol Biol 170:1–15. https://doi.org/10.1385/1-59259-234-1:1
199. Gershon D (2005) DNA microarrays: More than gene expression. Nature 437:1195–1198. https://doi.org/10.1038/4371195a
200. Pease AC, Solas D, Sullivan EJ, et al (1994) Light-generated oligonucleotide arrays for rapid DNA sequence analysis. Proceedings of the National Academy of Sciences 91:5022–5026.https://doi.org/10.1073/PNAS.91.11.5022
201. Ammar R, Smith AM, Heisler LE, et al (2009) A comparative analysis of DNA barcode microarray feature size. BMC Genomics 10:471. https://doi.org/10.1186/1471-2164-10-471
202. Wöhrle J, Krämer SD, Meyer PA, et al (2020) Digital DNA microarray generation on glass substrates. Scientific Reports 2020 10:1 10:1–9. https://doi.org/10.1038/s41598-020-62404-1
203. Liu J, Hansen C, Quake SR (2003) Solving the “world-to-chip” interface problem with a microfluidic matrix. Anal Chem 75:4718–4723. https://doi.org/10.1021/ac0346407

204. Fodor SPA, Read JL, Pirrung MC, et al (1991) Light-Directed, Spatially Addressable Parallel Chemical Synthesis. Science (1979) 251:767–773. https://doi.org/10.1126/SCIENCE.1990438
205. Hoffmann J, Trotter M, Von Stetten F, et al (2012) Solid-phase PCR in a picowell array for immobilizing and arraying 100 000 PCR products to a microscope slide. Lab Chip 12:3049–3054. https://doi.org/10.1039/C2LC40534B
206. Hughes TR, Mao M, Jones AR, et al (2001) Expression profiling using microarrays fabricated by an ink-jet oligonucleotide synthesizer. Nature Biotechnology 2001 19:4 19:342–347. https://doi.org/10.1038/86730
207. Nuwaysir EF, Huang W, Albert TJ, et al (2002) Gene Expression Analysis Using Oligonucleotide Arrays Produced by Maskless Photolithography. Genome Res 12:1749–1755. https://doi.org/10.1101/GR.362402
208. Golub TR, Slonim DK, Tamayo P, et al (1999) Molecular Classification of Cancer: Class Discovery and Class Prediction by Gene Expression Monitoring. Science (1979) 286:531–527. https://doi.org/10.1126/SCIENCE.286.5439.531
209. Bonner AE, Lemon WJ, You M (2003) Gene expression signatures identify novel regulatory pathways during murine lung development: implications for lung tumorigenesis. J Med Genet 40:408–417. https://doi.org/10.1136/JMG.40.6.408
210. Brachat A, Pierrat B, Xynos A, et al (2002) A microarray-based, integrated approach to identify novel regulators of cancer drug response and apoptosis. Oncogene 2002 21:54 21:8361–8371. https://doi.org/10.1038/sj.onc.1206016
211. Trevino V, Falciani F, Barrera-Saldaña HA (2007) DNA microarrays: a powerful genomic tool for biomedical and clinical research. Molecular Medicine 13:527. https://doi.org/10.2119/2006-00107.trevino
212. Conejero-Goldberg C, Wang E, Yi C, et al (2005) Infectious pathogen detection arrays: Viral detection in cell lines and postmortem brain tissue. Biotechniques 39:741–749. https://doi.org/10.2144/000112016
213. Wang D, Coscoy L, Zylberberg M, et al (2002) Microarray-based detection and genotyping of viral pathogens. Proc Natl Acad Sci U S A 99:15687–15692. https://doi.org/10.1073/pnas.242579699
214. Koltai H, Weingarten-Baror C (2008) Specificity of DNA microarray hybridization: characterization, effectors and approaches for data correction. Nucleic Acids Res 36:2395–2405. https://doi.org/10.1093/NAR/GKN087
215. Shi L, Jones WD, Jensen R V., et al (2008) The balance of reproducibility, sensitivity, and specificity of lists of differentially expressed genes in microarray studies. BMC Bioinformatics 9:1–19. https://doi.org/10.1186/1471-2105-9-S9-S10
216. Wheelan SJ, Martínez Murillo F, Boeke JD (2008) The incredible shrinking world of DNA microarrays. Mol Biosyst 4:726–732. https://doi.org/10.1039/B706237K
217. Draghici S, Khatri P, Eklund AC, Szallasi Z (2006) Reliability and reproducibility issues in DNA microarray measurements. Trends in Genetics 22:101–109. https://doi.org/10.1016/j.tig.2005.12.005
218. Jaksik R, Iwanaszko M, Rzeszowska-Wolny J, Kimmel M (2015) Microarray experiments and factors which affect their reliability. Biol Direct 10:1–14. https://doi.org/10.1186/s13062-015-0077-2
219. Gershon D (2005) DNA microarrays: More than gene expression. Nature 437:1195–1198. https://doi.org/10.1038/4371195a
220. Gershon D (2005) DNA microarrays: More than gene expression. Nature 437:1195–1198. https://doi.org/10.1038/4371195a
221. Afanassiev V, Hanemann V, Wölfl S (2000) Preparation of DNA and protein micro arrays on glass slides coated with an agarose film. Nucleic Acids Res 28:e66–e66. https://doi.org/10.1093/NAR/28.12.E66

222. Wöhrle J, Krämer SD, Meyer PA, et al (2020) Digital DNA microarray generation on glass substrates. Scientific Reports 2020 10:1 10:1–9. https://doi.org/10.1038/s41598-020-62404-1
223. Mohamad NR, Marzuki NHC, Buang NA, et al (2015) An overview of technologies for immobilization of enzymes and surface analysis techniques for immobilized enzymes. Biotechnology & Biotechnological Equipment 29:205–220. https://doi.org/10.1080/13102818.2015.1008192
224. Leenen EJTM, Dos Santos VAP, Grolle KCF, et al (1996) Characteristics of and selection criteria for support materials for cell immobilization in wastewater treatment. Water Res 30:2985–2996. https://doi.org/10.1016/S0043-1354(96)00209-6
225. Datta S, Christena LR, Rajaram YRS (2013) Enzyme immobilization: an overview on techniques and support materials. 3 Biotech 3:1–9. https://doi.org/10.1007/s13205-012-0071-7
226. Zucca P, Sanjust E (2014) Inorganic Materials as Supports for Covalent Enzyme Immobilization: Methods and Mechanisms. Molecules 2014, Vol 19, Pages 14139-14194 19:14139–14194. https://doi.org/10.3390/MOLECULES190914139
227. Ulman A (1996) Formation and structure of self-assembled monolayers. Chem Rev 96:1533–1554. https://doi.org/10.1021/cr9502357
228. Nonappa N (2023) Precision nanoengineering for functional self-assemblies across length scales. Chemical Communications 59:13800–13819. https://doi.org/10.1039/D3CC02205F
229. Kheyraddini Mousavi A, Leseman ZC, Palacio MLB, et al (2012) Biosensors. Encyclopedia of Nanotechnology 329–345. https://doi.org/10.1007/978-90-481-9751-4_129
230. End N, Schöning K-U (2004) Immobilized Biocatalysts in Industrial Research and Production. 273–317. https://doi.org/10.1007/B96879
231. Homaei AA, Sariri R, Vianello F, Stevanato R (2013) Enzyme immobilization: An update. J Chem Biol 6:185–205. https://doi.org/10.1007/s12154-013-0102-9
232. Alarcon-Angeles G, Álvarez-Romero GA, Merkoçi A (2018) Electrochemical Biosensors: Enzyme Kinetics and Role of Nanomaterials. Encyclopedia of Interfacial Chemistry: Surface Science and Electrochemistry 140–155. https://doi.org/10.1016/B978-0-12-409547-2.13477-8
233. Björneholm O, Öhrwall G, De Brito AN, et al (2022) Superficial Tale of Two Functional Groups: On the Surface Propensity of Aqueous Carboxylic Acids, Alkyl Amines, and Amino Acids. Acc Chem Res 55:3285–3293. https://doi.org/10.1021/acs.accounts.2c00494
234. Hanefeld U, Gardossi L, Magner E (2009) Understanding enzyme immobilisation. Chem Soc Rev 38:453–468. https://doi.org/10.1039/B711564B
235. Alarcon-Angeles G, Álvarez-Romero GA, Merkoçi A (2018) Electrochemical Biosensors: Enzyme Kinetics and Role of Nanomaterials. Encyclopedia of Interfacial Chemistry: Surface Science and Electrochemistry 140–155. https://doi.org/10.1016/B978-0-12-409547-2.13477-8
236. López-Quintela A, Prendes P, Pazos-Pellín M, et al (1998) Cis/Trans Reactivity: Epoxy−Amine Systems. Macromolecules 31:4770–4776. https://doi.org/10.1021/MA9713365
237. Riccardi CC, Fraga F, Dupuy J, Williams RJJ (2001) Cure kinetics of diglycidylether of bisphenol A– ethylenediamine revisited using a mechanistic model. J Appl Polym Sci 82:2319–2325. https://doi.org/10.1002/APP.2080
238. Smith S, Goodge K, Delaney M, et al (2020) A Comprehensive Review of the Covalent Immobilization of Biomolecules onto Electrospun Nanofibers.

Nanomaterials 2020, Vol 10, Page 2142 10:2142. https://doi.org/10.3390/NANO10112142
237. Riccardi CC, Fraga F, Dupuy J, Williams RJJ (2001) Cure kinetics of diglycidylether of bisphenol A– ethylenediamine revisited using a mechanistic model. J Appl Polym Sci 82:2319–2325. https://doi.org/10.1002/APP.2080
238. Smith S, Goodge K, Delaney M, et al (2020) A Comprehensive Review of the Covalent Immobilization of Biomolecules onto Electrospun Nanofibers. Nanomaterials 2020, Vol 10, Page 2142 10:2142. https://doi.org/10.3390/NANO10112142
239. Matsumoto M, Kaneko K, Hara M, et al (2021) Covalent immobilization of gold nanoparticles on a plastic substrate and subsequent immobilization of biomolecules. RSC Adv 11:23409–23417. https://doi.org/10.1039/D1RA03902D
240. Wu RH, Nguyen TP, Marquart GW, et al (2014) A Facile Route to Tailoring Peptide-Stabilized Gold Nanoparticles Using Glutathione as a Synthon. Molecules 2014, Vol 19, Pages 6754-6775 19:6754–6775. https://doi.org/10.3390/molecules19056754
241. Jazayeri MH, Amani H, Pourfatollah AA, et al (2016) Various methods of gold nanoparticles (GNPs) conjugation to antibodies. Sens Biosensing Res 9:17–22. https://doi.org/10.1016/J.SBSR.2016.04.002
242. Zhou Y, Andersson O, Lindberg P, Liedberg B (2004) Reversible hydrophobic barriers introduced by microcontact printing: Application to protein microarrays. Microchimica Acta 146:193–205. https://doi.org/10.1007/s00604-003-0174-2
243. Pham TA, Choi BC, Lim KT, Jeong YT (2011) A simple approach for immobilization of gold nanoparticles on graphene oxide sheets by covalent bonding. Appl Surf Sci 257:3350–3357. https://doi.org/10.1016/J.APSUSC.2010.11.023
244. Jain A, Cheng K (2017) The Principles and Applications of Avidin-Based Nanoparticles in Drug Delivery and Diagnosis. J Control Release 245:27. https://doi.org/10.1016/J.JCONREL.2016.11.016
245. Wilchek M, Bayer EA (1988) The avidin-biotin complex in bioanalytical applications. Anal Biochem 171:1–32. https://doi.org/10.1016/0003-2697(88)90120-0
246. Wang S, Hossain MZ, Han T, et al (2020) Avidin−biotin technology in gold nanoparticle-decorated graphene field effect transistors for detection of biotinylated macromolecules with ultrahigh sensitivity and specificity. ACS Omega 5:30037–30046. https://doi.org/10.1021/acsomega.0c04429
247. Wang S, Hossain MZ, Han T, et al (2020) Avidin−biotin technology in gold nanoparticle-decorated graphene field effect transistors for detection of biotinylated macromolecules with ultrahigh sensitivity and specificity. ACS Omega 5:30037–30046. https://doi.org/10.1021/acsomega.0c04429
248. Hendling M, Barišić I (2019) In-silico Design of DNA Oligonucleotides: Challenges and Approaches. Comput Struct Biotechnol J 17:1056–1065. https://doi.org/10.1016/j.csbj.2019.07.008
249. Jason CK, Marc JL, Jerrod JS, et al (2015) Multiplex pairwise assembly of array-derived DNA oligonucleotides. *Nucleic Acids Research*, Volume 44, Issue 5, 18 March 2016, Page e43. https://doi.org/10.1093/nar/gkv1177
250. Liu G (2021) Grand Challenges in Biosensors and Biomolecular Electronics. Front Bioeng Biotechnol 9:707615. https://doi.org/10.3389/fbioe.2021.707615
251. Timilsina SS, Jolly P, Durr N, et al (2021) Enabling Multiplexed Electrochemical Detection of Biomarkers with High Sensitivity in Complex Biological Samples. Acc Chem Res 54:3529–3539. https://doi.org/10.1021/acs.accounts.1c00382
252. Ranjan Srivastava V, Kumari R, Chandra P (2023) Miniaturized surface engineered technologies for multiplex biosensing devices. Electroanalysis 35:e202200355. https://doi.org/10.1002/ELAN.202200355

253. Puumala LS, Grist SM, Morales JM, et al (2022) Biofunctionalization of Multiplexed Silicon Photonic Biosensors. Biosensors 2023, Vol 13, Page 53 13:53. https://doi.org/10.3390/BIOS13010053
254. Liu G (2021) Grand Challenges in Biosensors and Biomolecular Electronics. Front Bioeng Biotechnol 9:707615. https://doi.org/10.3389/fbioe.2021.707615
255. Liu G (2021) Grand Challenges in Biosensors and Biomolecular Electronics. Front Bioeng Biotechnol 9:707615. https://doi.org/10.3389/fbioe.2021.707615
256. Ranjan Srivastava V, Kumari R, Chandra P (2023) Miniaturized surface engineered technologies for multiplex biosensing devices. Electroanalysis 35:e202200355. https://doi.org/10.1002/elan.202200355
257. Jarockyte G, Karabanovas V, Rotomskis R, Mobasheri A (2020) Multiplexed Nanobiosensors: Current Trends in Early Diagnostics. Sensors 2020, Vol 20, Page 6890 20:6890. https://doi.org/10.3390/S20236890
258. Lubken RM, De Jong AM, Prins MWJ (2020) Multiplexed Continuous Biosensing by Single-Molecule Encoded Nanoswitches. Nano Lett 20:2296–2302. https://doi.org/10.1021/acs.nanolett.9b04561
259. Bounegru AV, Apetrei C (2023) Tyrosinase Immobilization Strategies for the Development of Electrochemical Biosensors—A Review. Nanomaterials 2023, Vol 13, Page 760 13:760. https://doi.org/10.3390/NANO13040760
260. Faccio G (2018) From Protein Features to Sensing Surfaces. Sensors 2018, Vol 18, Page 1204 18:1204. https://doi.org/10.3390/S18041204
261. Campbell C, Casey A, Triplett G (2022) The effect of electron dose on positive polymethyl methacrylate resist for nanolithography of gold bowtie nanoantennas. Heliyon 8:e09475. https://doi.org/10.1016/j.heliyon.2022.e09475
262. Ren L, Chen B (2004) Proximity effect in electron beam lithography. International Conference on Solid-State and Integrated Circuits Technology Proceedings, ICSICT 1:579–582. https://doi.org/10.1109/ICSICT.2004.1435073
263. Naulleau P (2019) Optical Lithography. Comprehensive Nanoscience and Nanotechnology 1–5:387–398. https://doi.org/10.1016/B978-0-12-803581-8.10433-3
264. Luo C, Xu C, Lv L, et al (2020) Review of recent advances in inorganic photoresists. RSC Adv 10:8385–8395. https://doi.org/10.1039/C9RA08977B
265. Rahman F, Carbaugh DJ, Wright JT, et al (2020) A review of polymethyl methacrylate (PMMA) as a versatile lithographic resist – With emphasis on UV exposure. Microelectron Eng 224:111238. https://doi.org/10.1016/J.MEE.2020.111238
266. Rooks MJ, Kratschmer E, Viswanathan R, et al (2002) Low stress development of poly(methylmethacrylate) for high aspect ratio structures. Journal of Vacuum Science & Technology B: Microelectronics and Nanometer Structures Processing, Measurement, and Phenomena 20:2937–2941. https://doi.org/10.1116/1.1524971
267. Yasin S, Hasko DG, Ahmed H (2002) Comparison of MIBK/IPA and water/IPA as PMMA developers for electron beam nanolithography. Microelectron Eng 61–62:745–753. https://doi.org/10.1016/S0167-9317(02)00468-9
268. Knieling T, Lang W, Benecke W (2007) Gas phase hydrophobisation of MEMS silicon structures with self-assembling monolayers for avoiding in-use sticking. Sens Actuators B Chem 126:13–17. https://doi.org/10.1016/J.SNB.2006.10.023
269. Abdallah BG, Ros A (2013) Surface coatings for microfluidic-based biomedical devices. Microfluidic Devices for Biomedical Applications 63–99. https://doi.org/10.1533/9780857097040.1.63
270. Wasserman SR, Tao YT, Whitesides GM (1989) Structure and Reactivity of Alkylsiloxane Monolayers Formed by Reaction of Alkyltrichlorosilanes on Silicon Substrates. Langmuir 5:1074–1087. https://doi.org/10.1021/la00088a035

271. Labit H, Goldar A, Guilbaud G, et al (2008) A simple and optimized method of producing silanized surfaces for FISH and replication mapping on combed DNA fibers. Biotechniques 45:649–658. https://doi.org/10.2144/000113002
272. Wedler V, Quinones D, Peisert H, Schäffer E (2022) A Quick and Reproducible Silanization Method by Using Plasma Activation for Hydrophobicity-Based Kinesin Single Molecule Fluorescence–Microscopy Assays. Chemistry 28:. https://doi.org/10.1002/CHEM.202202036
273. Zou J, Stammers AC, Taladriz-Sender A, et al (2023) Fluorous-Directed Assembly of DNA Origami Nanostructures. ACS Nano 17:752–759. https://doi.org/10.1021/acsnano.2c10727
274. Nimse SB, Song K, Sonawane MD, et al (2014) Immobilization Techniques for Microarray: Challenges and Applications. Sensors 2014, Vol 14, Pages 22208-22229 14:22208–22229. https://doi.org/10.3390/S141222208
275. Li H, Xia H, Wang D, Tao X (2013) Simple synthesis of monodisperse, quasi-spherical, citrate-stabilized silver nanocrystals in water. Langmuir 29:5074–5079. https://doi.org/10.1021/la400214x
276. Schneider CA, Rasband WS, Eliceiri KW (2012) NIH Image to ImageJ: 25 years of image analysis. Nature Methods 2012 9:7 9:671–675. https://doi.org/10.1038/nmeth.2089
277. Franks K, Kestens V, Braun A, *et al.* (2019) Non-equivalence of different evaluation algorithms to derive mean particle size from dynamic light scattering data. *J Nanopart Res* 21, 195. https://doi.org/10.1007/s11051-019-4630-2
278. Khalid K, Ishak R, Chowdhury ZZ (2024) UV–Vis spectroscopy in non-destructive testing. Non-Destructive Material Characterization Methods 391–416. https://doi.org/10.1016/B978-0-323-91150-4.00021-5
279. Pinchuk A, Von Plessen G, Kreibig U (2004) Influence of interband electronic transitions on the optical absorption in metallic nanoparticles. J Phys D Appl Phys 37:3133. https://doi.org/10.1088/0022-3727/37/22/012
280. Joudeh N, Linke D (2022) Nanoparticle classification, physicochemical properties, characterization, and applications: a comprehensive review for biologists. Journal of Nanobiotechnology 2022 20:1 20:1–29. https://doi.org/10.1186/S12951-022-01477-8
281. Head-Gordon M, Grana AM, Maurice D, White CA (1995) Analysis of electronic transitions as the difference of electron attachment and detachment densities. Journal of physical chemistry 99:14261–14270. https://doi.org/10.1021/j100039a012
282. Ershov V, Tarasova N, Ershov B (2021) Evolution of Electronic State and Properties of Silver Nanoparticles during Their Formation in Aqueous Solution. International Journal of Molecular Sciences 2021, Vol 22, Page 10673 22:10673. https://doi.org/10.3390/IJMS221910673
283. Brahma SS, Nanda J, Sahoo NK, *et al* (2021) Phase transition, electronic transitions and visible light driven enhanced photocatalytic activity of Eu–Ni co-doped bismuth ferrite nanoparticles. Journal of Physics and Chemistry of Solids 153:110018. https://doi.org/10.1016/J.JPCS.2021.110018
284. Grasse EK, Torcasio MH, Smith AW (2016) Teaching UV-Vis Spectroscopy with a 3D-Printable Smartphone Spectrophotometer. J Chem Educ 93:146–151. https://doi.org/10.1021/acs.jchemed.5b00654
285. Marchuk I V., Cheverda V V., Strizhak PA, Kabov OA (2015) Determination of surface tension and contact angle by the axisymmetric bubble and droplet shape analysis. Thermophysics and Aeromechanics 22:297–303. https://doi.org/10.1134/S0869864315030038

286. Hu F, Li H, Liu X, et al (2015) Quantitative Characterization of Non-Classic Polarization of Cations on Clay Aggregate Stability. PLoS One 10:e0122460. https://doi.org/10.1371/JOURNAL.PONE.0122460
287. Petit T, Lounasvuori M, Chemin A, Bärmann P (2023) Nanointerfaces: Concepts and Strategies for Optical and X-ray Spectroscopic Characterization. ACS Physical Chemistry Au 3:263–278. https://doi.org/10.1021/acsphyschemau.2c00058
288. Krajczewski J, Ambroziak R, Kudelski A (2021) Photo-assembly of plasmonic nanoparticles: methods and applications. RSC Adv 11:2575–2595. https://doi.org/10.1039/D0RA09337H
289. Fuster HA, Wang X, Wang X, et al (2020) Programming van der Waals interactions with complex symmetries into microparticles using liquid crystallinity. Sci Adv 6:. https://doi.org/10.1126/sciadv.abb1327
290. Ferri G, Humbert S, Digne M, et al (2021) Simulation of Large Aggregate Particles System With a New Morphological Model. Image Analysis and Stereology 40:71–84. https://doi.org/10.5566/IAS.2488
291. Kovac Z, Sambucetti CJ (1992) Importance of Electrical Double Layer in Technological Applications. Electrochemistry in Transition 39–49. https://doi.org/10.1007/978-1-4615-9576-2_3
292. Meegoda JN, Hewage SA, Batagoda JH (2019) Application of the Diffused Double Layer Theory to Nanobubbles. Langmuir 35:12100–12112. https://doi.org/10.1021/acs.langmuir.9b01443
293. Li H, Wei S, Qing C, Yang J (2003) Discussion on the position of the shear plane. J Colloid Interface Sci 258:40–44. https://doi.org/10.1016/S0021-9797(02)00077-2
294. Sainath K, Ghosh P (2014) Electrical Properties of Silicone Oil-Water Interface In The Presence Of Ionic Surfactants And Salt: Importance In The Stability Of Oil-In-Water Emulsions. Chem Eng Commun 201:1645–1663. https://doi.org/10.1080/00986445.2013.823543
295. Ding W, Liu X, Song L, et al (2015) An approach to estimate the position of the shear plane for colloidal particles in an electrophoresis experiment. Surf Sci 632:50–59. https://doi.org/10.1016/J.SUSC.2014.08.024
296. Meegoda JN, Hewage SA, Batagoda JH (2019) Application of the Diffused Double Layer Theory to Nanobubbles. Langmuir 35:12100–12112. https://doi.org/10.1021/acs.langmuir.9b01443
297. Meegoda JN, Hewage SA, Batagoda JH (2019) Application of the Diffused Double Layer Theory to Nanobubbles. Langmuir 35:12100–12112. https://doi.org/10.1021/acs.langmuir.9b01443
298. Adair JH, Suvaci E, Sindel J (2001) Surface and Colloid Chemistry. Encyclopedia of Materials: Science and Technology 1–10. https://doi.org/10.1016/B0-08-043152-6/01622-3
299. Agmo Hernández V (2023) An overview of surface forces and the DLVO theory. ChemTexts 9:1–16. https://doi.org/10.1007/s40828-023-00182-9
300. Adair JH, Suvaci E, Sindel J (2001) Surface and Colloid Chemistry. Encyclopedia of Materials: Science and Technology 1–10. https://doi.org/10.1016/B0-08-043152-6/01622-3
301. Agmo Hernández V (2023) An overview of surface forces and the DLVO theory. ChemTexts 9:1–16. https://doi.org/10.1007/s40828-023-00182-9
302. Hierrezuelo J, Sadeghpour A, Szilagyi I, et al (2010) Electrostatic stabilization of charged colloidal particles with adsorbed polyelectrolytes of opposite charge. Langmuir 26:15109–15111. https://doi.org/10.1021/la102912u
303. Gao X, Kou Q, Ren K, et al (2022) Quantitative characterization of non-DLVO factors in the aggregation of black soil colloids. Scientific Reports 2022 12:1 12:1–13. https://doi.org/10.1038/s41598-022-09067-2

304. Boström M, Williams DRM, Ninham BW (2001) Specific Ion Effects: Why DLVO Theory Fails for Biology and Colloid Systems. Phys Rev Lett 87:168103. https://doi.org/10.1103/PhysRevLett.87.168103
305. Liu Y, Xi Y (2019) Colloidal systems with a short-range attraction and long-range repulsion: Phase diagrams, structures, and dynamics. Curr Opin Colloid Interface Sci 39:123–136. https://doi.org/10.1016/J.COCIS.2019.01.016
306. Spitzer JJ (2003) A consistent alternative to the dlvo theory. J Adhes 79:893–903. https://doi.org/10.1080/714906147
307. Digman MA, Gratton E (2011) Lessons in fluctuation correlation spectroscopy. Annu Rev Phys Chem 62:645–668. https://doi.org/10.1146/annurev-physchem-032210-103424
308. Dzakpasu R, Axelrod D (2004) Dynamic Light Scattering Microscopy. A Novel Optical Technique to Image Submicroscopic Motions. I: Theory. Biophys J 87:1279–1287. https://doi.org/10.1529/BIOPHYSJ.103.033837
309. Hawe A, Hulse WL, Jiskoot W, Forbes RT (2011) Taylor dispersion analysis compared to dynamic light scattering for the size analysis of therapeutic peptides and proteins and their aggregates. Pharm Res 28:2302–2310. https://doi.org/10.1007/S11095-011-0460-3
310. Pecora R (1985) Dynamic Light Scattering. https://doi.org/10.1007/978-1-4613-2389-1
311. Hassan PA, Rana S, Verma G (2015) Making sense of Brownian motion: Colloid characterization by dynamic light scattering. Langmuir 31:3–12. https://doi.org/10.1021/la501789z
312. Rademeyer P, Carugo D, Lee JY, Stride E (2014) Microfluidic system for high throughput characterisation of echogenic particles. Lab Chip 15:417–428. https://doi.org/10.1039/C4LC01206B
313. Min Y, Akbulut M, Kristiansen K, et al (2008) The role of interparticle and external forces in nanoparticle assembly. Nature Materials 2008 7:7 7:527–538. https://doi.org/10.1038/nmat2206
314. Bhattacharjee S (2016) DLS and zeta potential – What they are and what they are not? Journal of Controlled Release 235:337–351. https://doi.org/10.1016/J.JCONREL.2016.06.017
315. Karow AR, Götzl J, Garidel P (2015) Resolving power of dynamic light scattering for protein and polystyrene nanoparticles. Pharm Dev Technol 20:84–89. https://doi.org/10.3109/10837450.2014.910808
316. Zheng T, Cherubin P, Cilenti L, et al (2016) A simple and fast method to study the hydrodynamic size difference of protein disulfide isomerase in oxidized and reduced form using gold nanoparticles and dynamic light scattering. Analyst 141:934–938. https://doi.org/10.1039/C5AN02248G
317. Hackley VA, Clogston JD (2011) Measuring the Hydrodynamic Size of Nanoparticles in Aqueous Media Using Batch-Mode Dynamic Light Scattering. Methods in Molecular Biology 697:35–52. https://doi.org/10.1007/978-1-60327-198-1_4/
318. Rai M, Bonde S, Yadav A, et al (2021) Nanotechnology as a Shield against COVID-19: Current Advancement and Limitations. Viruses 2021, Vol 13, Page 1224 13:1224. https://doi.org/10.3390/V13071224
319. Sabapathi N, Ramalingam S, Aruljothi KN, et al (2023) Characterization and Therapeutic Applications of Biosynthesized Silver Nanoparticles Using Cassia auriculate Flower Extract. Plants 2023, Vol 12, Page 707 12:707. https://doi.org/10.3390/plants12040707
320. Kavaz D, Kirac F, Kirac M, et al (2017) Low Releasing Mitomycin C Molecule Encapsulated with Chitosan Nanoparticles for Intravesical Installation. J Biomater Nanobiotechnol 8:203–219. https://doi.org/10.4236/JBNB.2017.84014

321. Sreejivungsa K, Suchaichit N, Moosophon P, Chompoosor A (2016) Light-Regulated Release of Entrapped Drugs from Photoresponsive Gold Nanoparticles. J Nanomater 2016:. https://doi.org/10.1155/2016/4964693
322. Küçüktürkmen B, Öz UC, Bozkir A (2017) In Situ Hydrogel Formulation for Intra-Articular Application of Diclofenac Sodium-Loaded Polymeric Nanoparticles. Turk J Pharm Sci 14:56–64. https://doi.org/10.4274/TJPS.84803
323. Jiwaji M, Sandison ME, Reboud J, et al (2014) Quantification of Functionalised Gold Nanoparticle-Targeted Knockdown of Gene Expression in HeLa Cells. PLoS One 9:e99458. https://doi.org/10.1371/journal.pone.0099458
324. Jamil B, Habib H, Abbasi SA, et al (2016) Development of cefotaxime impregnated chitosan as nano-antibiotics: De Novo Strategy to Combat Biofilm Forming Multi-drug Resistant Pathogens. Front Microbiol 7:179982. https://doi.org/10.3389/fmicb.2016.00330
325. da Silva Campos WN, Leite AET, Sonego DA, et al (2017) Síntese e caracterização de nanopartículas de ouro conjugadas com curcumina e seus efeitos na osteoartrite experimental induzida. Ciência Rural 47:e20161001. https://doi.org/10.1590/0103-8478CR20161001
326. Gu C, Wu H, Ge G, et al (2016) In Vitro Effects of Hollow Gold Nanoshells on Human Aortic Endothelial Cells. Nanoscale Res Lett 11:1–10. https://doi.org/10.1186/s11671-016-1620-5
327. Aji A, Santosa SJ, Kunarti ES (2020) Effect of Reaction Time and Stability Properties of Gold Nanoparticles Synthesized by p -Aminobenzoic Acid and p -Aminosalicylic Acid. Indonesian Journal of Chemistry 20:413–421. https://doi.org/10.22146/IJC.44674
328. Wang M, Zhang Y, Fei Z, et al (2022) Hyaluronan Oligosaccharides-Coated Paclitaxel-Casein Nanoparticles with Enhanced Stability and Antitumor Activity. Nutrients 2022, Vol 14, Page 3888 14:3888. https://doi.org/10.3390/NU14193888
329. Zgura I, Badea N, Enculescu M, et al (2023) Burdock-Derived Composites Based on Biogenic Gold, Silver Chloride and Zinc Oxide Particles as Green Multifunctional Platforms for Biomedical Applications and Environmental Protection. Materials 16:1153. https://doi.org/10.3390/MA16031153
330. Mahapatro A, Singh DK (2011) Biodegradable nanoparticles are excellent vehicle for site directed in-vivo delivery of drugs and vaccines. J Nanobiotechnology 9:55.https://doi.org/10.1186/1477-3155-9-55
331. Ulyashin AG, Hadjadj A, Butt MA (2022) Thin-Film Coating Methods: A Successful Marriage of High-Quality and Cost-Effectiveness—A Brief Exploration. Coatings 2022, Vol 12, Page 1115 12:1115. https://doi.org/10.3390/COATINGS12081115
332. (2004) Sol-Gel Technologies for Glass Producers and Users. Sol-Gel Technologies for Glass Producers and Users. https://doi.org/10.1007/978-0-387-88953-5
333. Schneller T, Waser R, Kosec M, Payne D (2013) Chemical solution deposition of functional oxide thin films. Chemical Solution Deposition of Functional Oxide Thin Films 9783211993118:1–796. https://doi.org/10.1007/978-3-211-99311-8
334. Rio E, Boulogne F (2017) Withdrawing a solid from a bath: How much liquid is coated? Adv Colloid Interface Sci 247:100–114. https://doi.org/10.1016/J.CIS.2017.01.006
335. Lin T, Li Y, Wang J, You J (2021) Effect of PMMA Molecular Weight on Its Localization during Crystallization of PVDF in Their Blends. Polymers 2021, Vol 13, Page 4138 13:4138. http://dx.doi.org/10.3390/polym13234138
336. Ulyashin AG, Hadjadj A, Butt MA (2022) Thin-Film Coating Methods: A Successful Marriage of High-Quality and Cost-Effectiveness—A Brief Exploration. Coatings 2022, Vol 12, Page 1115 12:1115. https://doi.org/10.3390/coatings12081115

337. Krebs FC (2009) Fabrication and processing of polymer solar cells: A review of printing and coating techniques. Solar Energy Materials and Solar Cells 93:394–412. https://doi.org/10.1016/J.SOLMAT.2008.10.004
338. Cherrington R, Liang J (2016) Materials and Deposition Processes for Multifunctionality. Design and Manufacture of Plastic Components for Multifunctionality: Structural Composites, Injection Molding, and 3D Printing 19–51. https://doi.org/10.1016/B978-0-323-34061-8.00002-8
339. Akhtar K, Khan SA, Khan SB, Asiri AM (2018) Scanning Electron Microscopy: Principle and Applications in Nanomaterials Characterization. Handbook of Materials Characterization 113–145. https://doi.org/10.1007/978-3-319-92955-2_4
340. Sharif A (2016) Review on advances in nanoscale microscopy in cement research. Micron 80:45–58. https://doi.org/10.1016/J.MICRON.2015.09.010
341. Asmatulu R, Khan WS (2019) Characterization of electrospun nanofibers. Synthesis and Applications of Electrospun Nanofibers 257–281. https://doi.org/10.1016/B978-0-12-813914-1.00013-4
342. Xia F, Youcef-Toumi K (2022) Review: Advanced Atomic Force Microscopy Modes for Biomedical Research. Biosensors 2022, Vol 12, Page 1116 12:1116. https://doi.org/10.3390/BIOS12121116
343. Dichiarante V, Martinez Espinoza MI, Gazzera L, et al (2018) A Short-Chain Multibranched Perfluoroalkyl Thiol for More Sustainable Hydrophobic Coatings. ACS Sustain Chem Eng 6:9734–9743. https://doi.org/10.1021/acssuschemeng.8b00777
344. Scarratt LRJ, Steiner U, Neto C (2017) A review on the mechanical and thermodynamic robustness of superhydrophobic surfaces. Adv Colloid Interface Sci 246:133–152. https://doi.org/10.1016/J.CIS.2017.05.018
345. Ederth T, Ekblad T, Pettitt ME, et al (2011) Resistance of galactoside-terminated alkanethiol self-assembled monolayers to marine fouling organisms. ACS Appl Mater Interfaces 3:3890–3901. https://doi.org/10.1021/am200726a
346. Dietrich PM, Horlacher T, Girard-Lauriault PL, et al (2011) Adlayers of dimannoside thiols on gold: Surface chemical analysis. Langmuir 27:4808–4815. https://doi.org/10.1021/la104038q
347. Flynn GE, Withers JM, Macias G, et al (2017) Reversible DNA micro-patterning using the fluorous effect. Chemical Communications 53:3094–3097. https://doi.org/10.1039/C7CC00288B
348. Marchuk I V., Cheverda V V., Strizhak PA, Kabov OA (2015) Determination of surface tension and contact angle by the axisymmetric bubble and droplet shape analysis. Thermophysics and Aeromechanics 22:297–303. https://doi.org/10.1134/S0869864315030038
349. Hua Z, Xia Y, Srivannavit O, et al (2006) A versatile microreactor platform featuring a chemical-resistant microvalve array for addressable multiplex syntheses and assays. Journal of Micromechanics and Microengineering 16:1433. https://doi.org/10.1088/0960-1317/16/8/001
350. Schena M, Shalon D, Davis RW, Brown PO (1995) Quantitative Monitoring of Gene Expression Patterns with a Complementary DNA Microarray. Science (1979) 270:467–470. https://doi.org/10.1126/science.270.5235.467
351. Schena M, Shalon D, Davis RW, Brown PO (1995) Quantitative Monitoring of Gene Expression Patterns with a Complementary DNA Microarray. Science (1979) 270:467–470. https://doi.org/10.1126/science.270.5235.467
352. Fu X, Fu N, Guo S, et al (2009) Estimating accuracy of RNA-Seq and microarrays with proteomics. BMC Genomics 10:1–9. https://doi.org/10.1186/1471-2164-10-161

353. Tighe PJ, Ryder RR, Todd I, Fairclough LC (2015) ELISA in the multiplex era: potentials and pitfalls. Proteomics Clin Appl 9:406–422. https://doi.org/10.1002/PRCA.201400130
354. Puumala LS, Grist SM, Morales JM, et al (2022) Biofunctionalization of Multiplexed Silicon Photonic Biosensors. Biosensors 2023, Vol 13, Page 53 13:53. https://doi.org/10.3390/BIOS13010053
355. Ranjan Srivastava V, Kumari R, Chandra P (2023) Miniaturized surface engineered technologies for multiplex biosensing devices. Electroanalysis 35:e202200355. https://doi.org/10.1002/elan.202200355
356. Timilsina SS, Jolly P, Durr N, et al (2021) Enabling Multiplexed Electrochemical Detection of Biomarkers with High Sensitivity in Complex Biological Samples. Acc Chem Res 54:3529–3539. https://doi.org/10.1021/acs.accounts.1c00382
357. Liu G (2021) Grand Challenges in Biosensors and Biomolecular Electronics. Front Bioeng Biotechnol 9:707615. https://doi.org/10.3389/FBIOE.2021.707615
358. Nimse SB, Song K, Sonawane MD, et al (2014) Immobilization Techniques for Microarray: Challenges and Applications. Sensors 2014, Vol 14, Pages 22208-22229 14:22208–22229. https://doi.org/10.3390/S141222208
359. Nicholson RL, Ladlow ML, Spring DR (2007) Fluorous tagged small molecule microarrays. Chemical Communications 3906–3908. https://doi.org/10.1039/B712906H
360. Nicholson RL, Ladlow ML, Spring DR (2007) Fluorous tagged small molecule microarrays. Chemical Communications 3906–3908. https://doi.org/10.1039/B712906H
361. Song EH, Pohl NLB (2009) Fluorous-based small-molecule microarrays for protein, antibody and enzyme screening. http://dx.doi.org/104155/fmc0976 1:889–896. https://doi.org/10.4155/FMC.09.76
362. Flynn GE, Withers JM, Macias G, et al (2017) Reversible DNA micro-patterning using the fluorous effect. Chem Commun (Camb) 53:3094–3097. https://doi.org/10.1039/C7CC00288B
363. Zou J, Stammers AC, Taladriz-Sender A, et al (2023) Fluorous-Directed Assembly of DNA Origami Nanostructures. ACS Nano 17:752–759. https://doi.org/10.1021/acsnano.2c10727
364. Blin A, Cissé I, Bockelmann U (2014) Electronic hybridization detection in microarray format and DNA genotyping. Scientific Reports 2014 4:1 4:1–6. https://doi.org/10.1038/srep04194
365. Ioannidis JPA, Allison DB, Ball CA, et al (2009) Repeatability of published microarray gene expression analyses. Nature Genetics 2009 41:2 41:149–155. https://doi.org/10.1038/ng.295
366. Blin A, Cissé I, Bockelmann U (2014) Electronic hybridization detection in microarray format and DNA genotyping. Scientific Reports 2014 4:1 4:1–6. https://doi.org/10.1038/srep04194
367. Padín-González E, Lancaster P, Bottini M, et al (2022) Understanding the Role and Impact of Poly (Ethylene Glycol) (PEG) on Nanoparticle Formulation: Implications for COVID-19 Vaccines. Front Bioeng Biotechnol 10:882363. https://doi.org/10.3389/FBIOE.2022.882363
368. Kang DH, Kim HN, Kim P, Suh KY (2014) Poly(ethylene glycol) (PEG) microwells in microfluidics: Fabrication methods and applications. Biochip J 8:241–253. https://doi.org/10.1007/s13206-014-8401-y
369. Stasolla C, Van Zyl L, Egertsdotter U, et al (2003) The Effects of Polyethylene Glycol on Gene Expression of Developing White Spruce Somatic Embryos. Plant Physiol 131:49–60. https://doi.org/10.1104/PP.015214

370. Pan H, Xia Y, Qin M, et al (2015) A simple procedure to improve the surface passivation for single molecule fluorescence studies. Phys Biol 12:045006. https://doi.org/10.1088/1478-3975/12/4/045006
371. Han JH, Yoon JY (2009) Reusable, polyethylene glycol-structured microfluidic channel for particle immunoassays. J Biol Eng 3:1–6. https://doi.org/10.1186/1754-1611-3-6
372. Jo S, Park K (2000) Surface modification using silanated poly(ethylene glycol)s. Biomaterials 21:605–616. https://doi.org/10.1016/S0142-9612(99)00224-0
373. Nagasaki Y (2011) Construction of a densely poly(ethylene glycol)-chain-tethered surface and its performance. Polymer Journal 2011 43:12 43:949–958. https://doi.org/10.1038/pj.2011.93
374. Nagasaki Y (2011) Construction of a densely poly(ethylene glycol)-chain-tethered surface and its performance. Polymer Journal 2011 43:12 43:949–958. https://doi.org/10.1038/pj.2011.93
375. Zhang F, Liu MR, Wan HT (2014) Discussion about Several Potential Drawbacks of PEGylated Therapeutic Proteins. Biol Pharm Bull 37:335–339. https://doi.org/10.1248/BPB.B13-00661
376. Giridhar G, Manepalli RKNR, Apparao G (2017) Contact Angle Measurement Techniques for Nanomaterials. Thermal and Rheological Measurement Techniques for Nanomaterials Characterization 3:173–195. https://doi.org/10.1016/B978-0-323-46139-9.00008-6
377. Lößlein SM, Merz R, Müller DW, et al (2022) An in-depth evaluation of sample and measurement induced influences on static contact angle measurements. Scientific Reports 2022 12:1 12:1–16. https://doi.org/10.1038/s41598-022-23341-3
378. Scarratt LRJ, Steiner U, Neto C (2017) A review on the mechanical and thermodynamic robustness of superhydrophobic surfaces. Adv Colloid Interface Sci 246:133–152. https://doi.org/10.1016/J.CIS.2017.05.018
379. Dichiarante V, Martinez Espinoza MI, Gazzera L, et al (2018) A Short-Chain Multibranched Perfluoroalkyl Thiol for More Sustainable Hydrophobic Coatings. ACS Sustain Chem Eng 6:9734–9743. https://doi.org/10.1021/acssuschemeng.8b00777
380. Baek MG, Shin JE, Park SG (2020) Differences in ITO Interface Characteristics Change According to the Formation of Aromatic-Ring and Aliphatic Self-Assembled Monolayers. Crystals 2021, Vol 11, Page 26 11:26. https://doi.org/10.3390/CRYST11010026
381. Ye L, Lei X, Xu L, et al (2023) Gold nanoparticle-based immunochromatographic assay for the rapid detection of the SARS-CoV-2 Omicron variant. Mater Chem Front 7:4063–4072. https://doi.org/10.1039/D3QM00624G
382. Steel AB, Levicky RL, Herne TM, Tarlov MJ (2000) Immobilization of Nucleic Acids at Solid Surfaces: Effect of Oligonucleotide Length on Layer Assembly. Biophys J 79:975–981. https://doi.org/10.1016/S0006-3495(00)76351-X
383. Steel AB, Levicky RL, Herne TM, Tarlov MJ (2000) Immobilization of nucleic acids at solid surfaces: Effect of oligonucleotide length on layer assembly. Biophys J 79:975–981. https://doi.org/10.1016/S0006-3495(00)76351-X
384. Relógio A, Schwager C, Richter A, et al (2002) Optimization of oligonucleotide-based DNA microarrays. Nucleic Acids Res 30:e51–e51. https://doi.org/10.1093/NAR/30.11.E51
385. Flynn GE, Withers JM, Macias G, et al (2017) Reversible DNA micro-patterning using the fluorous effect. Chemical Communications 53:3094–3097. https://doi.org/10.1039/C7CC00288B

386. Ricci F, Lai RY, Heeger AJ, et al (2007) Effect of molecular crowding on the response of an electrochemical DNA sensor. Langmuir 23:6827–6834. https://doi.org/10.1021/la700328r
387. Nimse SB, Song K, Sonawane MD, et al (2014) Immobilization Techniques for Microarray: Challenges and Applications. Sensors 2014, Vol 14, Pages 22208-22229 14:22208–22229. https://doi.org/10.3390/S141222208
388. Schlapak R, Pammer P, Armitage D, et al (2006) Glass surfaces grafted with high-density poly(ethylene glycol) as substrates for DNA oligonucleotide microarrays. Langmuir 22:277–285. https://doi.org/10.1021/la0521793
389. Steel AB, Levicky RL, Herne TM, Tarlov MJ (2000) Immobilization of nucleic acids at solid surfaces: Effect of oligonucleotide length on layer assembly. Biophys J 79:975–981. https://doi.org/10.1016/S0006-3495(00)76351-X
390. Milton JA, Patole S, Yin H, et al (2013) Efficient self-assembly of DNA-functionalized fluorophores and gold nanoparticles with DNA functionalized silicon surfaces: the effect of oligomer spacers. Nucleic Acids Res 41:e80–e80. https://doi.org/10.1093/NAR/GKT031
391. Bujold KE, Hsu JCC, Sleiman HF (2016) Optimized DNA "nanosuitcases" for Encapsulation and Conditional Release of siRNA. J Am Chem Soc 138:14030–14038. https://doi.org/10.1021/jacs.6b08369
392. Milton JA, Patole S, Yin H, et al (2013) Efficient self-assembly of DNA-functionalized fluorophores and gold nanoparticles with DNA functionalized silicon surfaces: the effect of oligomer spacers. Nucleic Acids Res 41:e80–e80. https://doi.org/10.1093/NAR/GKT031
393. Hincapie R, Bhattacharya S, Keshavarz-Joud P, et al (2023) Preparation and Biological Properties of Oligonucleotide-Functionalized Virus-like Particles. Biomacromolecules 24:2766–2776. https://doi.org/10.1021/acs.biomac.3c00178
394. Rashid JIA, Yusof NA (2017) The strategies of DNA immobilization and hybridization detection mechanism in the construction of electrochemical DNA sensor: A review. Sens Biosensing Res 16:19–31. https://doi.org/10.1016/J.SBSR.2017.09.001
395. Steel AB, Levicky RL, Herne TM, Tarlov MJ (2000) Immobilization of nucleic acids at solid surfaces: Effect of oligonucleotide length on layer assembly. Biophys J 79:975–981. https://doi.org/10.1016/S0006-3495(00)76351-X
396. Steel AB, Levicky RL, Herne TM, Tarlov MJ (2000) Immobilization of nucleic acids at solid surfaces: Effect of oligonucleotide length on layer assembly. Biophys J 79:975–981. https://doi.org/10.1016/S0006-3495(00)76351-X
397. Jung Y, Jeong ML, Jung H, Bong HC (2007) Self-directed and self-oriented immobilization of antibody by protein G-DNA conjugate. Anal Chem 79:6534–6541. https://doi.org/10.1021/ac070484i
398. Peeters S, Stakenborg T, Reekmans G, et al (2008) Impact of spacers on the hybridization efficiency of mixed self-assembled DNA/alkanethiol films. Biosens Bioelectron 24:72–77. https://doi.org/10.1016/J.BIOS.2008.03.012
399. Miftakhov RA, Lapa SA, Kuznetsova VE, et al (2021) Effect of Spacers on DNA Probe Properties in Hybridization Analysis. Russ J Bioorg Chem 47:1345–1347. https://doi.org/10.1134/S1068162021060182
400. Halperin A, Buhot A, Zhulina EB (2006) Hybridization at a surface: The role of spacers in DNA microarrays. Langmuir 22:11290–11304. https://doi.org/10.1021/la0616606
401. Djebbi K, Shi B, Weng T, et al (2022) Highly Sensitive Fluorescence Assay for miRNA Detection: Investigation of the DNA Spacer Effect on the DSN Enzyme Activity toward Magnetic-Bead-Tethered Probes. ACS Omega 7:2224–2233. https://doi.org/10.1021/acsomega.1c05775

402. Peterson AW, Heaton RJ, Georgiadis RM (2001) The effect of surface probe density on DNA hybridization. Nucleic Acids Res 29:5163–5168. https://doi.org/10.1093/NAR/29.24.5163
403. Peterson AW, Heaton RJ, Georgiadis RM (2001) The effect of surface probe density on DNA hybridization. Nucleic Acids Res 29:5163–5168. https://doi.org/10.1093/NAR/29.24.5163
404. Gu Q, Josephs EA, Ye T (2022) Hybridization and self-assembly behaviors of surface-immobilized DNA in close proximity: A single-molecule perspective. Aggregate 3:e186. https://doi.org/10.1002/AGT2.186
405. Göppel T, Rosenberger JH, Altaner B, Gerland U (2022) Thermodynamic and Kinetic Sequence Selection in Enzyme-Free Polymer Self-Assembly Inside a Non-Equilibrium RNA Reactor. Life 12:567. https://doi.org/10.3390/life12040567
406. Breslauer KJ, Frank R, Blocker H, Marky LA (1986) Predicting DNA duplex stability from the base sequence. Proceedings of the National Academy of Sciences 83:3746–3750. https://doi.org/10.1073/PNAS.83.11.3746
407. Paul A, Farahat AA, Boykin DW, Wilson WD (2022) Thermodynamic Factors That Drive Sequence-Specific DNA Binding of Designed, Synthetic Minor Groove Binding Agents. Life 12:681. https://doi.org/10.3390/LIFE12050681
408. Song F, Krull UJ (2008) Selectivity of Hybridization Controlled by the Density of Solid Phase Synthesized DNA Probes on Glass Substrates. NATO Science for Peace and Security Series B: Physics and Biophysics 195–210. https://doi.org/10.1007/978-1-4020-6952-9_8
409. Watterson JH, Piunno PAE, Wust CC, Krull UJ (2000) Effects of Oligonucleotide Immobilization Density on Selectivity of Quantitative Transduction of Hybridization of Immobilized DNA. Langmuir 16:4984–4992. https://doi.org/10.1021/LA991508M
410. Peterson AW, Heaton RJ, Georgiadis RM (2001) The effect of surface probe density on DNA hybridization. Nucleic Acids Res 29:5163–5168. https://doi.org/10.1093/NAR/29.24.5163
411. Feng C, Liu X, Sun YF, Ren CL (2024) Double-Stranded DNA Immobilized in Lying-Flat and Upright Orientation on a PNIPAm-Coated Surface: A Theoretical Study. ACS Macro Lett 105–111. https://doi.org/10.1021/acsmacrolett.3c00647
412. Steel AB, Herne TM, Tarlov MJ (1998) Electrochemical Quantitation of DNA Immobilized on Gold. Anal Chem 70:4670–4677. https://doi.org/10.1021/AC980037Q
413. Flynn GE, Withers JM, Macias G, et al (2017) Reversible DNA micro-patterning using the fluorous effect. Chemical Communications 53:3094–3097. https://doi.org/10.1039/C7CC00288B
414. Hegde P, Qi R, Abernathy K, et al (2018) A Concise Guide to cDNA Microarray Analysis. https://doi.org/102144/00293bi01 29:548–562. https://doi.org/10.2144/00293BI01
415. Li J, Yao SQ (2009) “Singapore green”: A new fluorescent dye for microarray and bioimaging applications. Org Lett 11:405–408. https://doi.org/10.1021/ol802700w
416. Nishi K, Isobe SI, Zhu Y, Kiyama R (2015) Fluorescence-Based Bioassays for the Detection and Evaluation of Food Materials. Sensors 2015, Vol 15, Pages 25831-25867 15:25831–25867. https://doi.org/10.3390/S151025831
417. Okamura H, Yamano H, Tsuda T, et al (2023) Development of a clinical microarray system for genetic analysis screening. Pract Lab Med 33:e00306. https://doi.org/10.1016/J.PLABM.2022.E00306

418. Tighe PJ, Ryder RR, Todd I, Fairclough LC (2015) ELISA in the multiplex era: potentials and pitfalls. Proteomics Clin Appl 9:406–422. https://doi.org/10.1002/PRCA.201400130
419. Ranjan Srivastava V, Kumari R, Chandra P (2023) Miniaturized surface engineered technologies for multiplex biosensing devices. Electroanalysis 35:e202200355. https://doi.org/10.1002/elan.202200355
420. Timilsina SS, Jolly P, Durr N, et al (2021) Enabling Multiplexed Electrochemical Detection of Biomarkers with High Sensitivity in Complex Biological Samples. Acc Chem Res 54:3529–3539. https://doi.org/10.1021/acs.accounts.1c00382
421. Liu G (2021) Grand Challenges in Biosensors and Biomolecular Electronics. Front Bioeng Biotechnol 9:707615. https://doi.org/10.3389/FBIOE.2021.707615
422. Puumala LS, Grist SM, Morales JM, et al (2022) Biofunctionalization of Multiplexed Silicon Photonic Biosensors. Biosensors 2023, Vol 13, Page 53 13:53. https://doi.org/10.3390/BIOS13010053
423. Akarapipad P, Bertelson E, Pessell A, et al (2022) Emerging Multiplex Nucleic Acid Diagnostic Tests for Combating COVID-19. Biosensors 2022, Vol 12, Page 978 12:978. https://doi.org/10.3390/BIOS12110978
424. Jet T, Gines G, Rondelez Y, Taly V (2021) Advances in multiplexed techniques for the detection and quantification of microRNAs. Chem Soc Rev 50:4141–4161. https://doi.org/10.1039/D0CS00609B
425. Maurer K, Yazvenko N, Wilmoth J, et al (2010) Use of a Multiplexed CMOS Microarray to Optimize and Compare Oligonucleotide Binding to DNA Probes Synthesized or Immobilized on Individual Electrodes. Sensors 2010, Vol 10, Pages 7371-7385 10:7371–7385. https://doi.org/10.3390/S100807371
426. Miller MB, Tang YW (2009) Basic concepts of microarrays and potential applications in clinical microbiology. Clin Microbiol Rev 22:611–633. https://doi.org/10.1128/cmr.00019-09
427. Jet T, Gines G, Rondelez Y, Taly V (2021) Advances in multiplexed techniques for the detection and quantification of microRNAs. Chem Soc Rev 50:4141–4161. https://doi.org/10.1039/D0CS00609B
428. Shrestha D, Jenei A, Nagy P, et al (2015) Understanding FRET as a Research Tool for Cellular Studies. International Journal of Molecular Sciences 2015, Vol 16, Pages 6718-6756 16:6718–6756. https://doi.org/10.3390/IJMS16046718
429. Zou J, Stammers AC, Taladriz-Sender A, et al (2023) Fluorous-Directed Assembly of DNA Origami Nanostructures. ACS Nano 17:752–759. https://doi.org/10.1021/ACSNANO.2C10727
430. Ekins RP (1998) Ligand assays: from electrophoresis to miniaturized microarrays. Clin Chem 44:2015–2030. https://doi.org/10.1093/CLINCHEM/44.9.2015
431. Buchegger P, Sauer U, Toth-Székély H, Preininger C (2012) Miniaturized Protein Microarray with Internal Calibration as Point-of-Care Device for Diagnosis of Neonatal Sepsis. Sensors 2012, Vol 12, Pages 1494-1508 12:1494–1508. https://doi.org/10.3390/S120201494
432. Kricka LJ, Park JY, Li SFY, Fortina P (2005) Miniaturized detection technology in molecular diagnostics. Expert Rev Mol Diagn 5:549–559. https://doi.org/10.1586/14737159.5.4.549
433. Natalia A, Zhang L, Sundah NR, et al (2023) Analytical device miniaturization for the detection of circulating biomarkers. Nature Reviews Bioengineering 2023 1:7 1:481–498. https://doi.org/10.1038/s44222-023-00050-8
434. Call DR (2005) Challenges and Opportunities for Pathogen Detection Using DNA Microarrays. Crit Rev Microbiol 31:91–99. https://doi.org/10.1080/10408410590921736

435. Sedighi A, Li PCH (2014) Challenges and Future Trends in DNA Microarray Analysis. Comprehensive Analytical Chemistry 63:25–46. https://doi.org/10.1016/B978-0-444-62651-6.00002-7
436. Bañuls MJ, Jiménez-Meneses P, Meyer A, et al (2017) Improved Performance of DNA Microarray Multiplex Hybridization Using Probes Anchored at Several Points by Thiol-Ene or Thiol-Yne Coupling Chemistry. Bioconjug Chem 28:496–506. https://doi.org/10.1021/acs.bioconjchem.6b00624
437. Tian M, Tian Y, Li Y, et al (2014) Microarray Multiplex Assay for the Simultaneous Detection and Discrimination of Influenza A and Influenza B Viruses. Indian J Microbiol 54:211–217. https://doi.org/10.1007/s12088-013-0432-x
438. Onilude HA, Vega MS, Clark AW (2023) Functionalisation of 20 nm citrate-coated gold nanoparticles using perfluorodecanethiol. 12431:34–38. https://doi.org/10.1117/12.2649965
439. Ni C, Hu J (2016) The unique fluorine effects in organic reactions: recent facts and insights into fluoroalkylations. Chem Soc Rev 45:5441–5454. https://doi.org/10.1039/C6CS00351F
440. Cametti M, Crousse B, Metrangolo P, et al (2011) The fluorous effect in biomolecular applications. Chem Soc Rev 41:31–42. https://doi.org/10.1039/C1CS15084G
441. Pan Y (2019) The dark side of fluorine. ACS Med Chem Lett 10:1016–1019. https://doi.org/10.1021/acsmedchemlett.9b00235
442. Shaabani E, Amini SM, Kharrazi S, Tajerian R (2017) Curcumin coated gold nanoparticles: synthesis, characterization, cytotoxicity, antioxidant activity and its comparison with citrate coated gold nanoparticles. 4:115–125. https://doi.org/10.22038/NMJ.2017.21506.1227
443. Zeta deviation larger than the mean - how can that be? | Malvern Panalytical. https://www.malvernpanalytical.com/en/learn/knowledge-center/insights/zeta-deviation-larger-than-the-mean-how-can-that-be. Accessed 8 Apr 2024
444. Khalkho BR, Deb MK, Kurrey R, et al (2022) Citrate functionalized gold nanoparticles assisted micro extraction of L-cysteine in milk and water samples using Fourier transform infrared spectroscopy. Spectrochim Acta A Mol Biomol Spectrosc 267:120523. https://doi.org/10.1016/J.SAA.2021.120523
445. Zhao L, Jiang D, Cai Y, et al (2012) Tuning the size of gold nanoparticles in the citrate reduction by chloride ions. Nanoscale 4:5071–5076. https://doi.org/10.1039/C2NR30957B
446. Spampinato V, Parracino MA, La Spina R, et al (2016) Surface analysis of gold nanoparticles functionalized with thiol-modified glucose SAMs for biosensor applications. Front Chem 4:162427. https://doi.org/10.3389/FCHEM.2016.00008
447. Zhu J, Wang J, Zhan X, et al (2021) Role of Charge and Size in the Translocation and Distribution of Zinc Oxide Particles in Wheat Cells. ACS Sustain Chem Eng 9:11556–11564. https://doi.org/10.1021/acssuschemeng.1c04080
448. Drescher D, Büchner T, Schrade P, et al (2021) Influence of Nuclear Localization Sequences on the Intracellular Fate of Gold Nanoparticles. ACS Nano 15:14838–14849. https://doi.org/10.1021/acsnano.1c04925
449. Yazdani S, Daneshkhah A, Diwate A, et al (2021) Model for Gold Nanoparticle Synthesis: Effect of pH and Reaction Time. ACS Omega 6:16847–16853. https://doi.org/10.1021/acsomega.1c01418
450. Sakellari GI, Hondow N, Gardiner PHE (2020) Factors Influencing the Surface Functionalization of Citrate Stabilized Gold Nanoparticles with Cysteamine, 3-Mercaptopropionic Acid or l-Selenocystine for Sensor Applications. Chemosensors 2020, Vol 8, Page 80 8:80. https://doi.org/10.3390/chemosensors8030080

451. Balasubramanian SK, Yang L, Yung LYL, et al (2010) Characterization, purification, and stability of gold nanoparticles. Biomaterials 31:9023–9030. https://doi.org/10.1016/j.biomaterials.2010.08.012
452. Park JW, Shumaker-Parry JS (2014) Structural study of citrate layers on gold nanoparticles: Role of intermolecular interactions in stabilizing nanoparticles. J Am Chem Soc 136:1907–1921. https://doi.org/10.1021/JA4097384
453. Ahuja T, Chaudhari K, Paramasivam G, et al (2021) Toward vibrational tomography of citrate on dynamically changing individual silver nanoparticles. Journal of Physical Chemistry C 125:3553–3566. https://doi.org/10.1021/ACS.JPCC.0C09981
454. Alam AM, Shon YS (2021) Water-Soluble Noble Metal Nanoparticle Catalysts Capped with Small Organic Molecules for Organic Transformations in Water. ACS Appl Nano Mater 4:3294–3318. https://doi.org/10.1021/ACSANM.1C00335
455. Park JW, Shumaker-Parry JS (2015) Strong resistance of citrate anions on metal nanoparticles to desorption under thiol functionalization. ACS Nano 9:1665–1682. https://doi.org/10.1021/nn506379m
456. Park JW, Shumaker-Parry JS (2015) Strong resistance of citrate anions on metal nanoparticles to desorption under thiol functionalization. ACS Nano 9:1665–1682. https://doi.org/10.1021/NN506379M
457. Sakellari GI, Hondow N, Gardiner PHE (2020) Factors Influencing the Surface Functionalization of Citrate Stabilized Gold Nanoparticles with Cysteamine, 3-Mercaptopropionic Acid or l-Selenocystine for Sensor Applications. Chemosensors 2020, Vol 8, Page 80 8:80. https://doi.org/10.3390/chemosensors8030080
458. Park JW, Shumaker-Parry JS (2014) Structural study of citrate layers on gold nanoparticles: Role of intermolecular interactions in stabilizing nanoparticles. J Am Chem Soc 136:1907–1921. https://doi.org/10.1021/JA4097384/
459. Floate S, Hosseini M, Arshadi MR, et al (2003) An in-situ infrared spectroscopic study of the adsorption of citrate on Au(111) electrodes. Journal of Electroanalytical Chemistry 542:67–74. https://doi.org/10.1016/S0022-0728(02)01451-1
460. Gisbert-González JM, Cheuquepán W, Ferre-Vilaplana A, et al (2020) Citrate adsorption on gold: Understanding the shaping mechanism of nanoparticles. Journal of Electroanalytical Chemistry 875:114015. https://doi.org/10.1016/J.JELECHEM.2020.114015
461. Bajaj M, Wangoo N, Jain DVS, Sharma RK (2020) Quantification of adsorbed and dangling citrate ions on gold nanoparticle surface using thermogravimetric analysis. Scientific Reports 2020 10:1 10:1–7. https://doi.org/10.1038/s41598-020-65013-0
462. Contreras-Trigo B, Díaz-García V, Guzmán-Gutierrez E, et al (2018) Slight pH Fluctuations in the Gold Nanoparticle Synthesis Process Influence the Performance of the Citrate Reduction Method. Sensors 2018, Vol 18, Page 2246 18:2246. https://doi.org/10.3390/S18072246
463. Shi L, Buhler E, Boué F, Carn F (2017) How does the size of gold nanoparticles depend on citrate to gold ratio in Turkevich synthesis? Final answer to a debated question. J Colloid Interface Sci 492:191–198. https://doi.org/10.1016/J.JCIS.2016.10.065
464. Gozdalik JT, Adamczyk-Wozniak A, Sporzyński A (2018) Influence of fluorine substituents on the properties of phenylboronic compounds. Pure and Applied Chemistry 90:677–702. https://doi.org/10.1515/PAC-2017-1009
465. Paik WK, Han S, Shin W, Kim Y (2003) Adsorption of Carboxylic Acids on Gold by Anodic Reaction. Langmuir 19:4211–4216. https://doi.org/10.1021/La026836s
466. Smart BE (2001) Fluorine substituent effects (on bioactivity). J Fluor Chem 109:3–11. https://doi.org/10.1016/S0022-1139(01)00375-X

467. Grys DB, De Nijs B, Salmon AR, et al (2020) Citrate Coordination and Bridging of Gold Nanoparticles: The Role of Gold Adatoms in AuNP Aging. ACS Nano 14:8689–8696. https://doi.org/10.1021/ACSNANO.0C03050
468. Yang M, Chen D, Hu J, et al (2022) The application of coffee-ring effect in analytical chemistry. TrAC Trends in Analytical Chemistry 157:116752. https://doi.org/10.1016/J.TRAC.2022.116752
469. Deegan RD, Bakajin O, Dupont TF, et al (1997) Capillary flow as the cause of ring stains from dried liquid drops. Nature 1997 389:6653 389:827–829. https://doi.org/10.1038/39827
470. Wang C, Li L, Li J, et al (2023) Biomimetic Surface Engineering to Modulate the Coffee-Ring Effect for Amyloid-β Detection in Rat Brains. Biomimetics 8:581. https://doi.org/10.3390/BIOMIMETICS8080581
471. Zang D, Tarafdar S, Tarasevich YY, et al (2019) Evaporation of a Droplet: From physics to applications. Phys Rep 804:1–56. https://doi.org/10.1016/J.PHYSREP.2019.01.008
472. Mampallil D, Reboud J, Wilson R, et al (2015) Acoustic suppression of the coffee-ring effect. Soft Matter 11:7207–7213. https://doi.org/10.1039/C5SM01196E
473. Zargartalebi H, Hejazi SH, Sanati-Nezhad A (2022) Self-assembly of highly ordered micro- and nanoparticle deposits. Nature Communications 2022 13:1 13:1–11. https://doi.org/10.1038/s41467-022-30660-6
474. Mujawar LH, Norde W, Van Amerongen A (2012) Spot morphology of non-contact printed protein molecules on non-porous substrates with a range of hydrophobicities. Analyst 138:518–524. https://doi.org/10.1039/C2AN36104C
475. Sliz R, Czajkowski J, Fabritius T (2020) Taming the Coffee Ring Effect: Enhanced Thermal Control as a Method for Thin-Film Nanopatterning. Langmuir 36:9562–9570. https://doi.org/10.1021/acs.langmuir.0c01560
476. Eral HB, Augustine DM, Duits MHG, Mugele F (2011) Suppressing the coffee stain effect: how to control colloidal self-assembly in evaporating drops using electrowetting. Soft Matter 7:4954–4958. https://doi.org/10.1039/C1SM05183K
477. Mugele F, Baret JC (2005) Electrowetting: from basics to applications. Journal of Physics: Condensed Matter 17:R705. https://doi.org/10.1088/0953-8984/17/28/R01
478. Wang C, Li L, Li J, et al (2023) Biomimetic Surface Engineering to Modulate the Coffee-Ring Effect for Amyloid-β Detection in Rat Brains. Biomimetics 8:581. https://doi.org/10.3390/BIOMIMETICS8080581
479. Li H, Buesen D, Williams R, et al (2018) Preventing the coffee-ring effect and aggregate sedimentation by in situ gelation of monodisperse materials. Chem Sci 9:7596–7605. https://doi.org/10.1039/C8SC03302A
480. Yunker PJ, Still T, Lohr MA, Yodh AG (2011) Suppression of the coffee-ring effect by shape-dependent capillary interactions. Nature 2011 476:7360 476:308–311. https://doi.org/10.1038/nature10344
481. Ishigaki Y, Shimajiri T, Takeda T, et al (2018) Longest C–C Single Bond among Neutral Hydrocarbons with a Bond Length beyond 1.8 Å. Chem 4:795–806. https://doi.org/10.1016/j.chempr.2018.01.011
482. Kokkin DL, Zhang R, Steimle TC, et al (2015) Au-S Bonding Revealed from the Characterization of Diatomic Gold Sulfide, AuS. Journal of Physical Chemistry A 119:11659–11667. https://doi.org/10.1021/ACS.JPCA.5B08781
483. Kumar Y, Sinha ASK, Nigam KDP, et al (2023) Functionalized nanoparticles: Tailoring properties through surface energetics and coordination chemistry for advanced biomedical applications. Nanoscale 15:6075–6104. https://doi.org/10.1039/D2NR07163K

484. Serrano-Montes AB, De Aberasturi DJ, Langer J, et al (2015) A General Method for Solvent Exchange of Plasmonic Nanoparticles and Self-Assembly into SERS-Active Monolayers. Langmuir 31:9205–9213. https://doi.org/10.1021/ACS.LANGMUIR.5B01838
485. Song L, Xu B Bin, Cheng Q, et al (2021) Instant interfacial self-assembly for homogeneous nanoparticle monolayer enabled conformal “lift-on” thin film technology. Sci Adv 7:2852. https://doi.org/10.1126/SCIADV.ABK2852
486. Niu Z, He J, Russell TP, Wang Q (2010) Synthesis of Nano/Microstructures at Fluid Interfaces. Angewandte Chemie International Edition 49:10052–10066. https://doi.org/10.1002/ANIE.201001623
487. Binks BP (2002) Particles as surfactants—similarities and differences. Curr Opin Colloid Interface Sci 7:21–41. https://doi.org/10.1016/S1359-0294(02)00008-0
488. Oliveira ON, Caseli L, Ariga K (2022) The Past and the Future of Langmuir and Langmuir-Blodgett Films. Chem Rev 122:6459–6513. https://doi.org/10.1021/ACS.CHEMREV.1C00754
489. Stetsenko M, Margitych T, Kryvyi S, et al (2020) Gold Nanoparticle Self-Aggregation on Surface with 1,6-Hexanedithiol Functionalization. Nanomaterials 2020, Vol 10, Page 512 10:512. https://doi.org/10.3390/NANO10030512
490. Humbert C, Pluchery O, Lacaze E, et al (2013) Optical spectroscopy of functionalized gold nanoparticles assemblies as a function of the surface coverage. Gold Bull 46:299–309. https://doi.org/10.1007/s13404-013-0126-5
491. Pan JH, Peng CY, Lo CT, et al (2017) n-Hexane intoxication in a Chinese medicine pharmaceutical plant: a case report. J Med Case Rep 11:1–7. https://doi.org/10.1186/S13256-017-1280-9
492. Hinterwirth H, Kappel S, Waitz T, et al (2013) Quantifying thiol ligand density of self-assembled monolayers on gold nanoparticles by inductively coupled plasma-mass spectrometry. ACS Nano 7:1129–1136. https://doi.org/10.1021/NN306024A
493. Sun J, Xianyu Y, Jiang X (2014) Point-of-care biochemical assays using gold nanoparticle-implemented microfluidics. Chem Soc Rev 43:6239–6253. https://doi.org/10.1039/C4CS00125G
494. Ghosh P, Han G, De M, et al (2008) Gold nanoparticles in delivery applications. Adv Drug Deliv Rev 60:1307–1315. https://doi.org/10.1016/J.ADDR.2008.03.016
495. Rana S, Bajaj A, Mout R, Rotello VM (2012) Monolayer coated gold nanoparticles for delivery applications. Adv Drug Deliv Rev 64:200–216. https://doi.org/10.1016/J.ADDR.2011.08.006
496. Biju V (2014) Chemical modifications and bioconjugate reactions of nanomaterials for sensing, imaging, drug delivery and therapy. Chem Soc Rev 43:744–764. https://doi.org/10.1039/C3CS60273G
497. Nimse SB, Song K, Sonawane MD, et al (2014) Immobilization Techniques for Microarray: Challenges and Applications. Sensors 2014, Vol 14, Pages 22208-22229 14:22208–22229. https://doi.org/10.3390/S141222208
498. Carone A, Emilsson S, Mariani P, et al (2023) Gold nanoparticle shape dependence of colloidal stability domains. Nanoscale Adv 5:2017–2026. https://doi.org/10.1039/D2NA00809B
499. Busch RT, Karim F, Weis J, et al (2019) Optimization and Structural Stability of Gold Nanoparticle-Antibody Bioconjugates. ACS Omega 4:15269–15279. https://doi.org/10.1021/ACSOMEGA.9B02276
500. Njoki PN, Lim IIS, Mott D, et al (2007) Size Correlation of Optical and Spectroscopic Properties for Gold Nanoparticles. Journal of Physical Chemistry C 111:14664–14669. https://doi.org/10.1021/JP074902Z

501. Montaño-Priede JL, Sanromán-Iglesias M, Zabala N, et al (2023) Robust Rules for Optimal Colorimetric Sensing Based on Gold Nanoparticle Aggregation. ACS Sens 8:1827–1834. https://doi.org/10.1021/ACSSENSORS.3C00287
502. Jain PK, Huang W, El-Sayed MA (2007) On the universal scaling behavior of the distance decay of plasmon coupling in metal nanoparticle pairs: A plasmon ruler equation. Nano Lett 7:2080–2088. https://doi.org/10.1021/NL071008A
503. Barrow SJ, Wei X, Baldauf JS, et al (2012) The surface plasmon modes of self-assembled gold nanocrystals. Nature Communications 2012 3:1 3:1–9. https://doi.org/10.1038/ncomms2289
504. Borah R, Ninakanti R, Bals S, Verbruggen SW (2022) Plasmon resonance of gold and silver nanoparticle arrays in the Kretschmann (attenuated total reflectance) vs. direct incidence configuration. Scientific Reports 2022 12:1 12:1–19. https://doi.org/10.1038/s41598-022-20117-7
505. Huang X, El-Sayed MA (2010) Gold nanoparticles: Optical properties and implementations in cancer diagnosis and photothermal therapy. J Adv Res 1:13–28. https://doi.org/10.1016/J.JARE.2010.02.002
506. Abdollahramezani S, Hemmatyar O, Taghinejad M, et al (2022) Electrically driven reprogrammable phase-change metasurface reaching 80% efficiency. Nature Communications 2022 13:1 13:1–11. https://doi.org/10.1038/s41467-022-29374-6
507. Bang S, Kim J, Yoon G, et al (2018) Recent Advances in Tunable and Reconfigurable Metamaterials. Micromachines 2018, Vol 9, Page 560 9:560. https://doi.org/10.3390/MI9110560
508. Li MH (2009) Toxicity of perfluorooctane sulfonate and perfluorooctanoic acid to plants and aquatic invertebrates. Environ Toxicol 24:95–101. https://doi.org/10.1002/TOX.20396
509. Wang X, Zhang H, Chen Y, et al (2023) Promoted CF4 Decomposition via Enhanced Tricoordinated Al Active Sites. ACS ES and T Engineering. https://doi.org/10.1021/ACSESTENGG.3C00583
510. Colomer I, Chamberlain AER, Haughey MB, Donohoe TJ (2017) Hexafluoroisopropanol as a highly versatile solvent. Nature Reviews Chemistry 2017 1:11 1:1–12. https://doi.org/10.1038/s41570-017-0088
511. Anik MI, Mahmud N, Masud A Al, Hasan M (2022) Gold nanoparticles (GNPs) in biomedical and clinical applications: A review. Nano Select 3:792–828. https://doi.org/10.1002/NANO.202100255
512. Jain PK, Lee KS, El-Sayed IH, El-Sayed MA (2006) Calculated Absorption and Scattering Properties of Gold Nanoparticles of Different Size, Shape, and Composition: Applications in Biological Imaging and Biomedicine. Journal of Physical Chemistry B 110:7238–7248. https://doi.org/10.1021/JP057170O
513. Wang E, Lilly SJ, Ha Y, et al (2018) Nanoparticle Optical Properties: Size Dependence of a Single Gold Spherical Nanoparticle. J Phys Conf Ser 1083:012040. https://doi.org/10.1088/1742-6596/1083/1/012040
514. Ding Y, Huang PJJ, Zandieh M, et al (2023) Gold Nanoparticles Synthesized Using Various Reducing Agents and the Effect of Aging for DNA Sensing. Langmuir 39:256–264. https://doi.org/10.1021/ACS.LANGMUIR.2C02458
515. Mahmudin L, Suharyadi E, Utomo ABS, et al (2015) Optical Properties of Silver Nanoparticles for Surface Plasmon Resonance (SPR)-Based Biosensor Applications. Journal of Modern Physics 6:1071–1076. https://doi.org/10.4236/JMP.2015.68111
516. Husain S, Nandi A, Simnani FZ, et al (2023) Emerging Trends in Advanced Translational Applications of Silver Nanoparticles: A Progressing Dawn of Nanotechnology. Journal of Functional Biomaterials 2023, Vol 14, Page 47 14:47. https://doi.org/10.3390/JFB14010047

517. Sadowski Z, Maliszewska IH, Sadowski Z, et al (2011) Applications of Gold Nanoparticles: Current Trends and Future Prospects. Metal Nanoparticles in Microbiology 225–248. https://doi.org/10.1007/978-3-642-18312-6_10
518. Yeh YC, Creran B, Rotello VM (2012) Gold Nanoparticles: Preparation, Properties, and Applications in Bionanotechnology. Nanoscale 4:1871. https://doi.org/10.1039/C1NR11188D
519. Moustakas M, Dendrinou-Samara C, Milan J, et al (2022) Treasure on the Earth—Gold Nanoparticles and Their Biomedical Applications. Materials 2022, Vol 15, Page 3355 15:3355. https://doi.org/10.3390/MA15093355
520. Pan ZY, Zhou J, Zou HY, et al (2021) In situ investigating the size-dependent scattering signatures and sensing sensitivity of single silver nanocube through a multi-model approach. J Colloid Interface Sci 584:253–262. https://doi.org/10.1016/J.JCIS.2020.09.121
521. Evanoff DD, Chumanov G (2005) Synthesis and Optical Properties of Silver Nanoparticles and Arrays. ChemPhysChem 6:1221–1231. https://doi.org/10.1002/CPHC.200500113
522. Cunningham B, Engstrom AE, Harper BJ, et al (2021) Silver nanoparticles stable to oxidation and silver ion release show size-dependent toxicity in vivo. Nanomaterials 11:1516. https://doi.org/10.3390/NANO11061516
523. Smith DK, Miller NR, Korgel BA (2009) Iodide in CTAB prevents gold nanorod formation. Langmuir 25:9518–9524. https://doi.org/10.1021/LA900757S
524. Li H, Xia H, Wang D, Tao X (2013) Simple synthesis of monodisperse, quasi-spherical, citrate-stabilized silver nanocrystals in water. Langmuir 29:5074–5079. https://doi.org/10.1021/LA400214X
525. Li H, Xia H, Wang D, Tao X (2013) Simple synthesis of monodisperse, quasi-spherical, citrate-stabilized silver nanocrystals in water. Langmuir 29:5074–5079. https://doi.org/10.1021/LA400214X
526. Stetefeld J, McKenna SA, Patel TR (2016) Dynamic light scattering: a practical guide and applications in biomedical sciences. Biophys Rev 8:409–427. https://doi.org/10.1007/S12551-016-0218-6
527. Alluhaybi HA, Ghoshal SK, Alsobhi BO (2024) An overview of the unique absorption and scattering characteristics of gold nanoparticles: experimental and theoretical study. Journal of Taibah University for Science 18:2309702. https://doi.org/10.1080/16583655.2024.2309702
528. Kelly KL, Coronado E, Zhao LL, Schatz GC (2003) The optical properties of metal nanoparticles: The influence of size, shape, and dielectric environment. Journal of Physical Chemistry B 107:668–677. https://doi.org/10.1021/JP026731Y
529. Kurt A, Çelik Y (2020) Synthesis Of Quasi-Spherical Silver Nanoparticles by Chemical Reduction Route using Different Reducing Agents. Konya Journal of Engineering Sciences 8:828–838. https://doi.org/10.36306/KONJES.700622
530. Leopold N, Lendl B (2003) A New Method for Fast Preparation of Highly Surface-Enhanced Raman Scattering (SERS) Active Silver Colloids at Room Temperature by Reduction of Silver Nitrate with Hydroxylamine Hydrochloride. J Phys Chem B 107:5723–5727. https://doi.org/10.1021/JP027460U
531. Garg S, Rong H, Miller CJ, Waite TD (2016) Oxidative Dissolution of Silver Nanoparticles by Chlorine: Implications to Silver Nanoparticle Fate and Toxicity. Environ Sci Technol 50:3890–3896. https://doi.org/10.1021/ACS.EST.6B00037
532. Park JW, Shumaker-Parry JS (2014) Structural study of citrate layers on gold nanoparticles: Role of intermolecular interactions in stabilizing nanoparticles. J Am Chem Soc 136:1907–1921. https://doi.org/10.1021/JA4097384
533. Leopold N, Lendl B (2003) A New Method for Fast Preparation of Highly Surface-Enhanced Raman Scattering (SERS) Active Silver Colloids at Room Temperature by

Reduction of Silver Nitrate with Hydroxylamine Hydrochloride. J Phys Chem B 107:5723–5727. https://doi.org/10.1021/JP027460U
534. Leopold N, Lendl B (2003) A New Method for Fast Preparation of Highly Surface-Enhanced Raman Scattering (SERS) Active Silver Colloids at Room Temperature by Reduction of Silver Nitrate with Hydroxylamine Hydrochloride. J Phys Chem B 107:5723–5727. https://doi.org/10.1021/JP027460U
535. Garrido C, Weiss-López BE, Campos Vallette MM (2016) Surface-enhanced Raman scattering activity of negatively charged bio-analytes from a modified silver colloid. Spectroscopy Letters 49:11–18. https://doi.org/10.1080/00387010.2015.1046606
536. Németh Z, Csóka I, Semnani Jazani R, et al (2022) Quality by Design-Driven Zeta Potential Optimisation Study of Liposomes with Charge Imparting Membrane Additives. Pharmaceutics 2022, Vol 14, Page 1798 14:1798. https://doi.org/10.3390/PHARMACEUTICS14091798
537. Su KH, Wei QH, Zhang X, et al (2003) Interparticle coupling effects on plasmon resonances of nanogold particles. Nano Lett 3:1087–1090. https://doi.org/10.1021/NL034197F
538. Wu W Te, Chen CH, Chiang CY, Chau LK (2018) Effect of Surface Coverage of Gold Nanoparticles on the Refractive Index Sensitivity in Fiber-Optic Nanoplasmonic Sensing. Sensors 2018, Vol 18, Page 1759 18:1759. https://doi.org/10.3390/S18061759
539. Liu M, Zhu W, Huo P, et al (2021) Multifunctional metasurfaces enabled by simultaneous and independent control of phase and amplitude for orthogonal polarization states. Light: Science & Applications 2021 10:1 10:1–11. https://doi.org/10.1038/s41377-021-00552-3
540. Liu M, Zhu W, Huo P, et al (2021) Multifunctional metasurfaces enabled by simultaneous and independent control of phase and amplitude for orthogonal polarization states. Light: Science & Applications 2021 10:1 10:1–11. https://doi.org/10.1038/s41377-021-00552-3
541. Kumar N, Ghosh SK, Bhattacharyya S (2023) Thermally Switchable Metasurface for Controlling Transmission in the THz-gap. Plasmonics 1:1–9. https://doi.org/10.1007/s11468-023-02115-1
542. Ma Q, Bai GD, Jing HB, et al (2019) Smart metasurface with self-adaptively reprogrammable functions. Light: Science & Applications 2019 8:1 8:1–12. https://doi.org/10.1038/s41377-019-0205-3
543. Ma Q, Bai GD, Jing HB, et al (2019) Smart metasurface with self-adaptively reprogrammable functions. Light: Science & Applications 2019 8:1 8:1–12. https://doi.org/10.1038/s41377-019-0205-3
544. Das A, Santhosh S, Giridhar M, et al (2023) Dipodal Silanes Greatly Stabilize Glass Surface Functionalization for DNA Microarray Synthesis and High-Throughput Biological Assays. Anal Chem 95:15384–15393. https://doi.org/10.1021/ACS.ANALCHEM.3C03399
545. Wei Q, Huang L, Zentgraf T, Wang Y (2020) Optical wavefront shaping based on functional metasurfaces. Nanophotonics 9:987–1002. https://doi.org/10.1515/NANOPH-2019-0478
546. Binder WH, Lomoschitz M, Sachsenhofer R, Friedbacher G (2009) Reversible and irreversible binding of nanoparticles to polymeric surfaces. J Nanomater 2009:. https://doi.org/10.1155/2009/613813
547. Matsumoto M, Kaneko K, Hara M, et al (2021) Covalent immobilization of gold nanoparticles on a plastic substrate and subsequent immobilization of biomolecules. RSC Adv 11:23409–23417. https://doi.org/10.1039/D1RA03902D

548. Jazayeri MH, Amani H, Pourfatollah AA, et al (2016) Various methods of gold nanoparticles (GNPs) conjugation to antibodies. Sens Biosensing Res 9:17–22. https://doi.org/10.1016/J.SBSR.2016.04.002
549. Stevenson KA, Muralidharan G, Maya L, et al (2002) Covalent Attachment of Gold Nanoparticles to DNA Templates. J Nanosci Nanotechnol 2:397–404. https://doi.org/10.1166/JNN.2002.110
550. Mitchell MJ, Billingsley MM, Haley RM, et al (2020) Engineering precision nanoparticles for drug delivery. Nature Reviews Drug Discovery 2020 20:2 20:101–124. https://doi.org/10.1038/s41573-020-0090-8
551. Dutt Y, Pandey RP, Dutt M, et al (2023) Therapeutic applications of nanobiotechnology. Journal of Nanobiotechnology 2023 21:1 21:1–32. https://doi.org/10.1186/S12951-023-01909-Z
552. Blanco E, Shen H, Ferrari M (2015) Principles of nanoparticle design for overcoming biological barriers to drug delivery. Nature Biotechnology 2015 33:9 33:941–951. https://doi.org/10.1038/nbt.3330
553. Chen C, Posocco P, Liu X, et al (2016) Mastering Dendrimer Self-Assembly for Efficient siRNA Delivery: From Conceptual Design to In Vivo Efficient Gene Silencing. Small 12:3667–3676. https://doi.org/10.1002/SMLL.201503866
554. Wolfram J, Shen H, Ferrari M (2015) Multistage vector (MSV) therapeutics. Journal of Controlled Release 219:406–415. https://doi.org/10.1016/J.JCONREL.2015.08.010
555. Lalander CH, Zheng Y, Dhuey S, et al (2010) DNA-directed self-assembly of gold nanoparticles onto nanopatterned surfaces: Controlled placement of individual nanoparticles into regular arrays. ACS Nano 4:6153–6161. https://doi.org/10.1021/NN101431K
556. Gole MT, Yin Z, Wang MC, et al (2021) Large scale self-assembly of plasmonic nanoparticles on deformed graphene templates. Scientific Reports 2021 11:1 11:1–9. https://doi.org/10.1038/s41598-021-91697-z
557. Altug H, Oh SH, Maier SA, Homola J (2022) Advances and applications of nanophotonic biosensors. Nature Nanotechnology 2022 17:1 17:5–16. https://doi.org/10.1038/s41565-021-01045-5
558. Ferreira Q, Delfino CL, Morgado J, Alcácer L (2019) Bottom-Up Self-Assembled Supramolecular Structures Built by STM at the Solid/Liquid Interface. Materials 2019, Vol 12, Page 382 12:382. https://doi.org/10.3390/MA12030382
559. Liedel C, Lewin C, Tsarkova L, Böker A (2015) Reversible Switching of Block Copolymer Nanopatterns by Orthogonal Electric Fields. Small 11:6058–6064. https://doi.org/10.1002/SMLL.201502259
560. Hendrich K, Peng W, Vana P (2020) Controlled Arrangement of Gold Nanoparticles on Planar Surfaces via Constrained Dewetting of Surface-Grafted RAFT Polymer. Polymers 2020, Vol 12, Page 1214 12:1214. https://doi.org/10.3390/POLYM12061214
561. Onses MS, Nealey PF (2013) Tunable Assembly of Gold Nanoparticles on Nanopatterned Poly(ethylene glycol) Brushes. Small 9:4168–4174. https://doi.org/10.1002/SMLL.201300462
562. Barad HN, Kwon H, Alarcón-Correa M, Fischer P (2021) Large Area Patterning of Nanoparticles and Nanostructures: Current Status and Future Prospects. ACS Nano 15:5861–5875. https://doi.org/10.1021/ACSNANO.0C09999
563. Lalander CH, Zheng Y, Dhuey S, et al (2010) DNA-directed self-assembly of gold nanoparticles onto nanopatterned surfaces: Controlled placement of individual nanoparticles into regular arrays. ACS Nano 4:6153–6161. https://doi.org/10.1021/NN101431K

564. Wang L, Montagne F, Heinzelmann H, Pugin R (2011) Electrostatic-guided positioning of gold colloids using periodic nanopatterns produced by block copolymer lithography. J Mater Chem 21:1689–1692. https://doi.org/10.1039/C0JM02693J
565. Lusker KL, Li JR, Garno JC (2011) Nanostructures of functionalized gold nanoparticles prepared by particle lithography with organosilanes. Langmuir 27:13269–13275. https://doi.org/10.1021/LA202816K
566. Huang CH, Lee YC, Kudo T, et al (2023) Unidirectional Optical Swarming of Gold Nanoparticles on Lithographically Fabricated Gold Nanopatterns. Journal of Physical Chemistry C 127:19044–19054. https://doi.org/10.1021/ACS.JPCC.3C04949
567. Ahmad F, Salem-Bekhit MM, Khan F, et al (2022) Unique Properties of Surface-Functionalized Nanoparticles for Bio-Application: Functionalization Mechanisms and Importance in Application. Nanomaterials 2022, Vol 12, Page 1333 12:1333. https://doi.org/10.3390/NANO12081333
568. Bouvrée A, D'Orlando A, Makiabadi T, et al (2013) Nanostructured and nanopatterned gold surfaces: Application to the surface-enhanced Raman spectroscopy. Gold Bull 46:283–290. https://doi.org/10.1007/S13404-013-0127-4
569. Zheng J, Zhu Z, Chen H, Liu Z (2000) Nanopatterned Assembling of Colloidal Gold Nanoparticles on Silicon. Langmuir 16:4409–4412. https://doi.org/10.1021/LA991332O
570. Dong J, Carpinone PL, Pyrgiotakis G, et al (2020) Synthesis of Precision Gold Nanoparticles Using Turkevich Method. Kona 37:224. https://doi.org/10.14356/KONA.2020011
571. Bastús NG, Comenge J, Puntes V (2011) Kinetically controlled seeded growth synthesis of citrate-stabilized gold nanoparticles of up to 200 nm: Size focusing versus ostwald ripening. Langmuir 27:11098–11105. https://doi.org/10.1021/LA201938U
572. Turkevich J, Stevenson PC, Hillier J (1951) A study of the nucleation and growth processes in the synthesis of colloidal gold. Discuss Faraday Soc 11:55–75. https://doi.org/10.1039/DF9511100055
573. Dong J, Carpinone PL, Pyrgiotakis G, et al (2020) Synthesis of Precision Gold Nanoparticles Using Turkevich Method. KONA Powder and Particle Journal 37:224–232. https://doi.org/10.14356/KONA.2020011
574. Oliveira AEF;, Pereira AC;, Resende MAC;, et al (2023) Gold Nanoparticles: A Didactic Step-by-Step of the Synthesis Using the Turkevich Method, Mechanisms, and Characterizations. Analytica 2023, Vol 4, Pages 250-263 4:250–263. https://doi.org/10.3390/ANALYTICA4020020
575. Kimling J, Maier M, Okenve B, et al (2006) Turkevich Method for Gold Nanoparticle Synthesis Revisited. Journal of Physical Chemistry B 110:15700–15707. https://doi.org/10.1021/JP061667W
576. Maksong S, Yemor T, Yanmanee S, et al (2019) Effect of nanoparticle geometry on sensitivity of metal nanoparticle based sensor. IOP Conf Ser Mater Sci Eng 578:012036. https://doi.org/10.1088/1757-899X/578/1/012036
577. Bastús NG, Merkoçi F, Piella J, Puntes V (2014) Synthesis of highly monodisperse citrate-stabilized silver nanoparticles of up to 200 nm: Kinetic control and catalytic properties. Chemistry of Materials 26:2836–2846. https://doi.org/10.1021/CM500316K
578. Dong X, Ji X, Wu H, et al (2009) Shape control of silver nanoparticles by stepwise citrate reduction. Journal of Physical Chemistry C 113:6573–6576. https://doi.org/10.1021/JP900775B

579. Dheyab MA, Aziz AA, Khaniabadi PM, et al (2022) Monodisperse Gold Nanoparticles: A Review on Synthesis and Their Application in Modern Medicine. Int J Mol Sci 23:7400. https://doi.org/10.3390/IJMS23137400
580. Dheyab MA, Aziz AA, Khaniabadi PM, et al (2022) Monodisperse Gold Nanoparticles: A Review on Synthesis and Their Application in Modern Medicine. International Journal of Molecular Sciences 2022, Vol 23, Page 7400 23:7400. https://doi.org/10.3390/IJMS23137400
581. Muzzio M, Li J, Yin Z, et al (2019) Monodisperse nanoparticles for catalysis and nanomedicine. Nanoscale 11:18946–18967. https://doi.org/10.1039/C9NR06080D
582. Menichetti A, Mavridi-Printezi A, Mordini D, Montalti M (2023) Effect of Size, Shape and Surface Functionalization on the Antibacterial Activity of Silver Nanoparticles. Journal of Functional Biomaterials 2023, Vol 14, Page 244 14:244. https://doi.org/10.3390/JFB14050244
583. Chen H, Kou X, Yang Z, et al (2008) Shape- and size-dependent refractive index sensitivity of gold nanoparticles. Langmuir 24:5233–5237. https://doi.org/10.1021/LA800305J
584. Jeon H Bin, Tsalu PV, Ha JW (2019) Shape Effect on the Refractive Index Sensitivity at Localized Surface Plasmon Resonance Inflection Points of Single Gold Nanocubes with Vertices. Scientific Reports 2019 9:1 9:1–8. https://doi.org/10.1038/s41598-019-50032-3
585. Barbosa S, Agrawal A, Rodríguez-Lorenzo L, et al (2010) Tuning size and sensing properties in colloidal gold nanostars. Langmuir 26:14943–14950. https://doi.org/10.1021/LA102559E
586. Piriya V.S A, Joseph P, Daniel S.C.G. K, et al (2017) Colorimetric sensors for rapid detection of various analytes. Materials Science and Engineering: C 78:1231–1245. https://doi.org/10.1016/J.MSEC.2017.05.018
587. Wilson AJ, Devasia D, Jain PK (2020) Nanoscale optical imaging in chemistry. Chem Soc Rev 49:6087–6112. https://doi.org/10.1039/D0CS00338G
588. Takano S, Hasegawa S, Suyama M, Tsukuda T (2018) Hydride Doping of Chemically Modified Gold-Based Superatoms. Acc Chem Res 51:3074–3083. https://doi.org/10.1021/ACS.ACCOUNTS.8B00399
589. Lou D, Fan L, Jiang T, Zhang Y (2022) Advances in nanoparticle-based lateral flow immunoassay for point-of-care testing. View 3:20200125. https://doi.org/10.1002/VIW.20200125
590. Burgess D, Morris M, Subramanyam M, et al (2021) Applications of Nanoparticle-Antibody Conjugates in Immunoassays and Tumor Imaging. AAPS J 23:43. https://doi.org/10.1208/S12248-021-00561-5
591. Matsumoto M, Kaneko K, Hara M, et al (2021) Covalent immobilization of gold nanoparticles on a plastic substrate and subsequent immobilization of biomolecules. RSC Adv 11:23409–23417. https://doi.org/10.1039/D1RA03902D
592. Kusuma SAF, Harmonis JA, Pratiwi R, Hasanah AN (2023) Gold Nanoparticle-Based Colorimetric Sensors: Properties and Application in Detection of Heavy Metals and Biological Molecules. Sensors 2023, Vol 23, Page 8172 23:8172. https://doi.org/10.3390/S23198172
593. Nath N, Chilkoti A (2002) A colorimetric gold nanoparticle biosensor: Effect of particle size on sensitivity. Annual International Conference of the IEEE Engineering in Medicine and Biology - Proceedings 1:574–575. https://doi.org/10.1109/IEMBS.2002.1136957
594. Jain PK, Lee KS, El-Sayed IH, El-Sayed MA (2006) Calculated Absorption and Scattering Properties of Gold Nanoparticles of Different Size, Shape, and Composition: Applications in Biological Imaging and Biomedicine. Journal of Physical Chemistry B 110:7238–7248. https://doi.org/10.1021/JP057170O

595. Blakey I, Merican Z, Thurecht KJ (2013) A method for controlling the aggregation of gold nanoparticles: Tuning of optical and spectroscopic properties. Langmuir 29:8266–8274. https://doi.org/10.1021/LA401361U
596. Jain PK, Lee KS, El-Sayed IH, El-Sayed MA (2006) Calculated Absorption and Scattering Properties of Gold Nanoparticles of Different Size, Shape, and Composition: Applications in Biological Imaging and Biomedicine. Journal of Physical Chemistry B 110:7238–7248. https://doi.org/10.1021/JP057170O
597. Quevedo AC, Guggenheim E, Briffa SM, et al (2021) UV-Vis Spectroscopic Characterization of Nanomaterials in Aqueous Media. J Vis Exp. https://doi.org/10.3791/61764
598. Flatabø R, Holm VRA, Eidsvåg H, et al (2017) Light absorption and scattering of 40–170 nm gold nanoparticles on glass substrates. Journal of Vacuum Science & Technology B, Nanotechnology and Microelectronics: Materials, Processing, Measurement, and Phenomena 35:. https://doi.org/10.1116/1.4994113/591655
599. FRENS G (1973) Controlled Nucleation for the Regulation of the Particle Size in Monodisperse Gold Suspensions. Nature Physical Science 1973 241:105 241:20–22. https://doi.org/10.1038/physci241020a0
600. Chow MK, Zukoski CF (1994) Gold Sol Formation Mechanisms: Role of Colloidal Stability. J Colloid Interface Sci 165:97–109. https://doi.org/10.1006/JCIS.1994.1210
601. Bastús NG, Comenge J, Puntes V (2011) Kinetically controlled seeded growth synthesis of citrate-stabilized gold nanoparticles of up to 200 nm: Size focusing versus ostwald ripening. Langmuir 27:11098–11105. https://doi.org/10.1021/LA201938U
602. Nur H, Nasir SMd (2008) Gold Nanoparticles Embedded on the Surface of Polyvinyl Alcohol Layer. Malaysian Journal of Fundamental and Applied Sciences 4:. https://doi.org/10.11113/MJFAS.V4N1.33
603. Wrigglesworth EG, Johnston JH (2021) Mie theory and the dichroic effect for spherical gold nanoparticles: an experimental approach. Nanoscale Adv 3:3530–3536. https://doi.org/10.1039/D1NA00148E
604. Bastús NG, Comenge J, Puntes V (2011) Kinetically controlled seeded growth synthesis of citrate-stabilized gold nanoparticles of up to 200 nm: Size focusing versus ostwald ripening. Langmuir 27:11098–11105. https://doi.org/10.1021/LA201938U
605. Bastús NG, Comenge J, Puntes V (2011) Kinetically controlled seeded growth synthesis of citrate-stabilized gold nanoparticles of up to 200 nm: Size focusing versus ostwald ripening. Langmuir 27:11098–11105. https://doi.org/10.1021/LA201938U
606. Wei X, Popov A, Hernandez R (2022) Electric Potential of Citrate-Capped Gold Nanoparticles Is Affected by Poly(allylamine hydrochloride) and Salt Concentration. ACS Appl Mater Interfaces 14:12538–12550. https://doi.org/10.1021/ACSAMI.1C24526
607. Izci M, Maksoudian C, Gonçalves F, et al (2022) Gold nanoparticle delivery to solid tumors: a multiparametric study on particle size and the tumor microenvironment. J Nanobiotechnology 20:1–20. https://doi.org/10.1186/S12951-022-01727-9
608. Schaal PA, Simon U (2013) Guided immobilisation of single gold nanoparticles by chemical electron beam lithography. Beilstein journal of nanotechnology 4:336–344. https://doi.org/10.3762/BJNANO.4.39
609. Erola MOA, Partanen A, Okoro SC, et al (2014) Controlled assembly of gold nanorods on nanopatterned surfaces: Effects of surface materials, pH and surfactant. Microelectron Eng 121:76–79. https://doi.org/10.1016/J.MEE.2014.03.030

610. Schaal PA, Simon U (2013) Guided immobilisation of single gold nanoparticles by chemical electron beam lithography. Beilstein Journal of Nanotechnology 4:39 4:336–344. https://doi.org/10.3762/BJNANO.4.39
611. Lee JH, Cho HY, Choi HK, et al (2018) Application of Gold Nanoparticle to Plasmonic Biosensors. International Journal of Molecular Sciences 2018, Vol 19, Page 2021 19:2021. https://doi.org/10.3390/IJMS19072021
612. Nonoyama T, Tanaka M, Inai Y, et al (2011) Ordered nanopattern arrangement of gold nanoparticles on β-sheet peptide templates through nucleobase pairing. ACS Nano 5:6174–6183. https://doi.org/10.1021/NN200711X
613. Mi S, Santschi C, Kiss M, et al (2018) Size Control of Self-Organized Gold Nanoparticles on Nanopatterned Single Crystal Diamond. International Conference on Optical MEMS and Nanophotonics 2018-July: https://doi.org/10.1109/OMN.2018.8454531
614. Ahmad F, Salem-Bekhit MM, Khan F, et al (2022) Unique Properties of Surface-Functionalized Nanoparticles for Bio-Application: Functionalization Mechanisms and Importance in Application. Nanomaterials 2022, Vol 12, Page 1333 12:1333. https://doi.org/10.3390/NANO12081333
615. Vollath D, Fischer FD, Holec D (2018) Surface energy of nanoparticles – influence of particle size and structure. Beilstein Journal of Nanotechnology 9:2265. https://doi.org/10.3762/BJNANO.9.211
616. Wu C, Gao C (2023) Methods for ligand exchange. Encyclopedia of Nanomaterials 277–301. https://doi.org/10.1016/B978-0-12-822425-0.00005-1
617. Lee GM, Craik CS (2009) Trapping moving targets with small molecules. Science (1979) 324:213–215. https://doi.org/10.1126/SCIENCE.1169378
618. Bespalova M, Öz R, Westerlund F, Krishnan M (2022) Single-Molecule Trapping and Measurement in a Nanostructured Lipid Bilayer System. Langmuir 38:13923–13934. https://doi.org/10.1021/ACS.LANGMUIR.2C02203
619. Lakshmipriya T, Hashim U, Gopinath SCB, Azizah N (2016) Microfluidic-based biosensor: signal enhancement by gold nanoparticle. Microsystem Technologies 22:2389–2395. https://doi.org/10.1007/S00542-016-3074-1
620. Wang L, Montagne F, Heinzelmann H, Pugin R (2011) Electrostatic-guided positioning of gold colloids using periodic nanopatterns produced by block copolymer lithography. J Mater Chem 21:1689–1692. https://doi.org/10.1039/C0JM02693J
621. Onilude HA, Vega MS, Clark AW (2023) Functionalisation of 20 nm citrate-coated gold nanoparticles using perfluorodecanethiol. 12431:34–38. https://doi.org/10.1117/12.2649965
622. Garifullina A, Shen AQ (2019) Optimized Immobilization of Biomolecules on Nonspherical Gold Nanostructures for Efficient Localized Surface Plasmon Resonance Biosensing. Anal Chem 91:15090–15098. https://doi.org/10.1021/ACS.ANALCHEM.9B03780
623. Lednický T, Bonyár A (2020) Large Scale Fabrication of Ordered Gold Nanoparticle-Epoxy Surface Nanocomposites and Their Application as Label-Free Plasmonic DNA Biosensors. ACS Appl Mater Interfaces 12:4804–4814. https://doi.org/10.1021/ACSAMI.9B20907
624. Matsumoto M, Kaneko K, Hara M, et al (2021) Covalent immobilization of gold nanoparticles on a plastic substrate and subsequent immobilization of biomolecules. RSC Adv 11:23409–23417. https://doi.org/10.1039/D1RA03902D
625. Dhotel A, Chen Z, Delbreilh L, et al (2013) Molecular Motions in Functional Self-Assembled Nanostructures. International Journal of Molecular Sciences 2013, Vol 14, Pages 2303-2333 14:2303–2333. https://doi.org/10.3390/IJMS14022303

Publications

Onilude, H. A., Vega, M. S., Clark, A. W. (2023). Functionalisation of 20 nm citrate-coated gold nanoparticles using perfluorodecanethiol. In: SPIE OPTO (Vol. 124310A). San Francisco, California, United States of America. March 15. **https://doi.org/10.1117/12.2649965**

Conference Presentations/Proceedings

Onilude, H. A., Vega, M. S., Clark, A. W. (2022). Reversible immobilisation of fluorous-functionalised gold nanoparticles for reconfigurable plasmonics arrays. In James Watt School of Engineering Mini-Conference. Glasgow, May 22, 2022.

Onilude, H. A., Vega, M. S., Clark, A. W. (2023). Reversible immobilisation of metal nanoparticles for reconfigurable plasmonics arrays. In James Watt School of Engineering Mini-Conference. Glasgow, August 31, 2023.

Appendices

Appendix 1.

(a). Concentration of gold Nanoparticles (14.9 nm from SEM)

Moles of sodium citrate = mass / molar mass = 0.73525 g / 294.1 g/mol ≈ 0.0025 moles

Moles of gold chloride = mass / molar mass = 0.0985 g / 393.83 g/mol ≈ 0.00025 moles

The number of moles of gold (Au) nanoparticles can be assumed to be equal to the number of moles of gold chloride used.

14.9 nanometers = 14.9×10^{-9} meters = $14.9 \times 10^{-9} \times 10^{6}$ micrometres = 14.9×10^{-3} micrometers

Mass of gold = Moles of gold × Molar mass of gold

= 0.0002502 moles × 197 g/mol

≈ 0.0492894 g

In milligrams (mg):

Mass of gold in mg = 0.0492894 g × 1000 mg/g

≈ 49.2894 mg

Assuming spherical gold nanoparticles are produced, the volume of a single gold nanoparticle.

Volume of particle (V) = $(4/3)\ \pi r^3$

Where radius (r) is half of the diameter.

From SEM and ImageJ analysis, the size of the NP = 14.9 nm particle:

r = 14.9 nm / 2 = 7.45 nm

r = 7.45×10^{-9} m (since 1 nm = 10^{-9} m)

Therefore, volume equals

V = $(4/3)\ \pi\ (7.45 \times 10^{-9}\ m)^3$

≈ $1.725 \times 10^{-21}\ m^3$

Number of Au atoms = Moles of gold × Avogadro's number or constant

≈ 0.0002502 moles × $6.022 \times 10^{23}\ mol^{-1}$

≈ 1.5067×10^{20}

Total Au nanoparticles volume = Volume of one nanoparticle × Number of nanoparticles

≈ $1.725 \times 10^{-21}\ m^3$/particle × 1.5067×10^{20} particles

≈ $2.60 \times 10^{-1}\ m^3$

(ρ) = mass/volume

Volume of gold = Mass of gold/density of gold

= 49.2894 mg / (19.32 g/cm^3 (converted to mg/m^3))

= 49.2894 mg / 19.32 × 10^6 mg/m^3

≈ 2.55 × 10^{-6} m^3

In litres (since 1 m^3 = 1000 L):

Volume of gold in litres = 2.55 × 10^{-6} m^3 × 1000 L/m^3

≈ 2.55 × 10^{-3} L

Concentration in mg/mL = Mass of gold in mg / Volume of solution in mL

= 49.2894 mg / 500 mL

≈ 0.0986 mg/mL

Concentration in mol/dm^3 = Moles of gold / Volume of solution in dm^3

= 0.0002502 moles / 0.5 dm^3

The concentration of gold nanoparticles in 500 mL of solution **≈ 0.0005004 mol/dm^3**

Using 2 mL of the gold NPs dispersed into 3nl of ethanol gives a concentration.

$C_1V_1 = C_2V_2$

C1 = Initial concentration = **0.0986 mg/mL**

C2 = Final concentration =?

V1 = Initial volume = 2 mL

V2 = Final volume in ethanolic solution = 5 mL

C2 = 0.1972/5 = 0.03944 mg/mL or 2.0016x10^{-4} **mol/dm^3 (0.2 mM)**

(b.) **Concentration of gold Nanoparticles (35.53 nm from SEM)**

Moles of gold (III) chloride trihydrate = Concentration (mol/L) × Volume (L)

= 0.25 × 10^{-3} mol/L × 0.050 L

= 1.25 × 10^{-5} mol

The gold nanoparticles' volume is found using the diameter given by SEM, which is 35.53 nm. First, let's convert this to a radius in meters:

Radius (r) = Diameter / 2

= 35.53 nm / 2

= 17.765 nm

= 17.765 × 10^{-9} m (since 1 nm = 10^{-9} m)

Assuming that the NP is spherical. Volume, V equals

$V = (4/3)\ \pi r^3$

$V \approx (4/3)\ \pi\ (17.765 \times 10^{-9}\ m)^3$

$V \approx 2.350 \times 10^{-23}\ m^3$ per particle

Total volume of gold nanoparticles (mL)

≈ 177.0 mL

The density of gold is 19.3 g/cm^3, and the mass of gold in the nanoparticles is:

Mass = density × volume

= 19.3 g/cm^3 × 177.0 cm^3

= 3416.1 g

Converting the mass to milligrams (mg):

= 3,416,100.0 mg

The concentration of gold nanoparticles in mg/mL equals:

Concentration (mg/mL) = Mass of gold nanoparticles (mg) / Volume of solution (mL)

= 3,416,100 mg/ 50,000 mL

= 68.3 mg/mL

To calculate the concentration in mol/dm^3:

Molar concentration (mol/dm^3) = moles of gold / volume of solution (dm^3)

= 1.25×10^{-5} mol / 0.05 dm^3

= **2.5×10^{-4} mol/dm^3**

Using 2 mL of the gold NPs dispersed into 3 mL of ethanol gives a concentration:

$C_1V_1 = C_2V_2$

C1 = Initial concentration = **68.3 mg/mL**

C2 = Final concentration =?

V1 = Initial volume = 2 mL

V2 = Final volume = 5 mL

C2 = **68.3 mg/mL** * 2/5 = 27.32 mg/mL

= 0.14 **mol/dm^3**

(c.) **Silver NPs**

Moles of silver equals 0.01M *0.01L = 0.0001 moles

Molar mass of silver = 107.8682 g/mol

Moles per nanoparticle = Mass of a single NP / Molar mass

Moles per NP = 3.514 *10^{-19} g * 107.8682 g/mol

The average size of the silver NP from SEM = 40 nm

Density of silver = 10.49 g/cm^3

Volume of a single particle = Volume = (4/3) * π * (20 × $10^{-9\ m}$)^3

Volume = 3.351 * 10^{-23} m^3 per/NP

For a single nanoparticle, mass = volume * density

= 3.351 * 10^{-23} m^3 per/NP * 10.49

= 3.351 * 10^{-29} g

Molar mass of silver = 107.8682 g/mol

Moles per nanoparticle = Mass of a single NP / Molar mass

Moles per NP= 3.257 *10^{-21}moles

Total moles of silver = 0.01 M * 0.01 L = 0.0001 moles

Total number of NPs = Total moles / Moles per NP

Total NPs = 0.0001 moles *3.257 *10^{-21}moles/NP

= 3.07 * 10^{16}/ nanoparticles

Total mass = Mass of a single NP × Total number of NPs

Total mass = 3.514 * 10^{-19} g/NP * 3.07 * 10^{16}/ nanoparticles

Total mass = 1.078 g = 1078 mg

Concentration = Total mass / Volume of solution

Concentration = Total mass / Volume of solution = 10.78 mg/mL

Concentration in Molarity for 3 mL Solution:

Original molarity = 0.001 mol/dm^3

In 3 mL of ethanolic solution =**0.003 mM**

Appendix 2.

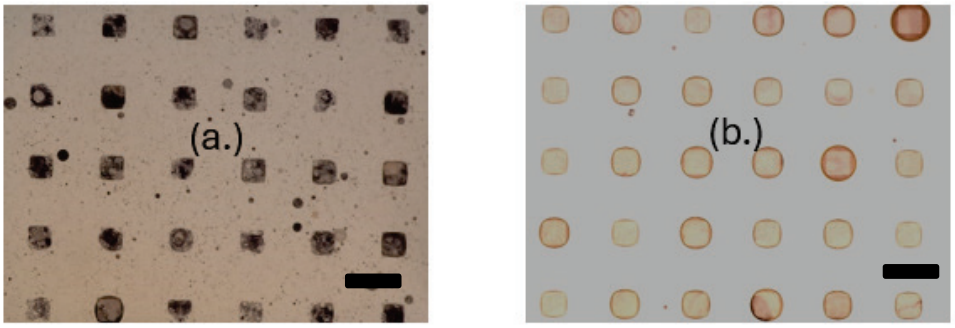

Figure 72: Comparison between (a.) citrate-coated silver NPs and (b.) HH-coated Silver NP after solvent washes in water. After washing, a black remnant or head was seen in (a.) but absent from (b.) Scale bar = 50 µm. 4x Mag.

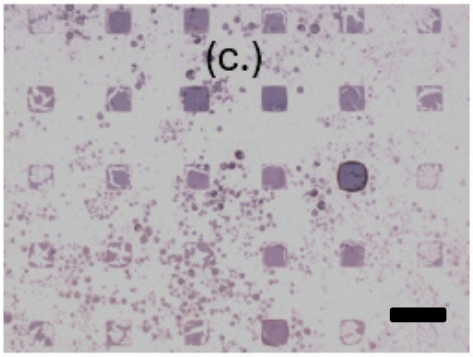

Figure 73 : The immobilisation of gold nanoparticles synthesised using the citrate-coated method after solvent exchange in water (c.). Scale bar = 50 µm. 4x Mag.

Appendix 3.

Other self-assembled layers formed with random patterns using the fluorous effects.

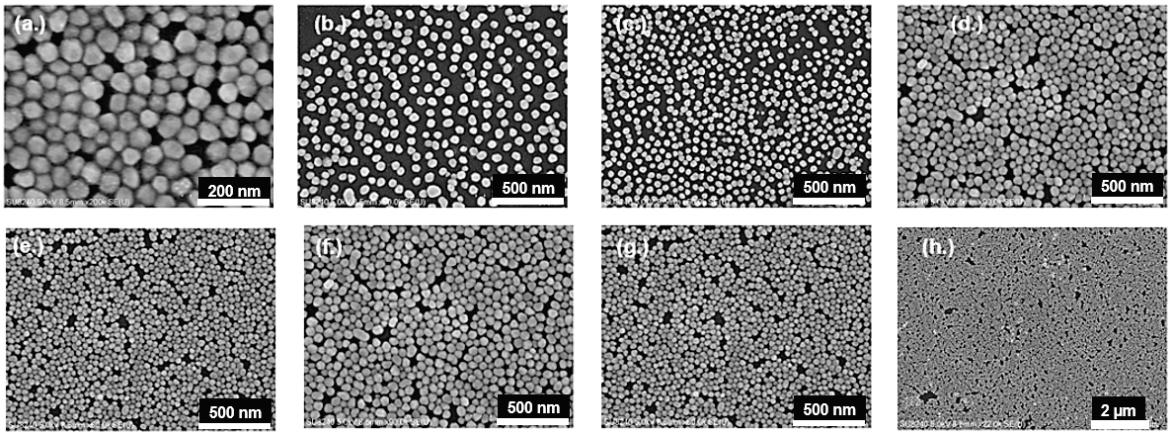

Figure 74: SEM micrographs showing the ability of fluorous modified 55 nm gold nanoparticles to form a self-assembly monolayer using the same protocol on bare glass. Images were taken at different regions on the surface.Various scale bars.

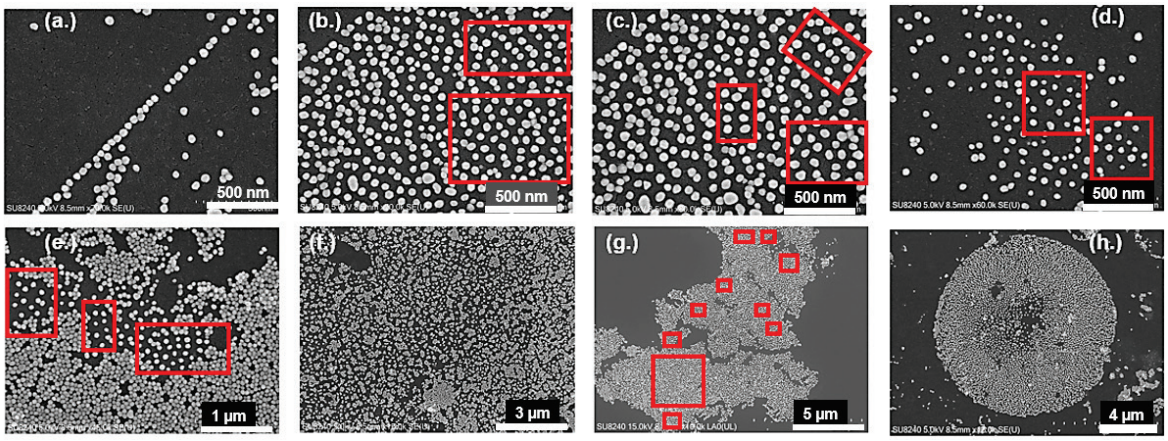

Figure 75: Figure a-h shows SEM micrographs with the ability of fluorous modified 55 nm gold nanoparticles to self-assemble and arrange into different structures on the fluorous modified surface. The red squares show areas where different patterns created by fluorous are visible. Various scale bars.